RESOLVING LOW ENERGY SPECTRAL PROPERTIES IN CORRELATED ELECTRON SYSTEMS

BY GOETZ MOELLER

A dissertation submitted to the

Graduate School—New Brunswick

Rutgers, The State University of New Jersey

in partial fulfillment of the requirements

for the degree of

Doctor of Philosophy

Graduate Program in Physics and Astronomy

Written under the direction of

G. Kotliar and A. E. Ruckenstein

and approved by

_____

_____

_____

_____

New Brunswick, New Jersey

October, 1994

© 1994
Goetz Moeller
ALL RIGHTS RESERVED

ABSTRACT OF THE DISSERTATION

Resolving Low Energy Spectral Properties in Correlated Electron Systems

by Goetz Moeller

Dissertation Director: G. Kotliar and A. E. Ruckenstein

We use the limit of infinite dimensionality to study the metal-insulator transition and the transfer of spectral weight in the Falicov-Kimball and Hubbard models.

The latter displays a non trivial critical point, the physics of which we analyze using a novel self-consistent projective technique. This allows us to determine the critical as well as the low temperature properties of the Hubbard model in the limit of infinite dimensions exactly. The method is general and can be applied to study any system exhibiting a separation of scales.

We furthermore propose a model which mimics the effect of $1/d$ corrections to the limit of infinite dimensionality. This permits us to discuss modifications of the Mott transition, as well as to investigate the competition between Kondo and RKKY interactions.

Preface

The results reported in Chapters 3 and 9 of this thesis were obtained under supervision of Prof. A. Ruckenstein. Chapters 4 through 8 were written under the direction of Prof. G. Kotliar.

A certain amount of overlap between some of the chapters has been allowed in order to enhance clarity and to make most of them essentially self-contained units.

Acknowledgements

My deepest gratitude goes to Gabi Kotliar, whose enthusiasm, constant encouragement and love of science have made working with him a truly intense, rewarding and fun experience.

Lots of thanks also to Andrei Ruckenstein for his support, his friendship, his tolerance and all the crazy discussions we had. Collaborating with him has been a true challenge, and I will always admire his upbeat, gentlemanly and artistic approach to the world.

Special thanks go to Marcelo Rozenberg. Collaborating and hanging out together have been provocative, stimulating and lots of fun.

Many thanks also to the other people I collaborated with over the years. I will never forget the long and thought-provoking exchanges with Vlad Dobrosavljević and the discussions full of excitement with Qimiao Si.

Acknowledgements furthermore go to my officemate, Stanko Barle, for his astounding patience, Henrik Kajüter for post-physics guidance, Marc Horbach and Eduardo Miranda for lots of discussions and lunches together, Ilias Perakis for stimulating discussions, Florian Gebhard and the Gang in Marburg, in particular Arne Schulze and Torsten Meier, for an exciting summer in Germany, and the many friends inside and outside of physics who have made the last years fun and enjoyable.

Finally, I would like to thank my parents for their love, support and encouragement during this period of my life.

Dedication

Dedicated to all the people who gave me
love and support, friendship and encouragement
and thus
happiness.

Table of Contents

Abstract ii

Preface iii

Acknowledgements iv

Dedication v

List of Figures ix

List of Abbreviations xvi

1. Introduction 1

1.1. Strong Correlations in Many-Electron Systems 1

1.2. The Focus of the Present Work 5

2. Infinite Dimensionality – A Primer 8

2.1. Infinite Dimensionality – A Mean-field Theory for Strongly Correlated Systems 8

2.2. An Explicit Example: The Hubbard Model in Infinite Dimensions . . . 10

2.3. The Anderson Connection 14

2.4. A Path to Solving Self-consistent Impurity Problems 14

3. Metal-to-Insulator Transition and Transfer of Spectral Weight in the Falicov-Kimball Model 21

4. The Mott Transition in the Hubbard Model 39

4.1. Methodology 42

4.2. Results 47

5. Doping the Hubbard Model 54

5.1. Coexistence at Finite Doping 54
5.2. Charge Susceptibility 56
5.3. Transfer of Spectral Weight 60

6. Resolving the Low Energy Properties: The Self-Consistent Projective Technique 66
6.1. Separation of Scales and How to Take Advantage of It 66
6.1.1. Determining the Physical Properties *at* the Critical Point 73
6.1.2. Determining the Physical Properties *near* the Critical Point . . . 74
6.2. The Explicit Form of the Canonical Transformation 77

7. Critical Properties of the Mott Transition in the Hubbard Model . 88
7.1. The Critical Point of the Half-Filled Hubbard Model 88
7.1.1. A Simple Toy Model 92
7.1.2. Numerical Solution to the Problem at Criticality 94
7.2. The Critical Properties of the Doped Hubbard Model 103
7.2.1. Determining the Position of the Resonance 103
7.2.2. Critical Properties at Finite Doping 111
7.3. The Approach to the Critical Point 117
7.3.1. Once Again: Analysis of the Toy Model 117
7.3.2. Approach to the Critical Point at Half-filling 118
7.3.3. Approach to the Critical Point Away from Half-filling 119

8. The Hubbard Model at Finite Temperatures 125
8.1. Numerical Implementation 126
8.2. Results 128

9. Beyond Infinite Dimensions—A Cluster Approach 137
9.1. The Model 139
9.2. Results 142
9.3. Beyond Perturbation Theory 151

9.4. Conclusions 154

10. Conclusion 155

Appendix A. Effective Low Energy Operators 159

A.1. Coefficients of the effective F_σ operators 159

A.2. Coefficients of the effective Hamiltonian $\mathcal{H}^{(3,can)}$ 160

A.3. Coefficients of the transformed number operator N_σ 161

Appendix B. Determination of the Critical Behavior: A $1+1$ Site Toy Anderson Model 162

Appendix C. Solution to the Insulator: A 2+1 Site Toy Model 167

Appendix D. The Self-Consistent Projective Technique: A $1+1$ Site Projected Toy Model 172

Appendix E. From Continued Fraction to Partial Fraction – Determining the Poles and Weights of G 175

Appendix F. Stability of $d = \infty$ Solutions 177

References 182

Vita 188

List of Figures

2.1. Illustration of the reduction to single site problem by integrating out sites 1 to m in a Bethe lattice 11

2.2. Relative difference between exact and fitted positive moments $\Delta m_1^+/m_1^+$, $\Delta m_2^+/m_2^+$, $\Delta m_3^+/m_3^+$, $\Delta m_4^+/m_4^+$ as obtained from the χ^2 fit method for $U = 2.7$ and half-filling as a function of the number of sites. 18

3.1. Pinning curves at $T = 0$ ($E_f = -0.5$) with impurity concentration (from left to right) $n_f = 1, 0$. 27

3.2. Conduction electron density of states at half filling ($n = 1$) for interaction strengths $U = 0.5$ (solid line), $U = 2.5$ (dotted line), $U = 4.5$ (dashed line). Energies are measured with respect to the center of the bare conduction band. 28

3.3. AC conductivity at half filling for interaction strengths $U = 0.5$ (solid line), $U = 2.5$ (dotted line), $U = 4.5$ (dashed line). 29

3.4. Imaginary part of the self energy at half filling ($n = 1$) for interaction strengths $U = 0.3$ (solid line), $U = 1.3$ (dotted line), $U = 2.3$ (dashed line). Energies are measured with respect to the chemical potential. . . 30

3.5. AC conductivity at $\omega = 0$ at half filling as a function of the interaction strength U for Gaussian density of states (solid line) and constant density of states (dotted line) 32

3.6. Conduction electron density of states for interaction strengths $U = 0.5$ (solid line), $U = 2.5$ (dotted line) and $U = 4.5$ (dashed line) for finite hole concentration ($n = 0.92$, $T = 0.1$, $E_f = 0$). Energies are measured with respect to the center of the bare conduction band. 33

3.7. AC conductivity for interaction strengths $U = 0.5$ (solid line), $U = 2.5$ (dotted line) and $U = 4.5$ (dashed line), for finite hole concentration ($n = 0.92$, $E_f = 0$, $T = 0.1$). 34

3.8. Imaginary part of the self energy for interaction strengths $U = 0.5$ (solid line), $U = 1.2$ (dotted line) and $U = 2.5$ (dashed line) for finite hole concentration ($n = 0.92$, $E_f = 0$, $T = 0.1$). Energies are measured with respect to the chemical potential. 35

3.9. Conduction electron density for fillings $n = 0.72$ (solid line), $n = 0.92$ (dotted line) and $n = 1$ (dashed line), ($U = 2.5$, $T = 0.1$, $E_f = 0$). Energies are measured with respect to the center of the bare conduction band. 36

3.10. AC conductivity for fillings $n = 0.72$ (solid line), $n = 0.92$ (dotted line) and $n = 1$ (dashed line), ($U = 2.5$, $T = 0.1$, $E_f = 0$). 37

4.1. Coexisting solutions for the Green functions at $T = 0$, $U = 2.7$ at half-filling. Also shown (but indistinguishable) are the fitted functions using a fictitious temperature "T"=0.005 and N=8 sites. 47

4.2. Density of states of the half-filled Hubbard model at $T = 0$, $U = 2.8$ corresponding to insulating (top, N=9 sites) and metallic (bottom, N=10 sites) solutions. A small broadening $\delta = 0.01$ of the poles is chosen to indicate their structure. 49

4.3. Total, kinetic and potential energies of metallic and insulating solutions in the coexistence region as functions of the interaction U for N=8 in the half-filled Hubbard model. In the inset we show the energy difference between the two solutions. 50

4.4. Difference between double occupancies of metallic and insulating solutions. Solid line: N=10 metal - N=9 insulator; solid dotted line: N=8 metal - N=7 insulator; thin dotted line: N=6 metal - N=5 insulator. Thin line: Extrapolation. 52

5.1. Coexistence region of metallic and insulating solutions at zero temperature and finite doping in the $\Delta\mu - U$ plane where $\Delta\mu = \mu - U/2$. (N=5 and partly N=7 sites for U_{c1}, μ_{c2} from Chap. 7. 55

5.2. Total particle concentration per site as a function of $\Delta\mu = \mu - U/2$ for interactions U=2.7, U=3.5, U=4.0, U=5.0 (Lanczos diagonalization, N=8 sites). 57

5.3. Spectral function of the Hubbard model at $T = 0$ for $U = 4$,$\delta = 0.01, 0.09, 0.2, 0.35, 0.51, 0.7$. The energies are measured with respect to the Fermi level. For clarity the resonance is marked with an arrow. The results were obtained using an N=8 particle cluster with broadening $\epsilon = 0.075$ of the poles. 59

5.4. a) Regimes of the Hubbard model in the $U - \Delta\mu$ plane where $\Delta\mu$ is the chemical potential measured with respect to the value at half filling. b)Regimes of the Hubbard model in the $U - n$ plane. 61

5.5. High energy spectral weight as a function of doping for $U = 3.5$, $U = 5.0$, $U = 8.0$ (N=8). Also shown is the $U = \infty$ value $w^+ = \frac{1}{2}(1 - \delta)$. The inset depicts the weight of the upper Hubbard band for $U = 5$ as obtained from the $1 + 1$ toy model in comparison with the result from Lanczos diagonalization. 64

6.1. Schematic plot of the spectral functions of the conduction electrons and of the impurity configurations, illustrating the separation of scales into low and high energy contributions. 69

6.2. Schematic representation of the canonical transformation 71

6.3. Energies of the lowest lying states (doublet, "empty" state and lowest lying higher energy state in $\mathcal{H}_{at}$ for $U = 3.5$ and $N = 5$ as a function of the chemical potential. The particle density ranges from $n = 0.6$ to $n = 1.0$. The inset shows the corresponding plot for $U = 4$. 87

7.1. $J_{spin} = 2\Gamma$ at half-filling as a function of the interaction analytically (2+1 toy model) and for cluster sizes $N = 3, 5, 7$. The value corresponding to the critical point U_c is marked with a circle. 95

7.2. Imaginary part of the Matsubara Green function versus the rescaled frequency $\tilde{\omega}_n$ for system size $N = 6, 8, 10$ and non-interacting (semi-circular) density of states. 96

7.3. Single particle spectral function as function of the rescaled frequency $\tilde{\omega}$ (N=10) with a broadenings $\epsilon = 0.01, 0.0235, 0.0075, 0.1$, and 0.2. Plot (f) shows the value of $-ImG(0^+)$ as a function of the broadening ϵ. . . 98

7.4. Real part of the local spin susceptibility as a function of the rescaled Matsubara frequency $\tilde{\nu}_n$ for $N = 10$. 100

7.5. J_{spin} and J_{pot} as a function of $\Delta\mu$ for $U = 3, 4, 5, 10$ with cluster sizes $N = 3, 5, 7$. Also shown (thin solid line) is the analytic result. 108

7.6. Position of the quasiparticle resonance for vanishing resonance width as a function of the interaction (solid). The dotted line indicates the beginning of the incoherent lower Hubbard bands as predicted by a ridid band picture. The position of the resonance is measured with respect to the center of gravity of the bands. The figure is reflection symmetric about the $\Delta\mu = \mu - U/2 = 0$ axis for electron doping. 109

7.7. J_{spin} (dashed line) and J_{pot} (dotted line) as a function of $\Delta\mu$ for $U = 40$ with cluster size $N = 7$ together with the exact $U = \infty$ result (solid line). 110

7.8. Scaling function of $-ImG(\omega + i\delta)$ with broadening $\delta = 0.1$ at the critical point (infinitesimal doping) for interactions $U = 5$ (solid line) and $U = 3.2$ (dashed line). 112

7.9. Rescaled Matsubara Green $-ImG(i\omega_n)$ at infinitesimal hole doping for interactions $U = 3$ (solid line), $U = 4$ (thick dashed line), and $U = 5$ (dotted line). (Projective technique, N=8) 113

7.10. Kondo coupling $\langle \vec{S} \cdot \vec{s}_L \rangle$ at the critical point as a function of the interaction U. Inset: J_{spin} and J_{pot} at the critical point as a function of the interaction U. 115

7.11. Generalized Wilson ratio $\frac{\chi_s/\chi_{s,loc}^{free}}{\gamma/\gamma^{free}}$ as a function of the interaction U. The inset shows the local spin susceptibility $\chi_s^{loc}(0)$ in units of $(g\mu_B/2)^2$. . . 116

7.12. Ratio of $\frac{\partial^2\bar{\Sigma}}{\partial\bar{\omega}^2}/(\frac{\partial\bar{\Sigma}}{\partial\bar{\omega}})^2|_{\bar{\omega}=0}$ for infinitesimal doping as a function of the interaction U. 117

7.13. Quasi-particle weight near the Mott transition at half-filling as obtained using the self-consistent projective technique. Shown are the results for clusters of N=6 and 8 sites in the low frequency region as well as 3 and 5 sites at high frequencies. The inset shows the low energy spectral weight as obtained from the full Hubbard model with 10 sites in comparison with the result from the self-consistent technique using N=8 (low en.) and N=5 (high en). 120

7.14. Low energy spectral weight w (thick line) and quasiparticle residue z (dotted line) near the Mott transition at half-filling as obtained using the self-consistent projective technique. Shown are the results for the cluster with N=8 sites in the low frequency region and N=5 sites at high frequencies. The inset shows the quasiparticle residue z as obtained from the full Hubbard model with 10 sites in comparison with the result from the self-consistent technique using N=8 (low en.) and N=5 (high en). . 121

7.15. Low energy spectral weight w (thick line) and quasiparticle residue z (dotted line) near the Mott transition for $U = 4$. (Self-consistent technique, $N = 6$ and $N = 8$ at low energies, $N = 5$ at high energies.) . . . 122

7.16. $\Sigma''(\omega = 0)z^2$ near the critical point for $U = 4$. (Self-consistent technique, $N = 8$ at low energies, $N = 5$ at high energies.) 123

8.1. Inverse quasiparticle scattering rate $\Sigma(\omega = 0, T)$ as a function of temperature in the half filled Hubbard model for interaction $U = 2.5$. Shown are the results obtained using the full Hubbard model with N=6 (thick dashed line) and the self-consistent projective technique (thick line) with N=6 (resonance) plus N=5 (high energy). The thin dashed line is obtained by fitting the data. 129

8.2. Transition temperature of the first order metal-insulator transition at half filling as a function of the interaction. 130

8.3. Particle number per site as a function of temperature for $U = 4$ and $\Delta\mu = -1.05$, -1.2, -1.4, and -1.6 using $N = 5 + 1$ cluster, exact diagonalization. 131

8.4. Single particle density of states $-ImG(\omega + i\delta)$ for $U = 4$ and $n = 0.9$ at temperatures $T = 0.02$, 0.06, and 0.1. $N = 5 + 1$ cluster, exact diagonalization, $\delta = 0.075$. 133

8.5. Inverse quasiparticle scattering rate $Im\Sigma(\omega = 0, T)$ as a function of temperature in the Hubbard model for interaction $U = 4.0$ and particle concentrations $n = 0.600$, $n = 0.698$, $n = 0.800$ and $n = 0.899$. From Hubbard with N=5+1 sites. 134

8.6. Inverse quasiparticle scattering rate $Im\Sigma(\omega = 0, T)$ as a function of temperature in the Hubbard model using the self-consistent projective technique (N=8 at low en., N=5 at high energies) for interaction $U = 4.0$ and $\mu = -1.05$ ($n \approx 0.95$). 135

8.7. Local susceptibility $\chi_s(\omega = 0, T)$ as a a function of temperature in the Hubbard model for interaction $U = 4.0$ and particle concentrations $n = 0.600$, $n = 0.698$, $n = 0.800$ and $n = 0.899$. Also shown are the corresponding susceptibilities for $U = 0$. 136

9.1. Lattice structure of the doubled Bethe lattice and effective two impurity cluster. 140

9.2. Second-order perturbation theory self energy diagram. 143

9.3. Phase diagram in the $U - t_{ab}$ plane. Shown are the spinodal lines and the second order points A and B. 144

9.4. Density of states for interactions a) $U = 0$ and b) $U = 1.5$ for $t_{ab} = 0.0, 0.25, 0.5, 0.75, 1.0$. 145

9.5. a) Quasiparticle residue $z = 1/(1 - \frac{\partial\Sigma}{\partial\omega})$ in the metallic phase as a function of the interaction U for $t_{ab} = 0.2$. b) Density of States ($-ImG(0^+)$ of metallic (solid line) and insulating (dotted line) solutions at $t_{ab} = 0.2$ as a function of the interaction U. 146

9.6. Density of States for $t_{ab} = 0.2$ and interactions $U = 1.0, 1.8, 2.6, 3.4$. . . 147

9.7. Difference between the energies of metallic and insulating solutions for $t_a b = 0.2$ as a function of the interaction U. 148

9.8. Specific heat as a function of temperature at U=2.5 for $t_{ab} = 0.0, 0.2, 0.4$. 150

9.9. Specific Heat at U=3.5 for $t_{ab} = 0.0, 0.15, 0.3$. 151

9.10. 153

F.1. Landau free energy for $t_{ab} = 0$, $U = 2.6$ and temperatures $T = 0.003 - 0.033$ in steps of $\Delta T = 0.006$. The inset shows the free energy difference between the two minima as a function of temperature. 181

List of Abbreviations

DOS	Density of states
QMC	Quantum Monte Carlo
IPT	Iterated perturbation theory

Chapter 1

Introduction

1.1 Strong Correlations in Many-Electron Systems

The discovery of the high temperature superconductors [1] in 1986 has sparked a renewed interest in the old problem of strong electronic correlations in condensed matter physics. In strongly correlated materials *itinerant* electrons are subject to a strong *local* Coulomb repulsion. The common feature in the theoretical description of strongly correlated systems is the necessity to go beyond the traditional concepts and methods of condensed matter physics, the independent particle approximations á la Hartree-Fock and perturbation theory.

While high temperature superconductivity as well as anomalous normal state properties [2] of the copper oxides are likely to be the most fascinating examples of strongly correlated electron systems, they are by far not the only ones. The archetypical case in which strong electronic correlations lead to highly non-trivial physical consequences is the Kondo effect [3, 4], in which conduction electrons scatter off a localized magnetic impurity, leading to a minimum in the electrical resistivity. Other examples are the physics of nuclear matter, liquid ^{3}He [5] and heavy Fermion materials [6]. In liquid ^{3}He [5] – due to its nuclear spin a fermionic system – the atoms experience a strong Coulomb repulsion as a result of the high density of the system. In the heavy Fermion compounds [6], f-electrons are subject to a screened and thus essentially *local* Coulomb interaction which can not be treated in a mean-field way.

In this thesis we will consider other important examples. These are the Mott-Hubbard metal-insulator transition [7] as observed e.g. in V_2O_3, as well as the redistribution of spectral weight between high and low energy scales in the density of states [8, 9, 10, 11] upon doping, as observed in spectroscopic measurements on (for

example) the cuprates.

Given a specific phenomenon, the job of the theoretical physicist is twofold: One has to find an appropriate model describing the phenomenon; given this, one has to proceed by solving the latter. In the following we will essentially be concerned with the second aspect, since many of the problems in the field of strong correlations are due to the fact, that there are only few non-trivial models that can be solved exactly, such that finding systematic approximations capturing the essential physics becomes a crucial and challenging undertaking.

As mentioned, in most of the systems mentioned above *itinerant* electrons are subject to a strong *local* Coulomb repulsion. Since even the simplest theoretical models describing strongly correlated electrons are not fully understood, we will mostly focus on what may be considered the simplest model capturing the competition between itinerant and local correlations, the single band Hubbard model. This model is given by the Hamiltonian

$$\mathcal{H} = -\sum_{i,j;\sigma} t_{ij,\sigma} f^{\dagger}_{i\sigma} f_{j\sigma} + U \sum_{i} n_{f\uparrow} n_{f\downarrow} - \mu \sum_{i} (n_{f\uparrow} + n_{f\downarrow}) \tag{1.1}$$

which describes fermions created by operators $f^{\dagger}_{i\sigma}$ hopping on a lattice with hopping amplitude $t_{ij,\sigma}$ and experiencing a strong on-site Coulomb repulsion U. On our way to understanding this problem we will also consider an even simpler relative, the Falicov-Kimball model, which is essentially a Hubbard model in which only one spin species has a kinetic term, i.e. $t_{ij;\uparrow} = t$, $t_{ij;\downarrow} = 0$.

It should be emphasized that the full Hubbard model is expected to describe some of the physics of strongly correlated materials (e.g. the metal-insulator transition), has been used successfully in the description of some of the materials exhibiting properties associated with strong correlations (e.g. ^{3}He [5], V_2O_3 [7, 12, 13]) and may account for the complex phenomenology seen in high temperature superconductors [14, 15].

The essential difficulty arises from the fact that traditional perturbative approaches [16] fail. This is due to the fact that an expansion in the kinetic energy, which is formally small, is a singular perturbation, while the interaction term in the physical systems of interest is quite large. Furthermore, the competition between local and

itinerant aspects characterizing strongly correlated electron systems leads to problems which are dominated by *several energy scales*. Those are generally harder to treat, and in the case of strong correlation often have the additional complication that one of those may become extremely small. The classic example is again the Kondo effect, in which virtual transitions to highly excited states lead to the appearance of a scattering resonance of very small width at the Fermi level [4].

In order to put this thesis into perspective, let us briefly recapitulate some of the approaches to the rather innocent looking Hubbard Hamiltonian which have been made over the decades.

Several simple models of strongly correlated systems, in particular the Hubbard model, can be solved *exactly* in one spatial dimension using Bethe Ansatz methods [17, 18]. While these solutions have given invaluable insights, the extraction of important physical information, in particular of dynamical correlation functions, is still not possible. Additionally, it is a matter of debate which features of the one-dimensional solutions survive in higher spatial dimensions. In particular, in the case of the Hubbard model, the Bethe ansatz solution shows that the model is insulating for any finite interactions U, which is known to be incorrect at least in the limit of infinite dimensions [19, 20, 21]. Moreover, the Hubbard model in one dimensions is not a Fermi liquid, a property for which there is no evidence in infinite dimensions.

Among the first serious attacks on the strong correlation problem in more than one dimension were the original papers by Hubbard [22, 23, 24] on the Hubbard model. Hubbard introduced various expansions around the atomic limit based on *equation of motion* and *diagrammatic schemes*, which are are decoupled in an uncontrolled way, While these approximations capture the high-energy features of the Hubbard model correctly, they are uncontrolled and violate sumrules as well as conservation laws, often failing to give sensible results in simple physical limits. Thus they cannot be trusted to adequately describe the low energy physics of the metallic regime.

At the same time, techniques based on variational trial wavefunctions [25, 26] were developed, yielding a good description of the metallic region, but failing to describe the incoherent high energy features correctly. In addition, these schemes still require the

evaluation of expectation values with rather complicated many-body wave functions, a formidable task which so far has been addressed successfully only numerically [27] and in infinite dimensions [28].

A highly successful approach to the strong correlation problem is based on *functional integrals with auxiliary fields* ("slave bosons", "slave fermions") [29, 30, 31, 32], which become exact when the size of the *symmetry group* N goes to infinity. While these have provided insights into the low energy behavior of the Hubbard model and its relatives, they are largely limited to the case in which the interaction strength goes to infinity (for extensions beyond this limit see Ref. [33]) and do not capture the incoherent features.

Numerical approaches [34] to the strong correlation problem based on the exact diagonalization of small clusters have led to important insights, but are troubled by the tremendous size of the Hilbert space involved. As an example, for a ten-site lattice in which the spin in z direction as well as the number of particles are conserved, the number of basisvectors spanning the Hilbert space at half-filling (i.e. one electron per site) is already 63504. Thus even state of the art computers cannot handle systems of sizes coming even remotely close to the systems encountered in real life. This does not only imply that finite size effects may be large, but in particular that the level spacings are much too large to capture the low energy physics accessed experimentally correctly. To obtain a resolution of $5meV$ or $50K$ for a one-dimensional system with a bandwidth of $1eV$, a 200 site cluster is needed. The total size of the Hilbert space at half-filling then is 10^{117} [35], a number already larger that the estimated number of particles in the universe.

One of the most promising approaches to the strong correlation problem is the limit of infinite dimensionality [36]. The major advantage of this framework is that for the first time it allows the formulation of a *systematic* mean-field approach to strongly correlated materials [37] in which all energy scales are treated on an equal footing. Since we believe that this framework is the most powerful technique currently at our disposal, we will use this approach in our investigations. We will review this approach and motivate our assessment in Chapter 2.

It should be emphasized that a tremendous amount of work has been done in the

field of strong correlations. Good reviews are found in the references cited, as well as in the comparatively recent books by E. Fradkin [38], P. Fulde [39], and A. Hewson [4].

1.2 The Focus of the Present Work

In this thesis we will use the limit of infinite dimensionality to study the physics of the Falicov-Kimball and Hubbard models, as well as propose a model which enables us to go beyond the limit of infinite dimensionality. In particular, we will develop a novel method, the *self-consistent projective technique*, which allows us to study the low energy features and the critical properties of models of strongly correlated fermions in infinite dimensions.

We will start by reviewing the essentials of the limit of infinite dimensionality in Chapter 2. This review emphasizes the aspect that in this limit a lattice model reduces to an impurity model in a self-consistently determined bath, yielding a natural mean-field theory of strongly correlated electron systems. Furthermore, we will describe a powerful technique [40] which enables us to efficiently solve the corresponding impurity model self-consistently.

In Chapter 3 we will study the metal-insulator transition, the transfer of spectral weight upon doping, as well as a possible scenario for the breakdown of Fermi liquid theory in the Falicov-Kimball model. Since this work was done *before* the techniques and approaches of the rest of the thesis were developed, it uses a slightly different approach to the limit of infinite dimensionality. Since the mechanisms for the phenomena studied are quite different in the Falicov-Kimball and Hubbard models, the study provides an interesting contrast to the physics described in the following chapters. We have therefore included it for pedagogical reasons. In order to preserve the continuity of the methods outlined in Chapter 2, the reader may choose to skip it on a first reading.

In Chapter 4 we will use the techniques developed in Chapter 2 in order to study the Mott metal-insulator transition in the Hubbard model at half-filling. In particular, we will establish the coexistence of metallic and insulating solutions over a finite range of interactions U and show that the transition at zero temperature is of second order.

Moreover, we will see that the transition is characterized by a vanishing low energy scale [19, 20, 21] which prevents us from investigating the critical properties. This will motivate the development of the self-consistent projective technique in Chapter 6.

Chapter 5 studies the Hubbard model away from half-filling and addresses the question of transfer of spectral weight, a hallmark of strongly correlated electron systems. The method we are using allows us to study the Hubbard model at finite doping and zero temperature for the first time in a reliable way. Using the mapping of the Hubbard model onto a self-consistent Anderson model [41] we will moreover gain considerable *analytic* understanding of the physics exhibited by the Hubbard model. Again we will encounter the existence of a vanishing energy scale at small doping, underlining the need for a new technique to address the low energy properties of models in infinite dimensions.

In Chapter 6 we will develop a novel technique, the *self-consistent projective technique*, which enables us to overcome the problems associated with the existence of two energy scales, in particular a vanishing energy scale, demonstrated in the previous chapters. The technique allows us to *eliminate* the high energy part of the problem in the spirit of the renormalization group [42] and to *reduce* it to an effective problem exhibiting only *one* scale which can be analyzed much more easily. It should be emphasized that the technique is general and can be applied to any problem exhibiting a separation of scales. Its strength derives from the fact that the high energy features enter into the low energy problem *solely* via numerical coefficients, in the spirit of Landau-Ginsburg theory [43]. The qualitative behavior of the model is therefore fully determined by the effective low energy problem. We will develop the method in detail for the case of the Hubbard model.

In Chapter 7 we will proceed by using the technique to analyze the critical properties of the Hubbard model at and away from half-filling, which for the first time can be done *exactly* in infinite dimensions. This yields results that can be directly compared to experimental data.

In Chapter 8 we will analyze some of the *finite temperature* properties of the Hubbard model using the full infinite d Hubbard model, as well the the self-consistently projected,

effective model, which allows us to reach temperatures unattainable using previous methods and techniques.

Finally, we will discuss the Hubbard model on a double-stranded Bethe lattice in the limit of infinite dimensions (Chapter 9). This leads to a two impurity problem embedded in a self-consistent medium mimicking the higher order $1/d$ effects of the single site problem. This allows us to examine qualitatively new physical questions, which are outside the scope of the $d = \infty$ limit of the Hubbard model, such as the competition between RKKY and Kondo interactions.

Chapter 2

Infinite Dimensionality – A Primer

2.1 Infinite Dimensionality – A Mean-field Theory for Strongly Correlated Systems

While the approaches mentioned in the introduction (other than infinite d) have led to important insights, they do not provide a mean-field theory of itinerant electron systems with strong correlations, which becomes *exact* in some well defined limit and is able to capture both high and low energy features correctly. A road towards a mean-field theory of strongly correlated electron systems was paved in a pioneering paper by Metzner and Vollhardt [44]. While until then it was well known that the limit of infinite spatial dimensions leads to a well defined mean-field theory for (mostly classical) *spin systems*, it was not clear, how a similar theory can be constructed for *itinerant systems* in which the physics is determined by the interplay between strong local repulsion and itinerant band behavior.

Metzner and Vollhardt realized that if the hopping matrix element t in the kinetic energy

$$T = -\sum_{\sigma,<i,j>} t_{ij} c^{\dagger}_{i\sigma} c_{j\sigma} \tag{2.1}$$

is scaled as

$$t \to t^* = \frac{t}{\sqrt{d}} \tag{2.2}$$

where d is the dimensionality of the system, a non-trivial limit in which both the kinetic *and* the potential energy remain finite results, such that the competition between them remains. It should be noted that such a scaling does not necessarily exist. In particular, the large-N limit mentioned above always leads to a *trivial* atomic limit [45].

In the case of a hypercubic lattice this leads to a (non-interacting) density of states

(DOS) which is Gaussian, i.e.

$$\rho_0(\epsilon) = \frac{1}{\sqrt{\pi}t} e^{-(\frac{\epsilon}{t})^2}. \tag{2.3}$$

The crucial consequence of this rescaling, however, is the fact that the single-particle Green function scales as

$$G^0_{ij} \sim \frac{1}{\sqrt{d}} \tag{2.4}$$

which in turn implies a *local*, i.e. momentum-independent, self-energy.

The momentum independence of the single particle Green function leads to considerable simplifications in the evaluation of diagrammatic expansions [46, 47] as well as in calculations involving variational wavefunctions [28, 48, 49]. In particular, it should be noted that the Gutzwiller approximation, an approximation commonly used in the evaluation of variational calculations, becomes exact in infinite d [49].

Brandt and Mielsch [50] observed that in the case of the Falicov-Kimball model, a simplified Hubbard model in which only one spin species is allowed to hop, the limit of infinite dimensionality allows for a mapping onto an atomic problem, which can be solved exactly. We will reexamine the solution to the Falicov-Kimball model in Chapter 3 from a different point of view.

Georges and Kotliar [41] showed how the idea of Brandt and Mielsch can be generalized to provide a natural mean-field theory of strongly interacting systems by allowing for a mapping of a *lattice* problem onto an impurity problem in a self-consistently determined medium. This is accomplished in the following way: Since the self-energy in infinite dimensions is a *local* quantity, it is possible to consider an auxiliary impurity problem with a single site action

$$S_{eff}[c, c^\dagger] = \int_0^\beta d\tau \int_0^\beta d\tau' \sum_\sigma c^\dagger_\sigma(\tau) G_0^{-1}(\tau - \tau') c_\sigma(\tau') + U \int_0^\beta d\tau n_\uparrow(\tau) n_\downarrow(\tau) \tag{2.5}$$

where G_0 contains all information about the other lattice sites and has the full imaginary time (and thus frequency) dependence. This is the result of the fact that the occupation of the impurity site undergoes quantum fluctuations between the allowed configurations of the impurity site, although no explicit hoppings are allowed.

The impurity problem has an associated self-energy defined through Dyson's equation as

$$G(i\omega_n) = \frac{1}{G_0^{-1}(i\omega_n) - \Sigma_{imp}[G_0](i\omega_n)}. \tag{2.6}$$

The mean-field equations then require that the local, site-diagonal Green function of the Hubbard model

$$G_{ii}(i\omega_n) = \int d\epsilon \frac{\rho_0(\epsilon)}{i\omega_n + \mu - \epsilon - \Sigma(i\omega_n)} \tag{2.7}$$

be the same as the impurity Green function G of the impurity model. The equations (2.5) - (2.7) thus provide a natural mean-field theory of strongly correlated electron systems in which G_0 describes the effect of all other electrons surrounding the site considered and thus constitutes the average field.

Although the effective impurity model is considerably simpler than the associated lattice problem, it remains a formidable many-body problem since G_0, which plays the role of the effective field has the full frequency dependence and is thus a function of infinitely many variables. It is this feature which distinguishes the mean-field theory of strongly correlated systems from the mean-field theory of, among others, spin systems, where the mean field is simply given by a single parameter (the effective field). This is due to the fact that the effective field describes several energy scales, which cannot be captured by a single parameter (for a clear presentation of these aspects, see the recent review by Kotliar [37]).

2.2 An Explicit Example: The Hubbard Model in Infinite Dimensions

A particularly clear path of reducing the lattice problem to an impurity problem is given by *integrating out* all lattice sites except the one at the origin. In the case of a *Bethe lattice* this can be done exactly, leading to an explicit form of G_0. While one may be tempted to reason that a Bethe lattice is highly artificial, since there are no closed loops, it can be argued that it is in fact closer to physical systems, since it has a *bounded* density of states (as opposed to the infinite tails of the Gaussian density of states) which is given by a semicircle of half-width $D = 2t$ and has the form

$$\rho_0(\epsilon) = \frac{2}{D}\sqrt{1 - (\frac{\epsilon}{D})^2}. \tag{2.8}$$

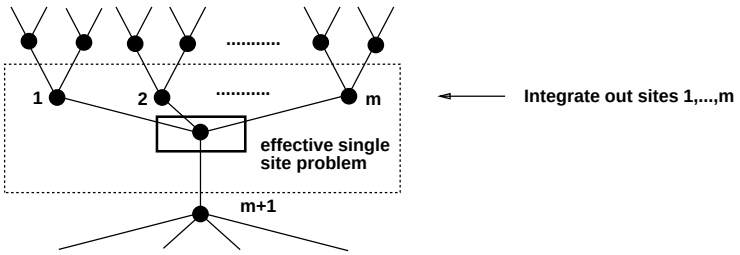

Figure 2.1: Illustration of the reduction to single site problem by integrating out sites 1 to m in a Bethe lattice

Since the derivation of the mean-field equations is particularly simple in the case of a Bethe lattice, and can easily be extended to more complicated lattice models (see also Chapter 9), we will give an explicit derivation of the mean-field equations for the case of the Hubbard model.

Consider the Bethe cluster of coordination number m (in the case of a Bethe lattice the coordination number m plays the role of the dimensionality d) depicted in Fig. 2.1. The partition function $\mathcal{Z}$ of the Hubbard model on a Bethe lattice is given as

$$\begin{aligned}\mathcal{Z} &= \int \prod \Big(\mathbf{D}\left[c_\sigma^* c_\sigma\right] \prod_{i=1}^{m+1} \mathbf{D}\left[c_{i\sigma}^* c_{i\sigma}\right] \Big) e^{-\int_0^\beta d\tau \sum_{i=1,\sigma}^{m} \left(c_{i\sigma}^*(\partial_\tau - \mu) c_{i\sigma} - t(c_\sigma^* c_{i\sigma} + h.c.) + \frac{U}{2} n_{i\sigma} n_{i\bar{\sigma}} \right)} \\ & \qquad e^{-\int_0^\beta d\tau \sum_\sigma \left(c_\sigma^*(\partial_\tau - \mu) c_\sigma - t(c_{m+1\sigma}^* c_\sigma + h.c.) + \frac{U}{2} n_\sigma n_{\bar{\sigma}} \right)} \mathcal{Z}\left[c_{i\sigma}^*, c_{i\sigma}\right] \end{aligned} \tag{2.9}$$

where $\mathcal{Z}\left[c_{m\sigma}^*, c_{m\sigma}\right]$ denotes the partition function in which the partial trace over the electrons of the m-th site and the branches connected to it has been taken. Integrating out the sites $1, ..., m$ as shown in Fig. 2.1 and using the equivalence of the sites of a Bethe lattice we find

$$\begin{aligned}\mathcal{Z}\left[c^*, c\right] &= \left[\int \prod \Big(\mathbf{D}\left[c_\sigma^* c_\sigma\right] \mathbf{D}\left[c_{1\sigma}^* c_{1\sigma}\right] \Big) \mathcal{Z}\left[c_1^*, c_1\right] \exp\left(-\int_0^\beta d\tau (-t)(c_\sigma^* c_{1\sigma} + h.c.) \right) \right]^m \\ & \qquad \exp\left(-\int_0^\beta d\tau \sum_\sigma c_\sigma^*(\partial_\tau - \mu) c_\sigma + \frac{U}{2} n_\sigma n_{\bar{\sigma}} \right). \end{aligned} \tag{2.10}$$

Defining $S_{eff}[c^*, c] = -\ln \mathcal{Z}[c^*, c]$, rescaling the hopping amplitude t as $t \to t/\sqrt{m}$ and expanding to lowest order in m one obtains an effective action in terms of the local single particle Green function $G(\tau - \tau') = -\langle \mathcal{T} c(\tau) c(\tau')^\dagger \rangle$ given as

$$S_{eff}[c, c^\dagger] = \int_0^\beta d\tau d\tau' c^*(\tau) G_0^{-1}(\tau - \tau') c(\tau') + \int_0^\beta d\tau n_\uparrow(\tau) n_\downarrow(\tau). \tag{2.11}$$

Fourier transforming one obtains the self-consistency equation

$$G_0^{-1}(i\omega_n) = i\omega_n + \mu - t^2 G(i\omega_n) \tag{2.12}$$

with $G(i\omega_n) = -\int_0^\beta \mathrm{e}^{i\omega_n \tau} \langle T_\tau c(\tau) c^\dagger(0) \rangle_{S_{eff}}$ and Matsubara frequencies $\omega_n = \frac{\pi}{\beta}(2n+1)$. It should be noted that we have restricted ourselves to the study of non-superconducting phases in which the expectation value $\langle T_\tau c_\uparrow(\tau) c_\downarrow(0) \rangle$ vanishes. We also use the fact that due to spin conservation $\langle T_\tau c_\sigma(\tau) c^\dagger_{\sigma'}(0) \rangle \sim \delta_{\sigma\sigma'}$.

We have thus mapped the *lattice* model onto an impurity model in a self-consistently determined bath of conduction electrons with self-consistency condition (2.12). Once self-consistency is reached, $G(i\omega) - G_{ii}(i\omega) = 0$, where G_{ii} is the local Green function of the lattice Hubbard model.

At this point it should be mentioned that the procedure as presented naturally leads to an expansion in $1/d$ if higher order terms in the expansion of (2.10) are retained. Going to higher order leads to the appearance of $2n$ point correlation functions of the form $\Gamma^{(n)}_{\sigma_1 \ldots \sigma_n}(\tau_1, \ldots, \tau_{2n}) = \langle \mathcal{T} c_{\sigma_1}(\tau_1) c_{\sigma_2}(\tau_2) \ldots c^*_{\sigma_{2n-1}}(\tau_{2n-1}) c^*_{\sigma_{2n}}(\tau_{2n}) \rangle$ coupling to a product of $2n$ fermion operators in the effective action (for the a discussion of this expansion in the disordered Hubbard model, see Ref. [51]). To order $(n = 2)$, these lead, in particular, to retardation effects in the Hubbard interaction. Again these higher correlation functions have to be determined self-consistently. While this leads to a natural loop expansion in a Hubbard model with disorder [51], it is far from clear how these equations can be truncated in the Hubbard model without disorder without violating conservation laws: While for $d = \infty$ one obtains a *conserving approximation* [52, 53] in which it is possible to define a generating functional Ω such that $\Sigma = \frac{\delta \Omega}{\delta G}$ and $\Sigma = \Sigma[G]$, taking functional derivatives in the presence of higher order terms does *not* lead to a closed set of equations. The question how the infinite d approximation can be extended systematically and consistently therefore remains an open question. In Chapter 9 we will follow a different path to address these questions. Other approaches based on cluster approaches are presently being developed [54].

Even in the case of $d = \infty$ in which "only" the single particle Green function has to

be determined self-consistently, the resulting mean-field theory remains a highly non-trivial many-body problem. In the case of the Falicov-Kimball model this can be solved exactly, leading to a set of coupled, non-linear equations. In the case of a Lorentzian density of states [55, 41] these can be analyzed analytically. In more complicated models like the Hubbard model, however, it is not possible to obtain analytical expressions for Green function and self-energy and the resulting impurity problem has to be solved numerically.

The first approaches to the Hubbard model in infinite dimensions [20, 19, 21, 56, 57] relied on Quantum Monte Carlo (QMC) simulations and iterated self-consistent second-order perturbation theory (IPT) in the spirit of Yamada and Yoshida [58, 59, 60] to solve the effective impurity model. While both methods were able to (and continue to) answer crucial questions and could elucidate the physics of the Hubbard and related models in infinite dimensions (establish the presence of a metal-to-insulator transition [20, 19, 21, 56, 57], indicate the presence of superconductivity in a two-band Hubbard model [61, 40], etc.) both suffer from inherent difficulties which cannot be overcome.

The Quantum Monte Carlo method is intrinsically a finite temperature approach and is limited—largely due to the limitations of todays computers—to fairly high temperatures. A detailed investigation of the experimentally and theoretically relevant *low temperature* regime is therefore not possible. In addition, the presence of statistical noise limits the accuracy of the results.

Second-order self-consistent perturbation theory gives excellent zero temperature results and can be shown to be exact in the strong as well as the weak-coupling limit of the half-filled Hubbard model. However, it suffers from different weaknesses. Near the metal to insulator transition higher order corrections become important such that this approximation is not sufficiently accurate to determine whether the Mott transition at $T = 0$ is first or second order. The perturbative approach is also known to fail away from half-filling [62]. Even at half-filling it exhibits pathologies which are known to be incorrect, such as a vanishing second derivative of the self-energy.

2.3 The Anderson Connection

A particularly fruitful approach to the problem, which forms the basis of the work on the Hubbard model presented in this thesis, has been suggested by Caffarel and Krauth [40] and, in a different form, by Si et al. [63]. The approach exploits the fact that the Hubbard model in infinite dimensions can be mapped onto an *actual* impurity problem, the single impurity *Anderson model* [41] in which, however, the bath of conduction electrons, usually taken to have a flat density of states, is determined self-consistently, such that the density of states is a complicated, frequency dependent, function. (In the case of more complicated lattice models the impurity models are generalized accordingly.)

The mapping can be accomplished easily in the following way: Starting with an Anderson Hamiltonian of the form

$$\mathcal{H}_{AM} = \sum_{k\sigma} \epsilon_k a^\dagger_{k\sigma} a_{k\sigma} + \sum_{k\sigma} (V_k a^\dagger_{k\sigma} f_\sigma + h.c.) + U n_{f\uparrow} n_{f\downarrow} - \mu(n_{f\uparrow} + n_{f\downarrow}) \quad (2.13)$$

one can integrate out the conduction electrons $a_{k\sigma}$ to obtain an action of the same form as found in the infinite dimensional Hubbard model *if* the bath electrons are chosen to fulfill the new self-consistency condition

$$t^2 G(i\omega) = \sum_k \frac{V_k^2}{i\omega_n - \epsilon_k}, \quad (2.14)$$

i.e. the density of states of the Anderson model is given as

$$\rho_{AM}(\epsilon) = \sum_k V_k^2 \delta(\epsilon - \epsilon_k). \quad (2.15)$$

One is thus left with the task of solving an Anderson model subject to the self-consistency condition (2.14). It should be emphasized that the resulting self-consistent Anderson problem is a Hamiltonian problem, which can be tackled with standard approaches, in particular with exact diagonalization methods.

2.4 A Path to Solving Self-consistent Impurity Problems

An appealing way to solving the resulting self-consistent impurity problem was proposed by Caffarel and Krauth and—using a similar approach—Si et al. [63]. The idea is

to solve the effective Anderson model on a *finite* cluster which – through the self-consistency condition – amounts to parametrizing the impurity Green function by a finite number of parameters $\{V_k, \epsilon_k\}$ where $k = 1, ..., N_{bath}$.

Starting from an initial guess for those parameters one determines the *ground state* using Lanczos methods (for a review see Refs. [64] and [65]). We are using the modified Lanczos as described in Ref. [66] modified such that at each step of the Lanczos procedure a tridiagonal submatrix of dimension $N_{sub} \times N_{sub}$ (instead of 2×2 as described in [66]) is diagonalized. This leads to a considerably better approximation to the ground state wavefunction.

At zero temperature, systems of up to ten sites can be handled easily on a workstation. For an analysis of the finite temperature properties, all eigenstates up to a cutoff given by the temperature are necessary and one has to resort to exact diagonalization, which limits the possible system sizes to a maximum number of sites $N = 6$. For a more detailed discussion of the procedure at finite temperature see the corresponding chapter.

Given the ground state it is possible to determine the zero temperature Green function using a continued fraction expansion. The zero temperature Green function can be decomposed into "particle" and "hole" contributions as

$$G(z) = G^p(z) + G^h(z) \tag{2.16}$$

with

$$G^p(z) = \langle gs | f_\sigma \frac{1}{z - (H - E_{gs})} f_\sigma^\dagger | gs \rangle \tag{2.17}$$

$$G^h(z) = \langle gs | f_\sigma^\dagger \frac{1}{z + (H - E_{gs})} f_\sigma | gs \rangle \tag{2.18}$$

where E_{gs} is the ground state energy. The respective contributions can be obtained from a continued fraction [67] expansion as

$$\langle f_0^{p/h} | \frac{1}{z \mp (H - E_0)} | f_0^{p/h} \rangle = \cfrac{\langle f_0^{p/h} | f_0^{p/h} \rangle}{z \pm E_0 - a_0^{p/h} - \cfrac{b_1^{p/h2}}{z \pm E_0 - a_1^{p/h} - \cfrac{b_2^{p/h2}}{z \pm E_0 - a_2^{p/h} - \ldots}}} \tag{2.19}$$

where

$$|f_0^p\rangle = f_\sigma^\dagger|gs\rangle \tag{2.20}$$

$$|f_0^h\rangle = f_\sigma|gs\rangle \tag{2.21}$$

$$|f_{n+1}\rangle = H|f_n\rangle - a_n|f_n\rangle - b_n^2|f_{n-1}\rangle \tag{2.22}$$

and with coefficients

$$a_n = \langle f_n|H|f_n\rangle \tag{2.23}$$

$$b_n^2 = \frac{\langle f_n|f_n\rangle}{\langle f_{n-1}|f_{n-1}\rangle} \tag{2.24}$$

$$b_0 = 0. \tag{2.25}$$

Having determined the Green function one is left with the task of closing the self-consistency, which is the crucial approximation involved in this scheme: While the Green function as determined from the continued fraction expansion is a true many-body Green function with a large number of poles, the number of sites in the bath, N_{bath}, and thus the number of poles this function is to be fitted to is considerably smaller. Caffarel and Krauth suggested implementing the self-consistency using a χ^2 fit, minimizing the expression

$$\chi^2_{GF} = \frac{1}{N_\Omega + 1}\sum_{i\omega_n}^{N_\Omega} |G(i\omega_n) - \sum_{k=1}^{N_{bath}} \frac{V_k^2}{i\omega_n - \epsilon_k}|^2 \tag{2.26}$$

which can be done efficiently and with great accuracy using a modification of the conjugate-gradient method from Numerical Recipes [68]. (It should be noted that we have found improved convergence if the routine is implemented such that it is truncated after a few iterations and restarted with the previous output.) Here the high-frequency cutoff is chosen to be larger than the largest energy scale in the problem such that changing it does not affect the results. The low frequency cutoff, which is given by the lowest frequency fitted (i.e. the temperature in any finite temperature calculation and a "fictitious" temperature $"T"$ at $T = 0$), is determined by the smallest pole in the Green function which is extracted as described in Appendix E. An incorrect low frequency cutoff can be recognized easily by large χ^2, an unphysical up- or downturn in $G(i\omega_n)$, and/or the fact that the program fails to converge.

An alternative procedure which was first suggested by Si et al. [63] and was also implemented to solve the Hubbard model [69] is based on the observation that the continued fraction expansion naturally lends itself to an interpretation of electrons hopping on two *chains*, such that the Hamiltonian of the bath is represented by two chains (as opposed to a star, as done in the fitting procedure). The new parameters can then be determined directly by truncating the continued fraction expansion and the minimization procedure is avoided altogether. While in principle the method has the additional advantage of preserving the moments of the density of states order by order, in practice an extra site at the origin has to be included in order to be able to feed back a metallic bath, which spoils this property.

We have found that—taking both χ^2_{GF} *and* moments as criteria, that the χ^2 fit gives a considerably better representation of the low-frequency behavior while at the same time representing the moments quite well. To illustrate this we display the normalized difference between the exact and the fitted moments $\Delta m_n^+/m_n^{+exact}$ for positive energies as obtained from the χ^2 method in Figure 2.2. Here $\Delta m_n^+ = m_n^{+exact} - m_n^{+fit}$ where $m_n^+ = \int_0^\infty d\epsilon \epsilon^n \rho(\epsilon_n)$ and where we have chosen the metallic solution at $U = 2.7$ and half filling. We clearly see that the representation of the moments is very good and improves as the number of sites increases.

It is also possible consider interpolations between both methods. This can be done by minimizing the expression

$$\chi^2 = c\chi^2_{GF} + (1-c)\frac{1}{N_{moment}} \sum_{i=1}^{N_{moment}} \Big((\Delta m_i^+/m_i^+)^2 + (\Delta m_i^-/m_i^-)^2 \Big). \qquad (2.27)$$

where $0 \leq c \leq 1$. This reduces to fitting the Green function only for $c = 1$ and fits moments only for $c = 0$. While we have not made a systematic investigation of this "hybrid" method, we found that in the cases considered the accuracy of the fit gets consistently worse if $c \neq 0, 1$ are considered. This can be seen by plotting χ^2 as a function of c: In the cases considered $\frac{d^2\chi^2}{dc^2} < 0$, i.e. $c = 0, 1$ correspond to local *minima* of $\chi^2(c)$. Additionally, we found that for an increasing admixture of "moment fitting" the structure in the spectral function was increasingly washed out. A rigorous analysis remains an interesting problem. Based on our experience we have thus used

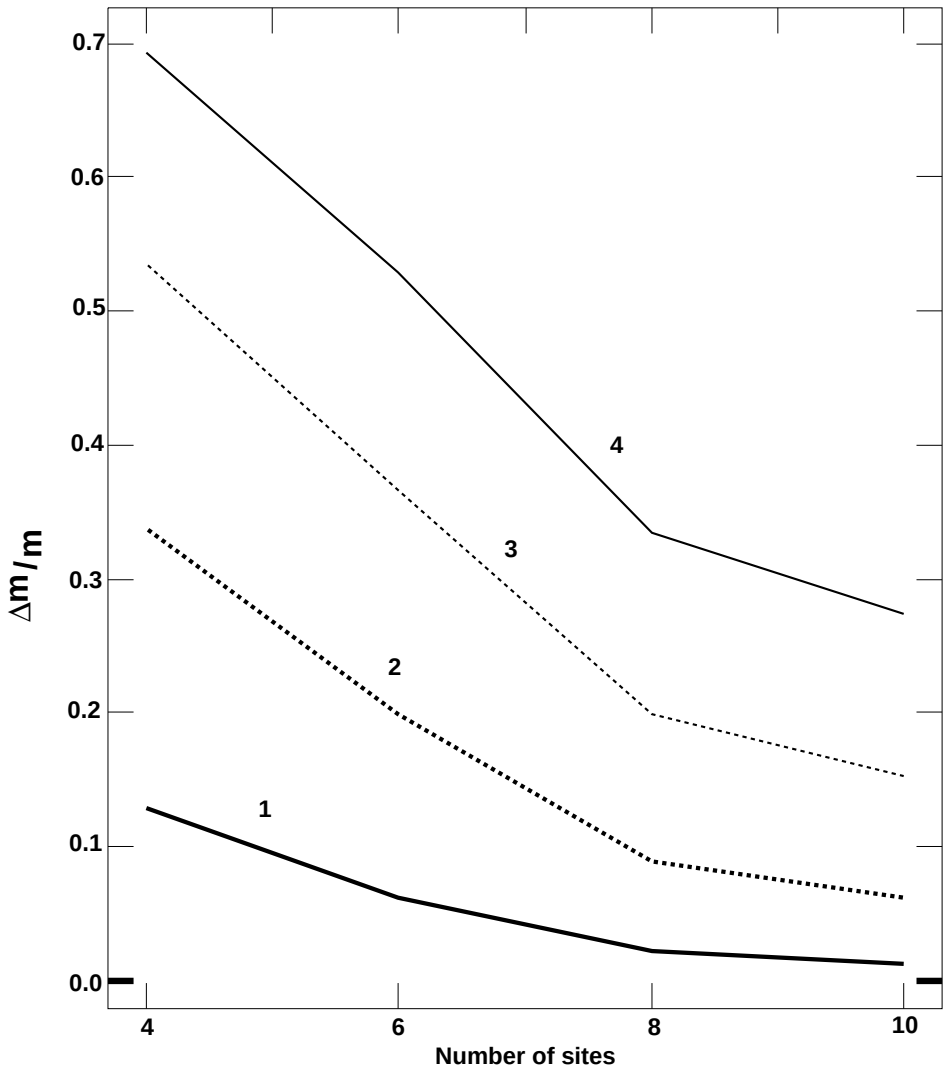

Figure 2.2: Relative difference between exact and fitted positive moments $\Delta m_1^+/m_1^+$, $\Delta m_2^+/m_2^+$, $\Delta m_3^+/m_3^+$, $\Delta m_4^+/m_4^+$ as obtained from the χ^2 fit method for $U = 2.7$ and half-filling as a function of the number of sites.

the self-consistency in the form (2.26) whenever the cluster approach is used.

Having extracted the new parameters $\{\epsilon_k, V_k\}$ from the fit, we iterate the procedure until convergence is achieved. An excellent convergence criterion is the ground state energy of the effective impurity model.

The method gives excellent results for any filling and agrees extremely well with known results and the existing schemes (Quantum Monte Carlo, iterated perturbation theory) in the parameter regimes in which those give reliable results. An essential limitation, however, is the fact that it is based on a cluster approach, implying a finite number of poles with a characteristic spacing depending on the system size. In the chapters on the *self-consistent projective technique* we will demonstrate, how this weakness can be overcome.

Once we have obtained the self-consistent solution to the problem, other physical quantities can be evaluated. Since we have the full ground state (and possibly the excited states as well) of the system, as well as a method to evaluate diagonal correlation functions, the continued fraction expansion, it is possible to determine other local correlation functions of the system.

In a straightforward extension of the previous paragraph we can determine the local spin susceptibility

$$\chi_s(i\nu_n) = (g\mu_B/2)^2 \int_0^\beta d\tau \mathrm{e}^{i\nu_n\tau} \langle T_\tau S_z(\tau) S_z(0)\rangle_{H_{eff}} \tag{2.28}$$

where $S_z = \frac{1}{2}(f_\uparrow^\dagger f_\uparrow - f_\downarrow^\dagger f_\downarrow)$ and Bose frequencies $\nu_n = n\pi T$.

Again we can decompose the function into "particle" and "hole" contributions as $\chi_s(i\omega_n) = \chi_s^p(i\omega_n) - \chi_s^h(i\omega_n)$ with

$$\chi_s^p(z) = \langle gs|S_z \frac{1}{z-(H-E_0)} S_z|gs\rangle \tag{2.29}$$

$$\chi_s^h(z) = \langle gs|S_z \frac{1}{z+(H-E_0)} S_z|gs\rangle. \tag{2.30}$$

Notice the minus sign, since we are calculating a bosonic function. The respective contributions can be obtained from a continued fraction [67] expansion as before, except that

$$|f_0^p\rangle = |f_0^h\rangle = S_z|gs\rangle. \tag{2.31}$$

It should also be pointed out that it is possible to calculate certain off-diagonal expectation values by reducing them to diagonal form using the identity

$$\begin{aligned}\langle A|\frac{1}{i\omega \pm (H-E)}|B\rangle &= \frac{1}{2}\Big((\langle A|+\langle B|)\frac{1}{i\omega \pm (H-E)}(|A\rangle+|B\rangle) \\ &- \langle A|\frac{1}{i\omega \pm (H-E)}|A\rangle - \langle B|\frac{1}{i\omega \pm (H-E)}|B\rangle\Big).\end{aligned} \tag{2.32}$$

where the matrix elements are assumed to be real. Finally we will also see, that energies and other expectation values can be determined easily using this method.

Given the fact that the system is represented by only a few poles, the accuracy is particularly impressive, especially if only one scale enters the problem. This can be checked by comparing the numerical results for the non-interacting system to the exact results. In this case almost perfect agreement for n versus μ curves, energies and susceptibilities can be achieved.

In this chapter we have seen, how the limit of infinite dimensionality allows us to map a lattice problem onto an impurity problem in a self-consistently determined bath of conduction electrons and outlined how this is a natural mean-field theory of many-body systems. We have presented a method to solve this resulting impurity problem numerically using an approach based on exact diagonalization and we have shown, how other physical quantities can be obtained using this approach. Use of this approach will be made in Chapter 4. In the next chapter we will first consider a model which is exactly solvable in infinite dimensions, the Falicov-Kimball model, and discuss some of its physics.

Chapter 3

Metal-to-Insulator Transition and Transfer of Spectral Weight in the Falicov-Kimball Model

In this chapter we will study the correlation induced metal-insulator transition, the transfer of spectral weight as well as a scenario for the breakdown of Fermi liquid theory [2] in the Falicov-Kimball model [70, 24, 25], a model which can be solved exactly [50] in the limit of infinite dimensions.

We shall see that the metal-insulator transition in this case differs fundamentally from the mechanism realized in the Hubbard model (see Chapter 4), since it proceeds simply by a band splitting as originally proposed by Hubbard [24]. Contrasting the two cases (we will discuss the Hubbard model in the following chapters) leads to further insights into the nature of the metal-insulator transition in various contexts.

The transfer of weight between upper and lower Hubbard band as a function of doping in this case manifests itself through the linear reduction of the high energy spectral weight, induced as a result of the decrease of the double occupancies with increasing doping. Again, this is fundamentally different from the scenario realized in the Hubbard model and should be contrasted with the results of Chapter 5.

Finally, we will investigate whether the Falicov-Kimball model can be used as the simplest model of a non-Fermi liquid metal. The breakdown of Fermi liquid theory requires the violation of Landau's basic assumption of the one-to-one correspondence between the low-energy excitation spectra of the interacting and non-interacting systems. This clearly requires the presence of qualitatively *new* low energy excitations which should not be associated with the low energy collective mode signaling the proximity to an *obvious* phase transition. While this does not necessarily imply the breakdown of Fermi liquid theory, as we shall see in the Hubbard model, it may provide a route to it:

A possible scenario is that these "zero-energy" modes arise from the transfer of spectral weight from the "upper Hubbard" band to the chemical potential, upon weakly doping the insulating state [71]. This excitation can be pictured as a "shake-up" satellite arising from the scattering of a conduction electron off the interband exciton (i.e., a bound state of a conduction hole at the chemical potential and a single-particle excitation in the upper band). Due to orthogonality catastrophe effects [71], these excitations are virtually dispersionless and thus contribute to the "incoherent" part of the spectrum. It is this special feature which prevents the system from undergoing a simple phase transition at any finite temperature.

As we will see, these effects are not present in the $d = \infty$ solution of the Falicov-Kimball model. Nevertheless this will turn out to be the simplest situation exhibiting transfer of spectral weight and a metal-to-insulator transition due to correlations. Furthermore it mimics the situation for the breakdown of Fermi liquid theory described above: it describes a spinless Fermi sea of "d"-electrons interacting with localized "f"-electrons. These are described by fermion operators d_i and f_i and represent, respectively, conduction and dispersionless upper Hubbard or charge-transfer bands.[1]

The corresponding Hamiltonian reads

$$\mathcal{H} = -t \sum_{<i,j>} d_i^\dagger d_j + \sum_i E_f f_i^\dagger f_i + U \sum_i d_i^\dagger d_i f_i^\dagger f_i - \mu \sum_i (d_i^\dagger d_i + f_i^\dagger f_i). \tag{3.1}$$

Here, U is the Coulomb potential, t is the nearest-neighbor hopping amplitude, E_f is the bare position of the local level, and μ is the chemical potential which governs the total electron density.

We note that, since the f-electrons have no dynamics of their own, the model (3.1) is formally identical to a single-particle scattering problem with a potential which is defined by the positions and occupancies of the localized states. The latter are

[1] The assumption of a dispersionless "upper band" requires some explanation: the physical argument is simply that, as far as the behavior of high-energy excitations (like those defining the upper band) is concerned, the physics of a weakly doped system is virtually identical to that of the underlying insulating state. In the latter, the presence of antiferromagnetic or charge density wave order leads to a dramatic decrease of the coherent bandwidth of single-particle excitations. This is well known, for example, from recent studies of the motion of a particle (or hole) in an ordered antiferromagnetic background [72]. Moreover, a finite doping generally leads to a further decrease of the coherent bandwidth due to the "orthogonality catastrophe".

determined self-consistently by minimizing the free energy. This procedure can be carried out exactly in the limit of infinite dimensions, where the f-electrons can be treated as uncorrelated. This was first realized by Brandt and Mielsch [50] who showed that in infinite dimensions the problem maps onto an effective single-site problem. Using this mapping, they and others studied various thermodynamic properties and static correlation functions. As discussed we will concentrate on the spectral properties, such as the single-particle Green function and the frequency-dependent conductivity, in order to study the transfer of spectral weight between high- and low-energy excitations, and to clarify the possible consequences for the physics of the metallic state.

We start with the observation that, in infinite dimensions, the coherent potential approximation (CPA) becomes exact for the model (3.1) in the disordered normal phase. In CPA [73] one assumes a local (i.e., momentum-independent), frequency-dependent self-energy, $\Sigma(z)$ $(z = \omega + i\delta)$, which describes the scattering off a single site in terms of the exact *local* Green function

$$G(z) = \int_{-\infty}^{\infty} d\epsilon \frac{\rho_o(\epsilon)}{z - \Sigma(z) - \epsilon}. \tag{3.2}$$

As we saw in the previous chapter, the locality of the self energy becomes exact in the limit of infinite dimensions, such that this assumption becomes exact in this limit. A self-consistent t-matrix approximation corrected for double counting leads to

$$\Sigma(z) = \frac{n_f U}{1 - [U - \Sigma(z)]G(z)}. \tag{3.3}$$

Here, n_f is the concentration of f-electrons and $\rho_o(\epsilon)$ is the non-interacting d-electron density of states. As shown by Metzner and Vollhardt [44], the limit of infinite dimensions on a hypercubic d-dimensional lattice requires a rescaling of the hopping amplitude as $t \to t/2\sqrt{d}$. Measuring all energies in units of $D = 2t$, the $d = \infty$ density of states takes the Gaussian form $\rho_o(\epsilon) = \frac{1}{\sqrt{\pi}} \exp(-\epsilon^2)$, and the local Green function can be written as

$$G(z) = -i\sqrt{\pi} \exp -(z - \Sigma(z))^2 erfc(\Sigma(z) - z), \tag{3.4}$$

where $erfc$ is the complementary error function.

Making connection with the framework developed in the previous chapter we would like to point out [53] that this can in principle be written in the form

$$G(z) = \frac{1-n_f}{G_0^{-1}} + \frac{n_f}{G_0^{-1} - U} \tag{3.5}$$

where G^0 is the self-consistently determined Green function of the corresponding impurity model. This displays explicitly the transfer of spectral weight in the conduction electrons and shows, that it proceeds as in the atomic solution to the Hubbard model. We will see a scenario which is quite different when analyzing the full Hubbard model.

As in the case of impurity scattering, the grand canonical potential is given by

$$\begin{aligned} \frac{\beta\Omega}{N} &= \beta(E_f - \mu)n_f + n_f \ln n_f + (1-n_f)\ln(1-n_f) \\ &\quad - \int_{-\infty}^{\infty} d\omega \rho(\omega) \ln(1 + \exp(\beta(\mu - \omega))). \end{aligned} \tag{3.6}$$

Here, β is the inverse temperature and $\rho(\omega) = -\frac{1}{\pi} Im\, G(z = \omega + i\delta)$ is the renormalized d-electron density of states. However, in our case the concentration of f_σ electrons has to be determined self-consistently by minimizing Ω with respect to n_f. This yields the expression

$$n_f = \frac{1}{\exp\left(\frac{E_f^{Ren} - \mu}{T}\right) + 1}, \tag{3.7}$$

in which the renormalized f-electron energy E_f^{Ren} is given by

$$E_f^{Ren} = E_f - T \int_{-\infty}^{\infty} d\omega \frac{\partial \rho(\omega)}{\partial n_f} \ln[1 + e^{\beta(\mu - \omega)}]. \tag{3.8}$$

Since $\frac{\partial \rho(z)}{\partial n_f} = -\frac{1}{\pi}\ Im \frac{\partial G(z)}{\partial n_f}$ and $\frac{\partial G(z)}{\partial n_f} = \frac{\partial G(z)}{\partial \Sigma(z)}(\frac{\partial \Sigma(z)}{\partial n_f}\ |_g\ + \frac{\partial \Sigma(z)}{\partial G(z)}\ |_{n_f}\ \frac{\partial G(z)}{\partial n_f})$, where $\frac{\partial \Sigma(z)}{\partial G(z)}\ |_{n_f}$ and $\frac{\partial \Sigma(z)}{\partial n_f}\ |_g$ are obtained from Eq. (3.3), we arrive at

$$\frac{\partial \rho(\omega)}{\partial n_f} = -\frac{U}{\pi} Im \frac{\frac{\partial G(z)}{\partial \Sigma(z)}}{1 - [U - 2\Sigma(z)]G(z) - [U - \Sigma(z)]\Sigma(z)\frac{\partial G(z)}{\partial \Sigma(z)}}. \tag{3.9}$$

Equations (3.4)-(3.9) completely determine the single-particle and thermodynamic properties of model (3.1) in the disordered state.

Before summarizing our results for the single-particle spectral function and the dynamical conductivity, a few comments concerning the derivation of the latter are in order. Due to the momentum independence of the self-energy in strictly infinite

dimensions [44] one can argue [74] that, in this limit, the vertex corrections to the current-current correlation function vanish identically for a vanishing external momentum. This follows explicitly by considering the extension of the conventional Ward identity [75] to the lattice:

$$q_0\Gamma_0(k+q,k) + \vec{\Delta}(q)\cdot\vec{\Gamma}(k+q,k) = G_k^{-1}(k+q) - G_k^{-1}(k), \tag{3.10}$$

where Γ_0 and $\vec{\Gamma}$ are the density and current vertex functions, respectively, $q = (\vec{q}, q_0 = \omega)$, and $\vec{\Delta}(q) = 2(\sin(\frac{q_1}{2}), \sin(\frac{q_2}{2}), ..., \sin(\frac{q_d}{2}))$ is the discrete lattice divergence in momentum space. $G_k(\vec{k},\omega)$ is the full single particle Green function given as $G_k(\vec{k},z) = \frac{1}{z-\epsilon(\vec{k})-\Sigma(z)}$, where we have used the fact that, in infinite dimensions the self-energy is momentum independent. As a result the interaction contribution to the $\vec{q}\to 0$ current vertex, which is an odd function under parity, must vanish. (Note, however, that the even-parity density vertex, Γ_0, is nontrivial!)

For our model, in which there is no dynamics of the f-electrons, the absence of vertex corrections to the conductivity is well known from the case of s-wave impurity scattering [73]. In this case the frequency-dependent conductivity can be obtained from the single-particle Green function by computing the particle-hole bubble multiplied by the square of the bare current vertex, $j_x(\vec{k}) = -tev_x = -\frac{te}{\sqrt{d}}\sin(k_x)$. Following the standard steps [16], and making use of the $d\to\infty$ limit to perform the momentum summation, we obtain the following simple expression for the real part of the dynamical conductivity:

$$Re\sigma_{xx}(\omega) = te^2\int_{-\infty}^{\infty} d\epsilon\rho_0(\epsilon)\int_{-\infty}^{\infty}\frac{d\omega'}{2\pi}A(\epsilon,\omega')A(\epsilon,\omega'+\omega)\frac{n_F(\omega')-n_F(\omega+\omega')}{\omega}, \tag{3.11}$$

where $A(\epsilon,\omega) = -2ImG_k(\epsilon,\omega)$ is the d-electron spectral function and $n_F(\omega)$ is the Fermi distribution.

We are now in position to discuss our results, which are obtained from a numerical solution of Eqs. (3.4)-(3.9). As is obvious from Eq. (3.7), at $T=0$, $n_f=0$ and $n_f=1$ are self-consistent solutions, corresponding to the conditions, $E_f^{Ren} > \mu$ and $E_f^{Ren} < \mu$. The associated self-energies are given by $\Sigma(z) = 0, U$, respectively, and therefore describe the physically trivial limit of a non-interacting conduction band (which, in

the case of $n_f = 1$, is shifted by the "Hartree" energy, U). (Here we ignore the finite temperature transition to a "chessboard" phase [50] by continuing the disordered state down to $T = 0$.) The physically "interesting" solutions, however, for which Σ becomes frequency dependent and acquires a finite imaginary part, are obtained only in the case of non-integral n_f. Such solutions correspond to situations in which the right hand side of Eq. (3.7), regarded as a function of n_f, is intersected by $F(n_f) = n_f$ along the rapidly varying part of the Fermi function, i.e., for E_f^{Ren} within an energy of order T^2/μ of the chemical potential, μ. (We note that this construction is sensible at any finite temperature, no matter how small.) This "pinning" of the renormalized f-level to the chemical potential occurs throughout a *region* in the $U - n$ plane ($n = n_f + n_c$ and n_c is the concentration of conduction electrons) for *any* value of the bare f-level energy, E_f, *inside* the conduction band. This is illustrated in Fig. 3.1 for a typical value of $E_f(= -.5)$. At half filling ($n_d + n_f = 1$), for the Gaussian density of states, the ground state remains, strictly speaking, metallic for all values of U. For small U the single-particle density of states (Fig. 3.2) shows a simple peak centered at the chemical potential, $\mu = U/2$, while the dynamical conductivity (Fig. 3.3) displays the usual Drude peak at $\omega = 0$. As a trivial consequence of the breakdown of translational invariance, as in the case of impurity scattering $\mathrm{Im}\Sigma(\omega)$ remains finite at $\omega = \mu$, also implying a finite width for the associated Drude peak. However, in the (particle-hole symmetric) metallic state at half filling the low frequency *corrections* to $\mathrm{Im}\Sigma$ are proportional to $(\omega - \mu)^2$ (see Fig. 3.4) and thus, one might still want to regard this state as a Fermi liquid. With increasing U the density of states at μ decreases exponentially, and the spectral weight appears equally distributed between the "lower" and "upper" Hubbard bands, centered, respectively, at energies 0 and U (Fig. 3.2). Correspondingly, the Drude weight in the conductivity (Fig. 3.3) decreases and reappears in the form of a high energy ("incoherent") peak centered at U, expressing the fact that, at half filling, the conduction process must involve hopping into sites occupied by f-electrons. The widths of the peaks in the density of states as well as of the features in the conductivity are determined by the maximum of $\mathrm{Im}\Sigma$ and the width of the bare Gaussian density of states, $\sqrt{2}D$. The decrease of the integrated weight of the high energy, "incoherent"

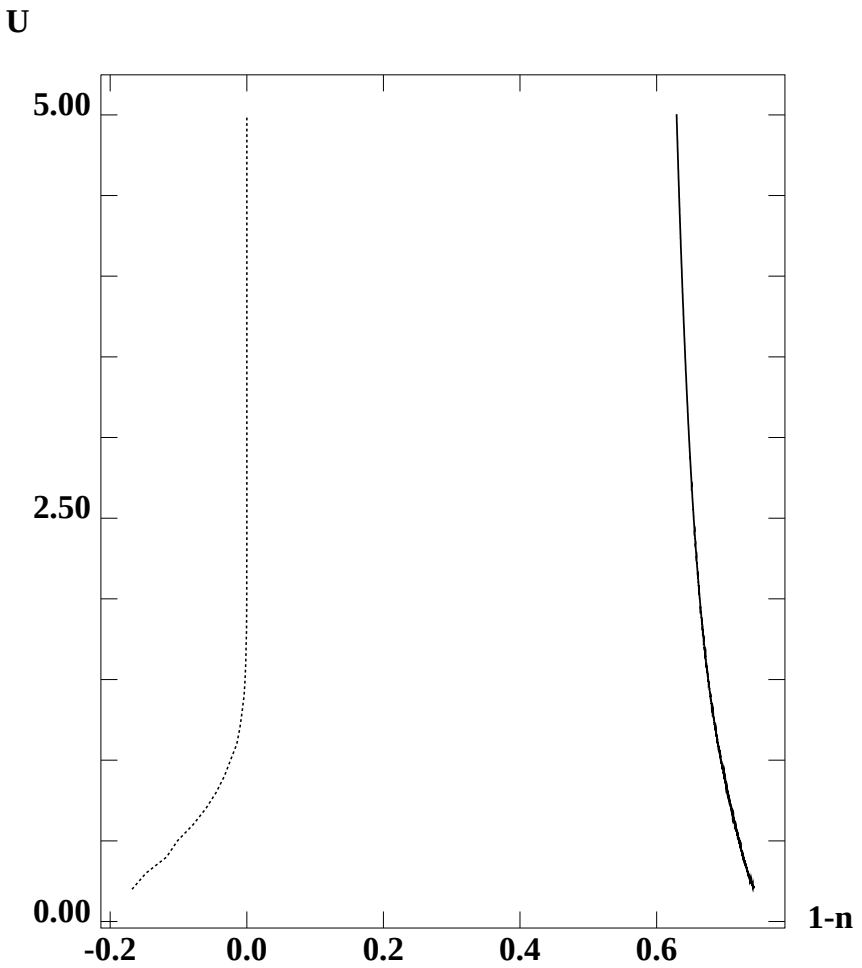

Figure 3.1: Pinning curves at $T = 0$ ($E_f = -0.5$) with impurity concentration (from left to right) $n_f = 1, 0$.

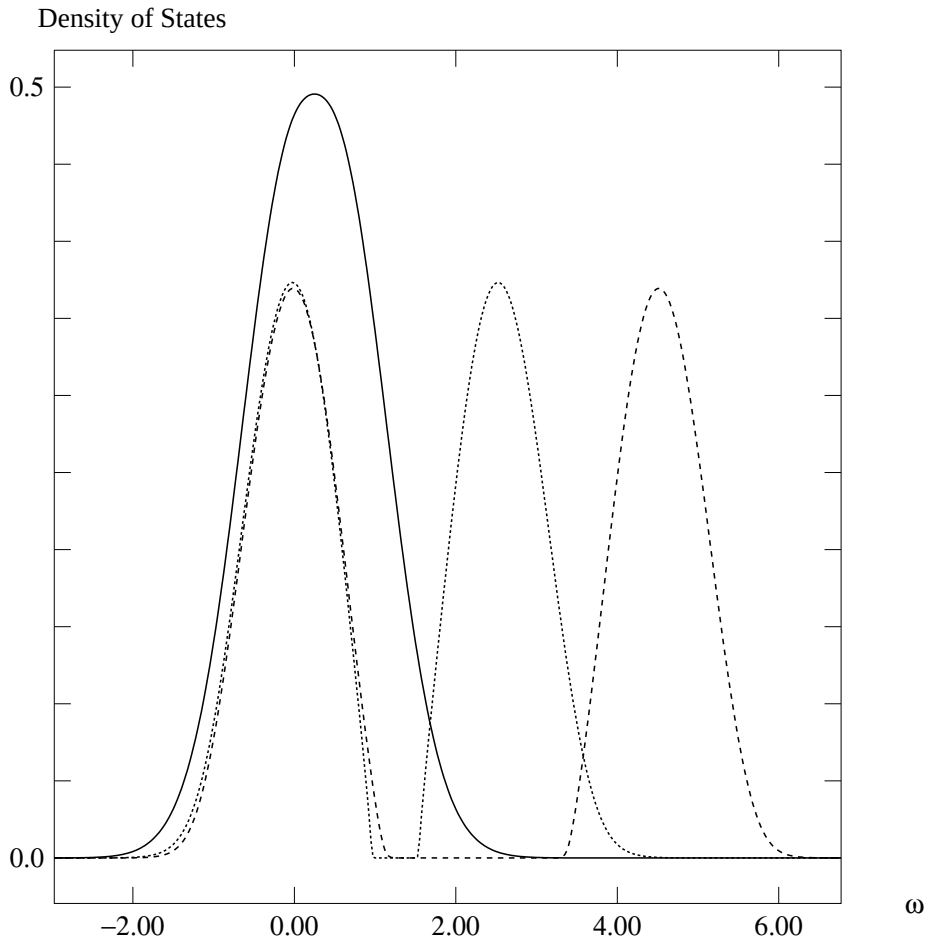

Figure 3.2: Conduction electron density of states at half filling ($n = 1$) for interaction strengths $U = 0.5$ (solid line), $U = 2.5$ (dotted line), $U = 4.5$ (dashed line). Energies are measured with respect to the center of the bare conduction band.

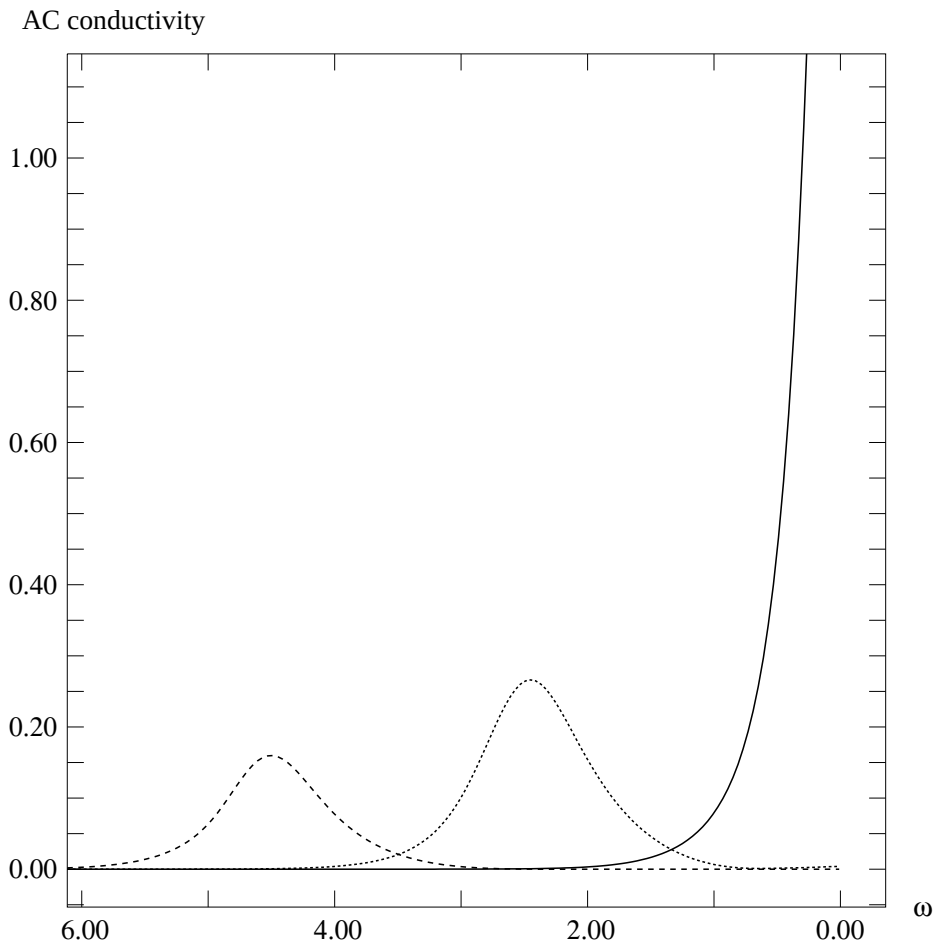

Figure 3.3: AC conductivity at half filling for interaction strengths $U = 0.5$ (solid line), $U = 2.5$ (dotted line), $U = 4.5$ (dashed line).

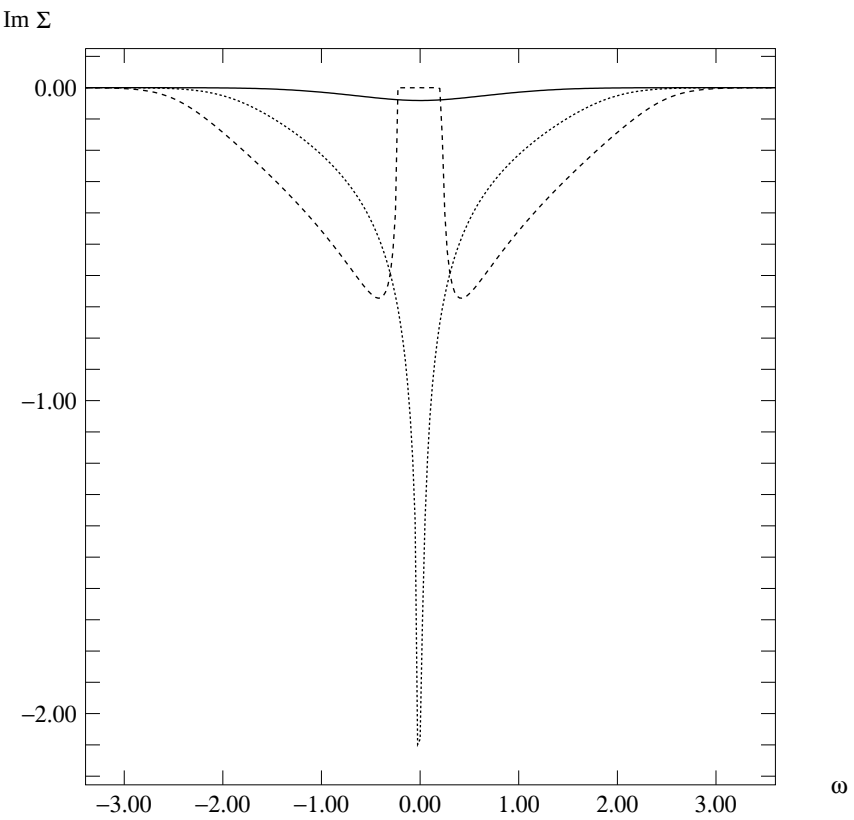

Figure 3.4: Imaginary part of the self energy at half filling ($n = 1$) for interaction strengths $U = 0.3$ (solid line), $U = 1.3$ (dotted line), $U = 2.3$ (dashed line). Energies are measured with respect to the chemical potential.

contribution to σ with increasing U is consistent with the f-sum rule, $\int d\omega Re\ \sigma_{xx}(\omega) = -\pi e^2 < T_x >$, and reflects the associated decrease in the average kinetic energy, $< T_x >$. (The spectral and f-sum rules are satisfied for all our spectra.)

Note that, in spite of the sharp decrease in both, $\mathrm{Im}\Sigma(\omega = \mu)$ and $\mathrm{Re}\sigma_{xx}(\omega = \mu)$ at $U \sim D$, there is no strict metal-to-insulator transition in the $d = \infty$ since exponentially small values of the density of states and DC conductivity still remain at μ and 0, respectively, for arbitrarily large interaction strengths. Although within our accuracy we cannot differentiate between the results for the Gaussian and bounded densities of states (Fig. 3.5), we expect that the latter does give rise to a genuine metal insulator transition. Note, however, that the transition simply occurs by a splitting of the bands, not by the collapse of a small energy scale as in the Hubbard model. We will discuss this issue at length in the following chapters.

To study the behavior of the spectra away from half filling as a function of U at fixed n and fixed E_f we must consider finite temperatures. In this regime nontrivial solutions are implemented by varying both n_f (which can take on values between 0 and 1) and μ. Our results are shown in Figs. 3.6 and 3.7.

For intermediate-to-strong values of U the "upper" and "lower" Hubbard bands have unequal weights, and the conductivity displays both a Drude peak at $\omega = 0$ as well as a high energy, "incoherent" contribution centered at U. For a fixed n, the single-particle density of states shows a shift of spectral weight from high to low energies with increasing U (Fig. 3.6). This is consistent with the decrease in n_f and the associated reduction in the number of sites available for double-occupancy. With increasing U, the behavior of the conductivity (Fig. 3.7) shows two effects: the average kinetic energy decreases, implying a decrease of both, Drude and finite frequency (incoherent) contributions. In addition, as in the single-particle spectrum, increasing U also leads to the transfer of weight from high to low energies, evidenced by the relative increase in the Drude weight. The latter effect is reflected in the "crossing" of the Drude weights with increasing U. We note that the leading correction to $Im\Sigma(\mu)$ is now linear in $(\omega - \mu)$ (Fig. 3.8), in contrast to the half-filled case. (This effect is due to particle-hole asymmetry and will only affect the subleading low-energy behavior of the conductivity.) The dependence

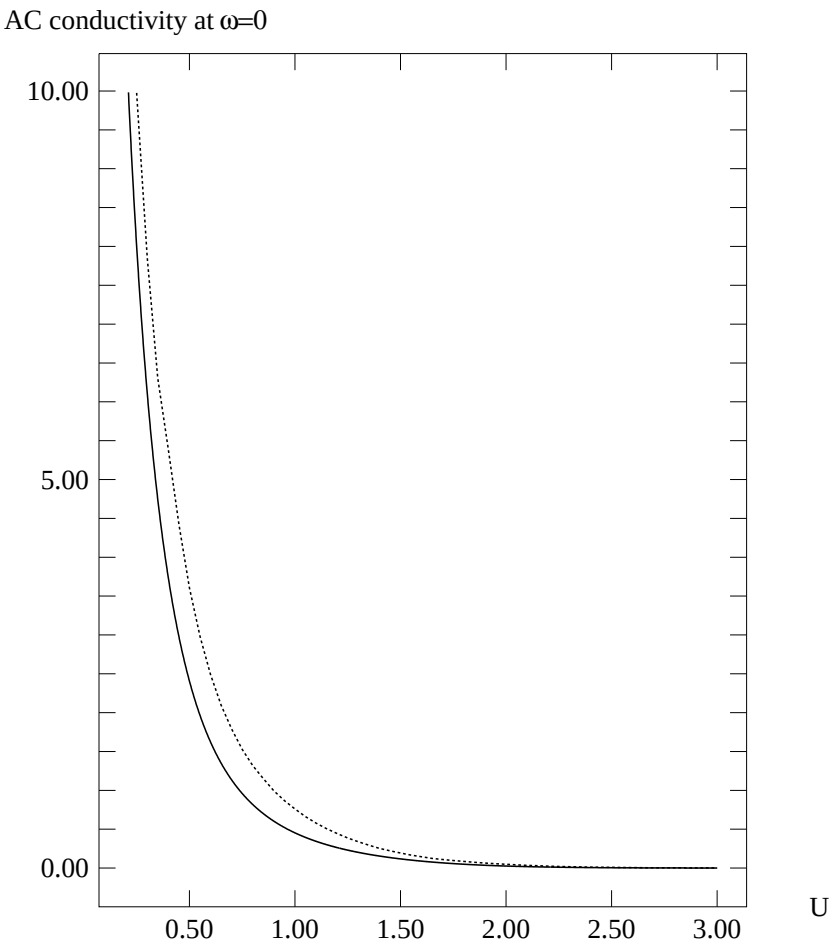

Figure 3.5: AC conductivity at $\omega = 0$ at half filling as a function of the interaction strength U for Gaussian density of states (solid line) and constant density of states (dotted line)

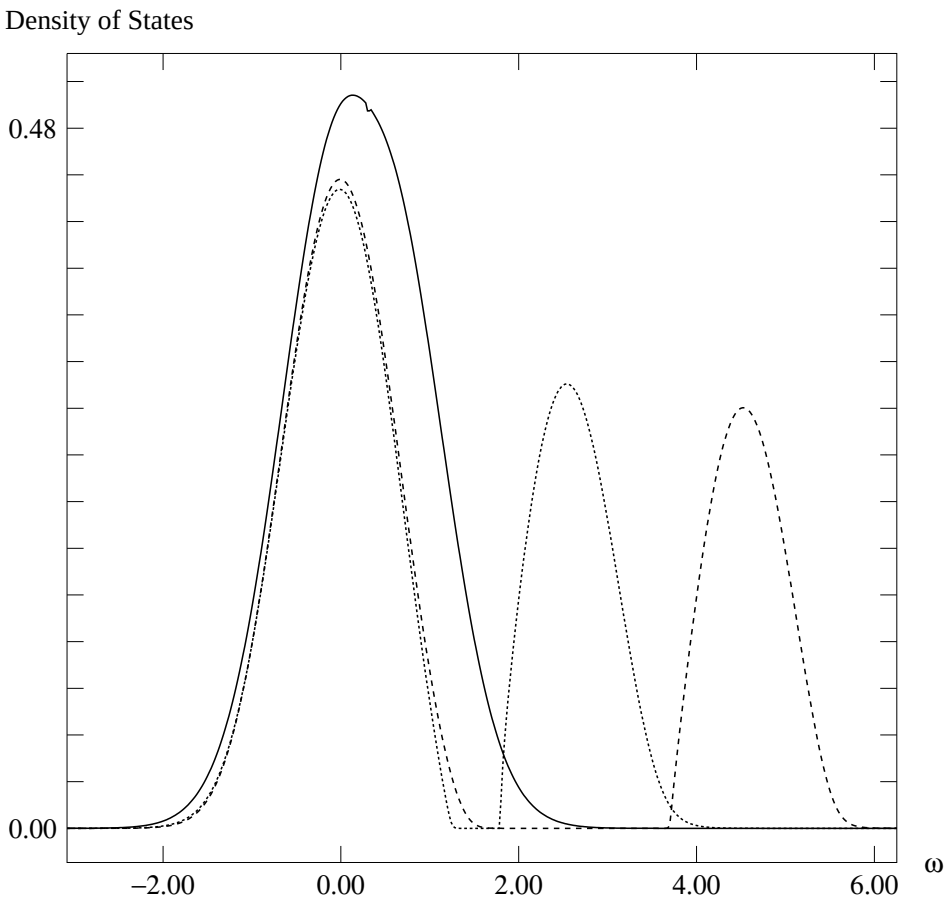

Figure 3.6: Conduction electron density of states for interaction strengths $U = 0.5$ (solid line), $U = 2.5$ (dotted line) and $U = 4.5$ (dashed line) for finite hole concentration ($n = 0.92$, $T = 0.1$, $E_f = 0$). Energies are measured with respect to the center of the bare conduction band.

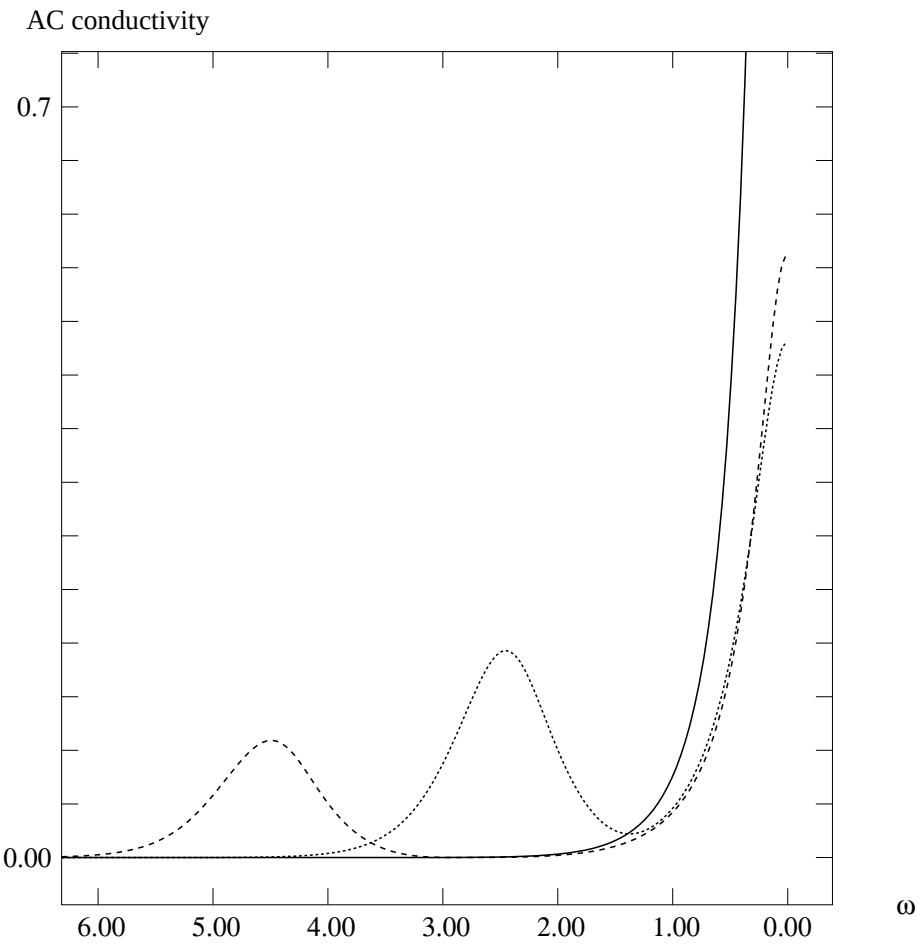

Figure 3.7: AC conductivity for interaction strengths $U = 0.5$ (solid line), $U = 2.5$ (dotted line) and $U = 4.5$ (dashed line), for finite hole concentration ($n = 0.92$, $E_f = 0$, $T = 0.1$).

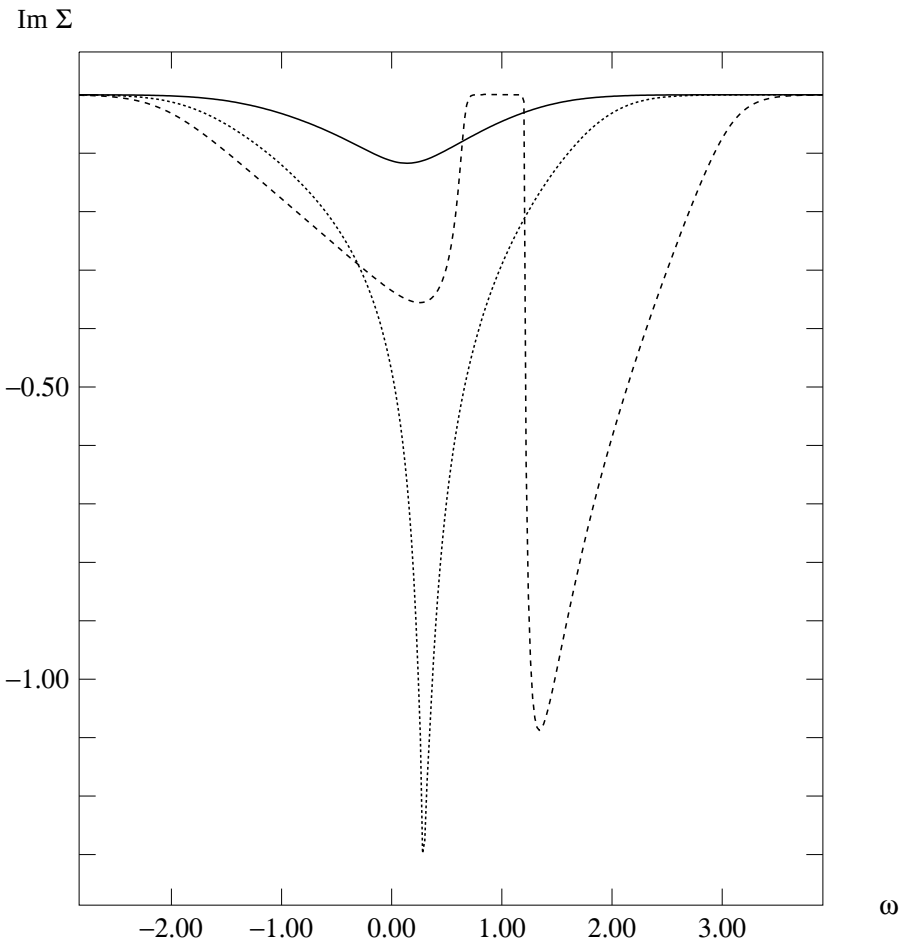

Figure 3.8: Imaginary part of the self energy for interaction strengths $U = 0.5$ (solid line), $U = 1.2$ (dotted line) and $U = 2.5$ (dashed line) for finite hole concentration ($n = 0.92$, $E_f = 0$, $T = 0.1$). Energies are measured with respect to the chemical potential.

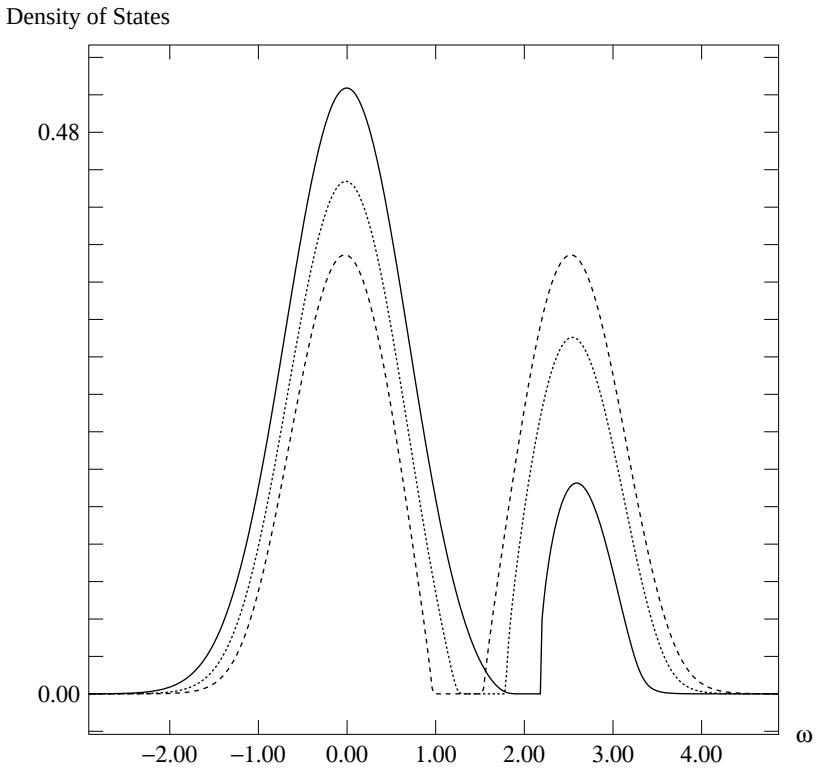

Figure 3.9: Conduction electron density for fillings $n = 0.72$ (solid line), $n = 0.92$ (dotted line) and $n = 1$ (dashed line), ($U = 2.5$, $T = 0.1$, $E_f = 0$). Energies are measured with respect to the center of the bare conduction band.

of the spectra on filling, for fixed values of U, is dominated by the variations of the f-level occupancy: The weight at μ increases with decreasing filling, with a corresponding decrease in the weight of the upper-band (Fig. 3.9). Similarly, the weight of the Drude peak in the conductivity increases at the expense of the high frequency part, as expected from the decrease in the number of scattering centers (Fig. 3.10).

It is worth noting that there are no low-temperature solutions with the bare f-level position above the band. One might have expected a nontrivial solution of this type as a result of an excitonic shift of the f-level towards the chemical potential. However, since the Hamiltonian (3.1) involves no fluctuations of the f-occupancy, the ground state does not contain such excitonic contributions. Thus, the mechanism for the breakdown of Fermi liquid theory alluded to in the introduction [71] is beyond the scope of the present treatment. Including these new effects requires the addition

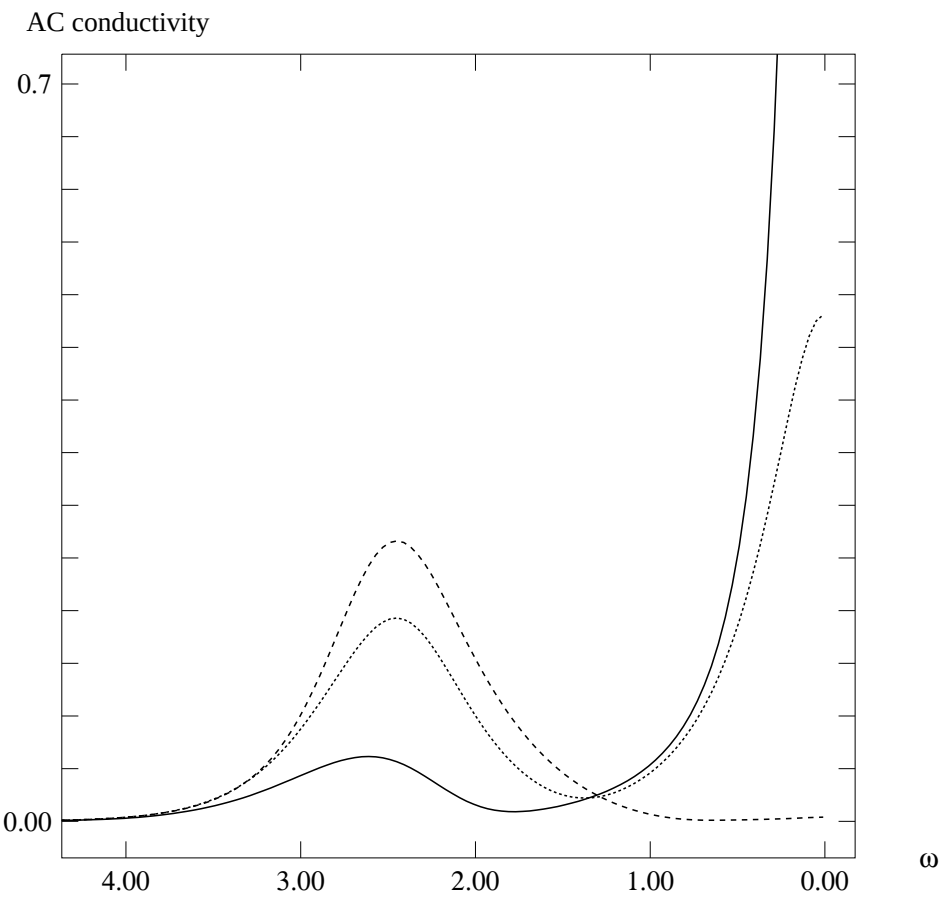

Figure 3.10: AC conductivity for fillings $n = 0.72$ (solid line), $n = 0.92$ (dotted line) and $n = 1$ (dashed line), ($U = 2.5$, $T = 0.1$, $E_f = 0$).

of a n_f-nonconserving contribution to the Hamiltonian, the simplest version of which would involve a hybridization interaction between the two bands. Nevertheless, the physics discussed here – especially the "pinning" of the renormalized f-level at the chemical potential – is expected to survive in certain multi-band extensions of the Falicov-Kimball model, even in the presence of weak hybridization [87].

In summary, we have computed the "exact" single particle spectra and the frequency-dependent conductivity for the simplified Hubbard model in infinite dimensions. The only nontrivial solutions involve an approximate "pinning" of the renormalized f-level within an energy of order T^2/μ of the chemical potential. The resulting physics is equivalent to that of a self-consistent impurity problem which, due to the broken translational symmetry, always leads to a finite value of $Im\Sigma(\omega = \mu)$. Although the disordered ground state is, strictly speaking, metallic for all fillings and interaction strengths, the behavior at half-filling at $U \sim \sqrt{2}D$ is virtually identical to that expected for a metal-to-insulator transition which occurs through a band splitting. This is clearly distinct from the metal-insulator transition that occurs in the Hubbard model, which, as we will see, is driven by the collapse of a quasiparticle resonance at the Fermi level. The transfer of spectral weight is solely a result of the fact that the number of doubly occupied (empty) sites changes as the system is doped. No non trivial transfer of weight occurs.

Chapter 4

The Mott Transition in the Hubbard Model

As mentioned in the introduction, the *correlation induced* metal-insulator transition (as opposed to the band insulator), generally known as the Mott or Mott-Hubbard transition constitutes one of the prime examples in which strong correlations between the electrons dominate the low-energy behavior of a physical system. The paradigmatic example for this metal-insulator transition is V_2O_3, where the transition was observed as early as 1946 [76]. While bandstructure calculations for this compound predict that it is metallic at low temperatures, one experimentally observes a metal-insulator transition as a function of temperature in which the conductivity drops drastically by seven orders of magnitude.

Ever since its discovery, the Mott transition has been the subject of intense experimental and theoretical (for references, see for example Refs. [7, 15]) investigations. From a theoretical point of view, several ideas have been put forward since the inception of the theoretical investigation by Mott [7, 77].

According to the simple picture originally proposed by Mott [7, 77], a strong local Coulomb repulsion U between two electrons on any given site leads to the splitting of a band of width $2D$ into two subbands, whose centers are separated by an energy gap U, the so-called "upper" and "lower Hubbard bands". One can view the two bands as corresponding to the propagation of doubly occupied and empty sites, respectively: If one particle is added to the half filled system one has to doubly occupy a site which costs an energy U. Since there are N (number of sites) ways to do this, these form a band of highly excited states. The same holds for the addition of a hole. If the system is half filled (one electron per site) and the gap between these two subbands, $U - D$, is *greater* than zero, the lower band is completely filled and separated from the upper

band by a finite gap. The system is therefore insulating. For $U - D < 0$ both bands touch and the system is conducting. It should be noted that this is exactly the scenario we observed in the Falicov-Kimball model in the previous chapter.

These early ideas were put on a more rigorous footing by Anderson [78, 79], who introduced the now so-called "Hubbard model", describing mobile electrons experiencing a strong on-site repulsion, as the simplest model of antiferromagnetic ("super") exchange in insulators. Independently, J. Hubbard [22, 23, 23] introduced the Hubbard Hamiltonian in his studies of the Mott transition, resulting in a picture similar to the Mott's. While treating the local aspects of the physics correctly, the simple picture is unfortunately incorrect, since his treatment fails to take the itinerant aspect of the problem into account correctly.

Gutzwiller [25], and Brinkman and Rice [26] treated the problem variationally, starting with the so-called Gutzwiller wavefunction, a filled Fermi sea of free electrons in which the number of doubly occupied sites is reduced variationally. Since this approach is based on a Fermi liquid point of view, it gives a good description of the metallic region. The mechanism driving the metal-insulator in this scenario is quite different, since the transition in this approach occurs through a continuous narrowing of the quasi-particle resonance, i.e. a diverging effective mass.

While both approaches (together with more sophisticated treatments) have yielded complementary insights into the problem, and one has thus obtained a good picture of the Mott-Hubbard transition, the approaches discussed so far fail to yield a systematic and unified approach treating high and low energy scales on an equal footing.

Over the past two years, new insights into the problem were gained using the limit of infinite dimensionality [36, 44], which we have discussed in Chapter 2 and used to solve the Falicov-Kimball model in the previous chapter. As we have seen, the limit of infinite dimensionality allows for a mapping of a variety of lattice models onto impurity problems in a self-consistently determined bath [53, 41] and is therefore a natural way to formulate a mean-field theory of itinerant systems.

Several groups [20, 19, 21] established the *existence* of a Mott transition in the Hubbard model at half-filling and showed, that – coming from the metallic side – it

occurs as described by Brinkman and Rice: A quasiparticle resonance at the Fermi level narrows *continuously* until at a critical value of the interaction, U_{c2}, the resonance disappears, leaving behind two well separated bands centered at $\pm U/2$. It should be emphasized that due to the fact that the density of states at the Fermi level in infinite dimensions is pinned to the non-interacting value, $ImG(0^+) = -2/D$, as was first pointed out by Müller-Hartmann [46], the transition has to occur through a narrowing of the Kondo resonance and cannot proceed by a shrinking of the resonance. In order to realize other scenarios it will be necessary to go beyond the limit of infinite dimensions (see Chapter 9 for a discussion of this aspect).

Coming from the insulating side, it is possible to obtain insulating solutions down to a value $U_{c1} < U_{c2}$, at which the resonance at the Fermi level pops up *discontinuously*. Between U_{c1} and U_{c2} both solutions coexist [12, 56].

At finite temperature, the difference between the free energy of the solutions is dominated by the entropy term. The large entropy, which is a result of the degeneracy of the ground state in the insulating case, makes it possible to unambiguously determine the existence of a first order transition line close to $U_{c1}(T)$. As the temperature is reduced, the free energy approaches the energy, therefore an accurate evaluation of the energy is necessary. Depending on which solution is lower in energy two very different scenarios may take place: If $E_{Ins} < E_{Met}$, the transition will be close to U_{c1} and the sudden destruction of the metallic state implies a first-order transition even at $T = 0$. On the other hand, in the case $E_{Met} < E_{Ins}$, the metallic solution continuously merges with the insulating one at U_{c2}, and the quasiparticles display a diverging renormalized mass [12].

A resolution of this issue using the approaches to the model used until now, the Quantum Monte Carlo method and second-order perturbation theory, has been impossible. While the limit $T = 0$ cannot be attained by Quantum Monte Carlo simulations, within the second-order perturbative approach the energies of the two solutions are almost degenerate, making the consideration of higher-order corrections necessary. As discussed in Chapter 2, an alternative numerical approach to the problem was introduced by Caffarel and Krauth [40] and Si et al. [63]. While the large d mean field

equations are *functional equations* for the Green function $G(i\omega_n)$, an approximation can be obtained by modeling $G(i\omega_n)$ using a finite number N of parameters, which reduces the functional equations to non-linear algebraic equations in N unknowns. Following this idea, two different parameterizations of the single particle Green function were introduced [40, 63]. Both take advantage of a mapping of the lattice problem onto an Anderson impurity model with a self-consistently determined bath. The N parameters that model $G(i\omega_n)$ define the hopping amplitudes and energies of the effective electron orbitals of the bath, as will be discussed in detail in next section. The resulting problem can then be solved at $T = 0$ by exact diagonalization of the effective Hamiltonian. This is followed by the new determination of the set of parameters, and the procedure is iterated until convergence is attained. The method is thus non-perturbative in nature and overcomes the problems of both Quantum Monte Carlo and perturbation theory, allowing for an accurate evaluation of the energies at $T = 0$.

In this chapter we apply this approach to the study of the Hubbard model at half-filling. We establish the coexistence of metallic and insulating solutions over a finite range of the interaction parameter U and show that at $T = 0$ the energy of the metallic solution is lower than the insulating one, implying that the metal-insulator transition in the Hubbard model with semicircular density of states is of second order. This justifies a posteriori the relevance of the earlier studies [57] of this quantum critical point which captures the essence of the Brinkman-Rice transition.

4.1 Methodology

In the limit of infinite dimensionality the Hubbard model with a half filled band, described by the Hamiltonian

$$\mathcal{H} = -t \sum_{<i,j>} f^{\dagger}_{i,\sigma} f_{j,\sigma} + U \sum_{i} (n_{fi\uparrow} - \frac{1}{2})(n_{fi\downarrow} - \frac{1}{2}), \tag{4.1}$$

can be reduced to an effective impurity problem, supplemented by a self-consistency condition [41]. As discussed in previous chapters we will focus on a Bethe lattice of infinite connectivity m, which in the non-interacting limit corresponds to a semicircular density of states of half width $2t$, where the hopping parameter t is rescaled in the

usual way as $t \to \frac{t}{\sqrt{m}}$. Integrating out the degrees of freedom other than the origin, one obtains an effective local action of the form

$$S_{eff}[c, c^\dagger] = \sum_\sigma \int_0^\beta d\tau d\tau' f_\sigma^\dagger(\tau) G_0^{-1}(\tau - \tau') f_\sigma(\tau') + U \int_0^\beta d\tau (n_{f\uparrow}(\tau) - \frac{1}{2})(n_{f\downarrow}(\tau) - \frac{1}{2}). \quad (4.2)$$

In the following we focus on the paramagnetic solution at half-filling. In this case the self-consistency condition reads

$$G_0^{-1}(i\omega_n) = i\omega_n - t^2 G(i\omega_n) \quad (4.3)$$

where $G(i\omega_n) = -\int_0^\beta d\tau e^{i\omega_n \tau} \langle T_\tau f(\tau) f^\dagger(0) \rangle_{S_{eff}}$ is the *local* Green function of the Hubbard model once self-consistency is reached. As we saw in Chapter 2 [41] an action of the same form can be obtained from an Anderson impurity model by integrating out the conduction electrons. Note that the self-consistency condition implies that the role of the hybridization function is played by the local Green function itself. Let us briefly recapitulate the procedure: $G(i\omega_n)$ is modeled by a finite set of parameters. In terms of the impurity problem, this represents an effective bath for the impurity with a finite number of poles. This effective impurity model is then solved by exact diagonalization and a new $G(i\omega_n)$ is calculated. A new set of parameters is then obtained from $G(i\omega_n)$ by approximating it by a function with a number of poles equal to the number of sites in the conduction electron bath. This number is in general smaller than the number of poles of $G(i\omega_n)$. Note that this represents a further approximation of the method (beyond the effective Hamiltonian being finite). The whole process is iterated until convergence of the parameters is achieved.

Exploiting these ideas, two new similar algorithms were proposed [40, 63], differing basically in the way the new set of parameters is obtained, that is, how the $G(i\omega_n)$ is parametrized by a smaller number of poles. We will consider both schemes and comment on their respective advantages and limitations.

As mentioned, the number of poles of $G(i\omega_n)$ is in general larger that the number of sites in the bath, therefore this approximation is an essential ingredient of the scheme. Caffarel and Krauth [40] proposed to obtain the new parameters by a χ^2 fit of $G(i\omega_n)$.

Starting with an Anderson Hamiltonian of the form

$$\mathcal{H}_{AM} = \sum_{k,\sigma} \epsilon_k c^\dagger_{k\sigma} c_{k\sigma} + \sum_{k,\sigma} (V_k c^\dagger_{k\sigma} f_\sigma + h.c.) + U(n_{f\uparrow} - \frac{1}{2})(n_{f\downarrow} - \frac{1}{2}) \qquad (4.4)$$

the self-consistency condition becomes

$$t^2 G(i\omega) = \sum_{k=1}^{N_s} \frac{V_k^2}{i\omega_n - \epsilon_k}. \qquad (4.5)$$

We thus have to minimize

$$\chi^2 = \sum_{i\omega_n}^{N_\Omega} |G(i\omega_n) - \sum_{k=1}^{N_{bath}} \frac{V_k^2}{i\omega_n - \epsilon_k}|^2 \qquad (4.6)$$

where we sum over frequencies $\omega_n = (2n+1)\pi T$. The "fictitious temperature" T simply serves as a low-frequency cutoff and is reduced systematically as the system size increases, since this leads to a more accurate description of the low-frequency region. The upper cutoff $N_\Omega \Delta\omega$ is chosen to be $\approx 2U$, beyond which the results no longer change significantly if the cutoff is changed. This leads to a new set of parameters V_k and ϵ_k. Note that this Hamiltonian effectively describes an impurity surrounded by a "star" of bath electrons.

It should be noted that in order to obtain a *metallic* solution one has to feed back a pole *at* the Fermi level in order to allow for the binding of a Kondo singlet. Depending on the value of the interaction, the system will flow to the insulating solution even in the coexistence region if this is not taken care of. Since the Green function obtained from the continued fraction representation *never* has poles exactly at zero, but two poles close to the origin (from particle and hole contributions, respectively) the low frequency cutoff has to be larger than the frequency position of the smallest pole of the Green function in order to allow for a collapse of the two lowest poles representing the Kondo resonance to one pole at zero.

In order to obtain the insulating solutions, the number of sites in the bath has to be even and one has to feed back an insulator. For $U > U_{c2}$ an insulator can be obtained with an odd number of particles in the bath if the site at the Fermi level effectively decouples from the system, i.e. the hopping between the impurity and the site at energy zero vanishes. Since the groundstate in that case is a degenerate doublet, one then has

to diagonalize the total spin $\vec{S}^2$ of the system in order to obtain the correct ground state. We also note also that the spectral sumrule has to be enforced explicitly.

An alternative route was introduced in the context of an extended Hubbard model [63]. This procedure takes advantage of the fact that the Green function $G(z)$ can be decomposed into "particle" and "hole" contributions as $G(z) = G^p(z) + G^h(z)$ with $G^p(z) = \langle gs|f_\sigma \frac{1}{z-(H-E_0)} f_\sigma^\dagger|gs\rangle$ and $G^h(z) = \langle gs|f_\sigma^\dagger \frac{1}{z+(H-E_0)} f_\sigma|gs\rangle$.

The respective contributions can be obtained from a continued fraction expansion as

$$\langle f_0^{p/h}|\frac{1}{\omega \mp (H-E_0)}|f_0^{p/h}\rangle = \cfrac{\langle f_0^{p/h}|f_0^{p/h}\rangle}{z \pm E_0 - a_0^{p/h} - \cfrac{b_1^{p/h\,2}}{z\pm E_0 - a_1^{p/h} - \cfrac{b_2^{p/h\,2}}{z\pm E_0 - a_2^{p/h} - \ldots}}} \tag{4.7}$$

where $|f_0^p\rangle = f_\sigma^\dagger|gs\rangle$, $|f_0^h\rangle = f_\sigma|gs\rangle$ and $|f_{n+1}\rangle = H|f_n\rangle - a_n|f_n\rangle - b_n^2|f_{n-1}\rangle$, $a_n = \langle f_n|H|f_n\rangle$, $b_n^2 = \frac{\langle f_n|f_n\rangle}{\langle f_{n-1}|f_{n-1}\rangle}$, $b_0 = 0$. This implies that G^p and G^h can be regarded as resulting from a Hamiltonian describing an impurity coupled to two chains with site energies $a_n^{p/h}$ and hopping amplitudes $b_n^{p/h}$. Again, the number of poles in the Green function is in general larger than the number of sites of the Hamiltonian and in order to close the self-consistency, the continued fraction expansion has to be truncated. The approximation in this scheme relies on the fact that the continued fraction representation captures exactly the moments of the energy of the Hamiltonian, up to the order retained in the continued fraction. It can thus be thought of as a moment by moment fitting. This scheme has the numerical advantage that it avoids the multidimensional fit of the Green function, but the disadvantage that it can be implemented practically only in the case of a semi-circular density of states. Unfortunately, in the metallic case an explicit extra site at the Fermi energy has to be introduced in order to allow to feed-back a metallic bath. The hopping parameter to this extra site is calculated by a single parameter minimization of the expression

$$\chi^2(\alpha) = \sum_{i\omega_{nL}}^{i\omega_{nH}} |G_A(i\omega_n, \alpha) - G(i\omega)|^2 \tag{4.8}$$

where now $G_A(i\omega_n, \alpha) = \frac{\alpha}{i\omega_n} + (1-\alpha)G_{N_C}(i\omega_n)$. G_{N_C} is the truncated Green function to length $N_C = N_{bath}/2$ and ω_L and ω_H are low and high energy cut-offs defined by the

lowest poles of G and G_{N_C}, respectively. Since this effectively changes the moments as spectral weight is taken from high energies to low energies, it spoils the moment-by-moment nature of the approximation. While the modification of the moments is small for a large number of sites, we believe that for the number of sites within reach with using current workstations, the χ^2 method is considerably better and will focus on the approach based on it for further results. Futher remarks regarding the two methods can be found in Chapter 2. All results in this thesis are obtained using the χ^2 fit of the Green function to close the self-consistency.

We obtain the ground state energy and wave function of the Anderson Hamiltonian by exact diagonalization (up to six sites) and the modified Lanczos technique (see Chapter 2). Systems of up to ten sites can be handled on a workstation. The zero temperature Green function of the local site is then obtained from a continued fraction expansion using the recursion method discussed above. Finally a new set of input parameters is obtained using the χ^2 fit and the method is iterated until convergence is achieved. Once we have obtained the self-consistent solution to the problem, we can extract the physical information needed. A major advantage of the formulation of the problem in terms of an Anderson impurity model is the fact that the energy of the Hubbard model can be obtained directly without frequency summations using Anderson model relations.

The kinetic energy per site is given as

$$\epsilon_{Kin} = \frac{2}{\beta N} \sum_{<j,k>} \sum_{i\omega_n} t G_{jk}(i\omega_n) e^{i\omega_n 0^+} . \tag{4.9}$$

Taking the limit of infinite coordination number this reduces to

$$\epsilon_{Kin} = \frac{2t^2}{\beta} \sum_{i\omega_n} G(i\omega_n)^2 e^{i\omega_n 0^+} . \tag{4.10}$$

Using the self-consistency condition (4.5), as well as the identity

$$\frac{2}{\beta} \sum_{i\omega_n} \sum_{k\sigma} \frac{V_k^2}{i\omega_n - \epsilon_k} \langle f_\sigma(i\omega_n) f_\sigma^\dagger(i\omega_n) \rangle = \sum_{k\sigma} V_k \langle f_\sigma^\dagger c_{k\sigma} + h.c. \rangle \tag{4.11}$$

we arrive at the expression for the kinetic energy

$$\epsilon_{Kin} = \sum_{k\sigma} V_k Re \langle gs | f_\sigma^\dagger c_{k\sigma} | gs \rangle. \tag{4.12}$$

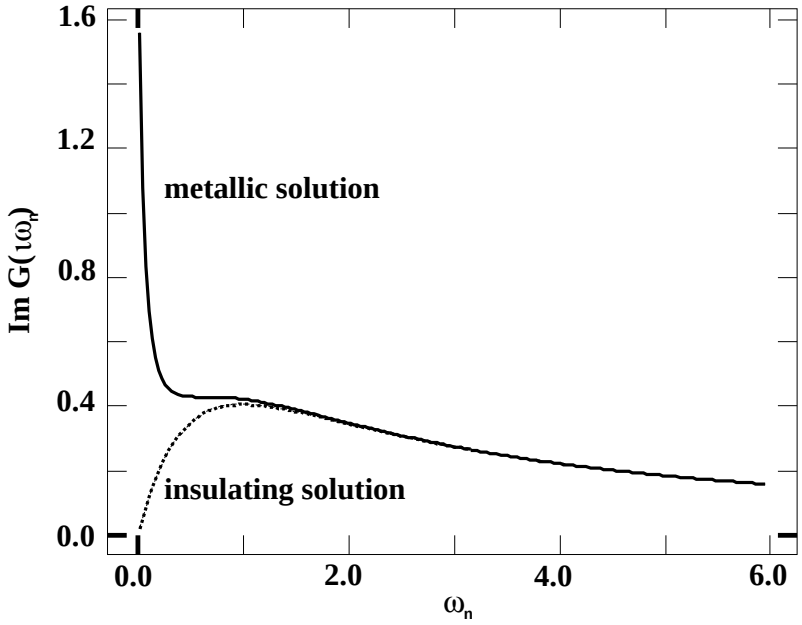

Figure 4.1: Coexisting solutions for the Green functions at $T = 0$, $U = 2.7$ at half-filling. Also shown (but indistinguishable) are the fitted functions using a fictitious temperature "T"=0.005 and N=8 sites.

The potential is simply obtained as

$$\epsilon_{Pot} = U\langle gs|n_{f\uparrow}n_{f\downarrow}|gs\rangle. \tag{4.13}$$

4.2 Results

In our analysis we have focused on two major aspects: The determination of the coexistence region in which both metallic and insulating solutions exist and the resolution of the controversy regarding the lowest energy solution, i.e. the question whether the Mott-Hubbard transition at zero temperature is first or second order.

We are able to obtain converged metallic and insulating solutions for a finite range of the interaction U. Metallic and insulating solutions for $U = 2.7$ inside the coexistence region as functions of $i\omega_n$ are shown in Fig. 4.1 (the half-bandwidth $2t$ is set equal to unity) [1]. The corresponding analytically continued Green functions giving the density of states are displayed in Fig. 4.2. Due to the cluster approach we are using, this gives

[1] Note that the pinning condition at $\omega = 0$ is fulfilled [46].

a discrete number of poles. The important feature to notice (this will be crucial in the following chapter) is the strong *separation of scales* exhibited in the metallic solution: Two broad, incoherent features comprising the upper and lower Hubbard bands are well separated from the narrow Kondo resonance at the Fermi level. The self-consistent projective technique we will develop in the following chapters we will exploit exactly this feature by eliminating the upper and lower Hubbard band altogether and focusing solely on the quasiparticle resonance. The insulator in the second case merely consists of high energy features (upper and lower Hubbard bands).

The kinetic, potential and total energies for the two solutions in the coexistence region are displayed in Fig. 4.3. Clearly, the metallic solution is lower in energy in the whole coexistence region. The energy difference between the solutions shown in the inset of Fig. 4.3 goes to zero as U_{c2} is approached, implying that the transition at zero temperature can indeed be classified as second order. This should be contrasted with the results from second-order perturbation theory, where the two solutions were found to cross in energy at an intermediate value of the interaction U. A point worth noticing (as was already observed within the perturbative approach) is that the energy difference between the solutions is much smaller than any energy scale of the problem. This is due to an almost perfect compensation of the gain in delocalization (kinetic) energy by the loss of energy through double occupancy (potential energy), in the metallic state compared to the insulator. Another important observation is that while finite size effects are apparent in the results for the kinetic and potential energy, the convergence of the total energy is much faster [80]. A few runs for a ten site system show essentially no difference to the results for eight sites, indicating that the thermodynamic limit has been reached.

As the critical point U_{c2} is approached from below, finite size effects become relevant for $U \approx 2.8$. This limitation of the scheme is due to the fact that as the low energy scale associated with the quasiparticle peak goes to zero close to the transition, the discrete nature of the approximation starts playing an important role and the Kondo resonance is represented by only a single pole. The validity of the procedure and therefore results for the energy therefore becomes less reliable. This is also reflected in the behavior of

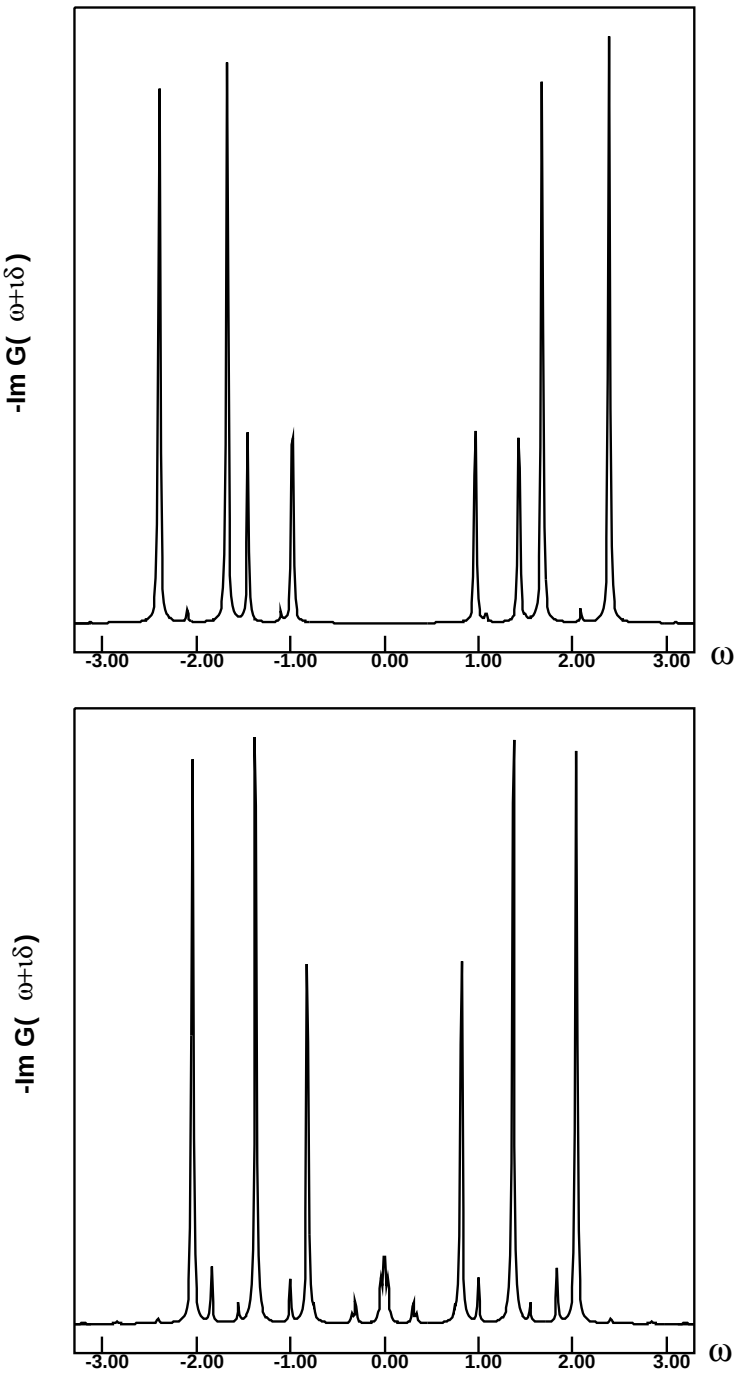

Figure 4.2: Density of states of the half-filled Hubbard model at $T = 0$, $U = 2.8$ corresponding to insulating (top, N=9 sites) and metallic (bottom, N=10 sites) solutions. A small broadening $\delta = 0.01$ of the poles is chosen to indicate their structure.

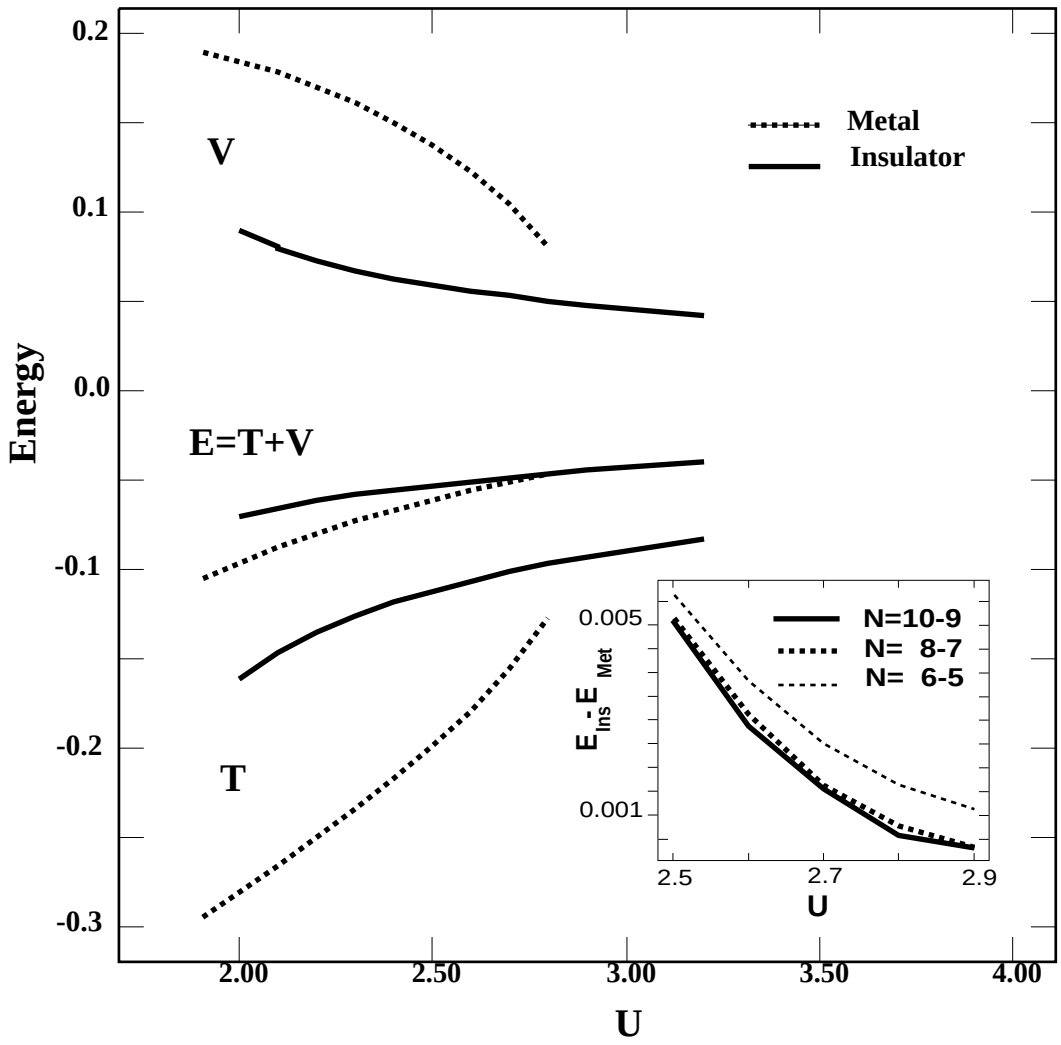

Figure 4.3: Total, kinetic and potential energies of metallic and insulating solutions in the coexistence region as functions of the interaction U for N=8 in the half-filled Hubbard model. In the inset we show the energy difference between the two solutions.

the quasiparticle weight $z = 1/(1 - \frac{\partial \Sigma}{\partial \omega})$, which goes to zero linearly for $U < 2.8$, but becomes non-linear beyond this value. Since this breakdown of linearity coincides with the point beyond which the Kondo resonance no longer shows any structure, we believe this to be a limitation of the approximation. In order to obtain an accurate description of the behavior near the transition a more sophisticated tool is clearly needed. An approach that remedies this problem, the self-consistent projective technique, will be developed and presented in the following chapters.

Due to these difficulties in the critical region and at small frequencies it is hard to extract the critical value U_{c2} from the quasiparticle weight using the present scheme. Some information, however, can be obtained using the difference between the *double occupancies* of metal and insulator which goes to zero at the transition, since it requires accurate information about the high-energy region. In Fig. 4.4 we display the difference between the double occupancies of metallic and insulating solutions. We see the excellent convergence as we go from eight to ten sites, but also notice the breakdown of the method in the critical region due to the strong separation of scales. Considering the linear region only, this can be represented by the functional form

$$n_{doub}^{met} - n_{doub}^{ins} = 0.05(U_c - U) \tag{4.14}$$

where $U_c = 2.96$, which differs from the exact value (see Chapter 7) of $U_c = 2.92$ by less than two percent. This can be compared to the result using the four boson approach of Kotliar and Ruckenstein [32, 81] which yields

$$n_{doub} = \frac{3\pi}{128}(U_c - U) \approx 0.07(U_c - U) \tag{4.15}$$

where $U_c = \frac{32}{3\pi}$. Note that in the 4 boson approach the double occupancy goes to zero at the metal insulator transition while it remains finite in infinite dimensions [12].

The fact that the transition is indeed second order and that the metallic solution is always lower in energy can also be seen from the following analytic argument. Using the Hellman-Feynman theorem we see that for metallic and insulating solutions $\frac{dE_{gs}}{dU} = \langle n_{f\uparrow} n_{f\downarrow} \rangle$. Integrating this equation between U_c and U one finds that $E_{gs}^I - E_{gs}^M > 0$ since the metal has a greater double occupancy. Thus U_{c2} is indeed

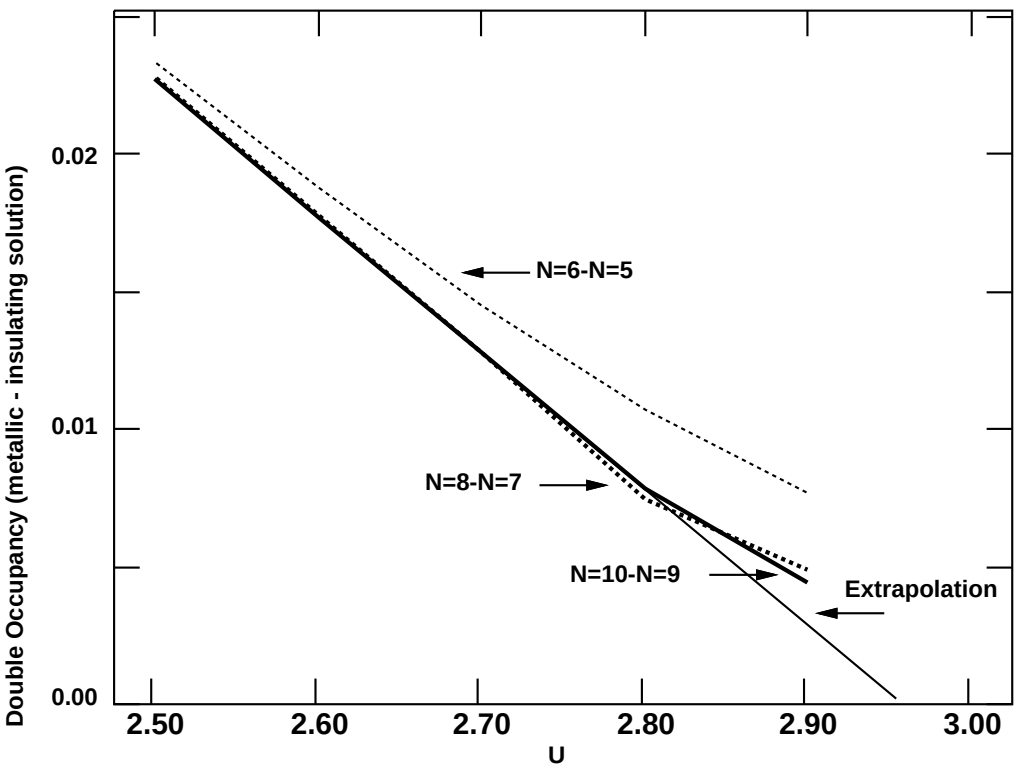

Figure 4.4: Difference between double occupancies of metallic and insulating solutions. Solid line: N=10 metal - N=9 insulator; solid dotted line: N=8 metal - N=7 insulator; thin dotted line: N=6 metal - N=5 insulator. Thin line: Extrapolation.

the physical transition at $T = 0$ in agreement with the numerical findings. Notice also that since the double occupancy difference is linear as shown in Figure 4.4, the energy difference is quadratic, explaining the smallness of the energy differences near the transition.

Finally, we would like to comment on the disappearance of the insulating solution at U_{c1}. While perturbation theory gives a $U_{c1} = 2.6$, the present scheme yields insulating solutions down to values $U_{c1} \approx 2.35$ which is smaller than the perturbative result but still does not indicate a closing of the gap as in the scenario described by Hubbard in which the gap closes continuously.

In conclusion, in this chapter we have resolved the standing questions regarding the metal-insulator transition in the Hubbard model in infinite dimensions, using a powerful algorithm to obtain Green functions at zero temperature, We were able to demonstrate the existence of a region in which metallic and insulating solutions coexist, which is in agreement with previous results, and showed that the metallic solution is always lower in energy. This implies that while at finite temperature the transition is first order, it becomes second-order at $T = 0$, similar to the work of Brinkman and Rice in the context of the Gutzwiller approximation [26, 57]. The method presented is very general as well as simple, especially when compared to Monte Carlo simulations. Unfortunately we also noted its limitations, in particular in the analysis of the critical behavior. We will show how these can be overcome, using the separation of scales pointed out in this chapter, in Chapter 6. In the following chapter we will proceed by analyzing the doped Hubbard model.

Chapter 5

Doping the Hubbard Model

The method of solving the Hubbard model in infinite dimensions by mapping it onto an Anderson model which is solved self-consistently using exact diagonalization as described earlier, has other major advantages. It is so far the *only* method that allows for an accurate investigation of the metal-insulator transition away from half-filling and at zero temperature, where both, perturbation theory and Quantum Monte Carlo methods, fail and thus allows us to determine physical quantities like the spectral functions, magnetic susceptibility and specific heat for different values of doping.

In this chapter we will focus on three aspects: We will analyze the behavior of n versus μ, in particular the charge susceptibility $dn/d\mu$ near the transition, which has been discussed controversially [82, 83] and extend the discussion of the coexistence region to the case of finite doping. This also allows for a preliminary investigation of the question *where* the states induced by doping the Mott insulator are generated, which is highly relevant in the light of the experiments on the cuprates [8, 9, 10, 11]. We will then discuss the question of transfer of spectral weight in the Hubbard model, which is again of strong experimental and theoretical [15, 71, 84, 85, 35] interest. We will restrict our discussion to the case of hole doping to keep the notation simple. Due to the particle-hole symmetry of the Hubbard model exactly the same arguments apply to the case of electron doping and all plots are symmetric with respect to particle and hole doping.

5.1 Coexistence at Finite Doping

We will begin by extending the discussion of the coexistence region to finite doping. While the coexistence of metallic and insulating solutions for values of the interaction

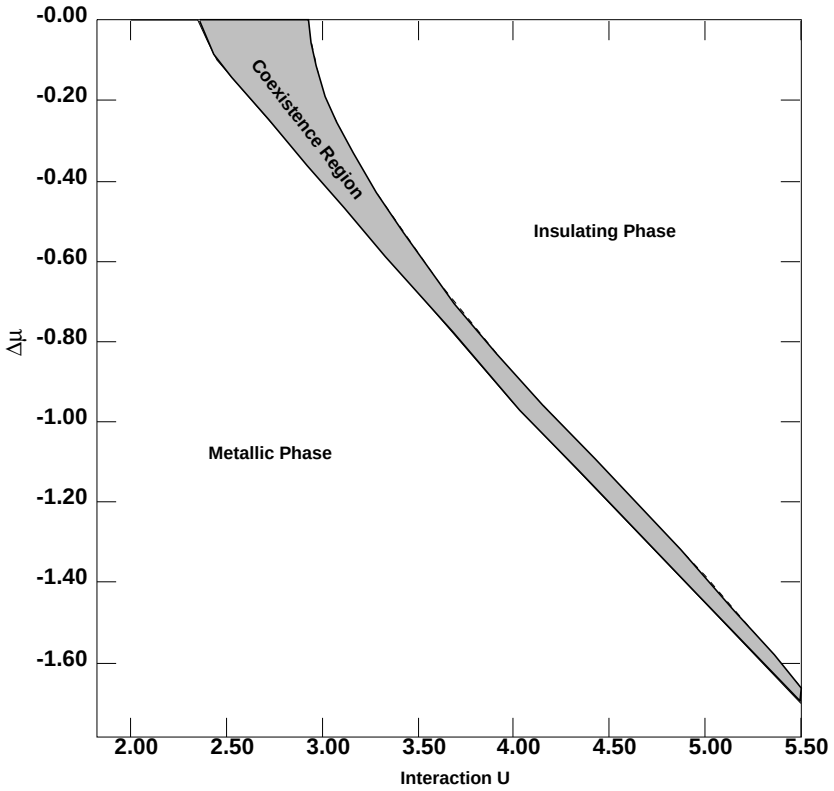

Figure 5.1: Coexistence region of metallic and insulating solutions at zero temperature and finite doping in the $\Delta\mu - U$ plane where $\Delta\mu = \mu - U/2$. (N=5 and partly N=7 sites for U_{c1}, μ_{c2} from Chap. 7.

between $\approx 2D$ and $\approx 3D$ at half filling is well established, it is not clear, whether this feature survives in the doped system. In particular, it has not been possible to stablize an insulating solution for interactions less than the critical U_{c2} for any finite doping [86] using the Quantum Monte Carlo method. On the other hand it is not clear, why the insulating solution should not survive as the chemical potential is changed based on continuity. The algorithm discussed in the previous chapter allows us to settle the question unambiguously. We find that it is indeed possible to stabilize insulating solutions for a finite chemical potential, such that the coexistence region extends over a finite area in the $\mu - U$ plane. The corresponding phase diagram is depicted in Fig. 5.1. No coexistence has been found for interactions $U < 2.35$.

From an inspection of the phase boundary as well as by looking at n vs. μ curves it

becomes obvious that as one approaches the metal from the insulating side the quasiparticle peak emerges discontinuously, i.e the transition is first order, as the chemical potential moves into the Hubbard band.

As in the case of half filling the insulator is always higher in energy, such that the metallic solution corresponds to the *physical* solution. In the following we will therefore focus on the disappearance of the *metallic solution* as coming from the metallic side. As in the case of half filling this happens through a continuous narrowing and finally disappearance of the quasiparticle peak and is thus a second order transition.

5.2 Charge Susceptibility

The behavior of the charge susceptibility $\chi_c = \partial n/\partial \mu$ as the Mott transition is approached from below, i.e. as $U - U_c \to 0^-$ has been discussed before [12] using the results obtained from Quantum Monte Carlo calculations. In particular, Rozenberg et al. observed, that the charge susceptibility remains finite for any $U < U_c$ and approaches zero at the transition, which is in marked contrast with the findings of Imada [82, 83], who observes a divergence of the charge susceptibility in Monte Carlo simulations of the two dimensional Hubbard model, which in turn leads to a diverging effective mass. As can be seen in Fig. 5.2, our calculations show that the charge susceptibility in infinite dimensions indeed remains finite, confirming the finite temperature QMC results of Ref. [12].

The more interesting feature, which we will confirm using the self-consistent projective technique to be developed in the next chapter, is that for values of the interaction larger than the critical U, the charge susceptibility remains finite for values of the chemical potential which are *in* the gap according to the rigid band picture. This indicates that the states generated for sufficiently low doping are formed *in* the gap. As can be seen from Fig. 5.2 the states are close to the center of the gap for $U \approx 3.5$ and approach the band edge as the interaction increases, while remaining well separated from the band as long as the doping is small. For larger values of doping the states merge with the lower Hubbard band.

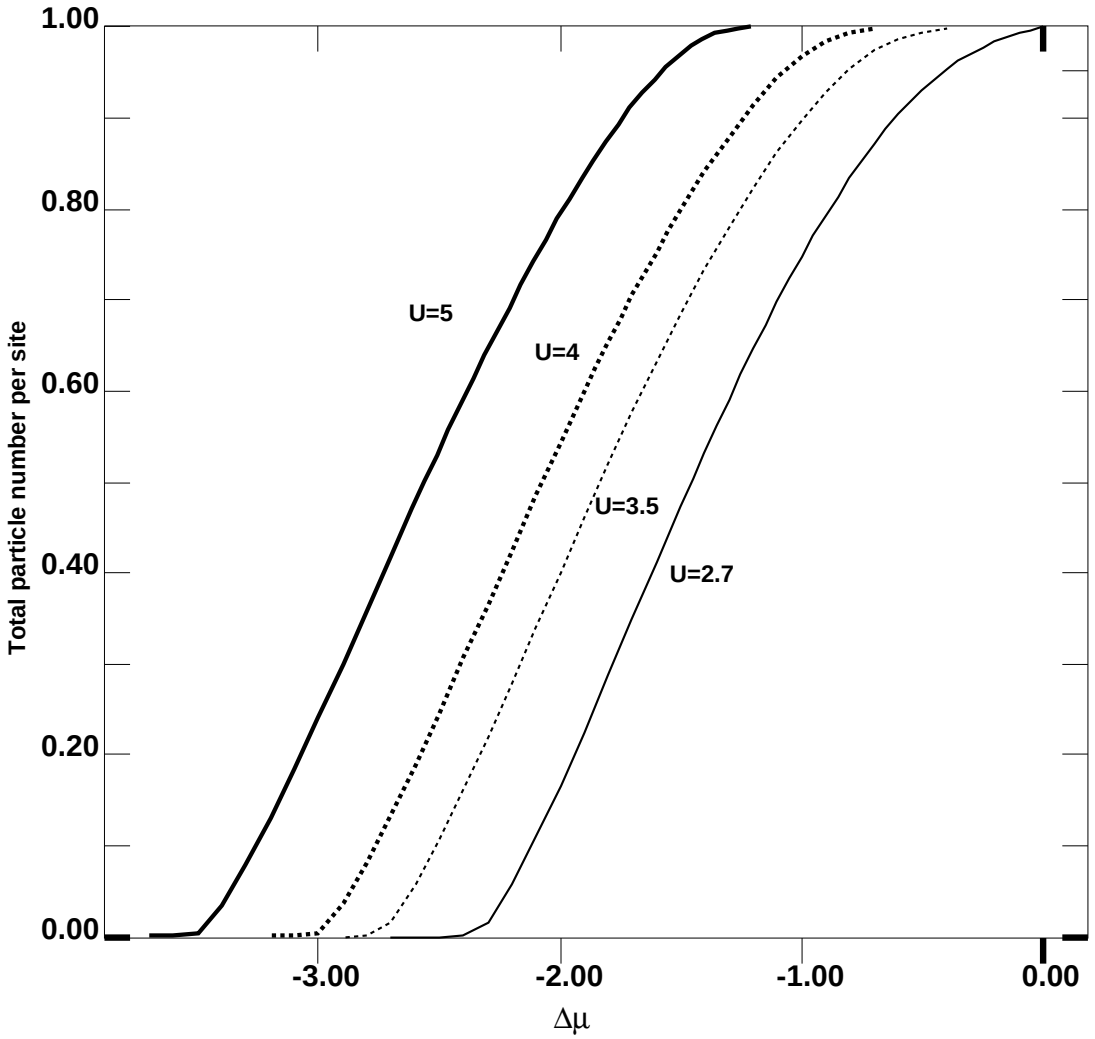

Figure 5.2: Total particle concentration per site as a function of $\Delta\mu = \mu - U/2$ for interactions U=2.7, U=3.5, U=4.0, U=5.0 (Lanczos diagonalization, N=8 sites).

This result is confirmed by looking at the spectral functions for moderate values of the interaction (in the example shown in Fig. 5.3 we have chosen $U = 4$ and dopings $\delta = 0.01, 0.086, 0.2, 0.35, 0.51, 0.7$). A careful inspection, which will be confirmed using the self-consistent projective technique, indicates that the resonance is split off from the band for small dopings and merges with the band only as the doping increases.

In the light of the following chapters it is instructive to describe this observation in terms of the self consistent Anderson model. The position of the resonance as a function of doping implies that one can distinguish three regimes in the effective Anderson model.

1. At half filling and for small values of the doping the doublet state $\{|\uparrow\rangle, |\downarrow\rangle\}$ is much lower in energy than the empty and doubly occupied states, $|\uparrow\downarrow\rangle$ and $|0\rangle$, which are essentially frozen out. There are virtually no charge fluctuations and the system is in the *local moment regime*, dominated by the quantum fluctuations between the two components of the doublet, $|\uparrow\rangle$ and $|\downarrow\rangle$. The resonance is separated by a finite energy gap from the lower Hubbard band and the system exhibits a clear *separation of scales*.

2. As the doping is increased, a crossover into the *mixed valence region* occurs, in which both spin fluctuations as well as charge fluctuations between empty and singly occupied sites occur. In this case there is no separation of scales between resonance and Hubbard bands anymore.

3. As the chemical potential is lowered even further, the system moves into the *empty orbital regime*, in which the impurity is predominantly unoccupied.

The three regimes can be distinguished quite nicely and easily by considering the expectation values $n_{single} = \sum_\sigma \langle (1 - n_\sigma) n_{\bar{\sigma}} \rangle$, $n_{empty} = \langle (1 - n_\sigma)(1 - n_{\bar{\sigma}}) \rangle$ and $n_{double} = \langle n_\sigma n_{\bar{\sigma}} \rangle$, which distinguish between local moment (n_{single} dominant), mixed valence (n_{empty} and n_{single} comparable), and empty orbital (n_{empty} dominant) regimes. Diagrams of the regimes in the $U - \Delta\mu$ and $U - n$ planes is depicted in Fig. 5.4. Since the crossover between the regimes is smooth, we have imposed the criterion that $n_{single} > 0.9$ for dominance of local moment behavior and $n_{empty} > 0.8$ for the empty

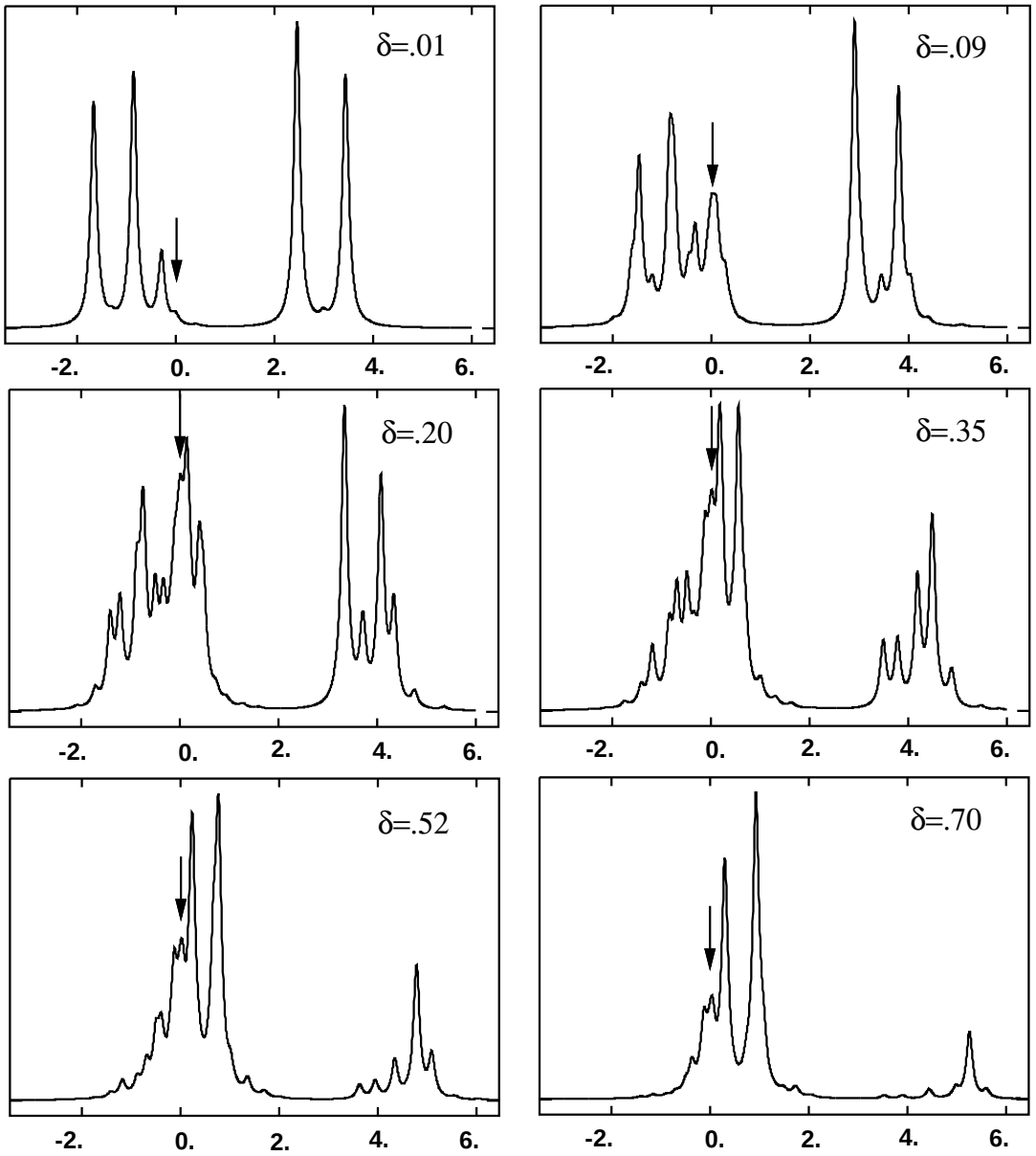

Figure 5.3: Spectral function of the Hubbard model at $T = 0$ for $U = 4$,$\delta = 0.01, 0.09, 0.2, 0.35, 0.51, 0.7$. The energies are measured with respect to the Fermi level. For clarity the resonance is marked with an arrow. The results were obtained using an N=8 particle cluster with broadening $\epsilon = 0.075$ of the poles.

orbital regime. Also sketched is the critical line μ_c beyond which the system insulating. This result will be obtained in Chapter 7.

We will confirm these observations in the following chapters using a powerful new method, the self-consistent projective technique, which enables us to determine the position of the resonance and the critical μ even more accurately and allows us to discuss the existence of the regimes from a different perspective.

5.3 Transfer of Spectral Weight

As mentioned in the introduction, and in parts of Chapter 3, another important question is the transfer of spectral weight in strongly correlated systems. This is observed experimentally using spectroscopic techniques [8, 11]. From a theoretical perspective it is intimately related to the validity of Fermi liquid theory [71, 15, 87, 88] and thus to the normal state properties of the model under consideration. This is particularly relevant, given the unusual normal state properties of the high-T_c materials [2].

In order to elucidate what transfer of spectral weight is all about and why it is a signature of strong electronic correlations, it is useful to contrast the cases of doping a semiconductor and doping a Mott insulator (a nice and more detailed account is given in Ref. [35].

Let us consider a semiconductor in which the valence band is fully occupied and the conduction band is completely empty. For simplicity consider a system with N sites, i.e. $2N$ single particle states due to spin degeneracy. Since the states in a semiconductor can be described in an independent particle framework and consist of states with energy ϵ_k which are either occupied or unoccupied, the spectral function has the form $\rho(\omega) = \frac{1}{2N}\sum_k \delta(\omega - \epsilon_k)$. In the undoped case, the chemical potential μ is in the center of the gap. If the system is doped with holes (electrons), the chemical potential shifts into the valence (conduction) band. It is important to realize that the spectral weights of valence and conduction bands, given as $w^+ = w^- = \frac{1}{2}$, remain unchanged and that *no new states* arise. It should also be pointed out that as one moves from hole doping to particle doping the chemical potential jumps by an amount

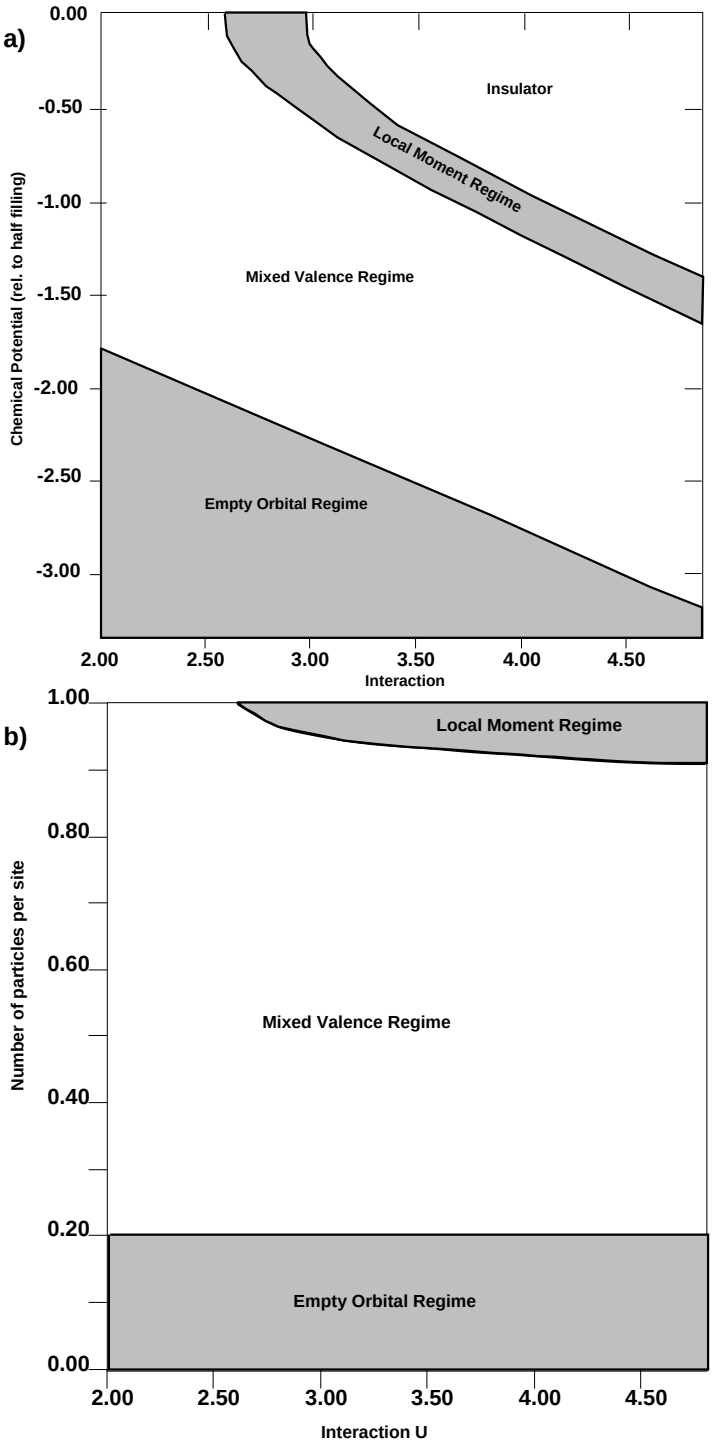

Figure 5.4: a) Regimes of the Hubbard model in the $U - \Delta\mu$ plane where $\Delta\mu$ is the chemical potential measured with respect to the value at half filling. b)Regimes of the Hubbard model in the $U - n$ plane.

equal to the gap.

In the case of the atomic limit of the Hubbard model, described by a Hamiltonian $H_{atomic} = \sum_i \Big(U n_{i\uparrow} n_{i\downarrow} - \mu(n_{i\uparrow} + n_{i\downarrow}) \Big)$ the situation is different. Since the upper band describes the propagation of doubly occupied sites, the weight of the upper band now depends on the doping δ, i.e. the concentration of holes (electrons) per site. In the case of hole doping the respective weights are now given as $w^- = \frac{1}{2}(1+\delta)$ and $w^+ = \frac{1}{2}(1-\delta)$ due to the presence of strong Coulomb correlations. Thus, through hole doping weight gets transferred from high to low energies. Recall that transfer of weight of this form is exactly what is observed in the Falicov-Kimball model [88, 50, 53]. In that case the gap remains intact and no new states are created in the gap. Also, once again the chemical potential exhibits a jump of order $U - 2D$, the band gap, as one goes from particle doping to hole doping.

Experimentally, other scenarios are observed. Allen et al. [10], for example, observe that for hole-doped compound $La_{2-x}Sr_xCuO_4$and for the electron doped compound $Nd_{2-x}Ce_xCuO_4$ new states are created in the insulator gap and that the chemical potential has essentially the same position in the gap for both hole and electron doping. In contrast to the semiconductor, the doping therefore produces new states, which arise by transferring weight from upper and lower Hubbard bands to the Fermi level.

It is therefore of interest to investigate the influence of the kinetic term on the transfer of spectral weight as described in the atomic Hubbard model. The crucial questions are, whether there are any regions in which new states arise in the gap and where the Fermi level moves as the doping is changed. While studies of these aspects exist [85, 35, 89] they are obtained primarily using exact diagonalization techniques and are thus subject to the problems associated with this technique.

Since we have seen that in the doped Hubbard states are generated in the gap (Fig. 5.3), one should expect that the reduction of spectral weight at high energies is enhanced due to the binding of the Kondo singlet at the origin. Moreover, one would expect non-linear effects to come in, such that it should be possible to parametrize the

high-energy spectral weight by the functional form

$$w^+ = \frac{1}{2}(1 - c_1\delta + c_2\delta^2). \tag{5.1}$$

For large values of the interaction this should approach the exact result $c_1 = 1$ and $c_2 = 0$ of the $U = \infty$ limit, which can be obtained using slave boson techniques (see i.e. Ref. [31]).

The high energy spectral weight, which is well separated from the remaining part of the spectrum and can therefore be extracted easily, is shown in Fig. 5.5 as a function of doping for several values of the interaction U. Also shown is the high energy spectral weight for the $U = \infty$ Hubbard model. Clearly the curves approach the exact $U = \infty$ result. The equations can be fitted well by the functional form (5.1) and the coefficients follow the expected behavior: c_1 is enhanced to ≈ 2.2 for $U = 3$ and decreases monotonically, approaching the $U = \infty$ value $c_1 = 1$, c_2 is $\approx 4.$ for $U = 3$ and approaches the $U = \infty$ value $c_2 = 0$.

The observed behavior can be understood from the self-consistent solutions of the two simplest toy models for the metallic and the insulating Hubbard model. The self-consistent $1 + 1$-site Anderson model, in which the bath of electrons is represented by one site at the Fermi level, gives a surprisingly good description of the metallic behavior and of the metal-insulator transition due to the fact that it allows for the binding of a singlet state at the Fermi level and thus exhibits a low energy features dominated by the Kondo effect. The $2 + 1$-site Anderson model, in which upper and lower band Hubbard bands are represented by one pole, respectively, gives a good picture of the insulating state. Both models are solved in Appendices B and C; here we will simply use the results derived there.

The crucial feature regarding the transfer of spectral weight, which can also be seen from the solution of the $2 + 1$-site insulator is the fact that the *only* self-consistent solution to order $(V/U)^2$ has *equal* hybridizations V^+ and V^- with upper and lower Hubbard bands, respectively. This implies directly that the weights of the upper and lower Hubbard bands are *equal*. Any *transfer* of spectral weight is thus necessarily due to the appearance of the Kondo resonance at the Fermi level and should be explicable

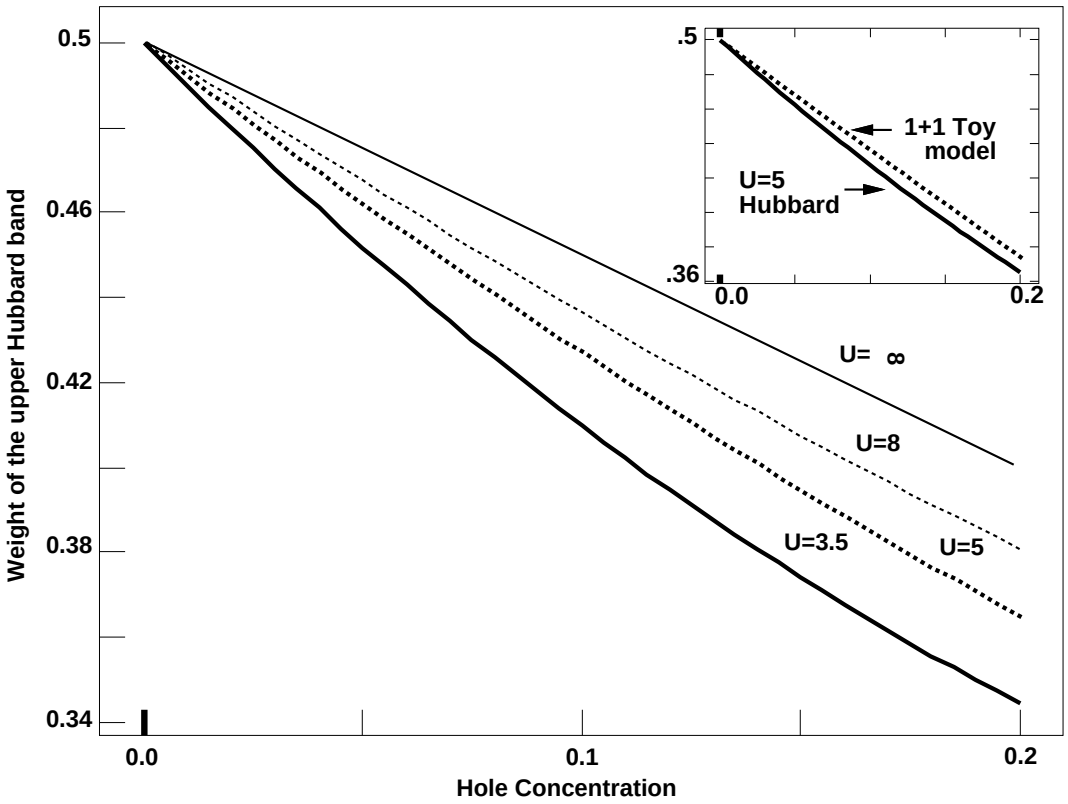

Figure 5.5: High energy spectral weight as a function of doping for $U = 3.5, U = 5.0$, $U = 8.0$ (N=8). Also shown is the $U = \infty$ value $w^+ = \frac{1}{2}(1 - \delta)$. The inset depicts the weight of the upper Hubbard band for $U = 5$ as obtained from the $1 + 1$ toy model in comparison with the result from Lanczos diagonalization.

from the solution of the $1+1$-site problem.

As demonstrated in the Appendix B (cf. Eq. (B.15)), the high energy spectral weight is of the form $\frac{1}{2N_{(0)}}(1-o(\frac{2V^2}{|E_{(0)}-|U}))^2$. Close to the transition $V \to 0$ and we can also expand in V/μ such that it assumes the form $\frac{1}{2}(1-o(\frac{2V^2}{\mu^2}))^2$ in agreement with Eq. (5.1). It is thus reduced from the insulating value as expected. From the explicit form of the ground state wavefunction (B.8), which to order V/μ is given as

$$|gs\rangle_{1+1} \quad = \quad \frac{1}{N}(|S2\rangle + \kappa_1|\uparrow\downarrow;0\rangle + \kappa_2|0;\uparrow\downarrow\rangle) \tag{5.2}$$

where again the κ_i are coefficients and the states are labelled as indicated in Appendix B, this can be seen to be the result of the admixture of the state $|0;\uparrow\downarrow\rangle = c^\dagger_\uparrow c^\dagger_\downarrow|0\rangle$ to the zeroth order singlet ground state $|S2\rangle$. Since in that state $|0;\uparrow\downarrow\rangle$ the impurity site is *empty*, this effectively reduces the weight of the upper band.

It is remarkable that our results are in excellent qualitative agreement with the experimentally observed transfer of spectral weight in the copper oxides [11], if the charge transfer gap in $La_{2-x}Sr_xCuO_4$ is interpreted as a Mott gap. A more careful study using a full two band model would be interesting.

In summary, we have studied the behavior of the Hubbard model in infinite dimensions as a function of doping. We have seen that at values of the interaction $U < U_{c2}$ metallic and insulating solutions coexist and that, as in the half-filled case, the metallic solution is lower in energy. For $U > U_{c2}$ doping induces states in the Hubbard gap which move towards the lower (upper) Hubbard band as the interaction or the hole (electron) doping concentrations are increased. For any value of the interaction a small doping concentration leads to states separated from the upper and lower Hubbard bands. We also observe an anomalous transfer of spectral weight from high energies to the Fermi level, which can be understood from the Kondo effect exhibited by the doped system.

Chapter 6

Resolving the Low Energy Properties: The Self-Consistent Projective Technique

6.1 Separation of Scales and How to Take Advantage of It

As was shown in several publications [20, 19, 21], and as we saw explicitly in the previous chapter, the metallic phase of the Hubbard model in infinite dimensions exhibits a *separation of scales* for intermediate and large values of the interaction ($U \geq 2.5D$) and for zero and small doping δ. This can be seen most clearly from the spectral functions as shown in Figures 4.2 and 5.3, which show the density of states of the Hubbard model at half-filling and for small doping.

Clearly, the spectra can be separated into three distinct features. The high energy features are given by the broad upper and lower Hubbard bands which are centered at energies $-\mu$ and $U - \mu$. At half-filling $\mu = U/2$, such that they are centered symmetrically about the Fermi level at $\pm U/2$. These are well separated from the narrow Kondo resonance at the Fermi level, the weight of which, w, goes to zero at the metal-to-insulator transition. The system of equations to be solved close to the transition contains two vastly different energy scales, given by the chemical potential μ and the width of the Kondo resonance, wD, rendering an accurate numerical treatment, in particular of the critical region, impossible.

In this chapter we will show, how we can use the natural separation of scales to our advantage by *eliminating* the high energy degrees of freedom, thereby reducing the full problem to an effective low energy problem containing only *one scale*, which can be tackled numerically. From the resulting effective problem one can easily obtain low frequency (temperature) results, as well as information about the critical behavior of the models considered. It is this idea that forms the basis of the self-consistent projective

technique.

While we develop and use the technique to study the particular case of the Hubbard model, the method is completely general and can be applied to any problem exhibiting a separation of scales, a common situation in strongly correlated electron systems. An essential feature of the method is the fact, that the high energy parts only enters via parameters which determine the detailed low energy behavior. In that sense it is similar to a Landau-Ginsburg analysis, in which high energy, short distance effects only determine the coefficients of the various terms of the Landau-Ginsburg functional.

In the case of the Hubbard model we will see that the self-consistent projective technique enables us to analyze the physical properties near the transition and the *exact* properties at the critical point, illustrating that it is a powerful technique to obtain the low frequency behavior of strongly correlated electron systems.

As one can see immediately from the spectral functions (Figures 4.2 and 5.3) the separation of scales implies that it is possible to decompose the single particle density of states $\rho(\epsilon)$ of the Hubbard model into high and low frequency parts as $\rho(\epsilon) = \rho^{low}(\epsilon) + \rho^{high}(\epsilon)$. Given the mapping of the Hubbard model onto a single impurity Anderson model [41]

$$\mathcal{H}_{AM} = \sum_{k\sigma} \epsilon_k c^\dagger_{k\sigma} c_{k\sigma} + \sum_{k\sigma} V_k (f^\dagger_\sigma c_{k\sigma} + h.c.) + U n_{f\uparrow} n_{f\downarrow} - \mu(n_{f\uparrow} + n_{f\downarrow}) \tag{6.1}$$

with self-consistency condition

$$\sum_k \frac{4V_k^2/D^2}{i\omega_n - \epsilon_k} = G[\epsilon_k, V_k](i\omega_n) \tag{6.2}$$

(recall that $t = D/2$) this implies, that we can also separate the variables ϵ_k and V_k describing the self-consistently determined bath of conduction electrons into sets $\{\epsilon_{k,H}, V_{k,H}\}$ corresponding to the high energy features and $\{\epsilon_{k,L}, V_{k,L}\}$ containing the low-energy states up to a cut-off given by the Kondo temperature or renormalized Fermi energy of the Hubbard model and carrying spectral weight

$$w = 4/D^2 \sum_{k \in low} V_{k,L}^2. \tag{6.3}$$

In terms of the regimes discussed in the previous chapter, the separation of scales occurs as long as the effective Anderson model is in the *local moment regime*, in which

the impurity site is fluctuating between the two spin configurations $|\uparrow\rangle$ and $|\downarrow\rangle$, which are much lower in energy (by an amount μ) than the empty and double occupied configurations $|0\rangle$ and $|\uparrow\downarrow\rangle$.

A schematic description of the separation of scales as well as of the effective low energy problem is shown in Fig. 6.1. It should be emphasized that the *particular* implementation of the self-consistent projective method to the Hubbard model developed in this thesis is restricted to the local moment regime. This is due to the fact that we assume a certain structure of the part of the Hamiltonian containing the high energy states. We shall see explicitly later, how it implicitly contains the information about the range of validity of the present implementation. It should be emphasized, however, it can be applied to other cases and other regimes.

In order to eliminate the high energy degrees of freedom, we first separate the impurity Hamiltonian $\mathcal{H}_{AM}$ into three parts as

$$\mathcal{H}_{AM} = \mathcal{H}_{at} + \mathcal{H}_b + \mathcal{H}_M. \tag{6.4}$$

$\mathcal{H}_{at}$ is given as

$$\mathcal{H}_{at} = U n_{f\uparrow} n_{f\downarrow} - \mu(n_{f\uparrow} + n_{f\downarrow}) + \sum_{\sigma,k} V_{k,H}(c^+_{k\sigma} f_\sigma + h.c.) + \sum_{\sigma,k} \epsilon_{k,H} c^+_{k\sigma} c_{k\sigma} \tag{6.5}$$

and can be thought of as an Anderson impurity in a semiconductor.

$$\mathcal{H}_b = \sum_{k,\sigma} wD\tilde{\epsilon_k} c^+_{k\sigma} c_{k\sigma} \tag{6.6}$$

describes a narrow band of low energy conduction electrons. Since the energy will turn out to be of order wD, we have introduced dimensionless, rescaled variables $\tilde{\epsilon}_k = \epsilon^L_k/(wD)$. The hybridization $\mathcal{H}_M$ with the low energy electrons is given by

$$\mathcal{H}_M = \sqrt{w} D \sum_\sigma (c^\dagger_{L\sigma} f_\sigma + h.c.) \tag{6.7}$$

with

$$c_{L\sigma} \equiv \sum_k 2\tilde{V}_k c_{k\sigma} \tag{6.8}$$

the local low energy conduction electron operators normalized to have canonical anti-commutation relations

$$\{c_{L\sigma}, c^\dagger_{L\sigma}\} \;=\; 1 \tag{6.9}$$

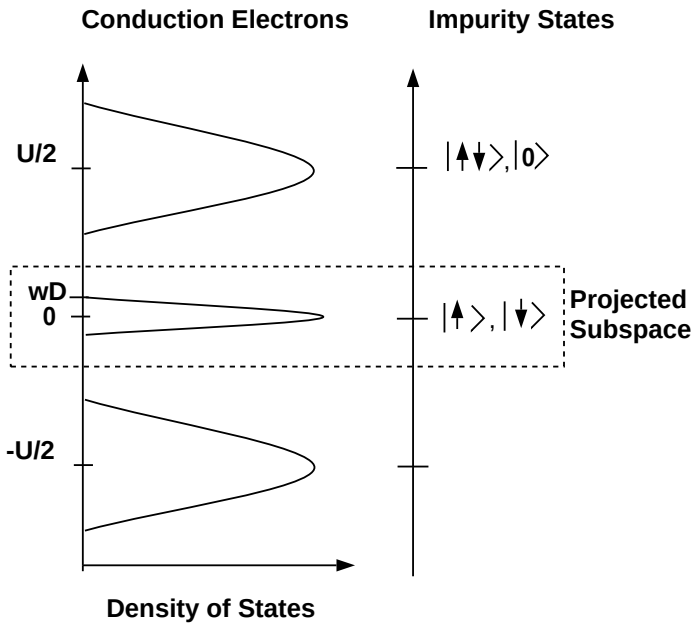

Figure 6.1: Schematic plot of the spectral functions of the conduction electrons and of the impurity configurations, illustrating the separation of scales into low and high energy contributions.

$$\{c_{L\sigma}, c_{L\sigma}\} = \{c^\dagger_{L\sigma} c^\dagger_{L\sigma}\} \quad = \quad 0. \tag{6.10}$$

Again we have rescaled the $V_{k,L}$ by introducing rescaled variables $\tilde{V}_k = V_{k,L}/(\sqrt{w}D)$, which thus shows explicitly the perturbative nature of the hybridization with the low energy band.

As long as we are in the local moment regime, which is the case in the critical region and thus the regime we will restrict ourselves to in this work, the contribution to the Hamiltonian containing the high energy states, $\mathcal{H}_{at}$, has low-lying spin doublet ground states $|\sigma\rangle_{H_{at}}$ with energy E^{at}_{gs}. These are separated by a gap of order μ from the high energy excited states. These high energy states (i.e. the excited states of $\mathcal{H}_{at}$) shall be denoted by $|\alpha\rangle$. This structure of the eigenstates can be seen most clearly by considering the impurity orbital *only*. The four possible states in that case are the doublet ground state $|\sigma\rangle = f^\dagger_\sigma|0\rangle$ with energy $-\mu$, which is well separated from the doubly occupied and empty states, $f^\dagger_\uparrow f^\dagger_\downarrow|0\rangle$ and $|0\rangle$, at energies $U-2\mu$ and zero, respectively. Hybridizing the single impurity with lower and upper Hubbard bands simply renormalizes the states by "dressing" them with particle-hole excitations without altering their transformation properties, i.e. the ground state remains a degenerate doublet.

Upon diagonalizing $\mathcal{H}_{at}$ the full Hamiltonian can be thus be decomposed into a high energy sector spanned by the states $\{|\alpha\rangle_{H_{at}}\} \otimes \{|\psi_L\rangle\}$, a low energy sector spanned by the states $\{|\sigma\rangle_{H_{at}}\} \otimes \{|\psi_L\rangle\}$ with $\{|\psi_L\rangle\}$ states of the $c^L_{k\sigma}$, and mixing terms. In order to obtain the effective low energy Hamiltonian, we perform a *canonical transformation* which eliminates the coupling between high and low energy subspaces and thus yields effective low and high energy Hamiltonians. We thus have to find an operator S mediating the transformation such that the effective Hamiltonian is block diagonal, i.e. find S such that

$$\mathcal{H}^{eff} = e^{-S}\mathcal{H}_{AM}e^{S} = \mathcal{H}^{eff}_L + \mathcal{H}^{eff}_H \tag{6.11}$$

where the subscripts L and H denote operators acting on the low and high energy sectors only, respectively. The action of the canonical transformation is depicted in Figure 6.2.

Notice that if the high energy band just consisted of a single state, this procedure

$$\mathcal{H} = \begin{pmatrix} H_{low} & H_{low-high} \\ H_{high-low} & H_{high} \end{pmatrix} \Rightarrow \mathcal{H}_{eff} = \begin{pmatrix} H_{low}^{eff} & 0 \\ 0 & H_{high}^{eff} \end{pmatrix}$$

Figure 6.2: Schematic representation of the canonical transformation

would be equivalent to a Schrieffer-Wolff canonical transformation [90]. The information about virtual excitations to high and low energy sectors is contained in the coefficients of the terms in the effective low and high energy Hamiltonians, respectively, as we will see explicitly later.

In order to preserve the clarity of the logic, let us proceed in our discussion by first giving a general outline of the procedure comprising the self-consistent projective technique and defer the discussion of the explicit form of canonical transformation and of the operators to the next section.

Having decomposed the Hamiltonian into high and low energy parts, we now have to transform operators, Green functions and self-consistency condition accordingly.

The canonical transformation amounts to performing a *basis transformation*, implying that *all operators* have to be transformed correspondingly. In particular, for the determination of the single particle Green function we thus obtain projected fermion operators

$$F_\sigma \equiv F_\sigma^{LL} + F_\sigma^{LH} + F_\sigma^{HL} + F_\sigma^{HH} \equiv e^{-S} f_\sigma e^{S}. \tag{6.12}$$

The superscripts HL and LH denote operators connecting low and high energy sectors. With those, the low and high energy contributions to the Green function assume the form

$$G_{low}(i\omega_n) = (\langle F_\sigma^{LL} \frac{1}{i\omega - (\mathcal{H}_L^{eff} - E_{gs})} F_\sigma^{LL\dagger} \rangle + \langle F_\sigma^{LL\dagger} \frac{1}{i\omega + (\mathcal{H}_L^{eff} - E_{gs})} F_\sigma^{LL} \rangle) \tag{6.13}$$

and

$$G_{high}(i\omega_n) = (\langle F_\sigma^{LH} \frac{1}{i\omega - (\mathcal{H}_H^{eff} - E_{gs})} F_\sigma^{\dagger HL} \rangle + \langle F_\sigma^{LH\dagger} \frac{1}{i\omega + (\mathcal{H}_H^{eff} - E_{gs})} F_\sigma^{HL} \rangle. \tag{6.14}$$

The self-consistency condition (6.2) can then be decomposed as

$$0 = \sum_k \frac{V_{k,L}^2}{i\omega_n - \epsilon_{k,L}} - t^2 G_{low}(i\omega_n)[V_{k,L}, \epsilon_{k,L}; V_{k,H}, \epsilon_{k,H}] \tag{6.15}$$

$$0 = \sum_k \frac{V_{k,H}^2}{i\omega_n - \epsilon_{k,H}} - t^2 G_{high}(i\omega_n)[V_{k,L}, \epsilon_{k,L}; V_{k,H}, \epsilon_{k,H}]. \tag{6.16}$$

Equations (6.15) and (6.16) are strictly equivalent to the original problem and form the basis of the self-consistent projective technique.

The crucial observation is the fact that a detailed analysis of the low frequency region (6.15) depends only weakly on the high energy part of the spectrum, which enters *only* through a few numerical coefficients, as we will see in the case of the Hubbard model. Conversely, the high energy part (6.16) only depends weakly on the low energy part. More precisely, the low energy part only enters via integrated quantities such as $\sum_k V_k^2 \epsilon_{k,L}$. There are therefore various levels on which the equations can be studied. In the model at hand, in which the physics is well understood, we will proceed by a *quantitative* analysis of the equations to a given order. In problems less well understood one can start by assuming a high energy phenomenology (i.e. a set of coefficients entering the low energy problem) and obtain *qualitative* insights by investigating the corresponding consequences for the low energy part. Again it is illuminating to make the connection to a Landau-Ginsburg approach, in which qualitative insights about a physical problem can be gained without knowledge of the numerical details.

In the case of the Mott transition we are interested in the numerical values of physical quantities near the Mott transition, i.e. the critical interaction, specific heat, and resistivity. Clearly we cannot perform the canonical transformation to all orders, but have to expand in the "small parameter" w as

$$S = \sqrt{w} S^{(1)} + w^{3/2} S^{(3)} + ... \tag{6.17}$$

We will see after we solve self-consistently for w that this expansion is justified, since the coeffients multiplying powers of w will turn out to be of order one in the relevant energy regime.

The expansion yields

$$\mathcal{H}_L^{eff} = w\mathcal{H}_L^{eff(1)} + w^2 \mathcal{H}_L^{eff(3)} + ... \tag{6.18}$$

$$\mathcal{H}_H^{eff} = \mathcal{H}_H^{eff(0)} + w\mathcal{H}_H^{eff(1)} + ... \tag{6.19}$$

and

$$F_\sigma^{LL} = \sqrt{w} F_\sigma^{LL(1)} + w^{3/2} F_\sigma^{LL(3)} + ... \tag{6.20}$$

$$F_\sigma^{LH} = F_\sigma^{LH(0)} + w F_\sigma^{LH(2)} + ... \tag{6.21}$$

as will become clear from the explicit form of the expansion discussed in the following section. Correspondingly the high and low energy contributions to the Green function can be expanded order by order as

$$G_{high}(i\omega_n) = G_{high}^{(0)}(i\omega_n) + w G_{high}^{(1)}(i\omega_n) \tag{6.22}$$

$$G_{low}(i\omega_n) = w G_{low}^{(1)}(i\omega_n) + w^2 G_{low}^{(2)}(i\omega_n). \tag{6.23}$$

Depending on whether we are interested in the properties *at* the critical point, at which $w \to 0$, or *near* the critical point, we have to solve the self-consistency equations (6.15) and (6.16) to order w or to order w^2.

6.1.1 Determining the Physical Properties *at* the Critical Point

For the determination of the physical properties *at the critical point* coming from the metallic side, for which $w \to 0^+$, it is clearly sufficient to treat the equations (6.15) and (6.16) to *lowest order* in w, i.e. we have to solve

$$0 = \sum_k \frac{V_{k,H}^2}{i\omega_n - \epsilon_{k,H}} - t^2 G_{high}^{(0)}(i\omega_n), \tag{6.24}$$

which to lowest order is independent of w, and

$$0 = \sum_k \frac{w D^2 \tilde{V}_k^2}{i\omega_n - \epsilon_{k,L}} - t^2 w G_{low}^{(1)}(i\omega_n). \tag{6.25}$$

We thus see that – as is intuitively obvious – at the critical point the *high energy* contributions are unaffected by the presence of the vanishing Kondo resonance at low energies, and one can therefore proceed in two steps:

1. One solves the lowest order high energy part described by the Hamiltonian $\mathcal{H}_H^{eff(0)}$ self-consistently. For a vanishing quasiparticle weight this simply corresponds to the solution to the insulating problem. This yields the lowest order coefficients entering the low energy Hamiltonian $w\mathcal{H}_L^{eff(1)}$ and thus determines the low energy properties.

2. One can then proceed by solving the low energy part at the critical point self-consistently using the coefficients obtained from the insulating solution.

Note that to lowest order the low energy spectral weight w drops out in Eq. (6.25), rendering the equation unstable except at the critical point. This is analogous to the familiar case of a Landau-Ginsburg expansion (see i.e. [43]), where in order to obtain a finite value for the order parameter in a second-order phase transition, terms in the Landau functional to fourth order need to be retained. We will see later, how the problem *at* the critical point can be solved in practice without going to higher orders.

6.1.2 Determining the Physical Properties *near* the Critical Point

The case *close to the critical point*, i.e. in which $U_c - U$ in the half filled case or $|\mu_c - \mu|$ away from half-filling are small, is more complicated. In this case the Kondo resonance has a finite weight w and one not only has to keep terms of order w^2 in the low energy part, but also terms of order w in the high energy part. This is due to the fact that a finite width of the Kondo resonance modifies the spectral weight of the high energy part of the problem to order w. In principle one thus has to solve the equations

$$0 = \sum_k \frac{V_{k,H}^2}{i\omega_n - \epsilon_{k,H}} - t^2 G_{high}^{(0)}(i\omega_n) - wt^2 G_{high}^{(1)}(i\omega_n) \tag{6.26}$$

$$0 = \sum_k \frac{wD^2 \tilde{V}_k^2}{i\omega_n - \epsilon_{k,L}} - t^2 w G_{low}^{(1)}(i\omega_n) - t^2 w^2 G_{low}^{(2)}(i\omega_n) \tag{6.27}$$

simultaneously. While this is a possible procedure, it is desirable to have, at least in principle, a procedure, in which one is left with a *single* equation for the low energy part *only*. This can be achieved in the following way.

1. We first solve the self-consistent insulator, i.e. the high energy part to lowest order in w, as done when determining the properties of the model at the critical point.

2. One now has to determine how the high energy $V_{k,H}$ are modified if the low energy $V_{k,L}$ change. This can be done in principle by expanding Eq. (6.16) around the

insulating solution. Let us define

$$\Lambda[V_{k,L},\epsilon_{k,L};V_{k,H},\epsilon_{k,H};\Delta] \equiv \sum_k \frac{V_{k,H}^2}{i\omega_n - \epsilon_{k,H}} - t^2 G_{high}(i\omega_n)[V_{k,H},\epsilon_{k,H};V_{k,H},\epsilon_{k,H}] \tag{6.28}$$

where Δ is the formally small parameter determining the proximity to the critical point and is thus given as $\Delta = U - U_c$ at half-filling and as $\Delta = \mu - \mu_c$ for finite doping. In terms of Λ the high-energy part of the self-consistency then simply reads

$$\Lambda[V_{k,H},\epsilon_{k,H};V_{k,H},\epsilon_{k,H};\Delta] = 0. \tag{6.29}$$

Close to the transition this can be expanded to lowest order in w and one obtains

$$0 = \frac{\partial\Lambda}{\partial(V_{k,L}^{(1)}V_{k',L}^{(1)})}V_{k,L}^{(1)}V_{k',L}^{(1)} + \frac{\partial\Lambda}{\partial\epsilon_{k,L}^{(1)}}\epsilon_{k,L}^{(1)} + \frac{\partial\Lambda}{\partial V_{k,H}^{(2)}}V_{k,H}^{(2)} + \frac{\partial\Lambda}{\partial\epsilon_{k,H}^{(2)}}\epsilon_{k,H}^{(2)} + \frac{\partial\Lambda}{\partial\Delta}\Delta. \tag{6.30}$$

Solving this matrix equation for $\epsilon_{k,H}^{(2)}$ and $V_{k,H}^{(2)}$ by performing a matrix inversion in principle gives explicit expressions for the $V_{k,H}^{(2)}$ and $\epsilon_{k,H}^{(2)}$ in terms of the low frequency parameters $V_{k,L}$ and $\epsilon_{k,L}$.

3. We can now insert these expression into the low frequency self-consistency condition (6.15) and thus obtain the correct high energy coefficients (to order w) as functions of the low frequency parameters. The low frequency is now consistently given to order w^2 and can be iterated until convergence is achieved. This gives the consistent solution of the low energy problem to order w^2.

In practice carrying out this procedure is prohibitively complicated numerically and we will resort to an *approximate scheme* to obtain the higher order corrections to the high energy Hamiltonian. This relies on information of the high energy bands from the solution of the full Hubbard model. Since we only need these to order w, we will see, that this indeed gives a consistent framework. We will outline the procedure used in the following.

1. We extract the information about the high energy features from the converged solution of the full Hubbard model. This gives the zeroth order $\{V_{k,H}\}$ and $\{\epsilon_{k,H}\}$ and thus the zeroth order weights of upper and lower Hubbard bands,

$w^{\pm}_{(0)} = 4/D^2 \sum_{k\in\pm} V^2_{k\pm}$ where $+$ and $-$ denote upper and lower Hubbard bands, respectively. Clearly, the weight of the Kondo resonance is not given accurately, such that $w^{\pm}$ are only correct to order w. However, it is still possible to determine the self-consistent modification of the latter to order w in the course of the iteration. This can be seen as follows. To leading order in w the high energy spectral weights close to the transition are given as $w^{\pm} = \frac{1}{2}(1 - c^{\pm} w)$ where $c^{\pm}$ is of order unity, as we saw in the previous section. We can therefore extract the coefficients $c^{\pm}$ *to leading order* from the solution of the Hubbard model, which are then given as $c^{\pm} = \frac{1}{w_{(0)}}(1 - 2w^{\pm}_{(0)})$. Here $w_{(0)}$ is the zeroth order weight of the Kondo resonance obtained frum the Hubbard model. This can be done unambiguously, since in the regime of interest the poles can be clearly separated into high and low energy contributions. The only approximation in this scheme is the assumption that the shape of the Hubbard bands is unchanged. This approximation is not as severe as it may seem, since the low energy part only sees *averages* of the high energy quantities.

2. Using the information about the high energy features we can now determine the coefficients $J^{||}_{\sigma\sigma'}$ and $J^{\perp}$ entering the low energy Hamiltonian. This is done by performing one iteration of the "insulator" obtained by considering the high energy features of the solution to the Hubbard model only (i.e. one explicitly removes the Kondo resonance from the solution to the Hubbard model).

3. We now determine the solution to the low energy problem using the coefficients $J^{||}_{\sigma\sigma'}$ and $J^{\perp}$, which gives us the $V^{(new)}_{k,L}$ entering the next iteration and therefore the new low energy spectral weight $w^{(new)}$.

4. We can now correct the high energy spectral weight using $w^{\pm} = \frac{1}{2}(1 - c^{\pm} w^{(new)})$. In order to fulfill the spectral sumrule, the $w^{\pm}$ are rescaled such that $w^{+} + w^{-} + w = 1$. The procedure is iterated beginning with step (2) until convergence is achieved.

Once again it should be emphasized that the only approximation in this scheme is the assumption that the high energy features do not change their shape, which can clearly

be justified as indicated.

We are now left with the determination of the *explicit* form of the operators entering the effective low energy problem. An efficient scheme to obtain these, as well as their explicit form will be given in the following section.

6.2 The Explicit Form of the Canonical Transformation

Let us proceed by discussing how the canonical transformation can be carried out efficiently to higher orders. As discussed we want to find a canonical transformation $\mathcal{U}$ eliminating the off-diagonal terms of the Hamiltonian connecting low and high energy sectors, such that the effective low energy Hamiltonian $\mathcal{H}^{eff} = \mathcal{U}^{-1}\mathcal{H}_{AM}\mathcal{U}$ is block diagonal. A convenient way to perform the canonical transformation is given by the canonical van Vleck perturbation theory [91]. $\mathcal{U}$ is chosen to have exponential form $\mathcal{U} = e^S$ where $S^\dagger = -S$. In addition, S is chosen to be purely off-diagonal. In order to obtain an order by order expansion of S, it is convenient to introduce a superoperator notation, in which with any operator O we associate a superoperator $\hat{O}$ defined as $\hat{O} \equiv [X, O]$ where X is any operator. This allows us to write the transformation as $e^{-S}He^S = e^{\hat{S}}H$. In order to generate an order by order expansion we can decompose this into even and odd contributions as

$$\mathcal{H}_D^{eff} = \cosh\hat{S}(\mathcal{H}_b + \mathcal{H}_H) + \sinh\hat{S}(V) \tag{6.31}$$

$$\mathcal{H}_{OD}^{eff} = \cosh\hat{S}(V) + \sinh\hat{S}(\mathcal{H}_b + \mathcal{H}_H) \equiv 0. \tag{6.32}$$

where the condition $\mathcal{H}_{OD}^{eff} = 0$ enforces the condition that the effective Hamiltonian has no terms connecting low and high energy sectors.

Rewriting Eq. (6.32) we obtain

$$[S, \mathcal{H}_b + \mathcal{H}_H] = \hat{S}\coth\hat{S}V \tag{6.33}$$

$$= \sum_{n=0}^{\infty} c_n \hat{S}^{2n} \tag{6.34}$$

with $c_0 = 1, c_1 = \frac{1}{3}, c_2 = -\frac{1}{45}, \ldots$.

Using Equations (6.34) and (6.31) we obtain the effective Hamiltonian as

$$\mathcal{H}_{eff} = \mathcal{H}_b + \tanh(\frac{1}{2}\hat{S})^{2n+1}V. \tag{6.35}$$

Defining $\tilde{V}$ through $V = \sqrt{w}\tilde{V}$ and expanding S in w as $S = \sqrt{w}S^{(1)} + wS^{(2)} + w^{3/2}S^{(3)} + ...$ we obtain the terms to third order as

$$\left[S^{(1)}, \mathcal{H}_b + \mathcal{H}_H\right] = \tilde{V} \tag{6.36}$$

$$\left[S^{(3)}, \mathcal{H}_b + \mathcal{H}_H\right] = \frac{1}{3}\left[\left[\tilde{V}, S^{(1)}\right], S^{(1)}\right]. \tag{6.37}$$

Since S and V are purely off-diagonal, all even terms are zero.

This enables us to obtain explicitly the action of $S^{(1)}$ and $S^{(3)}$ on the low energy subspace $\{|\lambda\rangle\}$ spanned by the states $\{|k\rangle\} \otimes \{|\sigma\rangle\}$ as

$$S^{(1)}|\lambda\rangle = -\frac{1}{H - \epsilon_\lambda} Q\tilde{V}|\lambda\rangle \tag{6.38}$$

$$S^{(3)}|\lambda\rangle = -\frac{1}{H - \epsilon_\lambda} Q\frac{1}{3}\left[\left[\tilde{V}, S^{(1)}\right], S^{(1)}\right]|\lambda\rangle \tag{6.39}$$

where $Q = \sum |\alpha\rangle\langle\alpha|$ is the projector onto the high energy subspace spanned by the states $\{|\alpha\rangle\}$.

Finally, we find the effective Hamiltonian to second order as

$$\mathcal{H}_{eff} = \mathcal{H}_b + \mathcal{H}_H + \frac{1}{2}\left[\sqrt{w}S^{(1)} + w^{3/2}S^{(3)}, V\right] - \frac{w^{3/2}}{24}\left[\left[\left[V, S^{(1)}\right], S^{(1)}\right], S^{(1)}\right]. \tag{6.40}$$

By inserting complete sets of states of the Hamiltonian $\mathcal{H}_{at}$, which since V and S are purely off-diagonal alternate between the states spanning the low energy subspace $\{|\lambda\}$, and the states spanning the high energy subspace $\{|\alpha\}$ the effective Hamiltonian can be obtained explicitly.

To order w the effective *high* energy Hamiltonian has the form

$$\mathcal{H}^H_{eff} = \mathcal{H}_H + \frac{1}{2}Q\left[\sqrt{w}S^{(1)}, V\right]Q \tag{6.41}$$

leading to the explicit representation

$$\begin{aligned}\mathcal{H}^H_{eff} &= \sum_\alpha \epsilon_\alpha |\alpha\rangle\langle\alpha| \\ &+ \frac{1}{8}\sum_{\alpha_1\alpha_2}\sum_{\sigma\sigma'}\Big(J^{H+}_{\alpha_1\alpha_2\sigma\sigma'} - J^{H-}_{\alpha_1\alpha_2\sigma\sigma'})|\alpha_1\rangle\langle\alpha_2|c^\dagger_{L\sigma}c_{L\sigma'} + J^{H-}|\alpha_1\rangle\langle\alpha_2|\Big)\end{aligned} \tag{6.42}$$

where

$$\begin{aligned}J^{H+}_{\alpha_1\alpha_2\sigma\sigma'} &= \left(\frac{D}{\epsilon_{\alpha_1} - \epsilon_\lambda} + \frac{D}{\epsilon_{\alpha_2} - \epsilon_\lambda}\right)\langle\alpha_1|f_\sigma|\lambda\rangle\langle\lambda|f^\dagger_{\sigma'}|\alpha_2\rangle \\ J^{H-}_{\alpha_1\alpha_2\sigma\sigma'} &= \left(\frac{D}{\epsilon_{\alpha_1} - \epsilon_\lambda} + \frac{D}{\epsilon_{\alpha_2} - \epsilon_\lambda}\right)\langle\alpha_1|f^\dagger_{\sigma'}|\lambda\rangle\langle\lambda|f_\sigma|\alpha_2\rangle.\end{aligned} \tag{6.43}$$

Note that the coefficients are constrained by rotational invariance, as well as the conservation of spin and charge, which leads to terms coupling densities as well as terms coupling spin.

The effective low energy Hamiltonian is

$$\mathcal{H}^L_{eff} = \mathcal{H}_b + \frac{1}{2}P\left[\sqrt{w}S^{(1)} + w^{3/2}S^{(3)}, V\right]P - \frac{w^{3/2}}{24}P\left[\left[\left[V, S^{(1)}\right], S^{(1)}\right], S^{(1)}\right]P \quad (6.44)$$

with $P = 1 - Q$ projecting onto the low energy subspace. The contribution $\frac{1}{2}P\left[S^{(1)}, \tilde{V}\right]P$ is given as

$$\frac{1}{2}P\left[S^{(1)} + S^{(3)}, \tilde{V}\right]P = -\sum_{\sigma} J^{\perp}_{kk'} c^{\dagger}_{k\sigma} c_{k'\bar{\sigma}} X_{\bar{\sigma}\sigma} - \sum_{\sigma\sigma'} J^{||}_{\sigma\sigma' kk'} c^{\dagger}_{k\sigma} c_{k'\sigma} X_{\sigma'\sigma'} \quad (6.45)$$

with

$$\begin{aligned} J^{\perp}_{kk'} &= \frac{D^2}{2}\tilde{V}_k\tilde{V}_{k'}\Big(\langle\bar{\sigma}|f_{\sigma}(\frac{1}{H-(E^{at}_{gs}+\epsilon_k)} + \frac{1}{H-(E^{at}_{gs}+\epsilon'_k)}f^{\dagger}_{\bar{\sigma}}|\sigma\rangle_{H_{at}} \\ &- \langle\bar{\sigma}|f^{\dagger}_{\bar{\sigma}}(\frac{1}{H-(E^{at}_{gs}-\epsilon_k)} + \frac{1}{H-(E^{at}_{gs}-\epsilon'_k)})f_{\sigma}|\sigma\rangle_{H_{at}}\Big) \end{aligned} \quad (6.46)$$

and

$$\begin{aligned} J^{||}_{kk'\sigma\sigma'} &= \frac{D^2}{2}\tilde{V}_k\tilde{V}_{k'}\Big(\langle\sigma'|f_{\sigma}(\frac{1}{H-(E^{at}_{gs}+\epsilon_k)} + \frac{1}{H-(E^{at}_{gs}+\epsilon'_k)})f^{\dagger}_{\sigma}|\sigma'\rangle_{H_{at}} \\ &- \langle\sigma'|f^{\dagger}_{\sigma}(\frac{1}{H-(E^{at}_{gs}-\epsilon_k)} + \frac{1}{H-(E^{at}_{gs}-\epsilon'_k)})f_{\sigma}|\sigma'\rangle_{H_{at}}\Big). \end{aligned} \quad (6.47)$$

Note that this also contains terms of order w^2 as a result of the expansion of the energy denominators in which $\epsilon_k \sim w$.

This expression can be simplified considerably and we will see that to order w it has the form of a Kondo Hamiltonian with (away from half filling) a potential scattering term. The terms of order w^2, renormalize the first order terms and give rise to an effective interaction between the bath electrons.

The Hamiltonian, as well as the operators, assume a particularly transparent form when expressed in terms of the operators

$$c_{L\sigma} \equiv 2\sum_k \tilde{V}_k c_{k\sigma} \quad (6.48)$$

introduced earlier, as well as the operators

$$c_{\epsilon L\sigma} \equiv 2\sum_k \tilde{V}_k \epsilon_k c_{k\sigma}. \quad (6.49)$$

The latter are the result of the expansion of the energy denominators and have been normalized such that

$$\{c_{\epsilon L\sigma}, c^\dagger_{L\sigma}\} = \bar{\epsilon} \tag{6.50}$$

where $\bar{\epsilon} = 4\sum_k \tilde{V}^2\tilde{\epsilon}_k$ is the first moment of the low energy spectral function and is expressed in terms of the rescaled energies $\epsilon_k = w\tilde{\epsilon}_k$. While these are not orthogonal, this does not affect our considerations.

The explicit form of the Hamiltonian to second order in w is given as

$$\mathcal{H}^{eff}_{low} = w\mathcal{H}^{eff(1)}_{low} + w^2\mathcal{H}^{eff(3)}_{low}. \tag{6.51}$$

Here, the first order contribution is given as

$$\mathcal{H}^{eff(1)}_{low} = D\sum_{k\sigma}\tilde{\epsilon_k}n_{k\sigma} - \frac{D}{4}\sum_\sigma J^{\perp(1)}X_{\bar{\sigma}\sigma}c^\dagger_{L\sigma}c_{L\bar{\sigma}} - \frac{D}{4}\sum_{\sigma\sigma'}J^{(1)}_{\sigma\sigma'}X_{\sigma'\sigma'}n_{L\sigma} \tag{6.52}$$

with

$$J^{\perp(1)} = D\left(\langle\bar{\sigma}|f_\sigma\frac{1}{H-E^{at}_{gs}}f^\dagger_{\bar{\sigma}}|\sigma\rangle_{Hat} - \langle\bar{\sigma}|f^\dagger_{\bar{\sigma}}\frac{1}{H-E^{at}_{gs}}f_\sigma|\sigma\rangle_{Hat}\right) \tag{6.53}$$

and

$$J^{(1)}_{\sigma\sigma'} = D\left(\langle\sigma'|f_\sigma\frac{1}{H-E^{at}_{gs}}f^\dagger_\sigma|\sigma'\rangle_{Hat} - \langle\sigma'|f^\dagger_\sigma\frac{1}{H-E^{at}_{gs}}f_\sigma|\sigma'\rangle_{Hat}\right). \tag{6.54}$$

We have used the standard Hubbard operators defined as $X_{\sigma\sigma'} = |\sigma\rangle\langle\sigma'|$ acting on the low energy impurity doublet.

Due to the fact that the system is rotational invariant we observe that $J_{\uparrow\uparrow} = J_{\downarrow\downarrow}$ and $J_{\uparrow\downarrow} = J_{\downarrow\uparrow}$. Defining the quantities

$$J^{(1)}_{pot} \equiv J^{(1)}_{\uparrow\uparrow} + J^{(1)}_{\uparrow\downarrow} \tag{6.55}$$

and

$$J^{(1)}_{spin} \equiv J^{(1)}_{\uparrow\uparrow} - J^{(1)}_{\uparrow\downarrow} \tag{6.56}$$

and again using rotational invariance we see that furthermore $J^{(1)}_{spin} = J^{\perp(1)}$ such that the Hamiltonian can be written as a Kondo Hamiltonian[1] of the form

$$\mathcal{H}^{eff(1)}_{low} = D\sum_{k\sigma}\tilde{\epsilon_k}n_{k\sigma} - \frac{D}{2}J^{(1)}_{spin}\vec{S}\cdot\vec{s}_L - \frac{DJ^{(1)}_{pot}}{8}(n_{L\uparrow}+n_{L\downarrow})(X_{\uparrow\uparrow}+X_{\downarrow\downarrow}) \tag{6.57}$$

[1]In contrast to the more common definition of J, we have defined J such that it is *negative*, i.e. $J_{spin} < 0$.

with $\vec{S} = \frac{1}{2}\sum_{\sigma\sigma'} X_{\sigma\sigma'}\vec{\sigma}_{\sigma\sigma'}$ the spin-$\frac{1}{2}$ operator acting on the $|\sigma\rangle_{at}$ states and $\vec{s}_L = \frac{1}{2}\sum_{\alpha\beta} c^+_{L\alpha}\vec{\sigma}_{\alpha\beta}c_{L\beta}$ the local spin operator of the low energy conduction electrons. Notice that the identity $X_{\uparrow\uparrow} + X_{\downarrow\downarrow} = 1$ can be used to simplify the result. We have left it explicit in Eq. (6.57) to illustrate the origin of the various contributions.

The second order contribution consists of two parts, resulting from the next order contribution from the canonical transformation and the expansion of the energy denominators in the coefficients J, respectively, and is given as

$$\mathcal{H}^{eff(3)}_{low} = \mathcal{H}^{eff(3,can)}_{low} + \mathcal{H}^{eff(3,exp)}_{low}. \tag{6.58}$$

The part resulting from the expansion of the denominators reads

$$\begin{aligned}\mathcal{H}^{eff(3,exp)}_{low} = &- \frac{D}{4}\sum_{\sigma} J^{\perp(3,exp)} X_{\bar{\sigma}\sigma}(c^\dagger_{\bar{\epsilon}L\sigma}c_{L\bar{\sigma}} + c^\dagger_{L\sigma}c_{\bar{\epsilon}L\bar{\sigma}} + h.c. \\ &- \frac{D}{4}\sum_{\sigma\sigma'} J^{(3,exp)}_{\sigma\sigma'} X_{\sigma'\sigma'}(c^\dagger_{\bar{\epsilon}L\sigma}c_{L\sigma} + c^\dagger_{L\sigma}c_{\bar{\epsilon}L\sigma})\end{aligned} \tag{6.59}$$

with

$$J^{\perp(3,exp)} = \frac{D^2}{2}(\langle\bar{\sigma}|f_\sigma \frac{1}{(H - E^{at}_{gs})^2} f^\dagger_{\bar{\sigma}}|\sigma\rangle_{Hat} + \langle\bar{\sigma}|f^\dagger_{\bar{\sigma}} \frac{1}{(H - E^{at}_{gs})^2} f_\sigma|\sigma\rangle_{Hat}) \tag{6.60}$$

and

$$J^{(3,exp)}_{\sigma\sigma'} = \frac{D^2}{2}(\langle\sigma'|f_\sigma \frac{1}{(H - E^{at}_{gs})^2} f^\dagger_{\sigma}|\sigma'\rangle_{Hat} + \langle\sigma'|f^\dagger_{\sigma} \frac{1}{(H - E^{at}_{gs})^2} f_\sigma|\sigma'\rangle_{Hat}). \tag{6.61}$$

Again the rotational symmetry can be made manifest by defining $J^{(3,exp)}_{pot} \equiv J^{(3,exp)}_{\uparrow\uparrow} + J^{(3,exp)}_{\uparrow\downarrow}$, $J^{(3,exp)}_{spin} \equiv J^{(3,exp)}_{\uparrow\uparrow} - J^{(3,exp)}_{\uparrow\downarrow}$ such that $J^{(3,exp)}_{spin} = J^{\perp(3,exp)}$ and defining $\vec{s}_{\bar{\epsilon}} \equiv \frac{1}{4}(c^\dagger_{\bar{\epsilon}\alpha}\vec{\sigma}_{\alpha\beta}c_\beta + c^\dagger_\alpha\vec{\sigma}_{\alpha\beta}c_{\bar{\epsilon}\beta})$ such that

$$\mathcal{H}^{(3,exp)}_{low} = \frac{D}{2}J^{(3,exp)}_{spin}\vec{S}\cdot\vec{s}_{\bar{\epsilon}L} + \frac{DJ^{(3,exp)}_{pot}}{8}\sum_\sigma (c^\dagger_{L\sigma}c_{\bar{\epsilon}L\sigma} + c^\dagger_{\bar{\epsilon}L\sigma}c_{L\sigma}). \tag{6.62}$$

Finally, the term from the next order of the canonical transformation gives

$$\begin{aligned}\mathcal{H}^{eff(3,can)}_{low} &= \frac{D}{4}\sum_\sigma \left((J^{(3,can)}_{\uparrow\uparrow} X_{\sigma\sigma} + J^{(3,can)}_{\uparrow\downarrow} X_{\bar{\sigma}\bar{\sigma}}) c^\dagger_{L\sigma}c_{L\sigma} + J^{\perp(3,can)} X_{\sigma\bar{\sigma}} c^\dagger_{L\bar{\sigma}}c_{L\sigma} \right) \\ &+ \frac{D}{16}J^{||(3,can)} n_{L\uparrow}n_{L\downarrow} \\ &\equiv \frac{D}{2}J^{(3,can)}_{spin}\vec{S}\cdot\vec{s}_L + \frac{DJ^{(3,can)}_{pot}}{8}(n_{\uparrow L} + n_{\downarrow L}) + \frac{D}{16}J^{||(3,can)} n_{L\uparrow}n_{L\downarrow}\end{aligned} \tag{6.63}$$

where we have relegated the explicit form of the coefficients $J^{(3,can)}$ to Appendix A.

The transformed f_σ-electron operators, F_σ, are obtained in an analogous fashion from the knowledge of the explicit form of $S^{(1)}$ and $S^{(3)}$. From $F_\sigma = e^{-S} f_\sigma e^{S}$, we get to third order

$$F_\sigma = f_\sigma + \left[f_\sigma, \sqrt{w}S^{(1)} + w^{3/2}S^{(3)}\right] + \frac{w}{2}\left[\left[f_\sigma, S^{(1)}\right], S^{(1)}\right] + \frac{w^{3/2}}{6}\left[\left[\left[f_\sigma, S^{(1)}\right], S^{(1)}\right], S^{(1)}\right]. \tag{6.64}$$

We will first give the explicit expressions for the F_σ^{LL} operators describing the low energy excitations and discuss their significance. From Eq. (6.64) we see that the contribution mediating transitions within the low energy subspace, which we need for the determination of G_{low} is given as

$$\begin{aligned} F_\sigma^{LL} &= P\left[f_\sigma, \sqrt{w}S^{(1)} + w^{3/2}S^{(3)}\right]P + \frac{w^{3/2}}{6}P\left[\left[\left[f_\sigma, S^{(1)}\right], S^{(1)}\right], S^{(1)}\right]P \\ &= \sqrt{w}F_\sigma^{LL(1)} + w^{3/2}F_\sigma^{LL(3)}. \end{aligned} \tag{6.65}$$

The equations can be expressed simply in terms of the operators and expectation values entering the Hamiltonian.

The first order term is then simply given as

$$F_\uparrow^{LL(1)} = -\frac{1}{2}\left((J_{\uparrow\uparrow}^{(1)}X_{\uparrow\uparrow} + J_{\uparrow\downarrow}^{(1)}X_{\downarrow\downarrow})c_\uparrow + J^{\perp(1)}X_{\downarrow\uparrow}c_\downarrow\right) \tag{6.66}$$

or, in terms of $J_{spin}^{(1)}$ and $J_{pot}^{(1)}$, as

$$F_\sigma^{LL(1)} = -\frac{1}{4}\left(J_{pot}^{(1)} + J_{spin}^{(1)}(X_{\sigma\sigma} - X_{\bar\sigma\bar\sigma})\right)c_\sigma - \frac{1}{2}J_{spin}^{(1)}X_{\bar\sigma\sigma}c_{\bar\sigma}. \tag{6.67}$$

The third order contribution to the transformed f_σ again has the contributions

$$F_\sigma^{(3)} = F_\sigma^{(3,exp)} + F_\sigma^{(3,can)} \tag{6.68}$$

which are given respectively as

$$\begin{aligned} F_\sigma^{LL(3,exp)} &= (J_{\sigma\sigma}^{(3,exp)}X_{\sigma\sigma} + J_{\bar\sigma\bar\sigma}^{(3,exp)}X_{\bar\sigma\bar\sigma})c_{\bar\epsilon L\sigma} + J^{\perp(3,exp)}X_{\bar\sigma\sigma}c_{\bar\epsilon L\bar\sigma} \\ &= \frac{1}{2}\left(J_{pot}^{(3,exp)} + J_{spin}^{(3,exp)}(X_{\sigma\sigma} - X_{\bar\sigma\bar\sigma})\right)c_{\bar\epsilon L\sigma} + J_{spin}^{(3,exp)}X_{\bar\sigma\sigma}c_{\bar\epsilon L\bar\sigma}. \end{aligned} \tag{6.69}$$

and

$$\begin{aligned} F_\sigma^{LL(3,can)} &= \frac{1}{2}\left[\frac{1}{2}\left(K_{pot}^{(3,can)} + K_{spin}^{(3,can)}(X_{\sigma\sigma} - X_{\bar\sigma\bar\sigma})\right)n_{L\bar\sigma}c_{L\sigma} + K_{spin}^{(3,can)}X_{\bar\sigma\sigma}n_{L\sigma}c_{L\bar\sigma}\right. \\ &+ \left.\frac{1}{2}\left(I_{pot}^{(3,can)} + I_{spin}^{(3,can)}(X_{\sigma\sigma} - X_{\bar\sigma\bar\sigma})\right)c_{L\sigma} + I_{spin}^{(3,can)}X_{\bar\sigma\sigma}c_{L\bar\sigma}\right]. \end{aligned} \tag{6.70}$$

Again, the explicit form of the coefficients can be found in the Appendix.

Due to the fact that we are not using the low-high operators explicitly in our procedure, we will not show their explicit form here. In general they are obtained to second order as

$$\begin{aligned} F_\sigma^{HL} &= Q\Big(f_\sigma - S^{(1)} f_\sigma S^{(1)} + \frac{1}{2}(S^{(1)}S^{(1)} f_\sigma + f_\sigma S^{(1)}S^{(1)})P\Big) \\ &= \sum_{\sigma'\alpha} |\alpha\rangle\langle\sigma'| \Big(\langle\alpha| f_\sigma |\sigma'\rangle - \langle\alpha| \frac{V}{H_{high} - E_{at}} f_\sigma \frac{V}{H_{high} - E_{at}} |\sigma'\rangle \\ &- \frac{1}{2}\langle\alpha| f_\sigma \frac{V}{H_{high} - E_{at}} \frac{V}{H_{high} - E_{at}} |\sigma'\rangle - \frac{1}{2}\langle\alpha| \frac{V}{H_{high} - E_{at}} \frac{V}{H_{high} - E_{at}} f_\sigma |\sigma'\rangle \Big). \end{aligned} \tag{6.71}$$

Considerable insight into the physical significance of these operators can be obtained by observing that the anticommutator of the transformed operators immediately yields the low energy spectral weight as can be seen directly from the structure of the low energy Green function (6.13). To simplify the calculation let us calculate the manifestly rotationally invariant quantity

$$\begin{aligned} A_{low} &= \frac{1}{2}\sum_\sigma \{F_\sigma^{LL}, F_\sigma^{LL\dagger}\} \\ &= w A_{low}^{(1)} + w^2 A_{low}^{(2)} + ... \end{aligned} \tag{6.72}$$

which gives the low energy spectral weight order by order in w. (Due to the fact that the Hamiltonian is rotationally invariant this holds without loss of generality.) The first order result is obtained by straightforward algebra using the first order operators (6.67) and yields

$$A_{low}^{(1)} = -\frac{1}{2}\Big(J_{spin}^{(1)2} (\vec{S}\cdot\vec{s}_L - \frac{3}{8}) - \frac{J_{pot}^{(1)2}}{8} \Big), \tag{6.73}$$

Using Eq. (6.72) as well as the fact that w is defined as the low energy spectral weight we obtain $A_{low}^{(1)} = 1$.

The scalar product $\vec{S}\cdot\vec{s}_L < 0$ due to the fact that the coupling is antiferromagnetic in the Kondo regime. It is noteworthy that to this order the result does not depend explicitly on the density of the bath electrons $\langle n_\uparrow + n_\downarrow\rangle$.

The terms of order w^2 have contributions from the third order operators and are given as

$$A_{low}^{(2)} = \frac{1}{2}\sum_\sigma \Big(\{F_\sigma^{(3)}, F_\sigma^{(1)\dagger}\} + \{F_\sigma^{(1)}, F_\sigma^{(3)\dagger}\} \Big) \tag{6.74}$$

which explicitly reads

$$\begin{aligned} A^{(2)}_{low} &= \frac{\bar{\epsilon}}{8}(J^{(1)}_{pot}J^{(3,exp)}_{pot} + 3J^{(1)}_{spin}J^{(3,exp)}_{spin}) - J^{(1)}_{spin}J^{(3,exp)}_{spin}\vec{S}\cdot\vec{s}_{\bar{\epsilon}} \\ &- J^{(3,can)}_{spin}J^{(1)}_{spin}(\vec{S}\cdot\vec{s}_L - \frac{3}{8}) - \frac{J^{(3,can)}_{pot}J^{(1)}_{pot}}{8} \\ &+ \frac{1}{4}\Big(\frac{1}{4}(J^{(1)}_{pot}K^{(3)}_{pot} + 3J^{(1)}_{spin}K^{(3)}_{spin})(n_{L\uparrow} + n_{L\downarrow}) \\ &- (K^{(3)}_{spin}J^{(1)}_{pot} + J^{(1)}_{spin}(2K^{(3)}_{spin} + K^{(3)}_{pot}))\vec{S}\cdot\vec{s}_L\Big). \end{aligned} \tag{6.75}$$

The anticommutators of the F^{LH}_σ can be evaluated analogously and give order by order the complement of the low energy operators. To lowest order in w one obtains $\frac{1}{2}\sum\{F^{LH(2)}_\sigma, F^{LH(2)\dagger}_\sigma\} = 1 - \frac{1}{2}\sum\{F^{LL(1)}_\sigma, F^{LL(1)\dagger}_\sigma\}$, so that the spectral sumrule is obeyed.

The explicit forms of Hamiltonian and operators as derived completes the set of self-consistent equations necessary to determine the low frequency behavior of the Hubbard model to second order in the weight of the quasiparticle resonance. In order to solve them we will proceed as elaborated in the case of the full Hubbard model by using a finite cluster to represent the Anderson model and by closing the self consistency using a χ^2 fitting of the low energy Green function to extract the new parameters parametrizing the low frequency bath. The details are presented in the subsequent chapters.

Notice finally that in order to evaluate other physical quantities, one once again has to evaluate the corresponding operators. Of particular importance is the number operator corresponding to the f_σ particles, since it gives the *physical* particle number in the Hubbard model This is given as

$$N_\sigma = e^{-S}n_\sigma e^S = n_\sigma - S^{(1)}n_\sigma S^{(1)} + \frac{1}{2}\left[S^{(1)}S^{(1)}n_\sigma + n_\sigma S^{(1)}S^{(1)}\right] + o(w^2). \tag{6.76}$$

The explicit result can be found in Appendix A. For the evaluation of the magnetic properties we furthermore need the transformed spin operator in z direction $\mathcal{S}_z = e^{-S}S_z e^S$ which can be obtained directly from the knowledge of the number operator (6.76) since $S_z = \frac{1}{2}(n_\uparrow - n_\downarrow)$.

Let us conclude this chapter by addressing the range of validity of the self-consistent projective technique. As emphasized, the technique *in its present form* relies on the

existence of a separation of scales, such that we can clearly separate the low lying states of $\mathcal{H}_{at}$ which enter the canonical transformation from the states higher in energy. This is obviously the case when the Kondo resonance is well separated from upper and lower Hubbard bands. In terms of the regimes discussed in the previous chapter, the effective Anderson model therefore needs to be in the local moment regime. It should be noted that in the mixed valence region the method can still be applied if one restricts the elimination of the high energy features to the upper Hubbard band only and includes the "empty" state in the set of low lying states. The effective Hamiltonian in that case assumes a slightly more complicated form. In the following chapter we will determine the position of the resonance for infinitesimal doping and see that for small doping the resonance is always separated from the bands, such that the method in that case is always applicable. We shall also see that the amount of doping "allowed" for the method to be applicable decreases as the interaction increases, since the position of the resonance approaches the band as the interaction is increased.

The crossover between local moment and mixed valence regimes as a function of doping, and therefore the breakdown of the prsesent form self-consistent projective technique, can be illustrated nicely in the following way: We solve the full Hubbard model for various dopings and remove the Kondo resonance from the converged solution, which leaves us with poles representing upper and lower band only. This determines the part of the Hamiltonian called $\mathcal{H}_{at}$ in the previous section. We can now determine the lowest lying states of this "semiconductor with impurity", which correspond to impurity states dressed by particle-hole excitations into the valence and conduction bands. As elaborated, for small values of doping the lowest lying states are a dressed doublet which is well separated, by an energy of order δD, from the dressed empty state. As the doping is increased, the energies of the doublet and the energy of the "empty" state get closer in energy until the dressed empty state is actually lower in energy than the doublet. This can be seen from the solution of the $2+1$ insulator by noting that for μ beyond a certain value (in the case of the 2+1 insulator this happens for $\mu < \sqrt{V - 2V^2/U}$) the ground state of the insulator is no longer in the $N = 3$ particle space but in the subspace containing $N = 2$ particles.

The self-consistent projective technique as developed for the Hubbard model breaks down once the energy separation is of the order δD, i.e. the width of the resonance. The positions of the lowest states for $U = 3.5$ as a function of the chemical potential are shown in Fig. 6.3. We would like to stress, that the idea behind the self-consistent technique transcends the particular implementation realized here, such that more sophisticated applications can be envisioned.

This concludes the development of the self-consistent projective technique. It enables us to determine for the first time the thermodynamic and some dynamic properties of the Hubbard model *at and near* the metal insulator transition. In particular, it allows for an accurate determination of the transition line, as well as the low temperature properties, which were not accessible using other methods. While in this chapter we have outlined the methodological as well as technical aspects of the method, we will proceed by applying it to the particular case of the Hubbard model.

In the following chapters we will obtain some physical quantities in the critical region. We will begin with an analysis of the critical point at half filling, determine the position of the resonance away from half filling and analyze the approach to Mott point. Finally, we will use the technique to study some of the finite temperature properties of the Hubbard model.

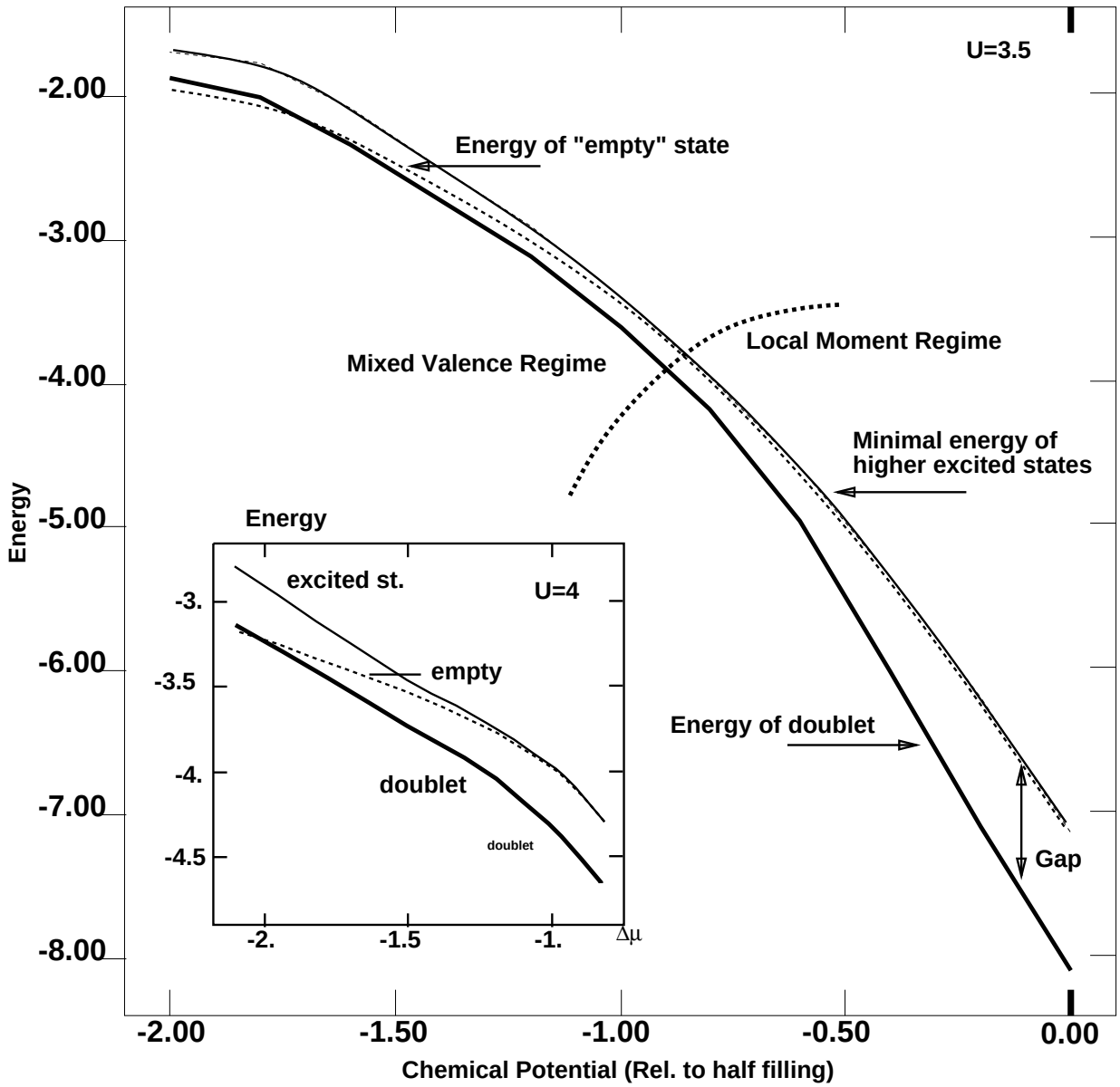

Figure 6.3: Energies of the lowest lying states (doublet, "empty" state and lowest lying higher energy state in $\mathcal{H}_{at}$ for $U = 3.5$ and $N = 5$ as a function of the chemical potential. The particle density ranges from $n = 0.6$ to $n = 1.0$. The inset shows the corresponding plot for $U = 4$.

Chapter 7

Critical Properties of the Mott Transition in the Hubbard Model

In the previous chapters we have outlined, in which sense the correlation driven metal-insulator transition is a fundamental problem in condensed matter physics. We have seen that from a theoretical point of view, the problem is fascinating because of its non-perturbative nature, the absence of a small parameter and the emergence of new low energy scales and have demonstrated, how the early ideas of Mott [92], Hubbard [22, 23, 24], Brinkman and Rice [26] have been put on a more quantitative footing by the development of a mean-field approach to the strong correlation problem which becomes exact in the limit of large lattice coordination [36]. Furthermore, we have demonstrated the existence of a Mott transition in the paramagnetic phase of the half-filled Hubbard model on frustrated lattices, which is driven by the collapse of an energy scale, the renormalized Fermi energy. Since problems exhibiting two widely separated energy scales are traditionally hard to analyze in the limit in which one of the energy scales goes to zero, we have proceeded by introducing a novel projective self-consistent approach to solving correlated electron problems in large dimensions exhibiting a clear separation of energy scales which overcomes these problems. We are now in the position to investigate the critical region more carefully, using the projective self-consistent technique.

7.1 The Critical Point of the Half-Filled Hubbard Model

In this section we will apply this self-consistent projective technique to the metal-insulator transition in the half-filled Hubbard model and extract, for the first time, exact information about the critical behavior at the transition in infinite dimensions. We calculate the single particle spectral function at the Mott transition, which can in

principle be measured in photoemission experiments. We establish that the coefficient of the ω^2 term in the imaginary part of the self-energy diverges as the square of the coefficient of the linear term in the specific heat and, with few additional assumptions, relate it to the observed T^2 resistivity in the $LaTiO_3$ system. We show that the local spin susceptibility diverges in the same way as the linear term in the specific heat and calculate their ratio, a generalized Wilson number. Finally, we show that the linear coefficient of the imaginary part of the dynamical spin susceptibility, relevant to both NMR and neutron scattering experiments, diverges as the square of the linear coefficient of the specific heat. For pedagogical reasons we will outline the method developed in the previous section again, since the equations assume a particularly simple form if the half-filled Hubbard model at criticality is considered.

We have seen explicitly that as the interaction strength U increases, the self-consistent single particle density of states, $\rho(\epsilon) = -\frac{1}{\pi} ImG(\epsilon + i0)$, of the half-filled Hubbard model develops a narrow peak about zero energy separated by regions of low spectral density from peaks near $\pm U/2$. At a critical value of U, U_c, [1] the narrow peak appears to vanish, leaving a paramagnetic insulating solution with a finite gap. Consequently we can separate the variables ϵ_k and V_k in the self-consistent Anderson model (6.1) into sets $\{\epsilon_{k,H}, V_{k,H}\}$ describing the high energy features and $\{\epsilon_{k,L}, V_{k,L}\}$ containing the low-energy behavior as discussed. $\rho^{low}(\epsilon)$ contains all states up to a cut-off that we take to be the Kondo temperature of the half-filled Hubbard model and carries spectral weight w

$$w = \sum_k 4V_{k,L}^2/D^2. \tag{7.1}$$

$\rho^{high}(\epsilon)$ describes the upper and lower Hubbard bands, in this case two incoherent features at energy scales $\pm\frac{U}{2}$ that carry spectral weight $1 - w$. The situation is thus the paradigmatic example for the application of the self-consistent projective technique. Since the goal of this section is the analysis of the behavior *at* the critical point U_c, at which the weight of the low energy resonance goes to zero, it is sufficient to use the

[1] Here, U_c corresponds to the interaction strength at the continuous transition found within second-order perturbation method by Zhang et al. in Ref. [19] and Ref. [56] which has been shown numerically [69] and analytically [93] to be the physical transition point at $T = 0$. See also the previous chapters.

self-consistent projective technique to *lowest order*.

Let us briefly recapitulate the procedure developed and elaborated in the previous chapter. We first separate the impurity Hamiltonian into three parts as

$$\mathcal{H}_{AM} = \mathcal{H}_{at} + \mathcal{H}_b + \mathcal{H}_M. \tag{7.2}$$

At half filling, $\mu = U/2$, such that $\mathcal{H}_{at}$ is given (up to a constant) as

$$\mathcal{H}_{at} = \frac{U}{2}\left(n_{f\uparrow} - \frac{1}{2}\right)\left(n_{f\downarrow} - \frac{1}{2}\right) + \sum_{\sigma,k} V_{k,H}(c^+_{k\sigma} f_\sigma + h.c.) + \sum_{\sigma,k} \epsilon_{k,H} c^+_{k\sigma} c_{k\sigma}. \tag{7.3}$$

and can be thought of as an Anderson impurity in a semiconductor.

$$\mathcal{H}_b = \sum_{k,\sigma} wD\tilde{\epsilon_k} c^+_{k\sigma} c_{k\sigma} \tag{7.4}$$

describes a narrow band of low energy conduction electrons. Since the energy will turn out to be of order wD, we again use the dimensionless, rescaled variables $\tilde{\epsilon}_k = \epsilon_{k,L}/(wD)$. The hybridization $\mathcal{H}_M$ with the low energy electrons is given by

$$\mathcal{H}_M = \sqrt{w} D \sum_\sigma (c^\dagger_{L\sigma} f_\sigma + h.c.) \tag{7.5}$$

with

$$c_{L\sigma} \equiv \sum_k 2\tilde{V}_k c_{k\sigma} \tag{7.6}$$

the local low energy conduction electron operators normalized to have canonical commutation relations; again we have rescaled the $V_{k,L}$ by introducing rescaled variables $\tilde{V}_k = V_{k,L}/(\sqrt{w}D)$.

Since in the half-filled case the Kondo resonance is in the center between lower and upper Hubbard bands, $\mathcal{H}_{at}$ has low-lying spin doublet ground states $|\sigma\rangle_{H_{at}}$ with energy E^{at}_{gs} which are separated by a gap of order $U/2$ from the excited states, such that the effective Anderson model is clearly in the local moment regime.

We now perform a canonical transformation to project out the excited states of $\mathcal{H}_{at}$ and derive an effective Hamiltonian, $\mathcal{H}^{eff}_L$, which acts on the low energy Hilbert space $\{|\sigma\rangle_{H_{at}}\} \otimes \{|\psi_L\rangle\}$ with $\{|\psi_L\rangle\}$ states of the $c^L_{k\sigma}$. As we have seen, this amounts to finding an operator S eliminating the transitions between low and high energy states, such that the effective low energy Hamiltonian is given as

$$\mathcal{H}_{eff} = e^{-S}\mathcal{H}e^S. \tag{7.7}$$

Since we are interested in the behavior *at* the critical point, it is sufficient to perform the canonical transformation to lowest order in w, leading to the effective low energy Hamiltonian (6.52)

$$\mathcal{H}_{low}^{eff(1)} = \mathcal{H}_b - \frac{D}{4}\sum_{\sigma} J^{\perp(1)} X_{\bar{\sigma}\sigma} c_{L\sigma}^{\dagger} c_{L\bar{\sigma}} - \frac{D}{4}\sum_{\sigma\sigma'} J_{\sigma\sigma'}^{(1)} X_{\sigma'\sigma'} n_{L\sigma} \tag{7.8}$$

with

$$J^{\perp(1)} = D\left(\langle\bar{\sigma}|f_{\sigma}\frac{1}{H-E_{gs}^{at}}f_{\bar{\sigma}}^{\dagger}|\sigma\rangle_{H_{at}} - \langle\bar{\sigma}|f_{\bar{\sigma}}^{\dagger}\frac{1}{H-E_{gs}^{at}}f_{\sigma}|\sigma\rangle_{H_{at}}\right) \tag{7.9}$$

and

$$J_{\sigma\sigma'}^{(1)} = D\left(\langle\sigma'|f_{\sigma}\frac{1}{H-E_{gs}^{at}}f_{\sigma}^{\dagger}|\sigma'\rangle_{H_{at}} - \langle\sigma'|f_{\sigma}^{\dagger}\frac{1}{H-E_{gs}^{at}}f_{\sigma}|\sigma'\rangle_{H_{at}}\right) \tag{7.10}$$

where again $X_{\sigma\sigma'} \equiv |\sigma\rangle\langle\sigma'|$ are Hubbard operators.

For the purpose of determining the properties *at* the critical point, we have seen that it is sufficient to consider the high energy contributions to lowest order. The parameters entering $\mathcal{H}_{at}$ can therefore be determined from the *insulating* solution of the Hubbard model at U_c as $V_k^H = V_k^H(U_c)$, which can be obtained using the methods elaborated on in the sections about the Hubbard model.

Due to rotational invariance and the absence of potential scattering at half-filling due to particle-hole symmetry, the matrix elements reduce to a single number $\Gamma \equiv D\langle\uparrow|f_{\downarrow}\frac{1}{\mathcal{H}_{at}-E_{gs}^{at}}f_{\uparrow}^{\dagger}|\downarrow\rangle_{\mathcal{H}at}$ which contains all the information about virtual transitions to the high energies subspace that is relevant to the low energy physics. In terms of the notation used in the previous chapter Γ is given as $\Gamma = J_{\uparrow\uparrow}^{(1)} = -J_{\uparrow\downarrow}^{(1)} = 2J^{\perp(1)}$.

To lowest order the low energy Hamiltonian can then be written in the compact form

$$\mathcal{H}_L^{eff(1)} = -wD\Gamma\vec{S}\cdot\vec{s}_L + \mathcal{H}_b + \text{const} \tag{7.11}$$

where again $\vec{S} = \frac{1}{2}\sum_{\sigma\sigma'} X_{\sigma,\sigma'}\vec{\sigma}_{\sigma\sigma'}$ the spin-$\frac{1}{2}$ operator acting on the $|\sigma\rangle_{at}$ states and $\vec{s}_L = \frac{1}{2}\sum_{\alpha\beta} c_{L\alpha}^{+}\vec{\sigma}_{\alpha\beta}c_{L\beta}$ the local spin operator of the low energy conduction electrons.

The low energy part of the impurity Green function G^{low} is now the time ordered Green function under $\mathcal{H}_L^{eff}$ of the canonically transformed f_{σ} operators of the original Anderson model, $F_{\sigma} = \mathrm{e}^{-S} f_{\sigma} \mathrm{e}^{S}$. In the half-filled case at criticality these can again be

written in terms of the single coefficient Γ and to lowest order in w are given by $\sqrt{w}$ times the effective low energy operators

$$F_\sigma^{(1)} = -\frac{D\Gamma}{2}\sum_{\sigma'}[(X_{\sigma\sigma} - X_{-\sigma-\sigma})c_{L\sigma} + 2X_{\sigma-\sigma}c_{L-\sigma}]. \tag{7.12}$$

We now see explicitly that the effective low energy Hamiltonian is reduced to an intermediate coupling Kondo problem with a single energy scale wD. The self-consistency condition requires that the Green function of F equals that of c_L. Introducing rescaled frequencies $i\tilde{\omega}_n = i\omega_n/(wD)$, and scaling out w it assumes the form

$$\sum_k \frac{4\tilde{V}_k^2}{i\tilde{\omega}_n - \tilde{\epsilon}_k} = G^{low}[\tilde{\epsilon}, \tilde{V}_k](i\tilde{\omega}_n). \tag{7.13}$$

The projective self-consistent method thus results in the closed set of equations (7.11-7.13) which form the basis of our low energy analysis.

7.1.1 A Simple Toy Model

Before discussing the full numerical solution, it instructive to consider a simple toy model in which the low energy part, i.e. the resonance, is represented by a single orbital. In this case the low energy effective Hamiltonian can be diagonalized exactly and it is therefore possible to gain some analytic insights. We have relegated the full solution to the appendix and just state the results.

The Hamiltonian to order w of this $1+1$ site model at half filling is given as

$$\mathcal{H}_{eff}^{toy} \quad = \quad -4(V^2/D)\Gamma\vec{S}\cdot\vec{s} \tag{7.14}$$

where $\vec{s} = \frac{1}{2}\sum_{\alpha\beta} c_\alpha^+ \vec{\sigma}_{\alpha\beta} c_\beta, c_\sigma$ are the fermion operators corresponding to the single orbital at the Fermi level and V denotes the hopping amplitude between conduction electron and impurity. Γ is given by the expectation value in the insulator $\Gamma = \langle\uparrow| f_\downarrow \frac{1}{H_{ins} - E_{ins}} f_\uparrow^\dagger |\downarrow\rangle_{at}$.

The ground state in this problem is given by the singlet state

$$|gs\rangle = \frac{1}{\sqrt{2}}(|\uparrow;\downarrow\rangle - |\downarrow;\uparrow\rangle) \tag{7.15}$$

where we use the convention $|\sigma;\sigma'\rangle = |\text{impurity state}_\sigma;\text{conduction electron}_{\sigma'}\rangle$. The transformed f_σ operator is given as

$$F_\sigma = -(V/D)\Gamma\Big((X_{\sigma\sigma} - X_{\bar{\sigma}\bar{\sigma}})c_\sigma + 2X_{\bar{\sigma}\sigma}c_{\bar{\sigma}}\Big). \tag{7.16}$$

Using the explicit forms of the excited states, which can be found in the appendix, we can calculate the low energy Green function, which is given by the expression

$$G_{low}(i\omega_n) = \frac{9\Gamma^2V^2}{2D^2}\left(\frac{1}{i\omega - E_{gs}} + \frac{1}{i\omega + E_{gs}}\right). \tag{7.17}$$

In order to close the self-consistency, which in the case of one bath electron at zero energy is given as $t^2G_{low}(i\omega_n) = \frac{V^2}{i\omega_n}$, we have to *collapse* the two poles of the full Green function and impose self-consistency on the spectral weight, which yields

$$(9/4)\Gamma^2V^2 = V^2. \tag{7.18}$$

We immediately see that, as discussed, this equation is unstable except at the critical point.

In order to determine the critical point explicitly, we now have to evaluate Γ. To lowest order, i.e. if upper and lower Hubbard bands are neglected completely, the high energy states entering Γ are just the high energy states of the impurity, such that $\Gamma^{(0+1)} = -\frac{2D}{U}$. A better approximation can be obtained analytically by solving the simplest insulator in which upper and lower Hubbard bands are represented by one pole, respectively. Again the explicit wave functions and energies can be found in the appendix. The value of Γ resulting from this $2+1$ insulator is given as $\Gamma^{(2+1)} = -\frac{2D}{U}(1 + \frac{6V_{high}^2}{U^2})$. Since at the critical point the high energy spectral weight is given by the value of the insulator, we find $V_{high}^2 = \frac{t^2}{2} = \frac{D^2}{8}$ such that $\Gamma^{(2+1)} = -\frac{2D}{U}(1 + \frac{3D^2}{4U^2})^2$.

Using this value in Eq. (7.18) we obtain $1 = \frac{9}{4}(\frac{2D}{U})^2(1 + \frac{3D^2}{4U^2})$. This equation has a solution for one value of U only which is the critical interaction. In this simple approximation this is given as $U_c = 3.22D$. It is interesting to note at this point that even this "bare bones" model gives a result that is close to the value obtained from a slave-boson calculation using the four boson scheme of Kotliar and Ruckenstein [32], which yields $U_c^{4\ boson} = 3.4D$. However, we will see that this is a comparatively bad

approximation to the value obtained numerically. This can be attributed to the fact that in the $1+1$ toy model the spin-spin coupling $\langle \vec{S} \cdot \vec{s}_l \rangle = -3/4$ which is considerably larger than the numerical value of -0.46. Note also that the Γ as obtained from the $2+1$ insulator is considerably lower than the value obtained using the full insulating solution. A comparison of the values for $J_{spin} = 2\Gamma$ in the $2+1$ insulator and in the full solution is shown in Figure 7.1.

7.1.2 Numerical Solution to the Problem at Criticality

Having gained some insight into the structure of the solution, we can now proceed by solving the self-consistent problem numerically in the more complicated case in which low and high energy contributions are given by numerous low-energy parameters $\tilde{\epsilon}_k$ and $\tilde{V}_k$, which have to be determined self-consistently. This is carried out iteratively using the zero-temperature algorithm [63, 40] described in the previous chapters. The functional equations (7.11) and (7.13) are truncated by representing the conduction electron bath in terms of a *finite* set of free electron orbitals $c^\dagger_{k\sigma}$, $k = 1, ..., N-1$, with the corresponding energy levels ϵ_k and hybridization matrix V_k. The ground state of the impurity problem, now defined on an N site cluster, is obtained by the modified Lanczos technique [94]. The local Green function as well as correlation functions are calculated using a continued fraction expansion [63, 67] as discussed in Chapter 2. The projected self-consistency condition (7.13) is again implemented in terms of a χ^2 fitting of the low frequency Matsubara Green function

$$\chi^2 = \sum_{\tilde{\omega}_n = \Omega_{min}}^{\Omega_{max}} |\sum_k \frac{\tilde{V}_k^2}{i\tilde{\omega}_n - \tilde{\epsilon}_k} - \langle F^\dagger F \rangle_{\tilde{\mathcal{H}}^{eff}_L}(i\tilde{\omega}_n)|^2 \tag{7.19}$$

where Ω_{min} and Ω_{max} are the low and high frequency cut-offs. Again, Ω_{min} is determined by the smallest pole of the continued fraction expansion of G^{low} and is reduced systematically as the system size increases. Ω_{max} is chosen big enough such that the results do not change. The solution is essentially independent of Ω_{max}.

As we saw in the previous chapter, looking at the high frequency limit of Eq. (7.13) we obtain the condition

$$1 = \langle \{F, F^\dagger\} \rangle = 2\Gamma^2 D^2 (3/8 - \langle \vec{S} \cdot \vec{s}_L \rangle_L) \tag{7.20}$$

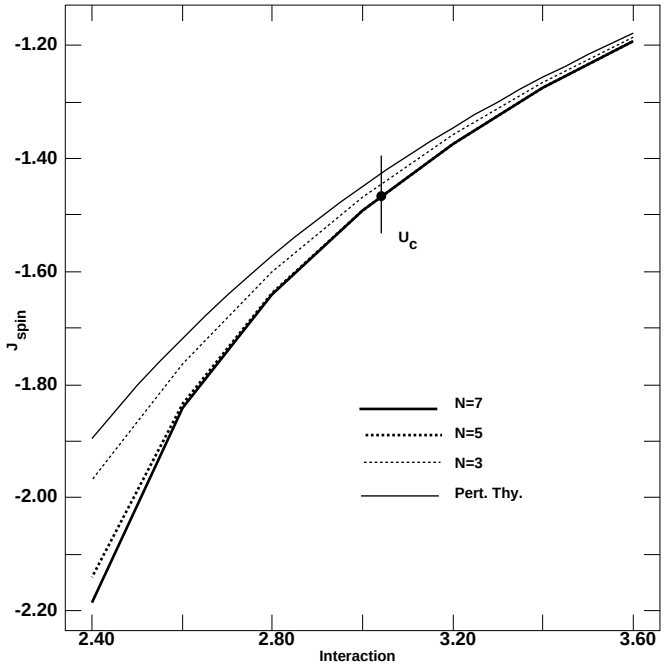

Figure 7.1: $J_{spin} = 2\Gamma$ at half-filling as a function of the interaction analytically (2+1 toy model) and for cluster sizes $N = 3, 5, 7$. The value corresponding to the critical point U_c is marked with a circle.

where $\langle \vec{S} \cdot \vec{s}_L \rangle_L$ is calculated in the self-consistent ground state of $\mathcal{H}_L^{eff}$. As in the case of the $1+1$ site toy model, this can be satisfied for one particular value of Γ and thus U only and is therefore the *exact* equation for U_c. A plot of $J_{spin} = 2\Gamma$ as a function of the interaction for cluster sizes $N = 3, 5, 7$ as well as the analytic result obtained from the solution to the $2+1$ site cluster is shown in Fig. 7.1

Since the equations are unstable except at the critical point we have to resort to a trick to obtain the solution at the critical point in practise. U_c can be determined by imposing the condition (7.20) *explicitly* by setting $\langle gs|F_\sigma F_\sigma^\dagger|gs\rangle = \langle gs|F_\sigma^\dagger F_\sigma|gs\rangle \equiv 1/2$ in the iteration and determining the interaction U such that this assumption is correct. The solution of the full non-linear problem as described in Section (7.3) gives an additional check of this procedure.

We have solved the equations for clusters of 4,6,8 and 10 sites. The critical interaction U_c is found to be essentially unchanged as the number of sites is increased from 4 to 10 and is obtained to be 2.92. The value for $\langle \vec{S} \cdot \vec{s}_L \rangle_L$ is found to be $\langle \vec{s} \cdot \vec{S}_L \rangle_L = -0.46$,

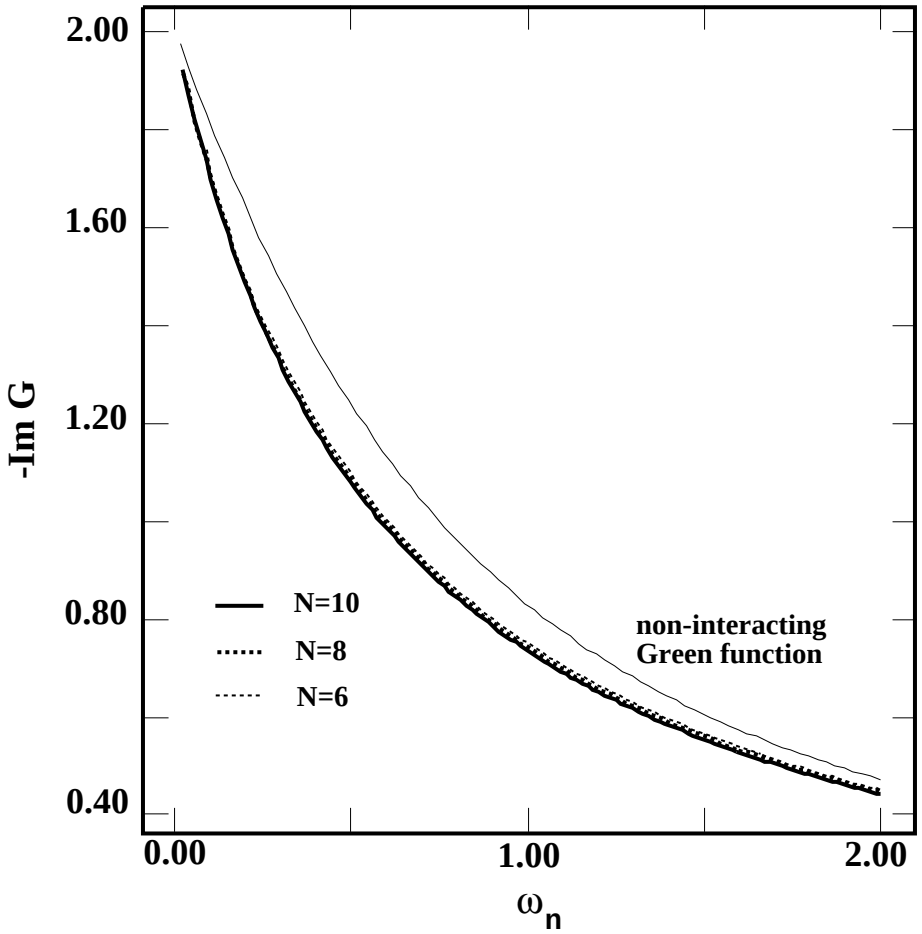

Figure 7.2: Imaginary part of the Matsubara Green function versus the rescaled frequency $\tilde{\omega}_n$ for system size $N = 6, 8, 10$ and non-interacting (semi-circular) density of states.

signaling the intermediate coupling nature of the associated Kondo problem at the critical point.

The Matsubara Green functions as functions of the rescaled Matsubara frequency for $N = 6$, 8 and 10 are shown in Fig. 7.2. The low frequency part of the Green function improves systematically as N increases, and remains essentially unchanged for $N = 8$ and 10. Also shown in Fig. 7.2 is the Green function for the non-interacting problem. The value of the scaled Green function at zero frequency is determined by the low energy self-consistency equation and is the same as that of the Green function of the non-interacting problem, $ImG(0^+) = -2/D$, consistent with the pinning of the density of states expected from Fermi liquid theory [46]. Notice that this provides a

highly non-trivial check of the numerics.

In Fig. 7.3 we show the single particle spectral function for $N = 10$ and different values of broadening of the poles ϵ. For very small broadening (Plot (a), $\epsilon = 0.01$) one can see the individual poles of the Green function. The large number of poles clearly demonstrates the power of the projection onto the low energy sectors.

A crucial question is how much the poles have to be broadened, i.e. which value of $\epsilon = 0.01$ is necessary to wash out the individual poles while retaining shape and structure of the spectral function. In principle, a criterion should be given by the pinning condition of the density of states. Unfortunately, this does not seem to give a clear way to determine the correct broadening, as can be seen in Fig. 7.3 (f), which depicts the value of $-ImG(0^+)$ as a function of broadening ϵ. Since the Green function never has a pole *at* the Fermi energy, $-ImG(0^+)$ does not reach the pinned value $2/D$, but stays below it by about 5%. Note also that in principle the "physical" ϵ should correspond to the maximum of the function, at which the dependence of $-ImG(0^+)$ on the broadening is weak. This in this case is given by $\epsilon = 0.0235$, and the corresponding spectral function is shown in Fig. 7.3 (b). Obviously this still has a large number of poles, and it is thus questionable, whether it reflects the true structure of the resonance. Further broadening on the other hand diminishes the value at zero even further. The resolution of the issue is not clear at this point.

The solution for the Green function also allows us to determine the rescaled self-energy $\Sigma^{low}(i\tilde{\omega}_n)$ by extracting from $\Sigma(i\omega_n) = i\omega_n - (D/2)^2 G(i\omega_n) - G^{-1}(i\omega_n)$ the terms with a singular dependence on w which are given as $\Sigma(i\tilde{\omega}_n) = -(D/2)^2 G(i\tilde{\omega}_n) - G^{-1}(i\tilde{\omega}_n)$.

Both $G^{low}(i\tilde{\omega}_n)$ and $\Sigma^{low}(i\tilde{\omega}_n)$ are analytic can therefore be expanded in power series. The coefficients can be obtained by fitting the functions by quadratic polynomials at low frequencies. The resulting expression for the self energy is then given as

$$\Sigma^{low}(i\tilde{\omega}_n) \quad = -1.7 i\tilde{\omega}_n - i1.2(i\tilde{\omega}_n)^2 sgn(\omega_n). \tag{7.21}$$

The term of the self-energy linear in $i\tilde{\omega}_n$ implies a quasi-particle residue $z \equiv (1 - \partial\Sigma/\partial i\omega_n)^{-1} = w/1.7$ which vanishes as the critical point is approached.

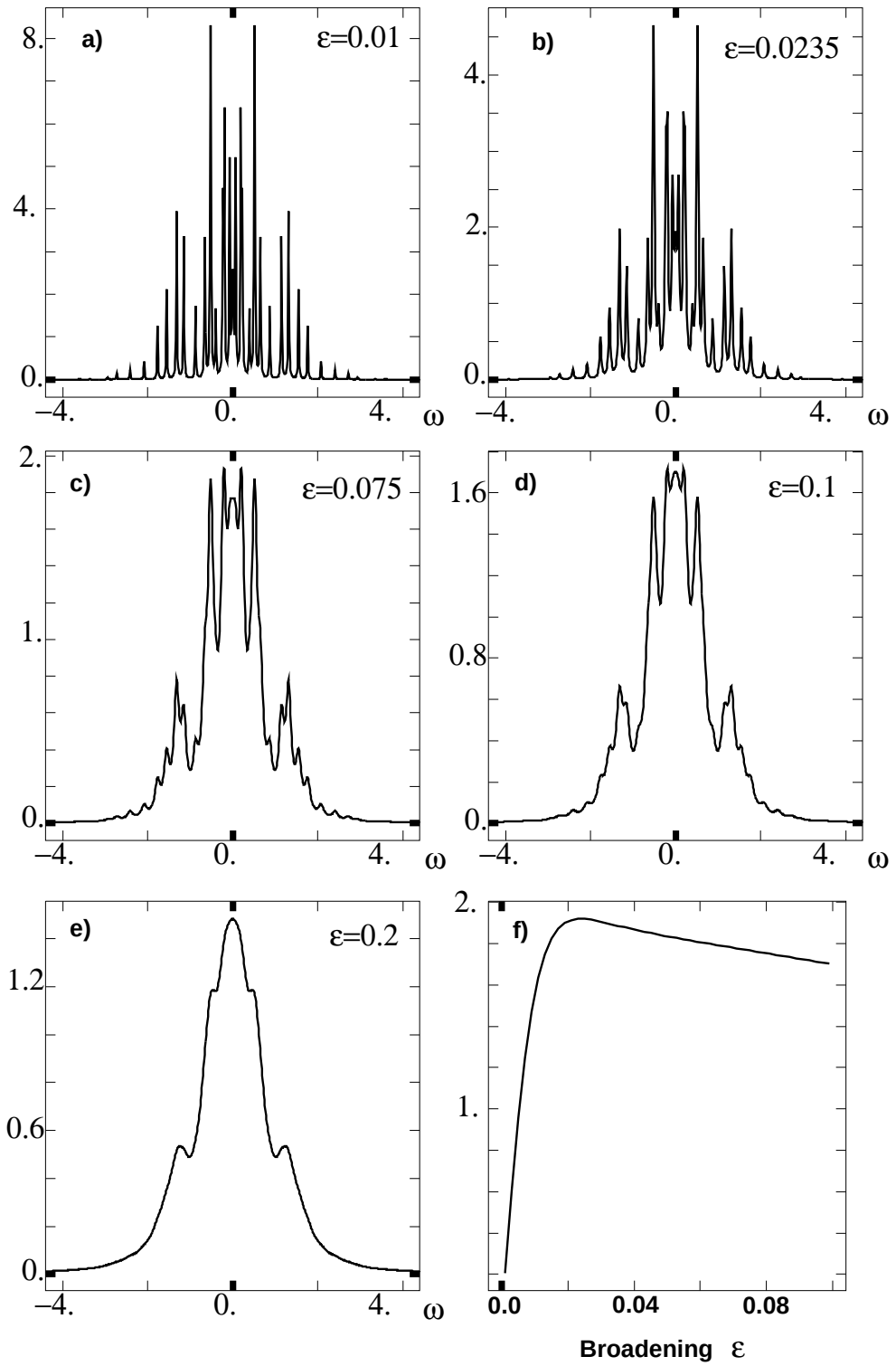

Figure 7.3: Single particle spectral function as function of the rescaled frequency $\tilde{\omega}$ (N=10) with a broadenings $\epsilon = 0.01, 0.0235, 0.0075, 0.1$, and 0.2. Plot (f) shows the value of $-ImG(0^+)$ as a function of the broadening ϵ.

The momentum-independence of the self-energy in infinite dimensions in turn leads to a quasi-particle mass $m^*/m = 1/z = 1.7/w$, and a linear coefficient of the specific heat,

$$\gamma = \frac{4\pi k_B^2}{3}\frac{1.7}{Dw} \tag{7.22}$$

which diverge at the critical point. This divergence is consistent with the Brinkman-Rice scenario of the Mott transition [26], as well as the previous result in the Hubbard model at half-filling within second-order perturbation theory [12, 56]. The term of the self-energy quadratic in $(i\tilde{\omega}_n)^2$ gives rise to an imaginary part of the analytically-continued self-energy

$$Im\Sigma(\omega + i0^+) = -\frac{1.2}{w^2}\frac{\omega^2}{D} \tag{7.23}$$

which also diverges at the critical point.

The local dynamical spin susceptibility

$$\chi_s(i\nu_n) = (g\mu_B/2)^2 \int_0^\beta d\tau e^{i\nu_n\tau}\langle T_\tau S_z(\tau)S_z(0)\rangle_{H_{eff}}, \tag{7.24}$$

where $S_z = \frac{1}{2}e^{-S}(f_\uparrow^\dagger f_\uparrow - f_\downarrow^\dagger f_\downarrow)e^S = B^2(X_{\uparrow\uparrow} - X_{\downarrow\downarrow})/2$ as given in the appendix. $B = 0.98$ is the overlap between the ground states of $\mathcal{H}_{at}$ and the state describing the bare f level (which is the ground state of $\mathcal{H}_{at}$ with V_k^H set to zero), and can also be calculated from a continued fraction expansion. The result in terms of rescaled frequency, $\chi_s(i\tilde{\nu}_n)$, is shown in Fig. 7.4.

At low frequencies, $\chi_s(i\tilde{\nu}_n)$ can be fitted by

$$\chi_s^{low}(i\tilde{\nu}_n) = (g\mu_B/2)^2(8 - 36|\tilde{\nu}_n|)/wD. \tag{7.25}$$

The local static susceptibility is given by the constant term of Eq. (7.25),

$$\chi_s = (g\mu_B/2)^2 8/(wD) \tag{7.26}$$

from which we derive a generalized Wilson ratio at the critical point,

$$R \equiv \frac{\chi_s/\chi_{s,loc}^{free}}{\gamma/\gamma^{free}} = 2.8 \tag{7.27}$$

where $\chi_{s,loc}^{free} = 16/(3\pi D)(\frac{g\mu_B}{2})^2$ and $\gamma_{free} = 4\pi k_B^2/(3D)$, are the static local spin susceptibility and the linear coefficient of the specific heat for the free electron gas with

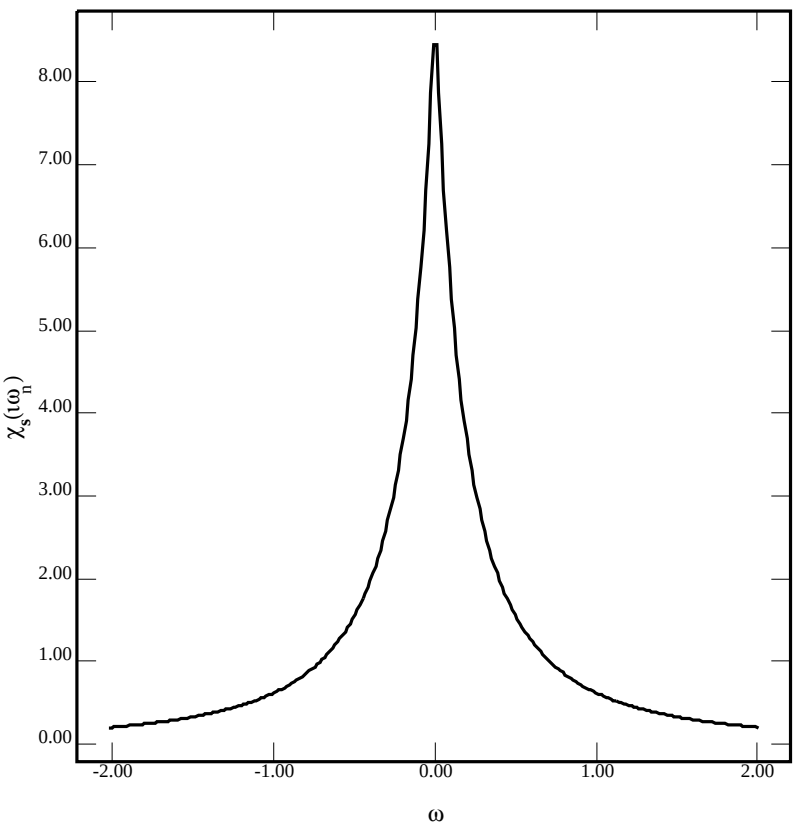

Figure 7.4: Real part of the local spin susceptibility as a function of the rescaled Matsubara frequency $\tilde{\nu}_n$ for $N = 10$.

a semicircular density of states, respectively. Compared to the universal value for the Anderson impurity model, $R_{AM} = 2$, the critical value R is enhanced. This enhancement can be understood from the self-consistent modification of the electron bath. Using $G_o^{-1} = i\omega_n - (D/2)^2 G(i\omega_n)$, and following the usual derivation [4], we arrive at a modified Ward identity given by

$$(\frac{4}{g\mu_B})^2 \chi_s + \chi_c = \frac{6}{\pi^2 k_B^2}\gamma + 2\int \frac{d\omega}{2\pi}\Gamma_{\uparrow\uparrow}(0,\omega) G_\uparrow^2(\omega)(D/2)^2 G'_\uparrow(\omega) \qquad (7.28)$$

where $\Gamma_{\uparrow\uparrow}$ is the full vertex function. Qualitatively, $\Gamma_{\uparrow\uparrow}$ diverges like $\#/(wD)$ as the critical point is approached, where (wD) comes in as the cutoff for the Curie-like term in the vertex function, leading to a finite enhancement to the Wilson ratio. This can be seen explicitly by considering the vertex of the atomic Hubbard model [95].

We note that the usual definition of the Wilson ratio in a lattice model is given in terms of the $\mathbf{q} = 0$ component of the static susceptibility. In large dimensions the $\mathbf{q}$ dependent susceptibility has a typical value χ_{loc} for a general $\mathbf{q}$ in the Brillouin zone which is different from the $\mathbf{q} = 0$ value, controlled by the magnetic exchange. In order to avoid the special features of the $\mathbf{q} = \mathbf{0}$ point in large dimensions we have used χ_{loc} in the definition of the generalized Wilson ratio. The enhancement of R is consistent with the ferromagnetic tendencies found in the Gutzwiller approximation [5] where the magnetic exchange is ignored as well.

Finally, the term of the imaginary part of the dynamical spin susceptibility linear in $|\tilde{\nu}_n|$ implies that $\lim_{\omega\to 0} \frac{\chi''_s(\omega+i0^+)}{\omega} = 36/(Dw)^2(g\mu_B/2)^2$. If we use χ_{loc} for the static spin susceptibility this implies a finite generalized Korringa ratio

$$K = \frac{\lim_{\omega\to 0}(\chi''_s(\omega + i0^+)/\omega)}{\pi\chi_s^2(i0^+)/2} = 0.3 \qquad (7.29)$$

at the critical point, which is again modified from the universal value for the infinite bandwidth Anderson model [96], $K_{AM} = 1$. Since χ_s is enhanced, the Korringa ratio is reduced.

Our results have direct implications for the Mott-Hubbard systems. The conductivity can be estimated by converting the ω^2 at zero temperature to $(\pi T)^2$ at finite

temperature and assuming that the self-energy we derived at the critical point also applies to the case of a hypercubic lattice in d dimensions [97]. This can be done in the following way. Using the Kubo formula, which in the limit of infinite dimensions does not have any vertex corrections [74, 88] as we saw in Chapter 3, the optical conductivity is given as [97]

$$\sigma(\omega) = \sum_{\sigma} \frac{e^2}{\hbar\nu} \int \frac{d\omega'}{4\pi} \int d\epsilon A(\epsilon,\omega') A(\epsilon,\omega'+\omega) \frac{n_F(\omega') - n_F(\omega'+\omega)}{\omega} \frac{1}{N_s} \sum_{\vec{k}} v_{k_x}^2 \delta(\epsilon - \epsilon_k). \tag{7.30}$$

For $\omega \to 0$ and $T \to 0$ one obtains the zero temperature DC conductivity as

$$\sigma_{DC} = \frac{2e^2}{\hbar\nu} \int \frac{d\epsilon}{4\pi} A(\epsilon,0)^2 \frac{1}{N_s} \sum_{\vec{k}} v_{k_x}^2 \delta(\epsilon - \epsilon_k) \tag{7.31}$$

where $A(\epsilon,\omega) = -2Im\frac{1}{\omega+i\delta-\epsilon-\Sigma(\omega)}$, ν the volume of a unit cell and $v_{k_x} = \partial\epsilon_{\vec{k}}/\partial k_x$. As shown in the previous chapters, the limit of infinite dimensionality provides a mean-field theory of the Hubbard model. Furthermore we have argued that the bare density of states on a Bethe lattice is a good approximation to the three dimensional case, since it is bounded. We can thus use the self-energies obtained numerically to calculate the spectral functions $A(\epsilon,\omega)$. For $Im\Sigma$ small (i.e. low temperatures) we can make the replacement

$$A(\epsilon,0)^2 = \left(2Im\Sigma(T)/(\epsilon^2 + Im\Sigma(T)^2)\right)^2 \to 2\pi\delta(\epsilon)/Im\Sigma(T) \tag{7.32}$$

in (7.31). Performing the ϵ integral using the δ-function we are then left with the evaluation of the expression $\frac{1}{N_s}\sum_{\vec{k}} v_{k_x}^2 \delta(\epsilon_k)$. In order to estimate the conductivity on a three dimensional cubic lattice, this can be evaluated numerically. Using $\epsilon_{\vec{k}} = -2\tilde{t}\sum_{i=1}^{d}\cos(k_i a)$ and rescaling $\tilde{t}$ as $\tilde{t} \to t/\sqrt{2d}$, which follows from the fact that the coordination number on a hypercubic lattice is given as $2d$ (note also that with this rescaling the second moment of Gaussian and semicircular DOS coincide), we obtain

$$S \equiv \frac{1}{N_s} \sum_{\vec{k}} v_{k_x}^2 \delta(\epsilon_k) = \frac{5.18\sqrt{2}}{\pi^3} \frac{t a^{d-2}}{\sqrt{d}}. \tag{7.33}$$

For $d = 3$ this gives $S = 0.14ta^2$. Using the approximation $\Sigma(T) \approx \frac{\pi^2}{2} T^2 \frac{\partial^2 Im\Sigma}{\partial(i\omega_n)^2}|_{\omega_n=0}$ the resistivity is thus given as

$$\rho(T) = AT^2 \tag{7.34}$$

where $A = \frac{14\pi^2 a\hbar Im\Sigma''(0)}{e^2 D}$. Using $\hbar/(e^2 k_B^4) = 4.14 \cdot 10^3 \Omega$ we obtain the finite ratio

$$\frac{A}{\gamma^2} = 7.9\left(\frac{\partial^2\tilde{\Sigma}}{\partial\tilde{\omega}^2}/(\frac{\partial\tilde{\Sigma}}{\partial\tilde{\omega}})^2\right)2.05 \times 10^3 a \ (\Omega m) \tag{7.35}$$

where a is the hypercubic lattice spacing in units of meter. Photoemission experiments [98] have indicated that $LaTiO_3$ is very close to the Mott transition point. As we saw in previous sections doping a Mott insulator at U_c introduces an energy scale wt which can be identified with wD we can use the results to interface with experiments. For $Sr_{1-x}La_xTiO_3$ with $x = 0.95$, which is close to the Mott transition, Eq. (7.35) yields $A/\gamma^2 = 14 \times 10^{-6}\Omega m$ when we use $a = 8.3 \times 10^{-10} m$ [99]. This result is of the same order of magnitude as the measured value $A/\gamma^2 = 6.4 \times 10^{-6}\Omega m$ [100].

In summary, we have applied the projective self-consistent approach developed in the previous chapter to the determine the critical properties at the Mott transition in the half-filled Hubbard model. We find low energy scaling functions that can be quantitatively related to experimental results in transition metal oxides.

7.2 The Critical Properties of the Doped Hubbard Model

We will proceed by determining the critical properties of the *doped* Hubbard model in an analogous fashion to the half filled case discussed in the previous section and investigate the question *where* the states induced by doping the Mott insulator are generated. As we have discussed before, this is highly relevant in the light of the experiments on the cuprates discussed earlier [8, 9, 10, 11]. Notice also that the exact position of the resonance is crucial to the applicability of the self-consistent projective technique as implemented in this thesis, since it relies on the existence of a separation of scales, i.e. the existence of a resonance well separated from the upper and lower Hubbard bands.

7.2.1 Determining the Position of the Resonance

In the case of half filling, which we discussed in the previous section, the Kondo resonance developed in the center between upper and lower Hubbard bands as long as one is in the metallic regime. Away from half filling and for values of the interaction slightly larger than the critical value it is clear that the position of the resonance also

develops inside the gap. This follows from continuity, i.e. from Luttinger's theorem. It is not clear, however, where the resonance develops for values of U considerably larger than U_c. The curves displaying the particle number as a function of doping shown in Fig. 5.2, and the spectral functions shown in Fig. 5.3 are strong evidence for the fact that the states generated upon doping are in fact generated in the gap. Additional support comes from the argument that the resonance will approach the Hubbard band *continuously* as the interaction is increased and the system is doped. However, doubts may be raised in particular due to the results from the rigid Mott-Hubbard picture [85] and the large-N approach [101]: In the Mott-Hubbard picture doping with electron or holes occupies preexisting states at the top or the bottom of the lower and upper Hubbard bands, respectively; in the large-N picture the doping *induces* states at the same place. In both cases the resonance is not separated from the upper and lower Hubbard bands. It is therefore desirable to determine the position of resonance i.e. the *critical* μ, μ_c, for infinitesimal doping δ^- in the mean-field treatment provided by infinite d.

The position of the quasiparticle peak, μ_c, as a function of the interaction U can be obtained in a similar way as the critical interaction U_c was obtained in the previous section. The analysis relies on the fact that *at* the transition the self-consistent projective technique can necessarily be applied, if the resonance develops *at or above* the lower Hubbard band (again we restrict ourselves to the hole doped case), which is clearly the case. This is due to the fact that in this case the sum of high energy and impurity parts of the Hamiltonian can once again be viewed as an impurity in a semiconductor. The lowest lying states of this contribution to the Hamiltonian are again given by a degenerate doublet, which at the critical point is separated from the higher lying states by an energy of order the half-bandwidth D. While this separation is no longer as large as in the case of half-filling, in which it is of order $U/2$, for small doping the expansion parameter $(wD)/D = w$ is still small and goes to zero as the doping $\delta^- \to 0$. The effective Anderson model is again in the local moment regime and the analysis is exactly analogous to the half-filled case.

Again, we first separate the impurity Hamiltonian into three parts as

$$\mathcal{H}_{AM} = \mathcal{H}_{at} + \mathcal{H}_b + \mathcal{H}_M \tag{7.36}$$

where in this case $\mathcal{H}_{at}$ is given as

$$\mathcal{H}_{at} = U n_{f\uparrow} n_{f\downarrow} - \mu(n_{f\uparrow} + n_{f\downarrow}) + \sum_{\sigma,k} V_{k,H}(c^+_{k\sigma} f_\sigma + h.c.) + \sum_{\sigma,k} \epsilon_{k,H} c^+_{k\sigma} c_{k\sigma}. \qquad (7.37)$$

The hybridization $\mathcal{H}_M$ with the low energy electrons is the same as given in the previous section.

As we saw in the previous chapter, to lowest order the effective Hamiltonian now has an additional potential scattering term and is given by Equation (6.57) as

$$\mathcal{H}^{eff(1)}_{low} = D \sum_{k\sigma} \tilde{\epsilon_k} n_{k\sigma} - \frac{D}{2} J^{(1)}_{spin} \vec{S} \cdot \vec{s}_L - \frac{D J^{(1)}_{pot}}{8} (n_{L\uparrow} + n_{L\downarrow})(X_{\uparrow\uparrow} + X_{\downarrow\downarrow}) \qquad (7.38)$$

with the $J^{(1)}$ as defined in Eqs. (7.8) and (7.9).

The projected f_σ electrons are accordingly given by $\sqrt{w}$ times the effective low energy operators (6.67) as

$$F^{LL(1)}_\sigma = -\frac{1}{4}\left(J^{(1)}_{pot} + J^{(1)}_{spin}(X_{\sigma\sigma} - X_{\bar{\sigma}\bar{\sigma}})\right) c_\sigma - \frac{1}{2} J^{(1)}_{spin} X_{\bar{\sigma}\sigma} c_{\bar{\sigma}}. \qquad (7.39)$$

where again $c_{L\sigma} = 2\sum_k \tilde{V}_k c_{k\sigma}$.

The condition for a vanishing resonance, i.e. for the critical point, once again is given as $1 = \{F^{(1)}_\sigma, F^{(1)\dagger}_\sigma\}$ which in the presence of potential scattering assumes the form

$$1 \;=\; -\frac{1}{2}\left(J^{(1)2}_{spin}(\vec{S} \cdot \vec{s}_L - \frac{3}{8}) - \frac{J^{(1)2}_{pot}}{8}\right). \qquad (7.40)$$

For a given value of U can now be satisfied for only two values of the chemical potential, $\mu^{\pm}_c(U)$, the position of the resonance at infinitesimal particle and hole doping, respectively.

In practice, μ_c is determined in the following way: (1) One obtains the solution to the *insulator* at half-filling, which gives the weights and poles of the high energy bands. (2) The poles are shifted by the chemical potential, i.e. $\epsilon^{high}_k \rightarrow \epsilon^{high}_k - \Delta\mu$, (with $\Delta\mu = \mu - U/2$) since all energies are measured with respect to the chemical potential. Here we use the fact that for infinitesimal doping (i.e. to lowest order in w) the upper and lower Hubbard bands are not modified. (3) Groundstate and groundstate energy of this "insulator" are obtained in order to determine $J^{(1)}_{spin}$ and $J^{(1)}_{pot}$, which is done easily

using the continued fraction expansion. (4) The self-consistently projected model is iterated to convergence with the $J^{(1)}$ as determined in (3). If the criterion (7.40) is not fulfilled, μ is changed and the procedure is repeated starting with (2).

As before, the system of equations is unstable unless one is directly *at* the critical point, and the condition (7.40) is enforced *explicitly* by setting the spectral weight to one and monitoring the violation of condition (7.40) as elaborated in the section describing the determination of the critical point at half filling.

Before discussing the numerical results it is again instructive to consider the implications of (7.40) analytically using the simple toy models discussed in the appendix. The structure of Eq. (7.40) implies that the critical μ_c is determined by two key ingredients, the spin-spin coupling $\vec{S}\cdot\vec{s}_L$, which is a *low energy* quantity, and the high energy coefficients J_{spin} and J_{pot}. These can be evaluated in the effective $1+1$ site Kondo Hamiltonian and in the $2+1$ site insulator, respectively. As in the half-filled case, the effective Kondo Hamiltonian yields $\vec{S}\cdot\vec{s}_L=-\frac{3}{4}$, which even for small U compares poorly with the numerical value, as we shall see in the following section. It is thus expected that a considerable improvement of any analytic approximation requires a more accurate treatment of the low energy part. The coefficients J_{spin} and J_{pot} are determined in Appendix D and are given by the expressions

$$\begin{aligned}
J_{pot}^{(1,2+1)} &= \frac{D}{U-\mu}+\frac{2DV^2}{(U-\mu)^3}-\frac{3DV^2}{2\mu U^2} \\
&- \frac{D}{2}\Big(\frac{1+\frac{V}{2\sqrt{2}U}-\frac{3V^2}{2U^2}}{\mu-\sqrt{2}V+\frac{V^2}{2U^2}}+\frac{1-\frac{V}{2\sqrt{2}U}-\frac{3V^2}{2U^2}}{\mu+\sqrt{2}V+\frac{V^2}{2U^2}}\Big) \\
J_{spin}^{(1,2+1)} &= -\frac{D}{U-\mu}+\frac{DV^2}{2\mu U^2}+\frac{2DV^2}{U-\mu}\Big(\frac{1}{U^2}-\frac{1}{(U-\mu)^2}\Big) \\
&- \frac{D}{2}\Big(\frac{1+\frac{V}{2\sqrt{2}U}-\frac{3V^2}{2U^2}}{\mu-\sqrt{2}V+\frac{V^2}{2U^2}}+\frac{1-\frac{V}{2\sqrt{2}U}-\frac{3V^2}{2U^2}}{\mu+\sqrt{2}V+\frac{V^2}{2U^2}}\Big)
\end{aligned} \tag{7.41}$$

with the common asymptotic value in the limit $U\to\infty$, $J_{spin}^{\infty}=J_{pot}^{\infty}=-\frac{D\mu}{\mu^2-2V^2}$. To order V/U one obtains

$$\begin{aligned}
J_{spin} &= -\frac{D\mu}{\mu^2-2V^2}-\frac{D}{U-\mu}-\frac{DV^2}{2U(\mu^2-2V^2)} \\
J_{pot} &= -\frac{D\mu}{\mu^2-2V^2}+\frac{D}{U-\mu}-\frac{DV^2}{2U(\mu^2-2V^2)}.
\end{aligned} \tag{7.42}$$

Together with the spin-spin coupling of the 1+1 Kondo model this yields $\mu^{\infty} = 1.03$, implying that the resonance is just above the band as U goes to infinity.

We have plotted the numerical results for J_{spin} and J_{pot} for interaction $U = 3, 4, 5$ and $U = 10$ with cluster sizes $N = 3, 5, 7$ together with the analytic result of (7.41) in Fig. 7.5. As the system size grows, the coefficients are essentially unchanged from $N = 6$ to $N = 8$. The analytic result is in good agreement with the numerical result for $N = 3$. Deviations are due to the fact that the analytic result is perturbative in V/U and that the self-consistently determined bands are not perfectly rigid (i.e. the assumption that they are centered at $U - \mu$ and μ, respectively, is not completely accurate). For larger values of μ the analytic result (7.41) is exact. Unfortunately, finite size effects for values of μ near the band edge, are large and the perturbative calculation underestimates the coefficients J_{spin} and J_{pot} by more than 10%. Since this encompasses the critical μ_c (=-0.88 D at $U = 4$) this gives rise to a large error in the determination of μ_c. The $2+1$ *analytic* approximation is therefore not sufficient to accurately obtain the critical behavior. Note also that inaccuracies in the determination of the critical behavior using simple toy models are due to both low and high energy contributions.

The *numerical* results for the critical μ, μ_c are displayed in Figure 7.6. Clearly the position of the resonance begins at U_c for which $\mu_c = U/2$ and sweeps through the gap continuously as the interaction is increased, approaching the line indicating the beginning of the lower Hubbard band as predicted by a rigid band picture.

Unfortunately, the *numerical* determination of J_{spin} and J_{pot} for large values of the interaction is also subject to a systematic error. This is a result of the fact that the finite number of poles representing upper and lower Hubbard bands does not permit an accurate determination of the *band edge*. For interactions close to U_{c2} in the half filled case the band edge is far away from the chemical potential, such that the exact position of the band edge does not play a role. J_{spin} and J_{pot} in this case can thus be computed accurately. As U increases, however, the critical μ_c moves towards the band edge, in which case the proximity to the band edge affects the numerically obtained values of J_{spin} and J_{pot}. This can be seen by the evaluation of both quantities for $U = \infty$ as functions of μ, in which case both are known exactly since they are simply

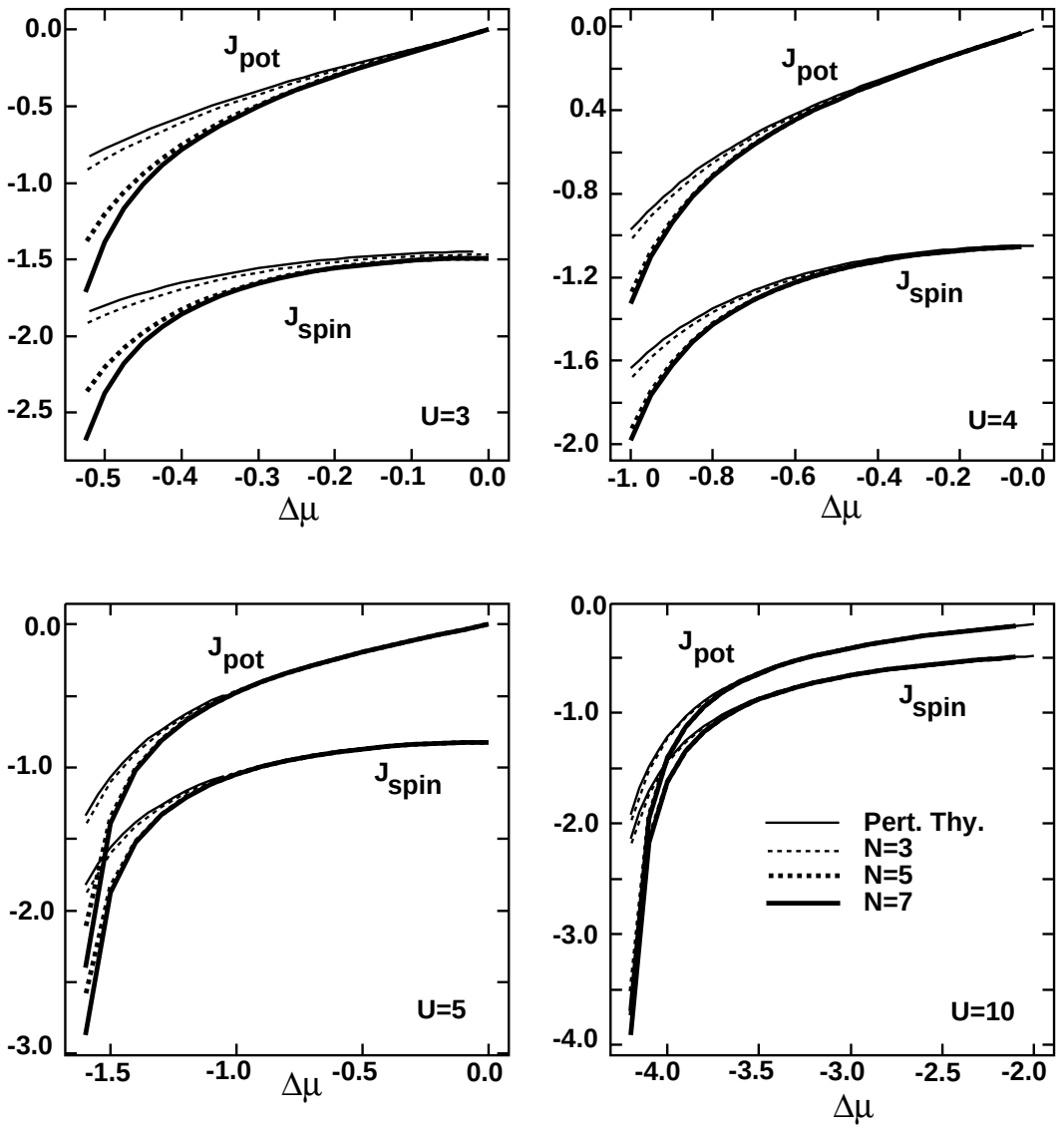

Figure 7.5: J_{spin} and J_{pot} as a function of $\Delta\mu$ for $U = 3, 4, 5, 10$ with cluster sizes $N = 3, 5, 7$. Also shown (thin solid line) is the analytic result.

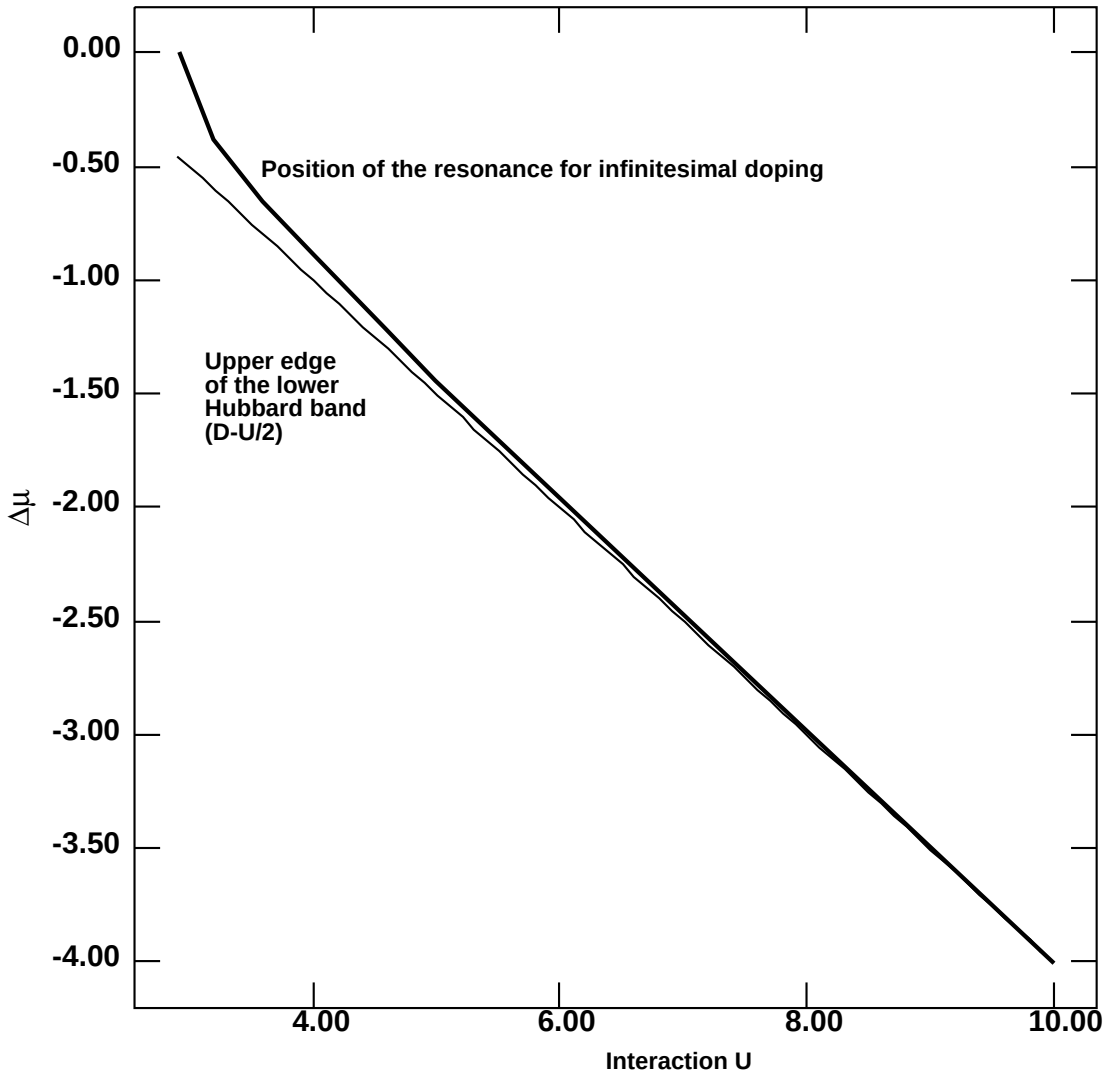

Figure 7.6: Position of the quasiparticle resonance for vanishing resonance width as a function of the interaction (solid). The dotted line indicates the beginning of the incoherent lower Hubbard bands as predicted by a ridid band picture. The position of the resonance is measured with respect to the center of gravity of the bands. The figure is reflection symmetric about the $\Delta\mu = \mu - U/2 = 0$ axis for electron doping.

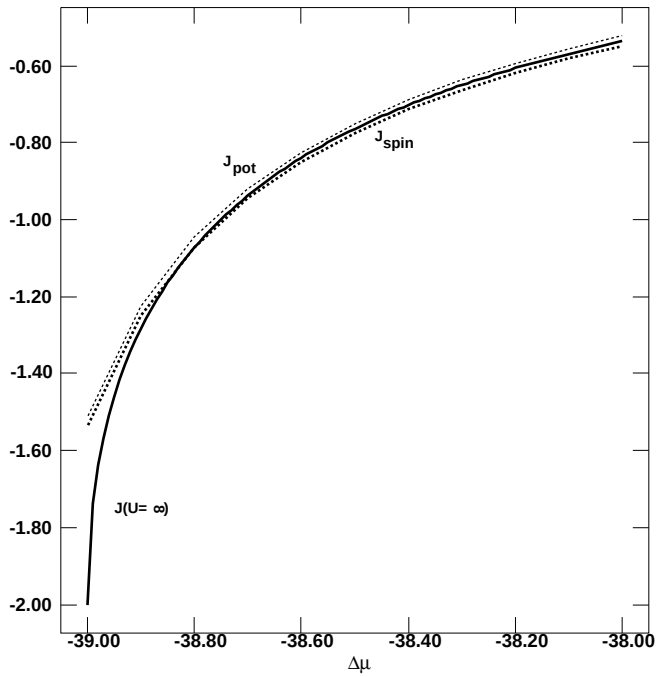

Figure 7.7: J_{spin} (dashed line) and J_{pot} (dotted line) as a function of $\Delta\mu$ for $U = 40$ with cluster size $N = 7$ together with the exact $U = \infty$ result (solid line).

given as $J_{spin} = J_{pot} = 2ReG(\omega = 0^+)$ where G is given by the rigid band picture as $ReG(0) = \frac{1}{D^2}(\mu - \sqrt{\mu - D} + U - \mu - \sqrt{U - \mu - D})$ for $\mu > D$. A comparison of the exact $U = \infty$ values to the numerical results for $U = 80$ is shown in Figure 7.7. The small difference between J_{spin} and J_{pot} gives a measure of the distance from their asymptotic value and indicates that this has essentially been reached. We see that for values of μ up to approximately 0.28 from the band edge the agreement between $J^{approx}(U = 80)$ and $J^{exact}(U = \infty)$ is very good, while they start deviating for smaller values of μ. This can be understood by noticing that the largest pole in the finite size cluster representing the lower Hubbard band is at a distance of $0.28D$ from the band edge of the exact rigid band result. As one can see the numerical result underestimates the values of J. Consequently Eq. (7.40) is therefore fulfilled for *larger* values of the chemical potential and it is to be expected that for values of U for which $\mu - D < 0.28$ (this yields a first approximation) the critical μ_c is in fact *larger* than the numerical result shown in Fig. 7.6 such that the critical μ_c is always outside the band. We have evaluated the critical μ_c using the exact J_{spin} and J_{pot} for $U = \infty$. We find $\mu_c(U = \infty) = 1.0185$, i.e. a *finite*

distance from the band edge, which we expect to be close to the asymptotic value. This is corroborated by the observation the the coupling $\langle \vec{S} \cdot \vec{s}_L \rangle$ saturates to the finite value $\langle \vec{S} \cdot \vec{s}_L \rangle = -0.23$. If μ_c approached the band edge for $U = \infty$, the coupling should go to zero as can be seen from Eq. (7.40) together with the results for $J(U = \infty)$. For small values of doping the quasiparticle resonance is thus always expected to be separated from the incoherent bands, even for large values of the interaction. The self-consistent projective technique as described can be therefore always be applied for dopings that are sufficiently small.

7.2.2 Critical Properties at Finite Doping

The analysis of the critical properties of the doped Hubbard model proceeds along the lines of the analysis we presented in the half-filled case. Since the numerically obtained critical μ_c for larger values of the interaction is corrected *upwards* if the full insulating solution is used, the quantities evaluated at criticality also change. However, we expect these changes to be small, which can be justified by observing that the critical properties as a function of U go to the correct asymptotic value for $U = \infty$, as will be demonstrated. This is due to the fact that the corrections to μ_c are comparatively small (of order $0.1D$), leading in turn to small changes in the correlation functions.

Again the spectral function displays considerable structure and is anything but a renormalized bare (semicircular) density of states. In Fig. 7.8 we display the spectral functions for values of the interaction $U = 5$ and $U = 3.2$. Evidently a clearly discernible peak in the low energy spectrum splits off as the interaction increases. We expect that any feature like this should be observable in photoemission spectroscopies. The fact that the spectral function is shifted upward can be interpreted as the result of the potential scattering term which acts as a positive chemical potential. However, due to the dependence on k the individual poles are shifted by different amounts.

The corresponding rescaled Matsubara Green functions at the critical point for interactions $U = 3, 4$ and $U = 5$ are shown in Fig. 7.9.

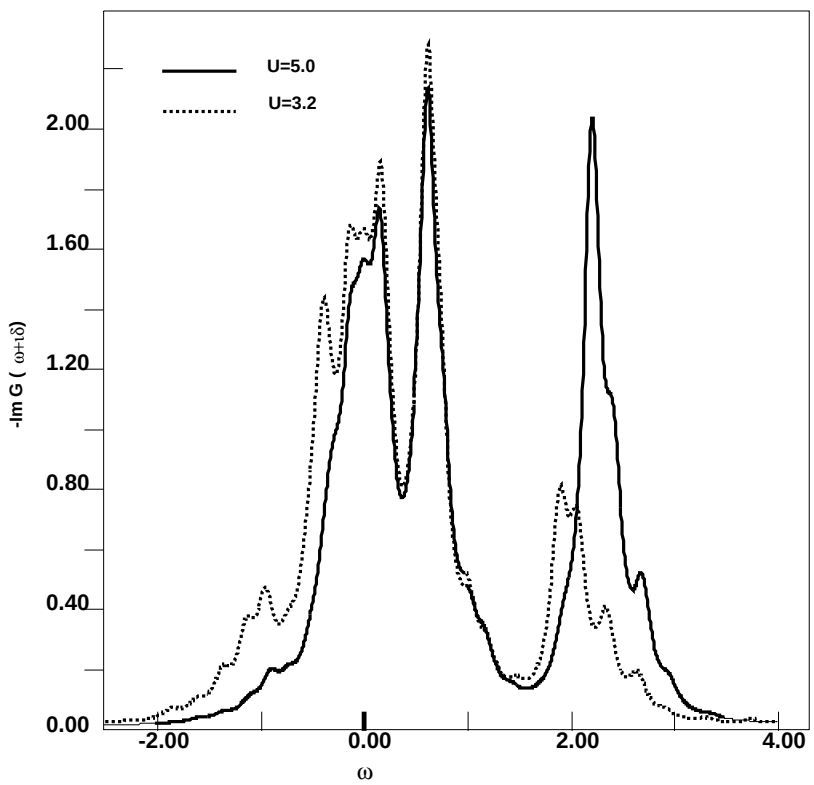

Figure 7.8: Scaling function of $-ImG(\omega + i\delta)$ with broadening $\delta = 0.1$ at the critical point (infinitesimal doping) for interactions $U = 5$ (solid line) and $U = 3.2$ (dashed line).

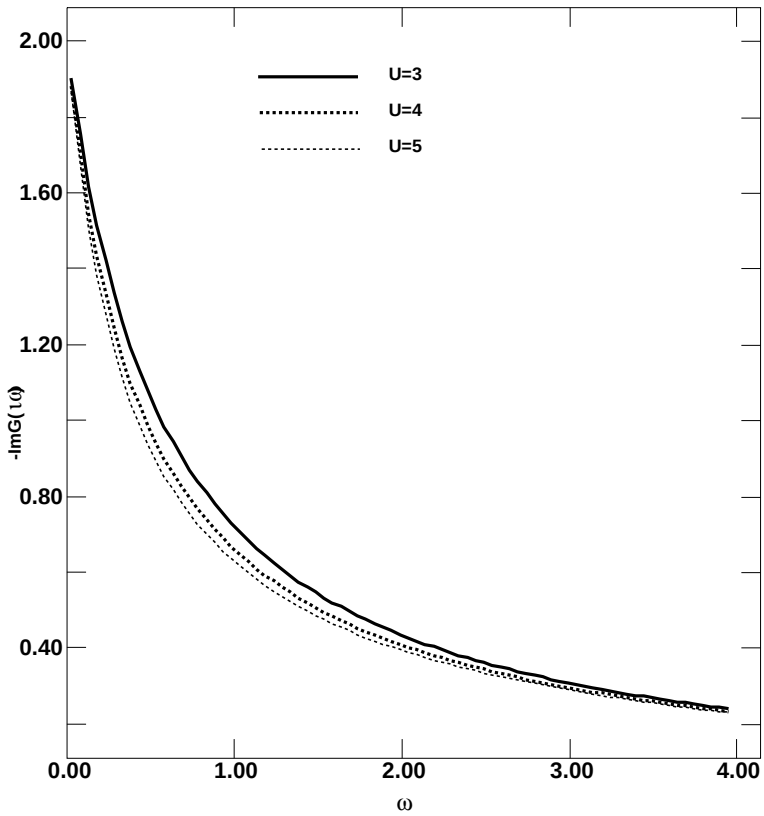

Figure 7.9: Rescaled Matsubara Green $-ImG(i\omega_n)$ at infinitesimal hole doping for interactions $U = 3$ (solid line), $U = 4$ (thick dashed line), and $U = 5$ (dotted line). (Projective technique, N=8)

The self-energy is again determined by extracting the singular pieces from

$$\Sigma(i\omega_n) = i\omega_n + \Delta\mu - t^2 G(i\omega_n) - G^{-1}(i\omega_n) \tag{7.43}$$

where $\Delta\mu = \mu - U/2$. The evaluation in this case requires some care, because the real part of $G_{high}(i\omega_n)$ contributing to Σ is finite at zero frequency. Since the frequency dependence is weak, it is sufficient to replace $G_{high}(i\omega_n)$ by its zero frequency value $G_{high}(0)$, which is obtained from the solution of the insulating problem. One thus obtains the rescaled low frequency part of Σ as

$$\tilde{\Sigma}_{low}(i\omega_n) = \Delta\mu - t^2 \tilde{G}_{low}(i\tilde{\omega}_n) - \left(\tilde{G}_{low}(i\tilde{\omega}_n) + G_{high}(0)\right)^{-1}. \tag{7.44}$$

Since the energies are measured with respect to the Fermi level, Luttinger's theorem in this case reads $0 = \mu - \Sigma(0)$. We find that it is obeyed, which provides a non trivial check of the numerical results. As a consequence we moreover notice that the pinning condition $ImG(0^+) = -2/D$ is again fulfilled.

The effective spin-spin coupling between the f_σ-electron and the bath decreases as the interaction increases, as can be seen from Fig. 7.10. This can be understood by plotting the coefficients J_{pot} and J_{spin} as functions of the interaction, which is shown in the inset of Fig. 7.10. We see that while the exchange term J_{spin} remains essentially unaltered as the interaction increases, J_{pot} varies strongly, indicating enhanced potential scattering. (Note, however, that again we expect the values of J_{spin} and J_{pot} to be corrected downward (to larger negative values) as discussed. This does not change the qualitative argument.) The results are in qualitative agreement with the $2 + 1$ approximation given in Eq. (7.41). Eq. (7.40) then immediately implies a weakening of the spin-spin coupling between impurity and bath electrons $\langle \vec{S} \cdot \vec{s}_L \rangle$ for increasing values of the interaction. This can be understood as being the result of the increasing repulsion between impurity and bath electrons due to the potential scattering term. Notice, however, that even for large values of the interaction the system remains in the intermediate coupling regime. (Recall that the result using the exact J_{spin} and J_{pot} for $U = \infty$ yields $\langle \vec{S} \cdot \vec{s}_L \rangle = -0.23$.)

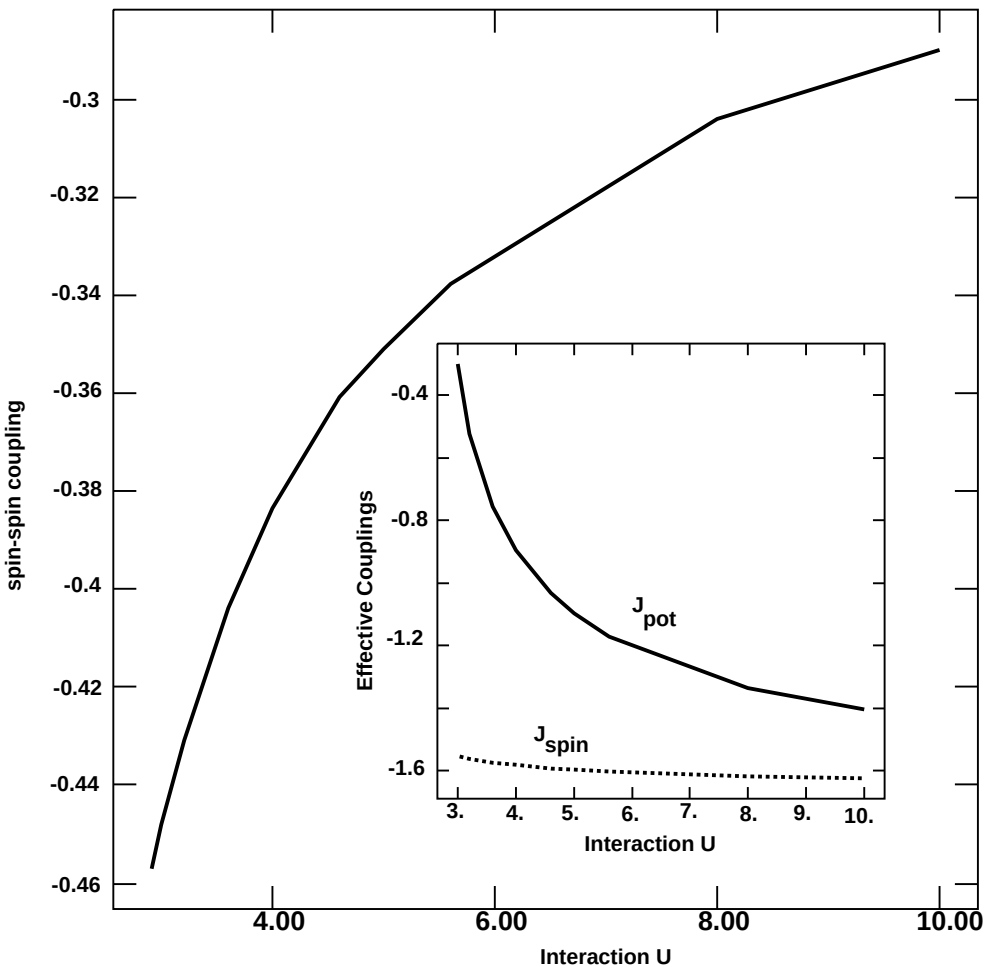

Figure 7.10: Kondo coupling $\langle \vec{S} \cdot \vec{s}_L \rangle$ at the critical point as a function of the interaction U. Inset: J_{spin} and J_{pot} at the critical point as a function of the interaction U.

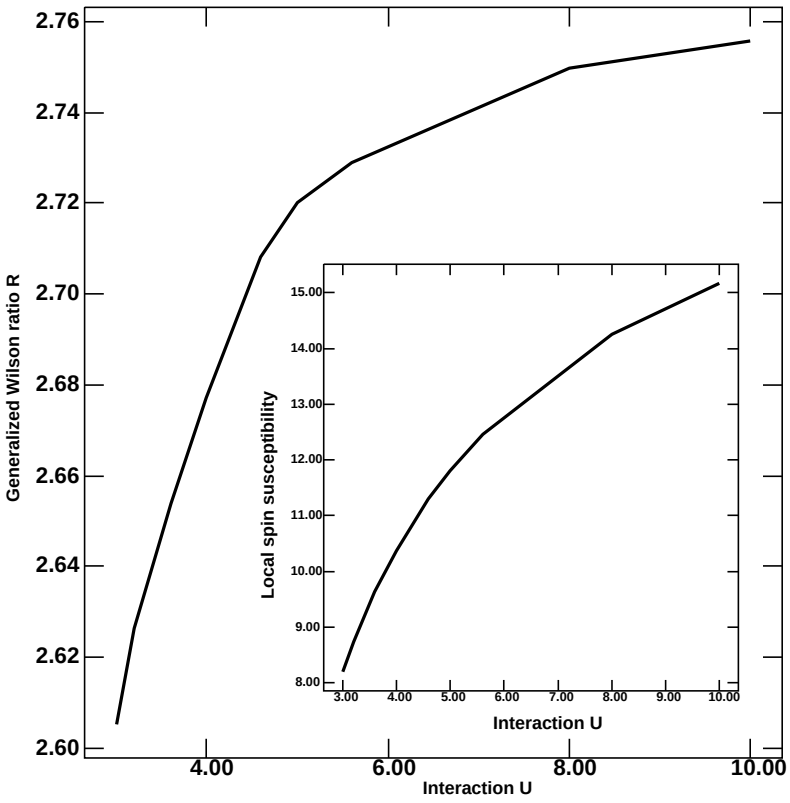

Figure 7.11: Generalized Wilson ratio $\frac{\chi_s/\chi_{s,loc}^{free}}{\gamma/\gamma^{free}}$ as a function of the interaction U. The inset shows the local spin susceptibility $\chi_s^{loc}(0)$ in units of $(g\mu_B/2)^2$.

The generalized Wilson ratio

$$R \equiv \frac{\chi_s/\chi_{s,loc}^{free}}{\gamma/\gamma^{free}} \tag{7.45}$$

as defined in (7.27), where again $\chi_{s,loc}^{free} = \frac{16}{3\pi}(\frac{g\mu_B}{2})^2$, grows slightly as the interaction increases as shown in Fig. 7.11 and goes to the asymptotic value (using the exact $J(U=\infty)$ result) $R = 2.77$. This can be attributed to the fact that coefficient of the divergent term of the local spin susceptibility grows faster that the corresponding term in effective mass of the quasiparticles.

Finally, the ratio of A/γ^2 in $\rho(T) = AT^2$ is again given by Eq. (7.35) as

$$\frac{A}{\gamma^2} = 7.9\left(\frac{\partial^2\tilde{\Sigma}}{\partial\tilde{\omega}^2}/(\frac{\partial\tilde{\Sigma}}{\partial\tilde{\omega}})^2\right)4.1\times10^3 a\ (\Omega m) \tag{7.46}$$

where a is the lattice spacing in meters. It is found to decrease with increasing U as shown in Fig. 7.12 which is as a result of enhanced scattering between the electrons. The

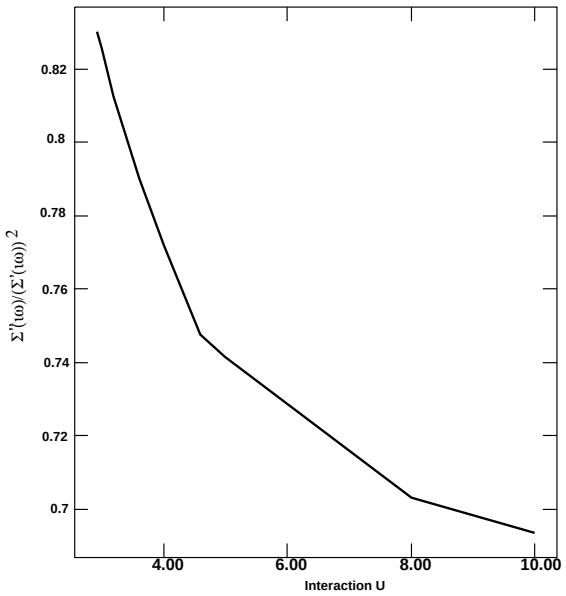

Figure 7.12: Ratio of $\frac{\partial^2\bar{\Sigma}}{\partial\bar{\omega}^2}/(\frac{\partial\bar{\Sigma}}{\partial\bar{\omega}})^2|_{\bar{\omega}=0}$ for infinitesimal doping as a function of the interaction U.

asymptotic value using the exact $U = \infty$ values of J is given as $\Sigma(i\omega)''/(\Sigma(i\omega)')^2 = 0.67$. It should be pointed out that since the coefficients in the series expansion of the self-energy are obtained by a fitting procedure, the results, especially of A/γ^2 have a large error of order 20%.

7.3 The Approach to the Critical Point

7.3.1 Once Again: Analysis of the Toy Model

Having obtained the critical properties, we can now proceed by analyzing the approach to the critical point at half filling, i.e. solve the full non-linear equations derived in the previous chapter. In order to elucidate the procedure, let us once again analyze the toy model introduced when we investigated the critical point. As discussed, the two modifications of the analysis when considering properties away from half filling arise from the fact that we have to include higher order contributions from the canonical transformation to the Hamiltonian, as well as modify the high energy spectral weight entering Γ to order w. Since we only have one site at zero energy we do not obtain any contributions due to the expansion of energy denominators to order w. Again the

calculation can be found in the appendix. The Hamiltonian to order w^2 is given as

$$\mathcal{H}_{eff}^{toy} = -4(V/D)^2\Gamma(1-4\Gamma^2)\vec{S}\cdot\vec{s} \tag{7.47}$$

and the transformed operator as

$$F_\sigma = -(V/D)\Gamma\left[\left((1-\frac{9}{2}\Gamma^2(V/D)^2)(X_{\sigma\sigma}-X_{\bar{\sigma}\bar{\sigma}})c_\sigma + 2X_{\bar{\sigma}\sigma}c_{\bar{\sigma}}\right) - 3\Gamma^2(V/D)^2(2n_\downarrow - 1)c_\uparrow\right]. \tag{7.48}$$

We readily compute the Green function which now reads

$$G_{low}(i\omega_n) = \frac{9\Gamma^2(V/D)^2}{2}(1-11\Gamma^2(V/D)^2)(\frac{1}{i\omega - E_{gs}} + \frac{1}{i\omega + E_{gs}}). \tag{7.49}$$

leading to a the self-consistency equation

$$1 = \frac{9}{4}\Gamma^2(1-11\Gamma^2(V/D)^2). \tag{7.50}$$

which determines the low energy spectral weight $w = 4V^2/D^2$ as a function of the interaction. In addition to this non-linearity, the modification of the upper and lower Hubbard bands due to the presence of the resonance leads to a modification of Γ. In the value of Γ as obtained from the $2+1$ insulator which was given as $\Gamma = \frac{2D}{U}(1+\frac{6V_{high}^2}{U^2})$, we now have to use the high energy spectral weight corrected to order w. Using the spectral sumrule this leads to $V_{high}^2 = \frac{D^2}{8}(1-4(\frac{2V}{D})^2)$. We can use this expression in Eq. (7.50). Expanding to order V^2 we get the spectral weight near the critical point as a function of the interaction as

$$w^{toy} = 0.52(U_c - U)/D + o((U_c - U)/D)^2. \tag{7.51}$$

Again this compares quite well with the result obtained in the four boson scheme [32, 81] which is given as $w^{4Boson} = \frac{3\pi}{16}(U_c - U)/D = 0.59(U_c - U)/D$.

7.3.2 Approach to the Critical Point at Half-filling

The full numerical treatment of the problem using the by now familiar Lanczos diagonalization proceeds as outlined in the previous chapter. We extract the information about the high energy bands from the solution to the full Hubbard model. Since the fourth oder terms in the Hamiltonian contain higher order correlation functions we have

to resort to exact diagonalization to obtain the high energy parameters entering the Hamiltonian. This constrains the number of sites representing the high energy bands to $4+1$. (Note that at criticality we only need to evaluate resolvent operators to obtain the coefficients entering the low energy Hamiltonian. This can be done easily using the continued fraction expansion.) A comparison of the results obtained from three and five sites in the upper band, together with six and eight in the effective low energy Hamiltonian, which is shown in Fig. 7.13 indicates that this is essentially converged. Another indication comes from the fact that the quasiparticle weight extrapolates to the correct critical U_c, which is obtained with $8+1$ sites in the high energy bands and $9+1$ sites at low frequencies.

The result obtained numerically for $4+1$ sites in the high energy part and $7+1$ sites in the low frequency region as shown in Fig. 7.13 is given as

$$w = 0.34(U_c - U)/D. \tag{7.52}$$

with $U_c = 2.92$. Since once again we have to fit the data in order to obtain the slope, the error bar is unfortunately of the order 20 percent.

Note that in this case quasiparticle residue $z = 1/(1 - \frac{\partial \Sigma}{\partial \omega})$ and low energy spectral weight w do *not* coincide. This is in striking contrast to the Gutzwiller approximation which does not distinguish between the two. The quasiparticle residue as a function of the interaction is given as

$$z = 0.2(U_c - U)/D. \tag{7.53}$$

with $U_c = 2.93$. While the slight disagreement between the critical interaction is clearly due to numerical inaccuracies, the slope of the quasiparticle residue is strikingly smaller than the corresponding quantity for the weight of the resonance. A comparison of the results for w and z is shown in Fig. 7.14.

7.3.3 Approach to the Critical Point Away from Half-filling

Let us conclude this chapter by discussing the properties close to the critical point in the doped Hubbard model. Since this is a situation which has been studied experimentally [100] we can compare our results for A/γ^2 directly to measured values in $Sr_{1-x}La_xTiO_3$.

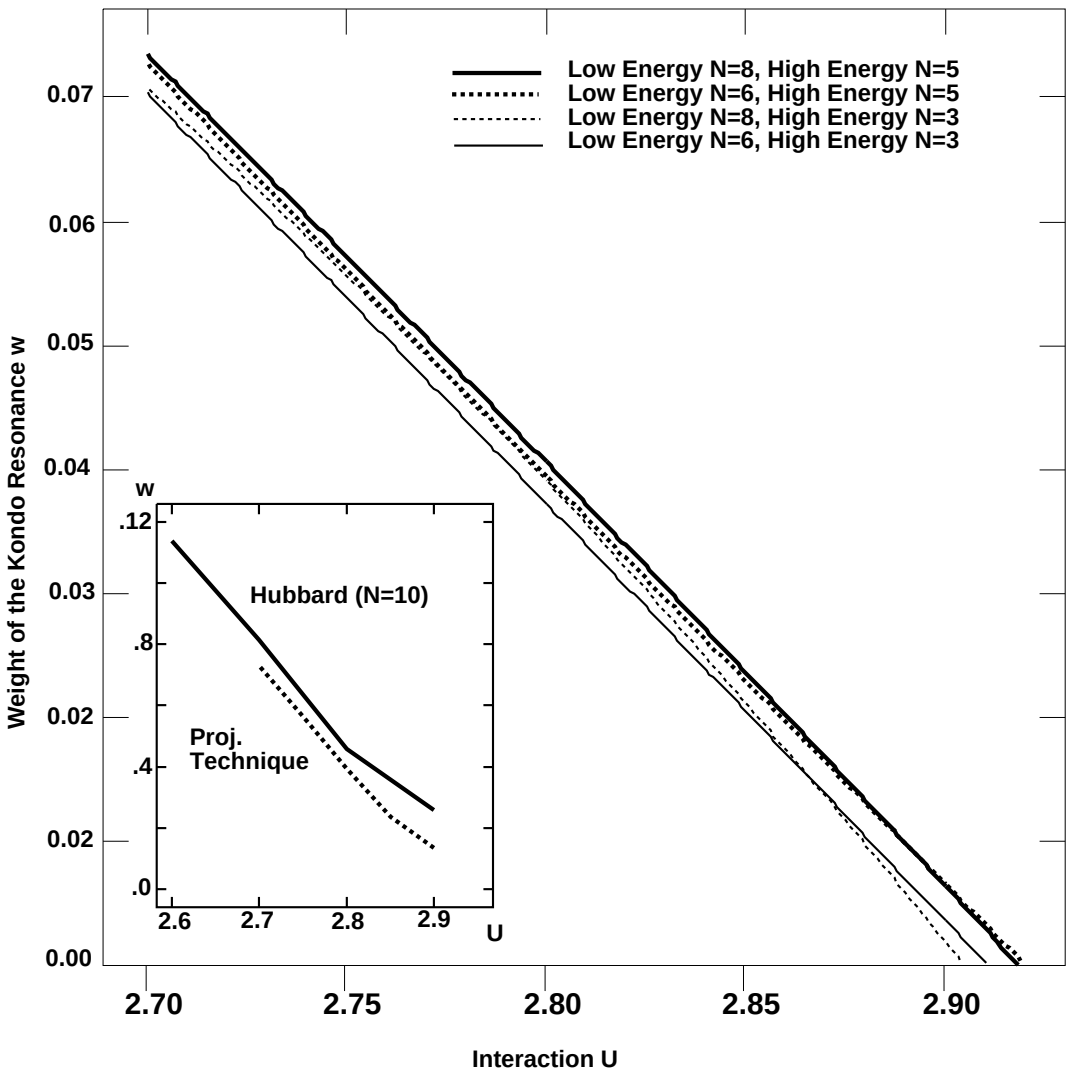

Figure 7.13: Quasi-particle weight near the Mott transition at half-filling as obtained using the self-consistent projective technique. Shown are the results for clusters of N=6 and 8 sites in the low frequency region as well as 3 and 5 sites at high frequencies. The inset shows the low energy spectral weight as obtained from the full Hubbard model with 10 sites in comparison with the result from the self-consistent technique using N=8 (low en.) and N=5 (high en).

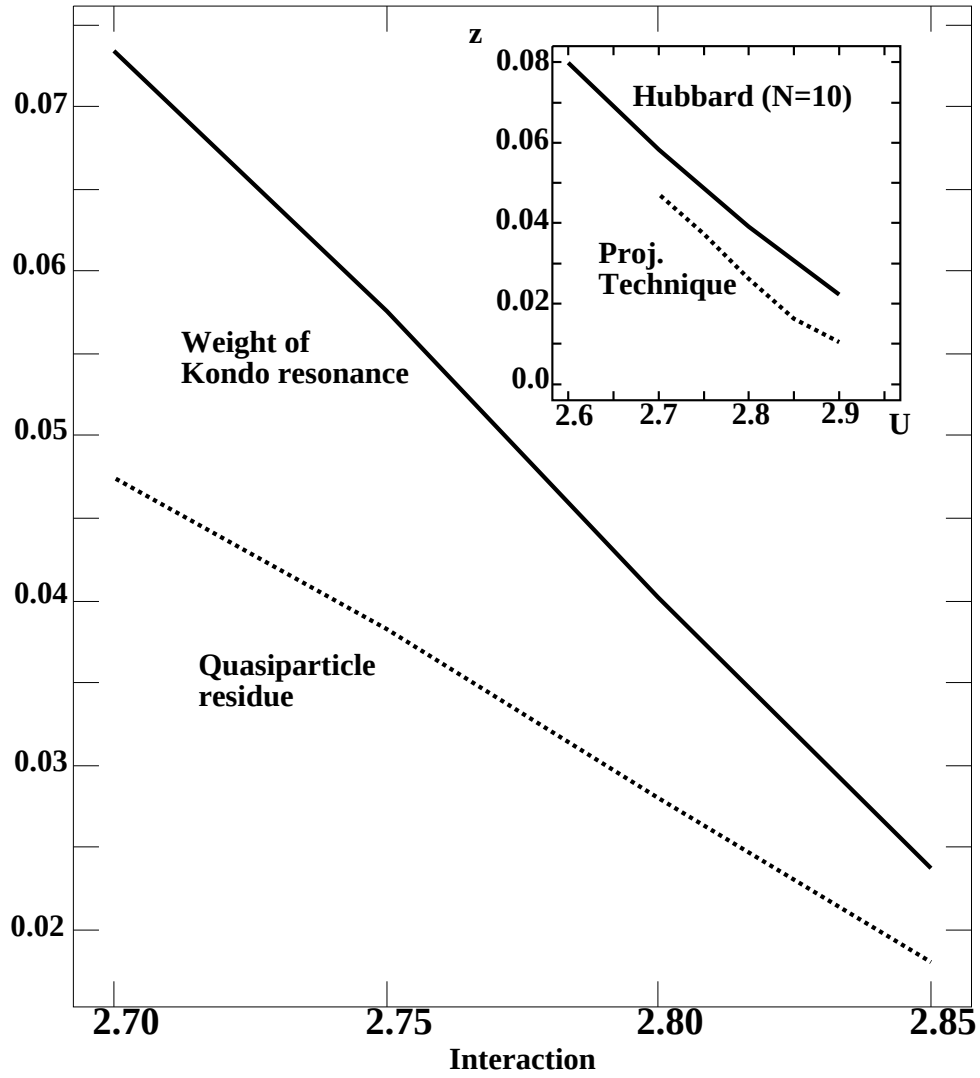

Figure 7.14: Low energy spectral weight w (thick line) and quasiparticle residue z (dotted line) near the Mott transition at half-filling as obtained using the self-consistent projective technique. Shown are the results for the cluster with N=8 sites in the low frequency region and N=5 sites at high frequencies. The inset shows the quasiparticle residue z as obtained from the full Hubbard model with 10 sites in comparison with the result from the self-consistent technique using N=8 (low en.) and N=5 (high en).

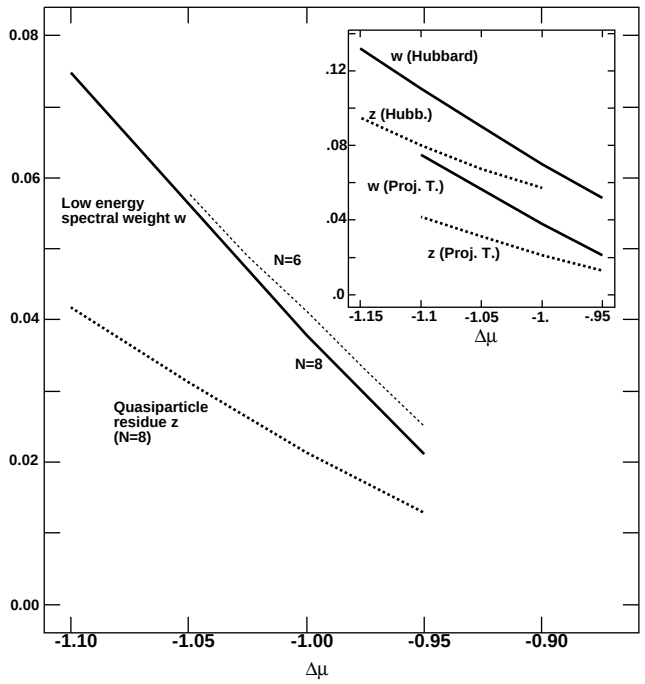

Figure 7.15: Low energy spectral weight w (thick line) and quasiparticle residue z (dotted line) near the Mott transition for $U = 4$. (Self-consistent technique, $N = 6$ and $N = 8$ at low energies, $N = 5$ at high energies.)

Following the same procedure as in the half-filled case, we again obtain low-energy spectral weight w and quasiparticle residue z close to the transition. For interaction $U = 4$ these are depicted in Fig. 7.15. While the convergence for $N = 6$ and $N = 8$ sites is not as good as at half-filling, which may be attributed to the fact that the separation of scales is considerably smaller, both extrapolate within one percent to the correct μ_c. This provides a check of the calculation. The curves depicted can by fitted as

$$w(U = 4) = 0.36(\Delta\mu_c - \Delta\mu)/D \tag{7.54}$$

and

$$z(U = 4) = 0.2(\Delta\mu_c - \Delta\mu)/D, \tag{7.55}$$

respectively with $\Delta\mu_c = -0.89$. Since z determines the low energy scale of the problem, the small prefactor leads to a small low energy region, as we shall see in the analysis of the finite temperature behavior.

Moreover, we can obtain the self-energy in form of a power series by fitting the numerical results. The ratio A/γ^2 can then be obtained as outlined in Eqs. (7.31 -

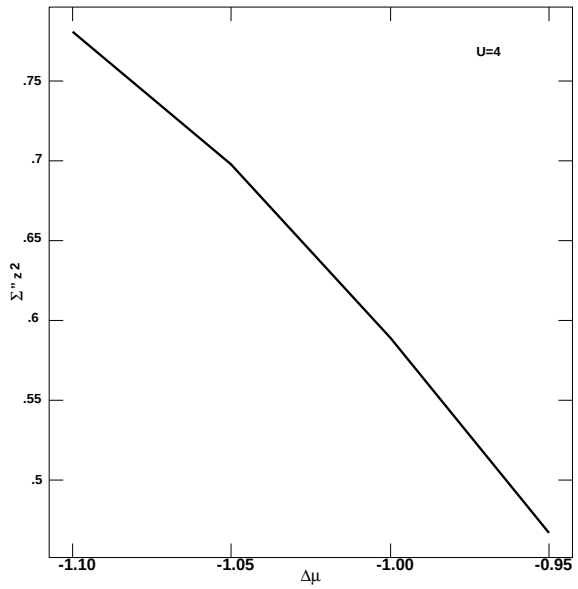

Figure 7.16: $\Sigma''(\omega = 0)z^2$ near the critical point for $U = 4$. (Self-consistent technique, $N = 8$ at low energies, $N = 5$ at high energies.)

7.35) and is given as

$$A/\gamma^2 = 7.9 z^2 \frac{\partial^2 \Sigma}{\partial \omega^2} 2.05 \times 10^3 a \ (\Omega m). \tag{7.56}$$

The ratio $z^2 \frac{\partial^2 \Sigma}{\partial \omega^2}$ is shown in Fig. 7.16 for interaction $U = 4$. While this does not approach the correct value for infinitesimal doping, they are of the same order of magnitude. The difference can be attributed to the large error in the determination of the second derivative of Σ, as well as the fact that we do not consider rescaled quantities in the case close to half filling which leads to additional inaccuracies. Since the experiments on $Sr_{1-x}La_xTiO_3$ [100] quoted earlier were done on doped samples, we can now improve our comparison to experiments. To lowest order the doping is given by the low energy spectral weight. For $w = 0.05$ we obtain, using the lattice spacing $a = 8.3 \times 10^{-10} m$ [99], $A/\gamma^2 = 9 \cdot 10^{-6} \Omega m$. This can be directly compared to the experimental value with $x = 0.05$ which is found to be $A/\gamma^2 = 6.4 \cdot 10^{-6} \Omega m$. Again this is of the same order of magnitude, and the correction to A/γ^2 due to finite doping goes in the right direction. Notice furthermore that the functional form is in qualitative agreement with the results obtained by Tokura et al..

This concludes the analysis of the critical point, as well as the approach to it. For

the first time we obtained quantitative results and insights into the critical region of the Hubbard model and evaluated scaling functions, as well as susceptibility, specific heat, transport time and low energy spectral weight. The results can be compared to experimental results on $Sr_{1-x}La_xTiO_3$ and are of the same order of magnitude.

Chapter 8

The Hubbard Model at Finite Temperatures

In the previous chapters we focused on the properties of the Hubbard model at zero temperature. In order to address some of the most intriguing experimental results on materials whose electronic behavior is dominated by strong correlations, in particular the unconventional normal state properties of the high T_c-oxide superconductors [102], a finite temperature formalism that is able to yield reliable low temperature results is necessary.

So far, most of the finite temperature calculations for the Hubbard model in infinite dimensions were obtained using Monte Carlo algorithms in combination with maximum entropy methods in order to obtain real frequency data from the Monte Carlo results [20, 97, 103, 104]. These were supplemented by results obtained from the finite U non-crossing approximation (NCA) [33]. Unfortunately, both methods are faced with systematic problems. As discussed, the Quantum Monte Carlo technique fails at low temperatures, and even a tool as sophisticated as the maximum entropy method is not able to give a reliable analytic continuation of the data with high resolution. The NCA results on the other hand are known to violate Fermi liquid theorems [105] at low temperatures.

In this chapter we will outline, how the self-consistent approach based on the mapping of the Hubbard model on an Anderson model outlined in Chapter 2 can be implemented efficiently for finite temperatures, and see that in combination with the self-consistent projective technique results at temperatures inaccessible by previous techniques can be obtained. In particular, we will present results for the local susceptibility and the value of the self energy at zero frequency, which at low temperatures essentially gives the inverse quasiparticle scattering rate and is thus directly proportional to the

DC resistivity.

8.1 Numerical Implementation

Let us briefly discuss some technical aspects regarding the implementation of the finite temperature formalism. As we saw in Chapter 2 the determination of zero temperature Green function and local susceptibility solely required knowledge of the exact ground state and ground state energy of the Hamiltonian under consideration which can be obtained easily using Lanczos diagonalization. Both correlation functions could then be obtained easily using a continued fraction expansion.

In the finite temperature case, the Green function is given by the trace over *all* eigenstates of the system as

$$G_\sigma(i\omega_n) = \frac{1}{Z}\int_0^\beta e^{i\omega_n\tau} trace\Big(e^{-\beta H}\mathcal{T}_\tau f_\sigma(\tau) f_\sigma^\dagger(0)\Big) \tag{8.1}$$

where $\omega_n = \frac{2\pi}{\beta}(2n+1)$ are Matsubara frequencies with $\beta = 1/T$ and $Z = \sum e^{\beta E_n}$ is the partition function. One therefore can no longer resort to Lanczos diagonalization, but has to diagonalize the full Hamiltonian matrix exactly. This limits the system sizes that can be diagonalized easily on a workstation (i.e. using the Numerical Recipes [68] routines TRED2 and TQLI) to a maximum of $N = 6$ sites.

While one can calculate the correlation functions exactly in terms of the matrix elements $|\langle n|f_\sigma^\dagger|m\rangle|^2$ ($\{|n\rangle\}$ are the eigenvectors of the system with corresponding eigenenergies $\{E_n\}$),by inserting complete sets of eigenstates in Eq. (8.1) the basis transformation necessary to evaluate the matrix elements is of order N^4. Thus even for $N = 6$, for which the largest blockmatrix in the Hamiltonian (using S_z and particle number as quantum numbers) has 400×400 elements, this basis rotation is extremely time consuming. The calculation can be simplified by writing the Green function in the form

$$\begin{aligned} G_\sigma(i\omega_n) &= \frac{1}{\tilde{Z}}\sum_m e^{-\beta(E_m - E_{gs})} \otimes \\ &\Big(\langle m|f_\sigma \frac{1}{i\omega_n - (H - E_m)} f_\sigma^\dagger|m\rangle + \langle m|f_\sigma^\dagger \frac{1}{i\omega_n + (H - E_m)} f_\sigma|m\rangle\Big) \end{aligned} \tag{8.2}$$

where in order to avoid numerical problems all energies are measured with respect to the ground state energy E_{gs} and where we have defined $\tilde{Z} = \sum e^{\beta(E_n - E_{gs})}$. We see that for a given temperature only the eigenstates up to a cutoff E_{cut} where $E_{cut} - E_{gs} \approx T$ enter. This greatly reduces the number of states that need to be stored and the number of contributions that needs to be evaluated. Furthermore, we can evaluate the particle and hole contributions to the correlation function using a continued fraction expansion (now based on the states $f_\sigma^\dagger|m\rangle$ and $f_\sigma|m\rangle$) as done at zero temperature, and summing over the relevant contributions.

In order to obtain the local susceptibility at zero frequency, some care has to be taken in order to treat the term leading to Curie-Weiss behavior (which is cut-off at low temperatures) properly. From the definition of χ_s

$$\begin{aligned}\chi_s(i\nu_n) &= (g\mu_B/2)^2 \frac{1}{\tilde{Z}} \sum_m e^{-\beta(E_m - E_{gs})} \otimes \\ &\left(\langle m|S_z \frac{1}{i\nu_n - (H - E_m)} S_z|m\rangle - \langle m|S_z \frac{1}{i\nu_n + (H - E_m)} S_z|m\rangle \right) \quad (8.3)\end{aligned}$$

where $i\nu_n$ are Bose frequencies and $S_z = \frac{1}{2}(n_\uparrow - n_\downarrow)$ one readily obtains

$$\begin{aligned}\chi_s(0) &= (g\mu_B/2)^2 \left(\frac{2}{\tilde{Z}} \sum_{\substack{m,n \\ E_n > E_m}} e^{-\beta(E_m - E_{gs})} |\langle n|S_z|m\rangle|^2 \frac{1 - e^{-(E_n - E_m)}}{-(E_n - E_m)} \right. \\ &+ \left. \frac{1}{\tilde{Z}} \sum_m e^{-\beta(E_m - E_{gs})} |\langle m|S_z|m\rangle|^2 (\frac{-1}{T}) \right). \quad (8.4)\end{aligned}$$

This can be evaluated efficiently, since S_z only connects states within the subspaces of fixed particle number and spin along the z axis.

Proceeding in this way it is possible to obtain converged solutions [1] for the full Hubbard model down to temperatures as low as $T = 0.02$. This is already of the order of the lowest temperatures that can be attained using the much more "expensive" Quantum Monte Carlo method. Combining the method with the self-consistent projective

[1] The question of convergence can be judged and measured using two different criteria. On one hand, the results should be such that they do not change as the number of sites in the system is increased. This is a reliable method if large system sized can be compared, as in the zero temperature calculations of the previous chapters. In the case of finite temperatures the corresponding statistics is rather poor, since only small systems can be considered. An alternative criterion is given by comparing the lowest frequencies of the "true" full Green function to the fitted Green function. If the temperatures used are too small, the fits are extremely inaccurate at low frequencies, indicating a breakdown of the approximation.

technique, temperatures at least as low as $T \approx \frac{1}{5}T_{Kondo}$ where T_{Kondo} is the width of the quasiparticle resonance can be achieved. This is beyond the reach of any other present method.

8.2 Results

As indicated in the introduction to the chapter, we are primarily focusing on the local susceptibility and the DC conductivity as determined from the quasiparticle scattering given by $Im\Sigma(0)^{-1}$.

At half filling the system remains a Fermi liquid at low temperatures in agreement with the results obtained using NCA and QMC [97, 104]. This can be seen particularly clearly in Fig. 8.1 which shows extrapolated value of $\Sigma(0)$ for the interaction $U = 2.5$. The plot shows the results obtained from the full Hubbard model with $N = 6$ (thick dashed line), which clearly break down for low temperatures (in this case $T \approx 0.007$), together with the results from the self-consistent projective technique (solid line) which breaks down for higher temperatures ($T = 0.008$). Clearly the self-consistent projective technique enables us to reach considerably lower temperatures ($T = .003$). The plot shows the results using $N = 5+1$ sites representing the Kondo resonance and $N = 4+1$ representing the high energy bands. It should be noted that going below these cluster sizes gives results which do not "connect" to the results obtained using the Hubbard model. Here, however, both techniques have a clear, although small, range in which they overlap. This provides a check of the self-consistent technique. Also shown (dotted line) is a fit of the data obtained from both methods. We see that the data can be fitted by the functional form

$$\Sigma(\omega = 0, T) = 3T + 1450T^2. \tag{8.5}$$

Since the quadratic term is dominant in the temperature range shown, this can be considered in good agreement with the Fermi liquid prediction

$$Im\Sigma(\omega = 0, T) \sim \rho(T) = AT^2. \tag{8.6}$$

Due to the fact that in the half filled case metallic and insulating solutions are extremely close in energy (as we saw in Chapter 7 the energy difference goes as $(U_c - U)^2$) we

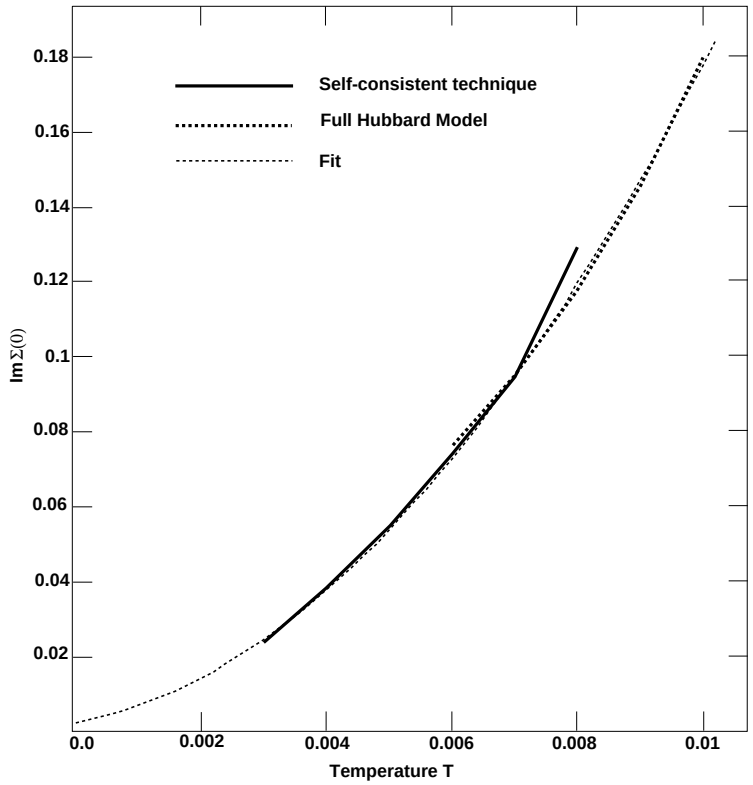

Figure 8.1: Inverse quasiparticle scattering rate $\Sigma(\omega = 0, T)$ as a function of temperature in the half filled Hubbard model for interaction $U = 2.5$. Shown are the results obtained using the full Hubbard model with N=6 (thick dashed line) and the self-consistent projective technique (thick line) with N=6 (resonance) plus N=5 (high energy). The thin dashed line is obtained by fitting the data.

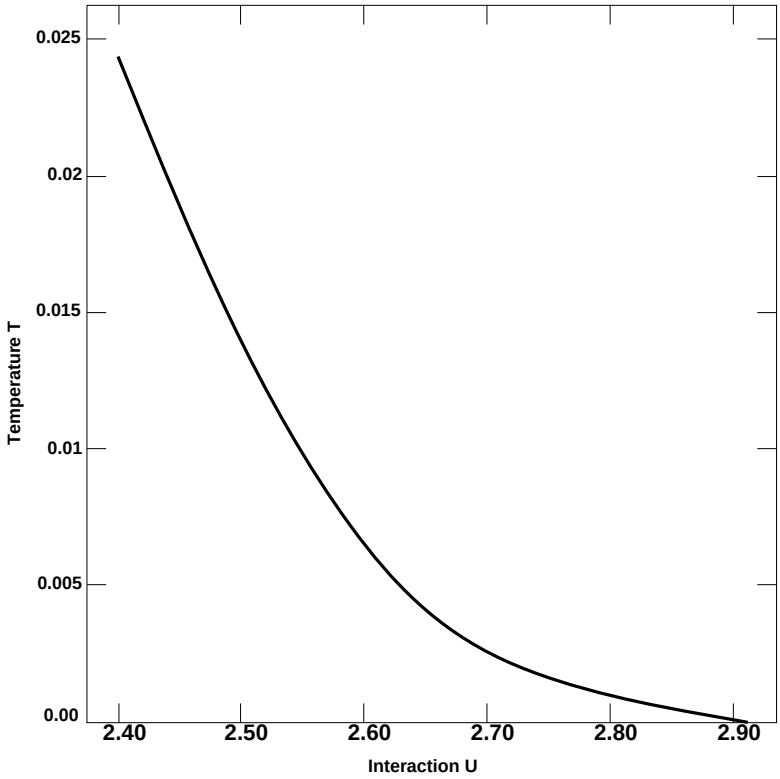

Figure 8.2: Transition temperature of the first order metal-insulator transition at half filling as a function of the interaction.

cannot reach higher temperatures than $T \approx 0.01$. Beyond this temperature the system becomes insulating even at interactions as low as $U = 2.5$.

This first order transition occurs for even lower temperatures as the interaction is increased and prevents us from comparing full and projectively obtained results for higher values of U. The corresponding phase boundary is shown in Fig. 8.2. This is to be compared with the results from second order perturbation theory [12], which gives considerably higher transition temperatures.

In order to obtain results at finite doping, care has to be taken in order to keep the particle number fixed, since the dependence of the particle number n_σ on temperature (for fixed μ) is quite strong. Results for $U = 4$ and some typical values of μ are shown in Fig. 8.3. Notice that this strong temperature dependence is in striking contrast to the T^2 behavior expected in a regular Fermi liquid and indicates the presence of a small energy scale beyond which Fermi liquid theory is restored.

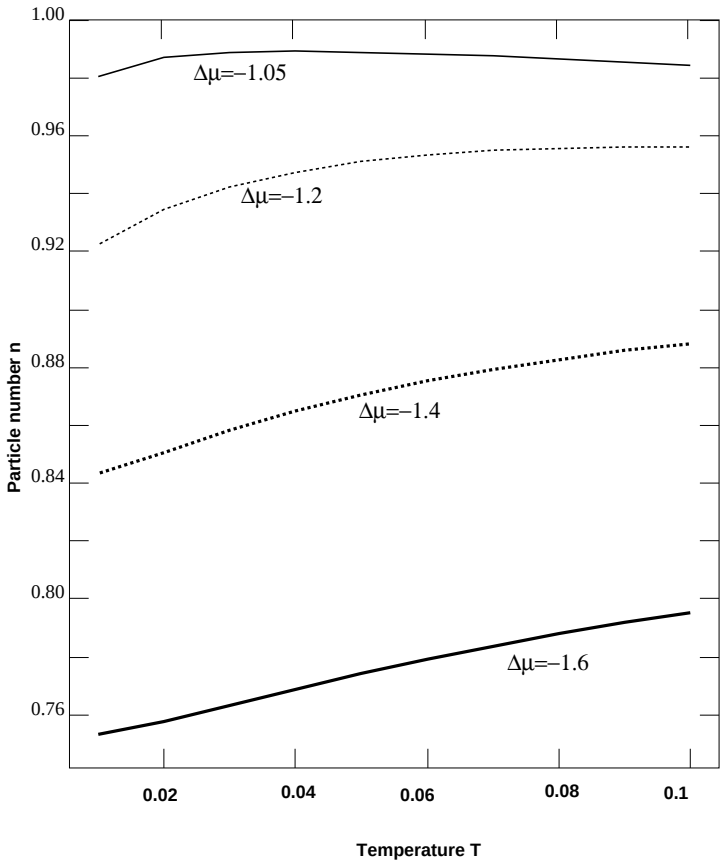

Figure 8.3: Particle number per site as a function of temperature for $U = 4$ and $\Delta\mu = -1.05, -1.2, -1.4$, and -1.6 using $N = 5 + 1$ cluster, exact diagonalization.

The consideration of the temperature dependence of the spectral function as shown in Figure 8.4 gives similar indications. In the figure we see the spectral density $-ImG(\omega + i\delta)$ at $U = 4$ and $n = 0.9$ for temperatures $T = 0.02, 0.06$ and 0.1. We see that the weight of the Kondo resonance at the Fermi level is reduced washed out quite rapidly as the temperature is increased, again indicating an underlying small energy scale.

The imaginary part of the self energy, $Im\Sigma(\omega = 0, T)$ exhibits a pronounced and extended linear region down to temperatures $T = 0.02$ (we used the full Hubbard code in this case). The results using the full Hubbard code are displayed in Fig. 8.5. For small doping and small temperatures one can use the self-consistent projective technique, which indicates that Fermi liquid behavior, i.e. a T^2 behavior of $\Sigma(T)$, does occur at very low temperatures. The result for $U = 4$ and $\Delta\mu = -1.05$, which corresponds to a doping of $\delta = 0.05$, is shown in Fig. 8.6. Figure 8.7 shows the local spin susceptibility $\chi_s(\omega = 0, T)$ as a function of temperature at dopings between $\delta = 0.1$ and $\delta = 0.4$ for a typical value of the interaction in the doped insulator, $U = 4$. Also shown are the non-interacting susceptibilities for the corresponding values of δ. Clearly, the local susceptibility $\chi_{loc}(T)$ is strongly enhanced compared to the non-interacting values and displays a strong rise down to temperatures as low as $T = 0.02$ and is cut-off only for temperatures lower than this. As in the quasiparticle scattering rate we thus find that the low temperature properties are determined by a *small energy scale*. This is not immediately obvious, since the naive expectation is that the smallest energy scale in the problem is given by δD. An understanding of the nature of this scale can be obtained from the toy $2 + 1$ Anderson model discussed in the appendix. Using the exact eigenstates and eigenenergies derived there it is possible to calculate the low temperature susceptibility analytically. Treating the doubly degenerate terms leading to the Curie like $1/T$ behavior with care one can show that the low temperature behavior of the susceptibility goes as

$$\chi(T) \approx C\frac{1 - e^{-\beta V^2/\mu}}{V^2/\mu} \tag{8.7}$$

where V^2 is the hopping between the impurity and the site at the Fermi level and

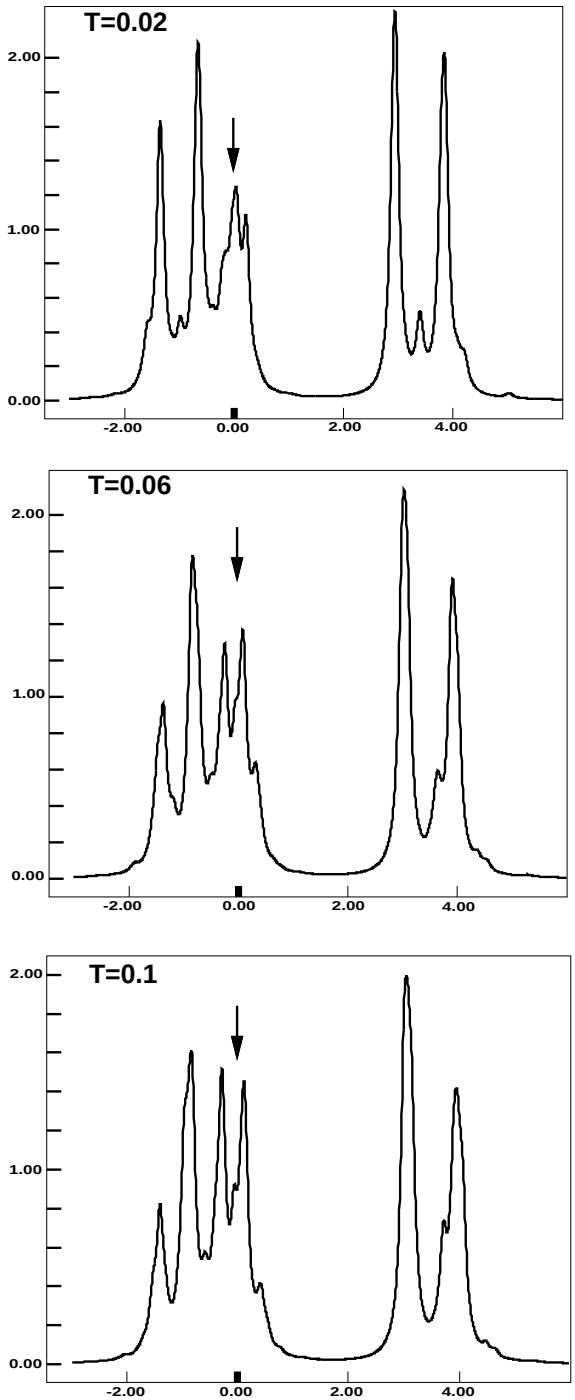

Figure 8.4: Single particle density of states $-ImG(\omega + i\delta)$ for $U = 4$ and $n = 0.9$ at temperatures $T = 0.02$, 0.06, and 0.1. $N = 5 + 1$ cluster, exact diagonalization, $\delta = 0.075$.

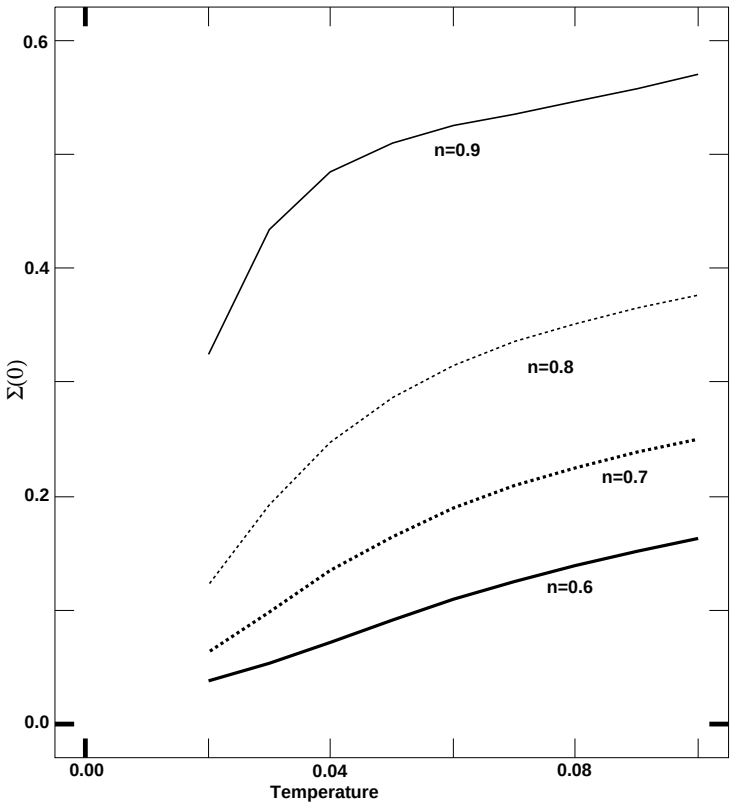

Figure 8.5: Inverse quasiparticle scattering rate $Im\Sigma(\omega = 0, T)$ as a function of temperature in the Hubbard model for interaction $U = 4.0$ and particle concentrations $n = 0.600$, $n = 0.698$, $n = 0.800$ and $n = 0.899$. From Hubbard with N=5+1 sites.

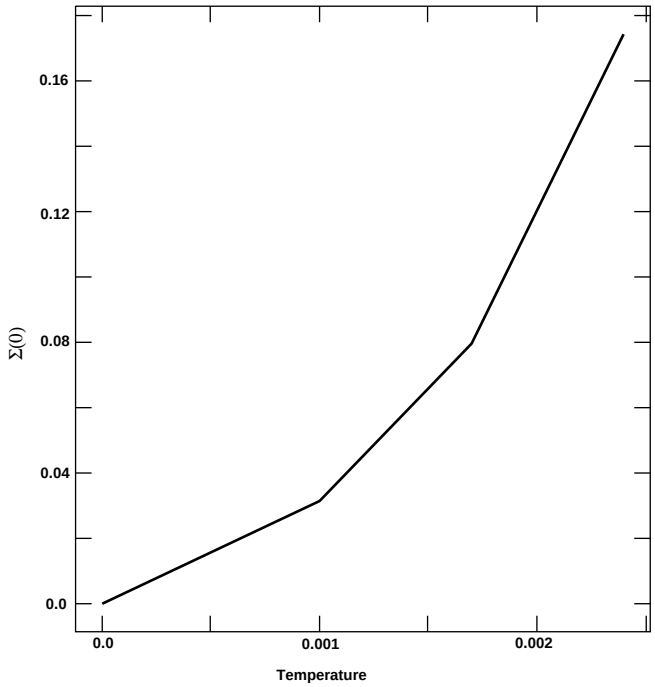

Figure 8.6: Inverse quasiparticle scattering rate $Im\Sigma(\omega = 0, T)$ as a function of temperature in the Hubbard model using the self-consistent projective technique (N=8 at low en., N=5 at high energies) for interaction $U = 4.0$ and $\mu = -1.05$ ($n \approx 0.95$).

V^2/μ is the energy difference between the singlet ground state and the doublet states with one particle removed. The low energy cutoff is thus given as V^2/μ. When solved self-consistently, even in this naive approximation correctly gives $T = 0.02$ as cutoff and therefore explains the results displayed in Figs. 8.7 and 8.5. This result can be confirmed by considering the corresponding quantity, given as $E^{N-1}_{doublet} - E^N_{gs}$ in the solution to the full problem, which is seen to yield the correct cutoff. Equivalently, this can be understood as the result of the small quasiparticle residue z as seen in the analysis of the approach to the critical point at finite doping.

In conclusion we have illustrated that exact diagonalization in combination with the self-consistent projective technique is an ideal tool to study strongly correlated electron systems at low temperatures. We see that due to the small energy scale given by the quasiparticle residue zD, resistivity as well as local susceptibility are linear down to very low temperatures and that the particle number is strongly temperature dependent.

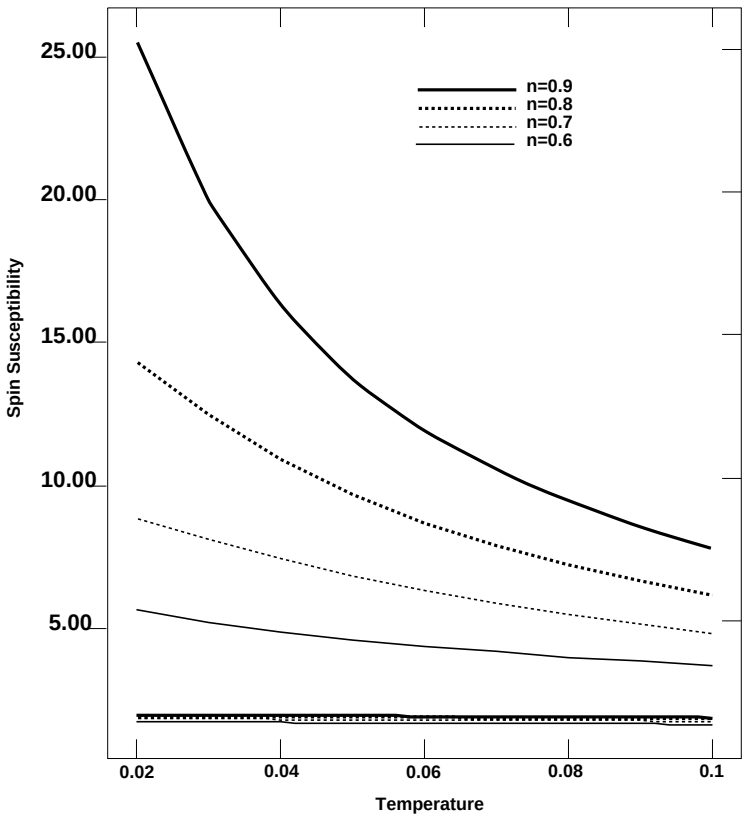

Figure 8.7: Local susceptibility $\chi_s(\omega = 0, T)$ as a a function of temperature in the Hubbard model for interaction $U = 4.0$ and particle concentrations $n = 0.600$, $n = 0.698$, $n = 0.800$ and $n = 0.899$. Also shown are the corresponding susceptibilities for $U = 0$.

Chapter 9

Beyond Infinite Dimensions—A Cluster Approach

In the previous chapters we have outlined, how the limit of infinite dimensionality provides a natural mean-field theory for itinerant many-body systems. We have applied it to the study of the Falicov-Kimball and Hubbard models and seen that it provides an intuitive and systematic framework for their study that yields experimentally relevant information. We have proceeded by developing a method to systematically study the low energy behavior of these models, providing us with a tool to study more realistic systems.

In spite of the successes of the $d = \infty$ mean-field approach, several questions are left unanswered and important physical effects cannot be addressed straightforwardly in the infinite d framework. The locality inherent in this formulation leads to the "pinning" of the density of states at the Fermi level [46], which is likely to be an artifact of mean-field theory. More precisely, this effect can be directly traced to the momentum independence [44] of the local self-energy, reflecting the lack of spatial correlations. In the context of strongly correlated, but weakly disordered systems [106, 51], the pinning condition was shown to result in a discontinuous jump of the DC conductivity at $T = 0$ – the minimum metallic conductivity. If the pinning is relaxed, it is conceivable that a continuous behavior of the conductivity would follow, thus qualitatively modifying our picture of transport near the metal-insulator transition [108].

Moreover, since the limit of infinite dimensions is based on the mapping onto a single-site (impurity) model, it cannot properly account for the competition between the Kondo effect and the spin-spin correlations between neighboring sites – the effect that we have argued is crucial in a number of physical situations. This is particularly bothersome, since the competition between the Kondo effect and the RKKY interactions

is a recurring theme in many of the most interesting phenomena associated with the physics of strong electronic correlations.

When the RKKY interactions predominate, the result is long-range magnetic ordering, as found in many heavy-fermion materials [6]. In situations where magnetic ordering is absent, the manifestations are more subtle, but often equally fundamental. In particular, it has been suggested [107] that this competition lies at the core of the proposed "two-fluid" behavior, and "micromagnetism" found in some non-magnetic heavy fermion systems. Another interesting class of systems where both the Kondo effect and the RKKY correlations are believed to be crucial are exemplified by doped semiconductors [108] near the metal-insulator transition. In these systems, non-Fermi liquid [109, 110] metallic behavior is observed, suggesting the coexistence of local moments and conduction electrons that seem decoupled from each other – another manifestation of the "two-fluid" behavior [111]. There are many further examples where these effects are of key importance. As it stands, the limit of infinite dimensions is not able to treat both the Kondo physics and the RKKY correlations on the same footing and provide a convincing picture of these interesting phenomena.

In order to address the limitations of the existing $d = \infty$ theory, a most straightforward approach would be to investigate systematic $1/d$ corrections resulting from finite dimensionality. Several different methods for performing such expansions have been proposed [106, 51], but each of these approaches result in formidable technical difficulties, making it difficult to address the finite dimensional effects in a simple and elegant fashion as we pointed out in Chapter 2. In this chapter, we take an alternative route: we propose to extend the existing theories *in* $d = \infty$ in a way that mimics the most important physical effects of finite dimensionality. Given the fact that the general large-dimensions philosophy is based on the mapping of a lattice models onto appropriate impurity models, the appropriate impurity model displaying the relevant physics is the two impurity Kondo (Anderson) model [115], which is often used as a simplest model for the study of the RKKY-Kondo competition. Using the methods outlined in Chapter 2 we can obtain a *lattice version* of this model by self-consistently embedding it in an appropriate medium. The resulting model which we call the two-impurity Kondo lattice

model, is the "minimum model" that allows us to go beyond the limitations imposed by the conventional $d = \infty$ approach, without performing uncontrolled or unjustified approximations.

In the rest of this chapter, we define and examine this the model, and indicate how the new features inherent to the RKKY-Kondo competition modify the standard $d = \infty$ results for the Hubbard model which we described in the previous chapters. We conclude that the RKKY interactions represent a *relevant* perturbation, relaxing the pinning condition and qualitatively modifying the nature of the metal-insulator transition.

9.1 The Model

We begin our discussion by defining the model that we consider, and derive the corresponding self-consistency conditions by performing the $d \to \infty$ limit. While the limit of infinite dimensions does not impose any restrictions on the lattice structure studied [53], the equations again become particularly simple and easy to derive in the case of a Bethe lattice. The *qualitative* features of the model will be identical as on other lattices, and the resulting spectral functions are closer to the three dimensional situation than for example on the $d = \infty$ hypercubic lattice. The "minimum model" that we propose is then obtained by *doubling* the Bethe lattice (with hopping t), and allowing the electrons to hop *between* the Bethe lattices with hopping t_{ab}. The geometry of the resulting lattice is shown (for coordination number $z = 3$) in Fig. 9.1. Denoting the creation operators corresponding to the two Bethe lattices with $a^\dagger_\sigma$ and $b^\dagger_\sigma$, the Hamiltonian can be written as

$$\begin{aligned} H &= -t \sum_{<i,j>,\sigma} (a^\dagger_{i\sigma} a_{j\sigma} + b^\dagger_{i\sigma} b_{j\sigma}) + t_{ab} \sum_{i\sigma} (a^\dagger_{i\sigma} b_{i\sigma} + h.c.), \\ &+ U \sum_{i\sigma} (n_{ai\sigma} n_{ai-\sigma} + n_{bi\sigma} n_{bi-\sigma}) - \mu \sum_{i\sigma} (n_{ai\sigma} + n_{bi\sigma}) \end{aligned} \tag{9.1}$$

where U is the Coulomb potential and t is the nearest-neighbor hopping amplitude; t_{ab} is the hopping amplitude between the two lattices.

It should be stressed at this point that this model clearly breaks translational invariance by singling out *pairs* of sites connected by hopping elements t_{ab}. While this feature

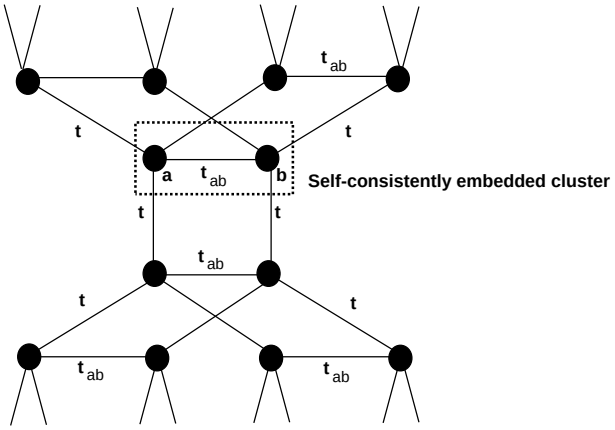

Figure 9.1: Lattice structure of the doubled Bethe lattice and effective two impurity cluster.

appears somewhat artificial in a uniform system in which all neighbors are equivalent, it leads to a *controlled* and non-trivial modification of the $d = \infty$ limit. [1] In contrast to the standard single band Hubbard model in infinite dimensions, in which electrons solely undergo *temporal* fluctuations, our model also allows for *spatial* fluctuations. A systematic expansion in $1/d$ [106, 51] (see also Chapter 2) includes exactly these processes and the model can therefore be interpreted as including some of the effects of finite dimensionality.

It is clear that the model by construction enables us to study nearest-neighbor spin-correlations. In physical terms, for t_{ab} large, the model favors the formation of singlet pairs (dimers) from the "a-b" sites. Interestingly, this symmetry breaking is not unreasonable in *disordered systems*, where each site a has another "preferred" neighboring site b, with which dimerization will be favored. This notion is at the heart of the "random singlet" ordering of Bhatt and Lee [112], describing the singular thermodynamics of doped semiconductors. Notice also that a variety of additional interpretations is possible. In particular, the model may alternatively viewed as a two band model or as two coupled layers.

[1] In recent work, Kotliar and Georges (private communication) have proposed a cluster $1/d$ expansion of the $d = \infty$ mean-field theory, based on single *and* two impurity models. While uncontrolled, it offers an elegant way of restoring the translational invariance in the cluster formulation. On physical as well as on technical grounds, we expect the results of such a formulation to be close to the findings presented in this chapter.

As in the case of the standard Hubbard model, the problem simplifies considerably in the large coordination (large dimension) limit. Rescaling the hopping amplitude t as $t \to \frac{t}{\sqrt{m}}$ ($m = z - 1$ is the "branching ratio" of the Bethe lattice), and taking the limit $m \to \infty$ we obtain an effective *two-impurity Anderson model* embedded in a self-consistently determined bath. We introduce spinors $\mathbf{c}^*_\sigma(\tau) = (a^*_\sigma(\tau), b^*_\sigma(\tau))$ and the matrix Green function

$$\mathbf{G}_\sigma(\tau - \tau') = \begin{pmatrix} -\langle \mathcal{T} a_\sigma(\tau) a^\dagger_\sigma(\tau')\rangle & -\langle \mathcal{T} a_\sigma(\tau) b^\dagger_\sigma(\tau')\rangle \\ -\langle \mathcal{T} b_\sigma(\tau) a^\dagger_\sigma(\tau')\rangle & -\langle \mathcal{T} b_\sigma(\tau) b^\dagger_\sigma(\tau')\rangle \end{pmatrix}, \tag{9.2}$$

with

$$\mathbf{G}(i\omega_n) = -\int_0^\beta e^{i\omega_n \tau} \langle T_\tau \mathbf{c}(\tau) \mathbf{c}^\dagger(0)\rangle_{S_{eff}}. \tag{9.3}$$

Notice that due to spin conservation $\mathbf{G}_\sigma = \delta_{\sigma\sigma'}\mathbf{G}_{\sigma\sigma'}$.

The effective action can then be written in matrix form as

$$S_{eff}[\mathbf{c}_\sigma, \mathbf{c}^*_\sigma] = -\sum_\sigma \sum_{i\omega_n} \mathbf{c}^*_{\sigma\mathbf{n}} \mathbf{G}^{-\mathbf{1}}_{\mathbf{0}}(i\omega_n) \mathbf{c}_{\sigma\mathbf{n}} + U \int_0^\beta d\tau (n_{a\uparrow} n_{a\downarrow} + n_{b\uparrow} n_{b\downarrow}) \tag{9.4}$$

where the self-consistency condition reads

$$\mathbf{G}^{-\mathbf{1}}_{\mathbf{0}}(i\omega_n) = \begin{pmatrix} i\omega_n + \mu & -t_{ab} \\ -t_{ab} & i\omega_n + \mu \end{pmatrix} - t^2 \mathbf{G}(\mathbf{i}\omega_\mathbf{n}). \tag{9.5}$$

While solving this model for general values of the parameters represents a highly nontrivial task, we immediately recognize some well known limiting cases. In the limit $t_{ab} = 0$, the two Bethe lattices decouple, and the model reduces to the well known single-band Hubbard model in $d = \infty$. As we saw, at half filling, this model undergoes a Mott transition at $U = U_{c_2}$, which is preceded by a formation of a pseudo-gap and the coexistence of a metallic and an insulating solution in the region $U = U_{c_1} < U < U = U_{c_2}$. The metallic solution, however, is lower in energy [69] at $T = 0$ throughout the coexistence region, so that $U = U_{c_2}$ represents a true zero-temperature critical point where the two solutions merge.

The other easily analyzable case is the noninteracting limit $U = 0$. Here, a band-crossing transition takes place, where the density of states at the Fermi level vanishes continuously and a gap opens at $t_{ab} = t$. The origin of this transition is easy to

understand: in the atomic limit $t_{ab} >> t$ the density of states reduces to the two (bonding and antibonding) levels at $E_{\pm} = \pm t_{ab}$. When the hopping t increases, these atomic levels broaden into bands of width $\approx 2t$, so that the gap closes when the two bands overlap, at $t_{ab} = t$.

9.2 Results

While the limit of infinite dimensions simplifies the original problem considerably, solving the corresponding impurity model is still a formidable task, as we saw only too clearly in the previous chapters. While we could in principle resort to the techniques developed in this thesis, we will resort to a particularly simple approach first proposed by Georges and Kotliar [41] based on solving the Anderson impurity model using second order perturbation theory, following Yamada and Yosida [58, 59, 60]. Due to the additional self-consistency this approach, often called the "iterated perturbation theory" (IPT) [21], still has non-perturbative character. It is exact in both limits of $U = 0$ and $U = \infty$ and displays a Mott metal-insulator transition. Detailed investigations based on other numerical approaches demonstrated [40, 69] the qualitative validity of most IPT predictions for the single-band Hubbard model in $d = \infty$. As compared to numerically exact solutions, IPT requires considerably less computational effort, and thus represents a valuable guide to the physics of $d = \infty$ electrons.

In the problem that we consider in this chapter, one has to solve a two impurity Anderson model – a task which is considerably more difficult than the simpler single impurity model. Furthermore, numerical Monte Carlo approaches [113] to the two impurity Anderson model have proven to be largely unsuccessful at the available computational level. Extending the exact diagonalization approaches and the self-consistent projective technique remains an open task. Taking these facts into consideration, we propose to begin the investigation of the problem considered using the IPT approach as a useful first attempt to gain insight into the RKKY-Kondo competition.

We will concentrate on the behavior at half-filling, where the Mott transition takes place at $t_{ab} = 0$, and investigate the modifications induced by turning on $t_{ab} \neq 0$.

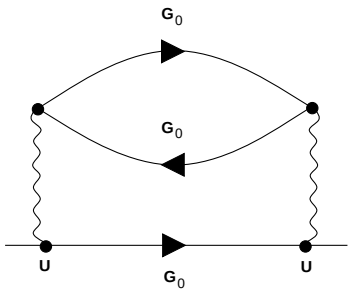

Figure 9.2: Second-order perturbation theory self energy diagram.

In order to apply IPT to the present model, we have to compute the second-order perturbation theory corrections around the non-magnetic Hartree-Fock solution. The second-order diagonal/off-diagonal self-energies in this case consist of only one diagram (see Fig. 9.2), respectively, and are given as

$$\Sigma_{xy}(\tau) = -U^2 G^0_{xy}(\tau) G^0_{xy}(-\tau) G^0_{xy}(\tau), \tag{9.6}$$

where $x, y = a, b$. Since the resulting equations have to be solved self-consistently, the solution is obtained by numerical iteration until convergence is found. We have determined the $T = 0$ phase diagram of the investigated model at half filling using the IPT approximation, and the results are presented in Fig. 9.3. At small values of U, as t_{ab} is increased, the behavior is qualitatively the same as at $U = 0$. A *continuous* transition takes place, at a critical value of the hopping $t^c_{ab}(U)$ that is found to decrease as U increases. This behavior reflects the fact that the gradual band broadening due to the Hubbard-Mott splitting tends to close the gap. As an illustration, we display the evolution of the DOS as the transition is approached in Fig. 9.4. at $U = 0$ (Fig. 9.4 a) and $U = 1.5$ (Fig. 9.4 b).Again, all energies are measured in units of the half-bandwidth $D = 2t$.

For larger values of U, a coexistence region of the metallic and insulating solutions is found, similarly as for $t_{ab} = 0$. The metallic solution is found for $U < U_{c_2}(t_{ab})$; we note the non-monotonic dependence of $U_{c_2}(t_{ab})$, which is first found to increase, and then to decrease as a function of t_{ab}. Thus, as compared with $t_{ab} = 0$, the addition of

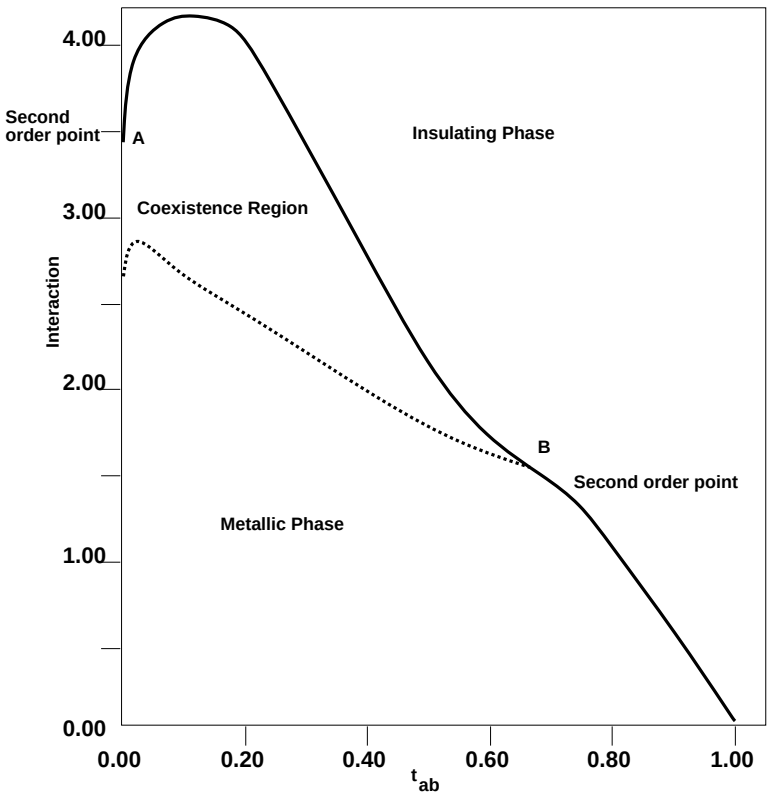

Figure 9.3: Phase diagram in the $U - t_{ab}$ plane. Shown are the spinodal lines and the second order points A and B.

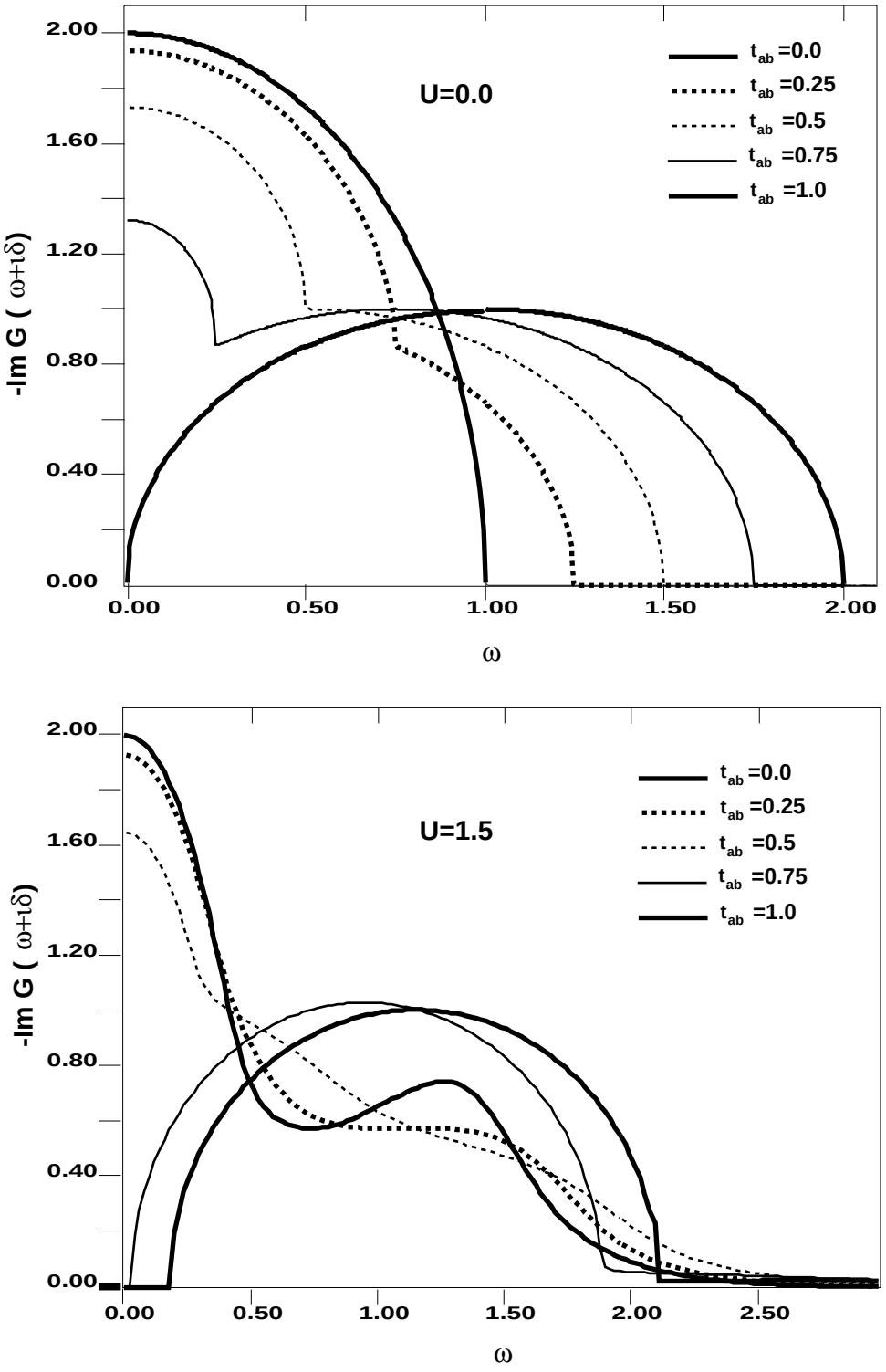

Figure 9.4: Density of states for interactions a) $U = 0$ and b) $U = 1.5$ for $t_{ab} = 0.0, 0.25, 0.5, 0.75, 1.0$.

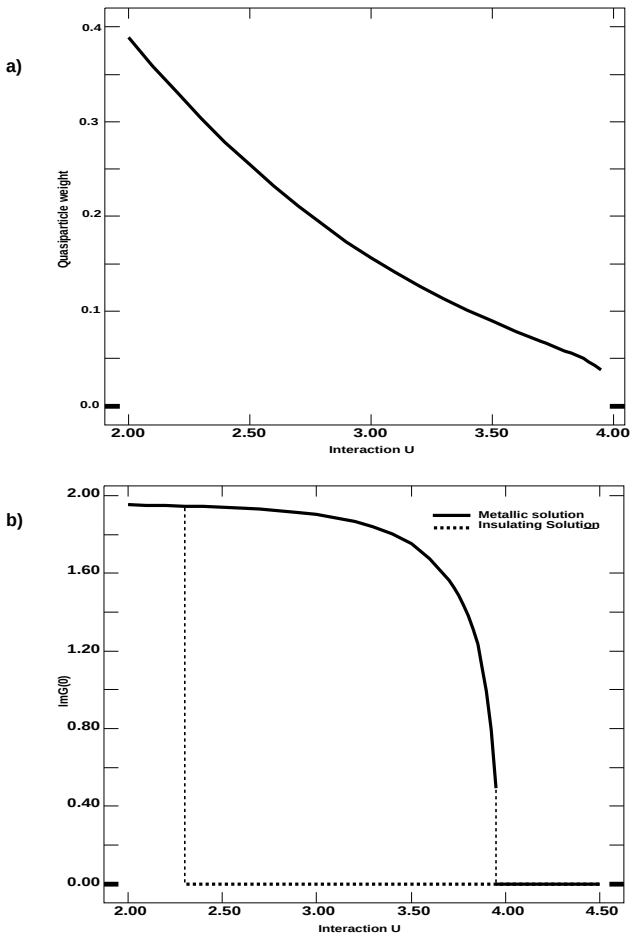

Figure 9.5: a) Quasiparticle residue $z = 1/(1 - \frac{\partial \Sigma}{\partial \omega})$ in the metallic phase as a function of the interaction U for $t_{ab} = 0.2$. b) Density of States $(-ImG(0^+)$ of metallic (solid line) and insulating (dotted line) solutions at $t_{ab} = 0.2$ as a function of the interaction U.

the RKKY correlation is found to extend the metallic region. More importantly, we find that the metallic solution disappears *discontinuously* at $U = U_{c_2}(t_{ab})$, in contrast to the $t_{ab} = 0$ behavior [19, 12]. The solution along this boundary is *not* characterized by a low energy scale, as seen by plotting the Kondo temperature (quasiparticle weight $z = 1/(1 - \frac{\partial \Sigma}{\partial \omega})$) on one site as a function of U, for $t_{ab} = 0.2$ (Fig. 9.5 a). The density of states is also discontinuous at this boundary (Fig. 9.5(b)). We note the pronounced dependence of the density of states at the Fermi energy on the interaction U – a clear violation of the "pinning condition" that is observed at $t_{ab} = 0$. This behavior is even more clearly seen by plotting the evolution of the metallic DOS as the boundary is

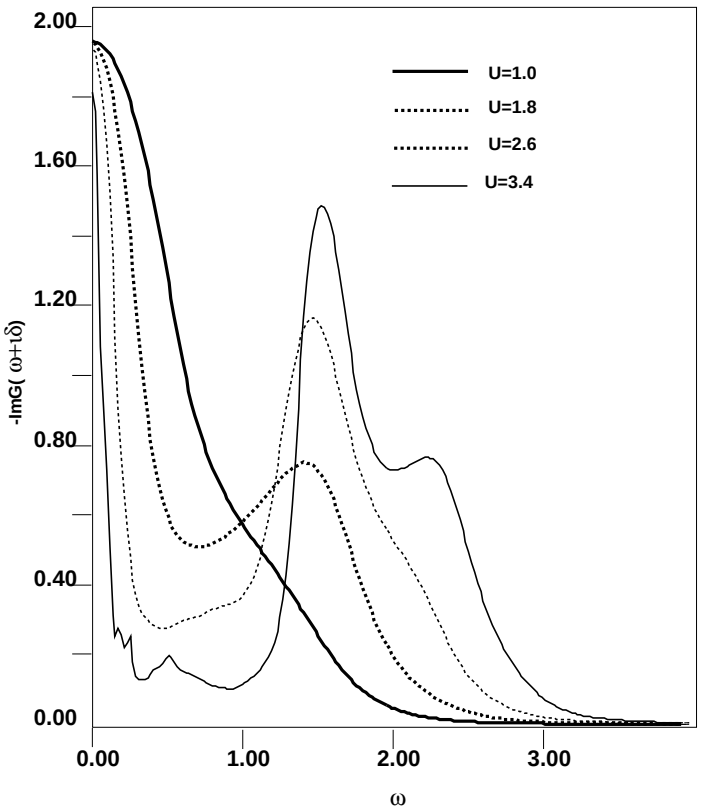

Figure 9.6: Density of States for $t_{ab} = 0.2$ and interactions $U = 1.0, 1.8, 2.6, 3.4$.

approached in Fig. 9.6. Clearly, in contrast to the situation at $t_{ab} = 0$, the metallic and insulating solutions *do not merge* at $U = U_{c_2}(t_{ab})$, so this boundary cannot be identified with a critical line.

Similar behavior is obtained by examining the stability of the insulating solution, which is found to *discontinuously* disappear at $U = U_{c_1}(t_{ab})$. As we can see from the phase diagram, Fig. 9.3, the boundaries $U_{c_1}(t_{ab})$ and $U_{c_1}(t_{ab})$ are found to join at the critical point "B" which is also the end of the band crossing transition critical line.

We thus find that in the entire coexistence region, the metallic and the insulating solutions merge only at two points: A ($t_{ab} = 0, U = U_{c_2}$) and B. In the rest of the phase diagram the two solutions are *disjoint* from each other, and the transition has a *first-order* character. This conclusion can be established even more rigorously by examining the *local stability* of each solution throughout the coexistence region. For this purpose, we have developed an approach that allows us to determine the stability, as described in

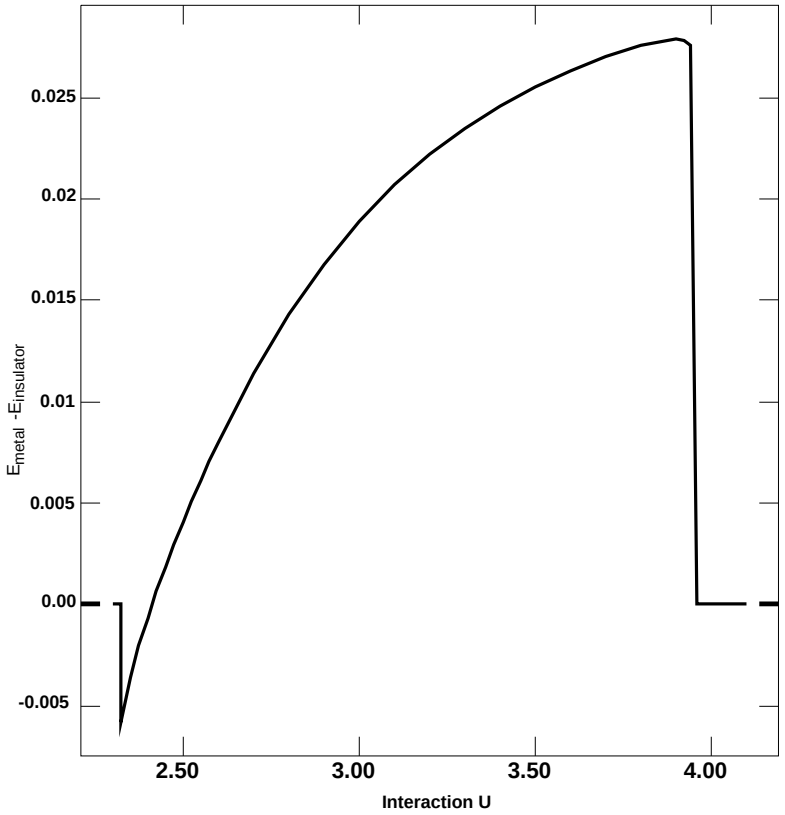

Figure 9.7: Difference between the energies of metallic and insulating solutions for $t_a b = 0.2$ as a function of the interaction U.

detail in the appendix. Using this method, we have established that both the metallic and the insulating solution *are locally stable*, supporting the first-order scenario. (Note that when the procedure is applied in the $t_{ab} = 0$ limit, we find that in the coexistence region, the insulating solution is locally *unstable* with respect to the metallic solution, in agreement with the results established in Chapter 4 [69].)

To obtain the location of the transition line, we have calculated the energies of the solutions, and determined the line where they coincide, as shown in Fig. 9.3. Since the solutions merge at points A and B (see Fig. 9.3), the energies of the solutions have to coincide there, and the (first order) transition line connects those two points. As an illustration, the energies of the two solutions are plotted for $t_{ab} = 0.2$ as a function of U in Fig. 9.7.

As we can see, in contrast to the $t_{ab} = 0$ findings, the *insulating* solution is lower

in energy for larger values of U, consistent with the first-order scenario. This result is perhaps not surprising, as the RKKY interactions are generally expected to stabilize the insulating solution.

In line with this first order scenario, the boundary lines $U_{c_1}(t_{ab})$ and $U_{c_2}(t_{ab})$ should be recognized as *spinodal* lines. An interesting question is why the two solutions merge at $t_{ab} = 0$, i. e. why is there a critical point there instead of a first-order transition. The existence of *bifurcations*, i. e. critical points is usually associated with spontaneous breakdown of some symmetry (e.g. up-down symmetry in the Ising model). In the case of the single-band Hubbard model in $d = \infty$ the relevant symmetry remains yet to be discovered.

The effects of the RKKY interactions are not limited to the modifications of the MIT scenario. They can also modify the thermodynamic behavior by affecting the dynamics of the collective spin fluctuations governing the finite temperature response. In order to investigate this aspect of the problem, we have computed the specific heat in the metallic and the insulating phases of our model. To illustrate the typical metallic behavior, we present results for the specific heat at $U = 2.5$, for three different values of $t_{ab} = 0,\ 0.2,\ 0.4$ in Fig. 9.8.

At $t_{ab} = 0$ we recognize the characteristic linear specific heat at $T << T_{Kondo} \sim 0.05$, corresponding to Fermi liquid behavior, a Schottky-like peak at $T \sim T_{Kondo}$ reflecting the binding energy of the Kondo singlet, and insulating-like behavior at $T \sim U/2$ due to charge fluctuations (Hubbard bands).

For $t_{ab} \neq 0$, i.e. as the RKKY interactions are introduced, a *new* feature appears in the intermediate energy range: the specific heat is enhanced at $T \sim J_{ab}$, reflecting the emergence of additional spin fluctuations with a characteristic energy corresponding to the RKKY exchange interaction $J_{ab} \approx 4t_{ab}^2/U$. For $t_{ab} = 0.4$ and $U = 2.5$ we estimate $J_{ab} \approx 0.08$, giving a ("Schottky") peak in the specific heat at $T_J \sim J/2 \approx 0.16$, exactly where the observed enhancement occurs.

This interpretation of the observed specific heat enhancement finds additional support by examining the corresponding behavior in the insulating regime. Typical results are presented in Fig. 9.9, where the specific heat is plotted for $U = 3.5$, and $t_{ab} = 0,\ 0.15$

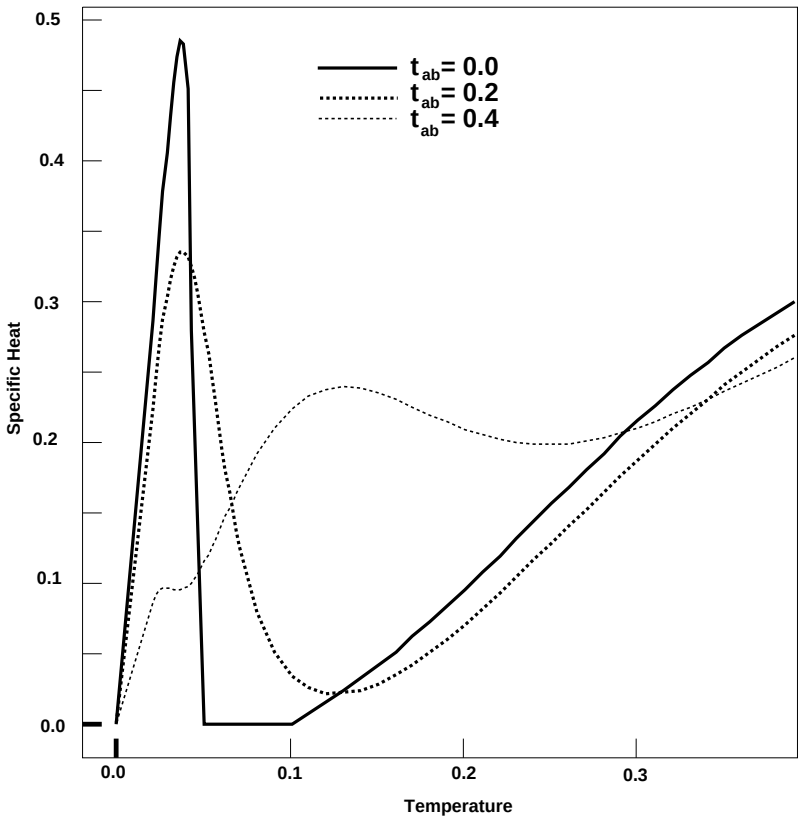

Figure 9.8: Specific heat as a function of temperature at U=2.5 for $t_{ab} = 0.0, 0.2, 0.4$.

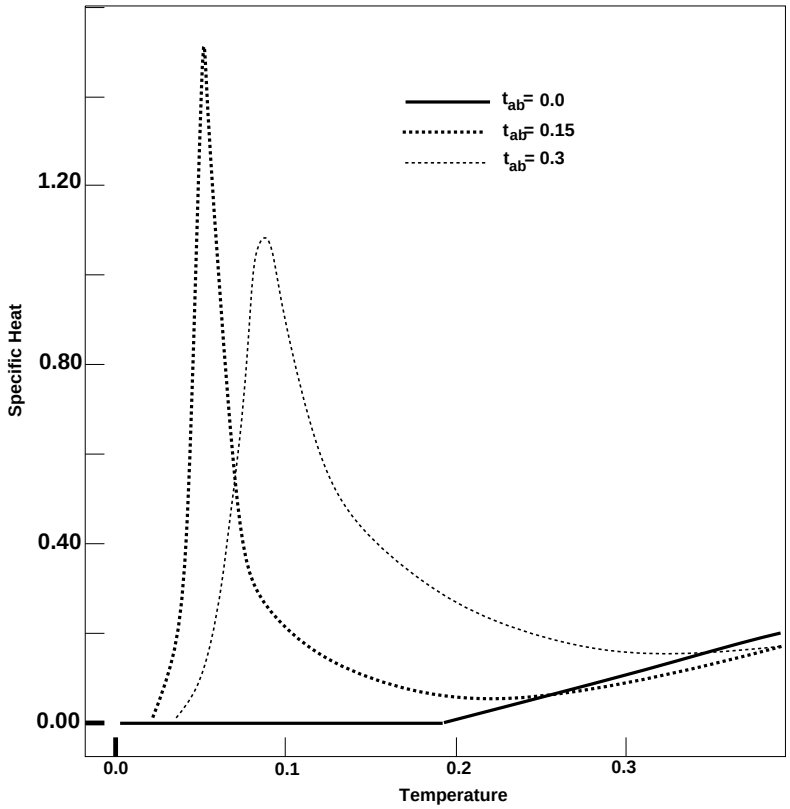

Figure 9.9: Specific Heat at U=3.5 for $t_{ab} = 0.0, 0.15, 0.3$.

and 0.3.

In absence of RKKY interactions ($t_{ab} = 0$) the specific heat is vanishingly small at low temperatures, reflecting the existence of the Mott-Hubbard gap. As in the metallic phase, the addition of RKKY interactions ($t_{ab} \neq 0$) induces specific heat enhancements in a comparable temperature range, at $T_J \approx 2t_{ab}^2/U$. We also note that the corresponding enhancement in the metallic state (Fig. 9.8) is much more spread-out in temperature, presumably reflecting the scattering of these fluctuations by the coupling to the particle-hole excitations.

9.3 Beyond Perturbation Theory

The solution of our model presented in the preceding section was based on an approximate scheme for the impurity problem – the perturbation theory approach of Yosida and Yamada [58, 59, 60]. While this techniques was utilized with impressive success in

previous $d = \infty$ studies [41, 56, 12], it is important to emphasize the limitations of this approach, and identify instances where most important problems can be expected.

When applied to single-impurity Anderson models, the approach of Yamada and Yoshida is generally expected to be at least qualitatively correct in the entire temperature range. In this case, the ground state is a (local) Fermi liquid, so that perturbation theory converges [114] and finite order corrections are sufficient. The situation is more complicated in two-impurity models such as the two-impurity Kondo (Anderson) model. Here, a critical point [115] is found at half-filling, separating the RKKY and Kondo regimes. The emergence of this critical point has a simple physical origin. It reflects the fact that two ground states with different symmetry are possible, corresponding to the Kondo spins being compensated either by conduction electrons (Kondo phase) or by each other (RKKY phase). This critical point, which reflects a degeneracy due to level crossing [116] signals a breakdown of a Fermi liquid description. As a result, we do not expect perturbative approaches to be accurate in the critical region. Indeed, if the two-impurity problem is treated in perturbation theory, the critical point is washed out into a smooth crossover.

Without providing a more elaborate treatment of the two-impurity problem, we can at least make estimates of the regions in parameter space where IPT could prove insufficient. Based on the information available from studies of the two impurity Kondo model [115] (2IKM) in a fixed bath, we expect that a critical point emerges when the RKKY interaction J_{ab} is comparable to the "bare" Kondo temperature $T^o_{Kondo} = T_{Kondo}(t_{ab} = 0)$. Since near U_{c_2} the Kondo temperature vanishes

$$T^o_{Kondo} \sim \frac{m_o}{m^*} \sim (U_{c_2} - U), \tag{9.7}$$

but the exchange interaction remains finite

$$J_{ab} \sim t^2_{ab}/U \tag{9.8}$$

one can expect that increasing U at finite t_{ab} drives the system from a Kondo to an RKKY metallic phase. The critical line where this could take place can be estimated by equating T^o_{Kondo} and J_{ab}, and using Eqs. (9.7)-(9.8), we find

$$U_{RKKY}(t_{ab}) \approx U_{c_2} - 4t^2_{ab}/U_{c_2}. \tag{9.9}$$

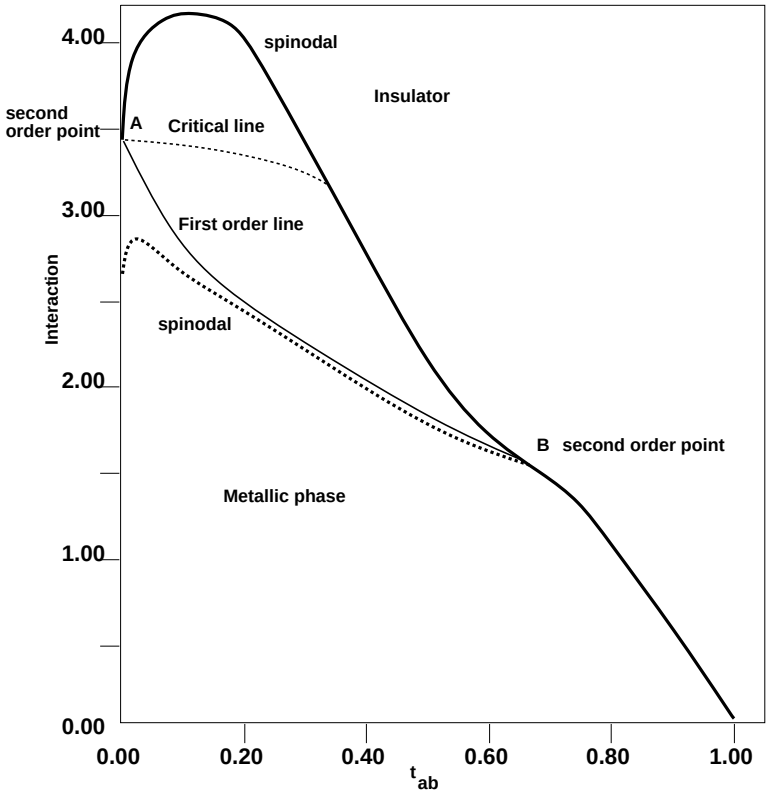

Figure 9.10:

This expression is valid only in the $t_{ab} \to 0$ limit, where to leading order we have ignored the modifications of the (self-consistently adapting) electronic bath. This estimate is plotted in Fig. 9.10, where it is compared with the perturbation theory predictions for the metallic phase boundary, and the location of the first-order metal-insulator transition. As we can see, according to IPT, the first order transition *preempts* the approach to the RKKY-Kondo critical line, supporting the validity of IPT-based predictions.

The IPT prediction that the introduction of RKKY interactions induces a first-order metal insulator transition finds additional support if we recall that a similar conclusion was obtained by introducing additional RKKY interactions in the large-N approaches to correlated electrons [117]. However, we emphasize that this approach did not have the two impurity Kondo physics build in, and, in particular, the possibility that the RKKY-Kondo competition induces a nontrivial critical point even on the impurity level.

An interesting question that deserves further study is the role of the two impurity Kondo model critical point in the destruction of the metallic phase. Of course, this question would be particularly relevant if additions of small perturbations, perhaps disorder, could stabilize the metallic phase to larger values of U, so that the relevant critical point becomes physically accessible.

9.4 Conclusions

In this chapter we addressed the role of short-ranged magnetic correlations in determining the behavior of strongly correlated electronic systems. To account for these effect, which are not properly treated by existing approaches, we propose a two-site cluster generalization of the Hubbard model in infinite dimensions as the simplest model containing the relevant physics. The model is mapped onto a two-impurity Kondo-Anderson model in a self-consistently determined bath, making it possible to directly address the competition between the Kondo effect and RKKY interactions in a lattice context.

Using a well known approximation scheme for solving the self-consistency conditions, we have determined the phase diagram of our model and discussed the modifications of the metallic behavior. We find that the addition of RKKY interactions induces a first-order metal-insulator transition, by energetically favoring the insulating phase. Additional low-energy spin fluctuations emerge, leading to enhancements of the specific heat in the intermediate temperature range, both in the metallic and insulating phases.

Chapter 10

Conclusion

In this thesis we have used the limit of infinite dimensionality to study the Mott transition and the transfer of spectral weight in the Hubbard model. In order to analyze the critical point, as well as the critical region of the Mott transition, we have developed a method, the self-consistent projective technique, that allows us to determine the critical properties *exactly* in the limit of infinite dimensions. This enables us to study the critical properties of of strongly correlated electron systems for the first time in a controlled limit. The results are contrasted with the mechanisms found in the Falicov-Kimball model, which can be solved exactly in the limit of infinite dimensionality. Furthermore, a model mimicking the effect of $1/d$ corrections to the limit of infinite dimensionality is proposed and studied.

In Chapter 2 we have provided a pedagogical introduction into the limit of infinite dimensionality. In particular, we describe a powerful numerical technique, based on the mapping of lattice models in infinite dimensions onto self-consistent single impurity models, that enables us to solve the latter in an efficient and accurate way.

Chapter 3 studies the Falicov-Kimball model in the limit of infinite dimensionality. The single particle spectral density as well as the AC conductivity for various interactions and fillings are computed. We see that the metal-insulator transition in this model at half filling proceeds through the opening of a gap. No coherent features at the Fermi level emerge. The transfer of spectral weight occurs simply through the diminishing of the number of doubly occupied sites as the system is doped. We furthermore establish the existence of a region in which the renormalized f electron energy is pinned to the Fermi level.

In Chapters 4 and 5 we have studied the Hubbard model at and away from half

filling. As compared to the Falicov-Kimball model, this model is characterized by two energy scales: broad, incoherent features at high energies, as well as a narrow quasiparticle resonance at the Fermi level. The metal-insulator transition occurs through the continuous narrowing of a quasiparticle peak at the Fermi level. Using the framework outlined in Chapter 2 we establish the coexistence of metallic and insulating solutions over a finite range of interactions U and chemical potential μ, in agreement with the results obtained using the Quantum Monte Carlo method and perturbation theory. For the first time we are able to unambiguously show that the metallic solution is always lower in energy, and that the transition at zero temperature is therefore of second order. This numerical result is backed by analytic considerations.

We also study the transfer of spectral weight, as well as the position of states induced by doping the system. Since for moderate values of the interaction we find that these are induced *in* the gap, this is of high experimental relevance. We see that while the method we are using is extremely successful as long as the distance to the critical region is finite, it fails close to the transition and does not enable us to study critical, as well as low temperature properties. It is the interest in exactly these regimes which motivates the development of the self-consistent projective technique in Chapter 6.

The self-consistent projective technique uses the separation of scales in the problem to our advantage: It enables us to eliminate the high energy contributions completely, and reduce the full problem to an effective problem having a *single energy scale* only. The latter is thus considerably more amenable to analytical as well as numerical studies and provides us with a powerful tool to study the critical region with unprecedented accuracy, and determine the *exact* critical properties. The method is general and can be applied to any problem exhibiting a separation of scales. Its generality and success furthermore derives from the fact that the dependence of the low frequency part on the high energy features is weak, such that a phenomenological knowledge of these is sufficient to obtain qualitatively correct results for the critical properties. It is therefore in the spirit of the familiar Landau-Ginsburg theory of phase transitions. Chapter 6 provides the formal development of the method for the case of the Hubbard model.

In Chapter 7 we illustrate the power of the method by applying it to the study of

the critical properties of the Hubbard model. In the half-filled case we find that the resulting effective problem is an intermediate coupling Kondo model. For the first time we are able to obtain the accurate value of the critical interaction, U_c, and determine the spectral function at the critical interaction. We are also able to compute ratios of divergent quantities, like the ratio of specific heat coefficient and linear term in the specific heat (generalized Wilson ratio), the ratio A/γ^2, where A is the coefficient of the quadratic term in the resistivity, as well as a generalized Korringa ratio. Connections with experiments are made.

The corresponding analysis is done away from half filling, in which case we again obtain an intermediate coupling effective Kondo model. Due to potential scattering the Kondo coupling is reduced with increasing interaction strength. We are able to determine exactly the critical μ_c, the position of the quasiparticle resonance for infinitesimal doping, and establish that the resonance for small doping is always separated from the band. In particular, for intermediate values of the interaction doping induces states well in the gap. The method thus puts our previous result on a rigorous footing. Spectral functions, Wilson ratio, as well as A/γ^2 are obtained. The analysis of the approach to the critical point allows us to determine the slope of the quasiparticle weight as a function of $U - U_c$ and $\mu - \mu_c$, respectively.

In Chapter 8 we analyze the properties of the Hubbard model at finite temperatures, using the full model as well as the self-consistent projective technique. The self-consistent technique in this case enables us to reach temperatures which could not be accessed reliably using any other method. We find clear Fermi liquid behavior at low temperatures and observe the emergence of a new low energy scale dominating the low temperature behavior. Analytical as well as numerical arguments show that this scale is set by the "Kondo temperature" given by the energy difference between ground state energy and energy of the doublet state in the subspace with one less particle.

Based on this success, we are therefore convinced that the method can be used to address many of the open problems in the field of strong electronic correlations, e.g. the breakdown of Fermi liquid theory [118, 119] and superconductivity [61, 40]. Applications of the method to other problems are currently under investigation [120].

We conclude the thesis by proposing a model which enables us to mimic the physics which results once corrections of order $1/d$ are considered. In particular, it allows us to study the competition between Kondo and RKKY interactions. We furthermore observe that the pinning condition of the infinite dimensional limit gets weakened once charge fluctuations are considered. Using the techniques developed in this thesis, a detailed study of the critical behavior of models of this type is within reach.

Appendix A

Effective Low Energy Operators

A.1 Coefficients of the effective F_σ operators

Defining the matrix elements

$$M^{(-)}_{\sigma\sigma'}(\mu) = \langle\mu|f_\sigma|\sigma'\rangle \tag{A.1}$$

$$M^{(+)}_{\sigma\sigma'}(\mu) = \langle\mu|f_\sigma|\sigma'\rangle \tag{A.2}$$

where $\{|\mu\rangle\}$ are high energy states of $\mathcal{H}_{at}$, and the expressions

$$\begin{aligned}
\Delta_{\uparrow\uparrow} &= M^{(+)2}_{\uparrow\uparrow} - M^{(-)2}_{\uparrow\uparrow} \\
\Delta_{\uparrow\downarrow} &= M^{(+)2}_{\uparrow\downarrow} - M^{(-)2}_{\uparrow\downarrow} \\
\alpha &= \frac{D}{2(\epsilon_{\mu_2} - \epsilon_{gs})} + \frac{D}{\epsilon_{\mu_1} - \epsilon_{gs}} \\
\beta &= \frac{D}{2(\epsilon_{\mu_2} - \epsilon_{gs})} \\
\mathcal{D}(\mu_1,\mu_2) &= \frac{D^2}{4}\left(\frac{1}{\epsilon_{\mu_2} - \epsilon_{gs}} + \frac{1}{\epsilon_{\mu_2} - \epsilon_{gs}}\right)
\end{aligned} \tag{A.3}$$

we obtain

$$\begin{aligned}
I^{(3,can)}_{spin} &= \sum_{\mu_1\mu_2} \mathcal{D}(\mu_1,\mu_2)\Big[(\alpha+\beta)(\Delta_{\uparrow\downarrow} - \Delta_{\uparrow\uparrow})(M^{-}_{\uparrow\uparrow} + M^{-}_{\uparrow\downarrow}) \\
&+ \beta\Big(M^{(-)2}_{\uparrow\downarrow}(\Delta_{\uparrow\uparrow} - \Delta_{\uparrow\downarrow}) + (M^{(-)2}_{\uparrow\uparrow} - M^{(-)2}_{\uparrow\downarrow})\Delta_{\uparrow\downarrow}\Big) \\
&- \alpha\Big(M^{(+)2}_{\uparrow\downarrow}(\Delta_{\uparrow\uparrow} - \Delta_{\uparrow\downarrow}) + (M^{(+)2}_{\uparrow\uparrow} - M^{(+)2}_{\uparrow\downarrow})\Delta_{\uparrow\downarrow}\Big)\Big]
\end{aligned} \tag{A.4}$$

$$\begin{aligned}
I^{(3,can)}_{pot} &= \sum_{\mu_1\mu_2} \mathcal{D}(\mu_1,\mu_2)\Big[-(\alpha+\beta)(\Delta_{\uparrow\uparrow} + \Delta_{\uparrow\downarrow})(M^{-}_{\uparrow\uparrow} + M^{-}_{\uparrow\downarrow}) \\
&+ \beta\Big(M^{(-)2}_{\uparrow\uparrow}(2\Delta_{\uparrow\uparrow} - \Delta_{\uparrow\downarrow}) + M^{(-)2}_{\uparrow\downarrow}(2\Delta_{\uparrow\downarrow} - \Delta_{\uparrow\uparrow})\Big) \\
&- \alpha\Big(M^{(+)2}_{\uparrow\uparrow}(2\Delta_{\uparrow\uparrow} - \Delta_{\uparrow\downarrow}) + M^{(+)2}_{\uparrow\downarrow}(2\Delta_{\uparrow\downarrow} - \Delta_{\uparrow\uparrow})\Big)\Big]
\end{aligned} \tag{A.5}$$

$$
\begin{aligned}
K_{spin}^{(3,can)} &= \sum_{\mu_1\mu_2} \mathcal{D}(\mu_1,\mu_2)\Big[\alpha\Big((M_{\uparrow\downarrow}^{(+)2}-M_{\uparrow\uparrow}^{(-)2})(\Delta_{\uparrow\uparrow}-\Delta_{\uparrow\downarrow})-(M_{\uparrow\uparrow}^{(+)2}-M_{\uparrow\downarrow}^{(+)2})\Delta_{\uparrow\uparrow} \\
&+ (M_{\uparrow\uparrow}^{(-)2}-M_{\uparrow\downarrow}^{(-)2})\Delta_{\uparrow\downarrow}\Big) \\
&+ \beta\Big((M_{\uparrow\uparrow}^{(+)2}-M_{\uparrow\downarrow}^{(-)2})(\Delta_{\uparrow\uparrow}-\Delta_{\uparrow\downarrow})+(M_{\uparrow\uparrow}^{(-)2}-M_{\uparrow\downarrow}^{(-)2})\Delta_{\uparrow\uparrow} \\
&- (M_{\uparrow\uparrow}^{(+)2}-M_{\uparrow\downarrow}^{(+)2})\Delta_{\uparrow\downarrow}\Big] \qquad \text{(A.6)} \\
K_{pot}^{(3,can)} &= \sum_{\mu_1\mu_2} \mathcal{D}(\mu_1,\mu_2)(\alpha+\beta)\Big((M_{\uparrow\uparrow}^{(-)2}-M_{\uparrow\uparrow}^{(+)2})\Delta_{\uparrow\downarrow}+(M_{\uparrow\downarrow}^{(-)2}-M_{\uparrow\downarrow}^{(+)2})\Delta_{\uparrow\uparrow} \\
&+ (M_{\uparrow\uparrow}^{(+)2}-M_{\uparrow\downarrow}^{(+)2}-M_{\uparrow\uparrow}^{(-)2}+M_{\uparrow\downarrow}^{(-)2})(\Delta_{\uparrow\uparrow}-\Delta_{\uparrow\downarrow})\Big). \qquad \text{(A.7)}
\end{aligned}
$$

Here we have used the fact that due to the fact that the states

$$
\{|T+\rangle = \frac{1}{\sqrt{2}}(f_\uparrow^\dagger|\downarrow\rangle + f_\downarrow^\dagger|\uparrow\rangle, f_\downarrow^\dagger|\downarrow\rangle, f_\uparrow^\dagger|\uparrow\rangle\} \qquad \text{(A.8)}
$$

form a triplet, such that

$$
\sum_\mu \frac{D}{(\epsilon_\mu-\epsilon_{at})^n} M_{\uparrow\downarrow}^{(+)} M_{\downarrow\uparrow}^{(+)} = \sum_\mu \frac{D}{(\epsilon_\mu-\epsilon_{at})^n}(M_{\uparrow\downarrow}^{(+)2}-M_{\uparrow\downarrow}^{(+)2}). \qquad \text{(A.9)}
$$

Analogously, the triplet states $\{\ |T-\rangle = \frac{1}{\sqrt{2}}(f_\uparrow|\downarrow\rangle - f_\downarrow|\uparrow\rangle,\ f_\downarrow|\downarrow\rangle,\ f_\uparrow|\uparrow\rangle\ \}$ lead to the identity

$$
\sum_\mu \frac{D}{(\epsilon_\mu-\epsilon_{at})^n} M_{\uparrow\downarrow}^{(-)} M_{\downarrow\uparrow}^{(-)} = \sum_\mu \frac{D}{(\epsilon_\mu-\epsilon_{at})^n}(M_{\uparrow\downarrow}^{(+-)2}-M_{\uparrow\downarrow}^{(-)2}). \qquad \text{(A.10)}
$$

Since M and Δ depend on μ we have (for notational transparency) ordered them such that the left matrix element depents on μ_1 and the right one one μ_2.

A.2 Coefficients of the effective Hamiltonian $\mathcal{H}^{(3,can)}$

Using the same definitions as in the previous sections of the Appendix we obtain for the coefficients entering the effective Hamiltonian (6.63)

$$
\begin{aligned}
J_{spin}^{(3,can)} &= \sum_{\mu_1\mu_2} \frac{1}{2}\mathcal{D}(\mu_1,\mu_2)\frac{1}{\epsilon_{\mu_1}-\epsilon_{gs}}\frac{1}{\epsilon_{\mu_2}-\epsilon_{gs}}(\Delta_{\uparrow\uparrow}-\Delta_{\uparrow\downarrow})(M_{\uparrow\downarrow}^{(+)2}+M_{\uparrow\uparrow}^{(-)2}) \qquad \text{(A.11)} \\
J_{pot}^{(3,can)} &= \sum_{\mu_1\mu_2} \frac{1}{8}\mathcal{D}(\mu_1,\mu_2)\frac{1}{\epsilon_{\mu_1}-\epsilon_{gs}}\frac{1}{\epsilon_{\mu_2}-\epsilon_{gs}} \\
&\otimes \Big(2(M_{\uparrow\uparrow}^{(+)2}+M_{\uparrow\downarrow}^{(-)2}+M_{\uparrow\downarrow}^{(+)2}+M_{\uparrow\uparrow}^{(-)2})-\Delta_{\uparrow\uparrow}-\Delta_{\uparrow\downarrow}\Big) \qquad \text{(A.12)}
\end{aligned}
$$

$$
\begin{aligned}
J^{||(3,can)} &= \sum_{\mu_1\mu_2} \frac{1}{2}\mathcal{D}(\mu_1,\mu_2)\frac{1}{\epsilon_{\mu_1}-\epsilon_{gs}}\frac{1}{\epsilon_{\mu_2}-\epsilon_{gs}} \\
&\otimes \quad (4\Delta_{\uparrow\uparrow}\Delta_{\uparrow\downarrow} - \Delta_{\uparrow\downarrow}\Delta_{\uparrow\downarrow} - \Delta_{\downarrow\downarrow}\Delta_{\downarrow\downarrow}).
\end{aligned} \tag{A.13}
$$

A.3 Coefficients of the transformed number operator N_σ

The transformed number operator (6.76) is given as

$$
\begin{aligned}
N_\sigma &= \sum_{\sigma'} X_{\sigma'\sigma'} \Big[\langle\sigma'|n_\sigma|\sigma'\rangle \\
&+ \frac{w}{4}\sum_{\alpha_1\alpha_2\sigma_1} \frac{\langle\alpha_1|n_\sigma|\alpha_2\rangle}{(\epsilon_{\alpha_1}-\epsilon_\sigma)(\epsilon_{\alpha_2}-\epsilon_\sigma)} \\
&\otimes \quad \Big(n_{L\sigma_1}(\langle\sigma'|f_{\sigma_1}|\alpha_1\rangle\langle\alpha_2|f^\dagger_{\sigma_1}|\sigma'\rangle - \langle\sigma'|f^\dagger_{\sigma_1}|\alpha_1\rangle\langle\alpha_2|f_{\sigma_1}|\sigma'\rangle) + \langle\sigma'|f^\dagger_{\sigma_1}|\alpha_1\rangle\langle\alpha_2|f_{\sigma_1}|\sigma'\rangle \Big) \\
&- \frac{w}{4}\sum_{\alpha_1\sigma_1} \frac{\langle\sigma'|n_\sigma|\sigma'\rangle}{(\epsilon_{\alpha_1}-\epsilon_\sigma)^2} \Big(n_{L\sigma_1}(|\langle\alpha_1|f^\dagger_{\sigma_1}|\sigma'\rangle|^2 - |\langle\alpha_1|f_{\sigma_1}|\sigma'\rangle|^2) + |\langle\alpha_1|f_{\sigma_1}|\sigma'\rangle|^2 \Big) \Big]
\end{aligned} \tag{A.14}
$$

Appendix B

Determination of the Critical Behavior: A $1+1$ Site Toy Anderson Model

Some insights into the Mott transition as well as the transfer of spectral weight in the Hubbard model in infinite dimensions can be obtained by examining the behavior of a simple $1+1$ site toy Anderson model, in which the conduction electron bath is represented by a single site at the Fermi level.[1] While this has poles at the Fermi level, as well as at high energies, implying that we cannot demand self-consistency rigorously, we can impose self-consistency for the low frequency part. This leads to a qualitatively correct approximation to the low frequency results, as can be seen by solving the corresponding *projected* toy model as done in Appendix D. It therefore gives a good first-order description of the transfer of spectral weight, whose non trivial aspects are *solely* due to the binding of a singlet at low frequencies. This can be seen from the solution to the insulating toy model given in Appendix C.

The $1+1$ site toy Hamiltonian is given as

$$H = \sum_{\sigma} \Big(V(c_{\sigma}^{\dagger} f_{\sigma} + h.c.) - \mu f_{\sigma}^{\dagger} f_{\sigma} \Big) + U n_{f\uparrow} n_{f\downarrow}. \tag{B.1}$$

We want to obtain the low energy contribution to the Green function to order $(V/\mu)^4$ *exactly*, i.e. *all* terms of order V^4 are kept, in order to be able to study the critical region (as we have seen, this implies that we need the non-linear terms).

We will use the following notation for states: $|\sigma;0\rangle \equiv f_{\sigma}^{\dagger}|0\rangle$, $|0;\sigma\rangle \equiv c_{\sigma}^{\dagger}|0\rangle$ with the ordering $|\uparrow\downarrow;\uparrow\downarrow\rangle = f_{\uparrow}^{\dagger} f_{\downarrow}^{\dagger} c_{\uparrow}^{\dagger} c_{\downarrow}^{\dagger}|0\rangle$.

---

[1] If the high energy states are integrated out using the self-consistent projective technique, this becomes equivalent to the $1+1$ site *projected* problem in which the high energy states are the high energy states of the impurity site *only*. Consequently, it leads to the same low energy behavior. The corresponding projected problem is worked out in Appendix D and agrees with the solution to this problem when expanded to order V^4. This provides a non-trivial check on the higher order contributions to the effective Hamiltonian.

Ground State

Since we are interested in contributions to order V^4/μ^2, the best way to proceed is to solve the problem exactly and expand to the order desired at the end. We diagonalize exactly the lowest energy singlet state

$$|S2\rangle = \frac{1}{\sqrt{2}}(|\uparrow;\downarrow\rangle - |\downarrow;\uparrow\rangle) \tag{B.2}$$

and the "empty" state $|0;\uparrow\downarrow\rangle$, yielding the zeroth order ground state

$$|gs\rangle_{(0)} = \frac{1}{N_{(0)}}(|S2\rangle + \frac{\sqrt{2}V}{E_{(0)-}}|0;\uparrow\downarrow\rangle) \tag{B.3}$$

and the excited state

$$|ex\rangle_{(0)} = \frac{1}{N_{(0)}}(|0;\uparrow\downarrow\rangle - \frac{\sqrt{2}V}{E_{(0)-}}|S2\rangle) \tag{B.4}$$

where $N^2_{(0)} = 1 + \frac{2V^2}{E^2_{(0)-}}$ and with energies

$$E_{(0)\mp} = \frac{1}{2}(-\mu \mp \sqrt{\mu^2 + 8V^2}) \equiv \frac{1}{2}(-\mu \mp \Delta) \tag{B.5}$$

where $\Delta \equiv \sqrt{\mu^2 + 8V^2}$. Admixing the state $|\uparrow\downarrow;0\rangle$ leads to a Hamiltonian matrix

$$H_2 = \begin{pmatrix} E_{(0)-} & 0 & \sqrt{2}V/N_{(0)} \\ 0 & E_{(0)+} & -\frac{2V^2}{N_{(0)}E_{(0)-}} \\ \sqrt{2}V/N_{(0)} & -\frac{2V^2}{N_{(0)}E_{(0)-}} & U - 2\mu \end{pmatrix}. \tag{B.6}$$

We can easily obtain the first order ground state energy as

$$E^{(1)}_{gs} = -\frac{1}{2}(\mu + \sqrt{\mu^2 + 8V^2}) + \frac{4V^2}{N^2_{(0)}(U - 2\mu - E_{(0)-})} \tag{B.7}$$

and the ground state wave function to the order necessary as

$$\begin{aligned} |gs\rangle &= \frac{1}{NN_{(0)}}\Big((1 + \frac{4V^2}{\Delta E^2_{(0)-}N^2_{(0)}(U - 3/2\mu + \Delta/2)})|S2\rangle \\ &+ \frac{\sqrt{2}V}{E_{(0)-}}(1 - \frac{2V^2}{\Delta N^2_{(0)}(U - 3/2\mu + \Delta/2)})|0;\uparrow\downarrow\rangle \\ &- \frac{\sqrt{2}V}{U - 3/2\mu + \Delta/2}(1 - \frac{2V^2}{(U - 3/2\mu + \Delta/2)^2})|\uparrow\downarrow;0\rangle\Big) \end{aligned} \tag{B.8}$$

where $N^2 = 1 + \frac{2V^2}{(U-3/2\mu+\Delta/2)^2}$.

Excited States

The determination of the Green function using the Lehmann representation now requires the states in which one particle has added to the ground state (particle excitations) and the states in which one particle has been removed from the ground state (hole excitations). Since the system is rotationally invariant, we can focus on the up Green function defined as

$$G_\uparrow(i\omega) = \sum_n \frac{|\langle n|f_\uparrow^\dagger|gs\rangle|^2}{i\omega - (E_n - E_{gs})} + \frac{|\langle n|f_\uparrow|gs\rangle|^2}{i\omega + (E_n - E_{gs})}. \tag{B.9}$$

We thus need the states having overlap with $f_\uparrow^\dagger|gs\rangle$ and $f_\uparrow|gs\rangle$

N=1 particle, $S_z = -1$ subspace

The only two states in this subspace, $|\downarrow;0\rangle, |0;\downarrow\rangle$, can be diagonalized exactly, giving the exact eigenstates

$$|1,+\rangle = \frac{1}{N_1}(|0;\downarrow\rangle - \frac{V}{E_{1-}}|\downarrow;0\rangle) \tag{B.10}$$

$$|1,-\rangle = \frac{1}{N_1}(|\downarrow;0\rangle + \frac{V}{E_{1-}}|0;\downarrow\rangle) \tag{B.11}$$

where $N_1^2 = 1 + \frac{V^2}{E_{1-}^2}$ and $E_{1\pm} = \frac{1}{2}(-\mu \pm \sqrt{\mu^2 + 4V^2})$.

N=3 particle, $S_z = 1$ subspace

The two states $|\uparrow;\uparrow\downarrow\rangle, |\uparrow\downarrow,\uparrow\rangle$ can be diagonalized exactly giving the exact eigenstates

$$|3,-\rangle = \frac{1}{N_3}(|\uparrow;\uparrow\downarrow\rangle + \frac{V}{U - 2\mu - E_{3-}}|\uparrow\downarrow;\uparrow\rangle) \tag{B.12}$$

$$|3,+\rangle = \frac{1}{N_3}(|\uparrow\downarrow;\uparrow\rangle - \frac{V}{U - 2\mu - E_{3-}}|\uparrow;\uparrow\downarrow\rangle) \tag{B.13}$$

where $N_3^2 = 1 + \frac{V^2}{(U-2\mu-E_{3-})^2}$ and $E_{3\pm} = \frac{1}{2}(U - 3\mu \pm \sqrt{(U-\mu)^2 + 4V^2})$.

Green Function

We can now determine the Green function, which is found to be

$$\begin{aligned} G(i\omega) &= \frac{V^2}{2N^2N_3^2N_{(0)}^2} \frac{\left(\frac{1}{(U-2\mu-E_{3-})^2} - \frac{2}{E_{(0)-}}(1 - \frac{2V^2}{\Delta N_{(0)}^2(U-3/2\mu+\Delta/2)})\right)^2}{i\omega - (E_{3-} - E_{gs})} \\ &+ \frac{V^2}{2N^2N_1^2N_{(0)}^2} \frac{\left(\frac{1}{E_{1-}} - \frac{2}{U-3/2\mu+\Delta/2}(1 - \frac{2V^2}{(U-3/2\mu+\Delta/2)^2})\right)^2}{i\omega + (E_{1-} - E_{gs})} \end{aligned} \tag{B.14}$$

$$+ \quad \frac{\frac{1}{2N^2N_3^2N_{(0)}^2}(1+\frac{2V^2}{E_{(0)-}-(U-2\mu-E_{(0)-})})^2}{i\omega-(E_{3+}-E_{gs})} + \frac{\frac{1}{2N^2N_1^2N_{(0)}^2}(1+\frac{2V^2}{E_{1-}-(U-2\mu-E_{(0)-})})^2}{i\omega+(E_{1+}-E_{gs})}.$$

The poles and weight can be read of readily using the expressions for the energies obtained in this section.

The lowest excitation energy within the $N=2$ partice subspace is given as $\Delta E^{triplet-singlet} = \sqrt{\mu^2+8V^2} \approx \mu$. The lowest hole and partice excitation are respectively given as $\Delta E^{hole} = \frac{1}{2}(-\sqrt{\mu^2+4V^2}+\sqrt{\mu^2+8V^2}) \approx \frac{V^2}{\mu}$ and $\Delta E^{particle} = \frac{1}{2}(U-2\mu-\sqrt{(U-\mu)^2+4V^2}+\sqrt{\mu^2+8V^2}) \approx \frac{2V^2}{\mu}$. (Here the expansions are only valid near the critical point, i.e. for vanishing V.) We see that $E_{3-}-E_{gs}$ and $E_{1-}-E_{gs}$ are of order V^2/μ which sets the low energy scale of the problem determining the low temperature behavior. This is elaborated in Chapter 9.

To determine the *critical behavior* we impose self-consistency, i.e. require $t^2G = \frac{V^2}{i\omega}$. Close to the critical point, we can expand in V/μ and obtain, using $t^2 = 1/4$ and omitting the high energy bands, the condition

$$\begin{aligned} 1 &= \frac{1}{8}\Bigg[\frac{5}{(U-\mu)^2}+\frac{5}{\mu^2}+\frac{8}{\mu(U-\mu)} \\ &- V^2\left(\frac{29}{(U-\mu)^4}+\frac{29}{\mu^4}+\frac{48}{\mu^3(U-\mu)}+\frac{48}{\mu(U-\mu)^3}+\frac{44}{\mu^2(U-\mu)^2}\right)\Bigg]. \end{aligned} \quad \text{(B.15)}$$

As mentioned before the *same* condition is obtained from the *projected* 1+1 site problem analyzed in Appendix D, if the only excited states entering the "Kondo coupling" are the high energy impurity states.

Limiting Cases

In the **half-filled case** in which $\mu = U/2$ we immediately obtain the critical U for which the weight of the quasiparticle resonance V^2 goes to zero. Setting $V=0$ in Equation (B.15) implies that $U_c = 3$. The quasiparticle weight close to the transition is obtained from $(1-\frac{44V^2}{U^2})\frac{9D^2}{U^2} = 1$ as $V^2 = \frac{1}{22}U_c(U_c-U)$. We see that the quasiparticle weight vanishes linearly with a slope $s = -2U_c/(11D) = -0.55$. This compares rather well with the exact value $s_{exact} = -0.34$ obtained in Chapter 7, if one considers the drastic nature of the approximation.

It is amusing to note, that the (wrong) result obtained in this section almost coincides with the result obtained from the four boson approach of Kotliar and Ruckenstein

[32, 81] which can be worked out easily in the Hubbard model. This yields a double occupancy $d^2 = (1-U/U_c)/4$, a quasiparticle weight $4V^2/D^2 = 8d^2(1-2d^2)$ where on a Bethe lattice $U_c = 32/(3\pi)$. Taken together this implies a slope $s_{4Boson} = 3/16\pi = 0.59$.

In the case of **finite doping** we obtain the critical μ_c for which the quasiparticle weight vanishes. This determines the position of the Kondo resonance at infinitesimal doping. For $V = 0$ Eq. (B.15) reduces to

$$\frac{5}{(U/2+\tilde{\mu})^2} + \frac{5}{(U/2-\tilde{\mu})^2} + \frac{8}{(U/2+\tilde{\mu})(U/2-\tilde{\mu})} = 8, \tag{B.16}$$

where $\tilde{\mu} = \mu - U/2$ such that $\tilde{\mu}_c^2 = \frac{1}{4}(\frac{1}{2} + U^2\sqrt{10U^2+\frac{1}{4}})$. While for interactions $U < 4.3D$ the resonance is clearly outside the lower or upper Hubbard bands, for $U \to \infty$ $\tilde{\mu}_c = \pm(-.87 + U/2)$, i.e. the resonance is found *inside* the lower band. The latter is again is in disagreement with the numerical results, which is not surprising, since the model does not contain any information about the high energy bands.

Appendix C

Solution to the Insulator: A 2+1 Site Toy Model

A minimal model for the insulating state is given by an impurity coupled to an effective bath consisting of two sites, representing upper and lower Hubbard bands, respectively. We thus consider a Hamiltonian in which the upper band is given by a pole at and energy $\epsilon^+ = U - \mu$, while the lower Hubbard band is represented by a pole at $\epsilon^- = -\mu$, such that the separation of the bands is U. The explicit form of the Hamiltonian therefore is

$$\mathcal{H}_{Ins}^{Toy} = \sum_{\sigma} \Big(V_+ c_{+\sigma}^\dagger f_\sigma + V_- c_{-\sigma}^\dagger f_\sigma + h.c. + (U-\mu) c_{+\sigma}^\dagger c_{+\sigma} - \mu (c_{-\sigma}^\dagger c_{-\sigma} + f_\sigma^\dagger f_\sigma) \Big) + U n_{f\uparrow} n_{f\downarrow} \tag{C.1}$$

We will use the following notation for states: $|$impurity; lower band, upper band$\rangle$ where the ordering of the operators is such that the fully filled system is given by the state $f_\uparrow^\dagger f_\downarrow^\dagger c_{-\uparrow}^\dagger c_{-\downarrow}^\dagger c_{+\uparrow}^\dagger c_{+\downarrow}^\dagger |0\rangle = |\uparrow\downarrow;\uparrow\downarrow,\uparrow\downarrow\rangle$. Our goal is to self-consistently determine the Green function of the system to order $(V/U)^2$ in perturbation theory. The contributions of order $(V/\mu)^2$ are treated exactly, such that the results become exact in the limit $U \to \infty$.

Ground State Clearly, the ground state is in the sector with three particles and is a *degenerate doublet*. When determining the Green function both ground states contribute with equal weights and have to be traced over. The doublet can be determined fully in perturbation theory and is given as

$$|gs,\sigma\rangle = \frac{1}{N_{gs}} \Big(|\sigma;\uparrow\downarrow,0\rangle + \frac{V_-}{U} |\uparrow\downarrow;\sigma,0\rangle - \frac{V_+}{U} |0;\uparrow\downarrow,\sigma\rangle \Big) \tag{C.2}$$

where $N_{gs}^2 = 1 + \frac{V_-^2+V_+^2}{U^2}$ and $\epsilon_{gs} = -3\mu - \frac{V_-^2+V_+^2}{U}$.

In order to determine the Green function

$$G(i\omega_n) = \frac{1}{2} \sum_{n,\sigma} \Big(\frac{|\langle n|f_\uparrow^\dagger|gs,\sigma\rangle|^2}{i\omega_n - (\epsilon_n - \epsilon_{gs})} + \frac{|\langle n|f_\uparrow|gs,\sigma\rangle|^2}{i\omega_n + (\epsilon_n - \epsilon_{gs})} \Big) \tag{C.3}$$

we need the states in the $N = 2$ and $N = 4$ particle sectors connected to the ground state through action of $f_\uparrow$ or $f_\uparrow^\dagger$.

Particle Excitations: $N = 4$

The states $|\uparrow\downarrow;\uparrow\downarrow,0\rangle$ and $|S4\rangle \equiv \frac{1}{\sqrt{2}}(|\uparrow;\uparrow\downarrow,\downarrow\rangle - |\downarrow;\uparrow\downarrow,\uparrow\rangle)$ are degenerate and have to be diagonalized exactly before admixing other states perturbatively. This yields the states

$$|\mp 4\rangle^{(0)} = \frac{1}{\sqrt{2}}\Big(|\uparrow\downarrow;\uparrow\downarrow,0\rangle \mp |S4\rangle\Big) \tag{C.4}$$

with energies $E^{(0)}_{\mp 4} = U - 4\mu \mp \sqrt{2}V_+$. These admix with the state

$$|E4\rangle^{(0)} = \frac{1}{N_{4E}}\Big(V_+|0;\uparrow\downarrow,\uparrow\downarrow\rangle - \frac{V_-}{\sqrt{2}}|S4ex\rangle\Big) \tag{C.5}$$

where $N_{4E} = \sqrt{V_+^2 + V_-^2/2}$ and $|S4ex\rangle = \frac{1}{\sqrt{2}}(|\uparrow\downarrow;\uparrow,\downarrow\rangle - |\uparrow\downarrow;\downarrow,\uparrow\rangle)$, leading to the Hamiltonian matrix

$$H_4 = \begin{pmatrix} U - 4\mu - \sqrt{2}V_+ & 0 & -\sqrt{V_+^2 + V_-^2/2} \\ 0 & U - 4\mu + \sqrt{2}V_+ & \sqrt{V_+^2 + V_-^2/2} \\ -\sqrt{V_+^2 + V_-^2/2} & \sqrt{V_+^2 + V_-^2/2} & 2U - 4\mu \end{pmatrix}. \tag{C.6}$$

The small energy splitting between the states $|\mp 4\rangle^{(0)}$ leads to the occurrence of terms in which $V_\pm$ appears in the denominator when applying straightforward perturbation theory. We thus have to be careful when determining the eigenstates to order $V_\pm^2/U^2$. By explicitly solving for the eigenvalues of H_4 and expanding to order V^3/U^2, we obtain the eigenvalues

$$E_{\mp 4} = U - 4\mu \mp \sqrt{2}V_+ - \frac{V_+^2 + V_-^2/2}{U}(1 - \frac{\sqrt{2}V_+}{U} + \frac{V_+^2 + V_-^2/2}{2\sqrt{2}V_+U}) \tag{C.7}$$

with corresponding eigenstates

$$\begin{aligned} |4\mp\rangle &= \frac{1}{N_4}\Big(\frac{1}{\sqrt{2}}(1 \mp \frac{V_+^2 + V_-^2/2}{2\sqrt{2}V_+U} + \frac{V_+^2 + V_-^2/2}{2U^2})|\uparrow\downarrow;\uparrow\downarrow,0\rangle \mp \frac{V_-}{\sqrt{2}U}|S4ex\rangle \\ &\mp \frac{1}{\sqrt{2}}(1 \pm \frac{V_+^2 + V_-^2/2}{2\sqrt{2}V_+U} - \frac{V_+^2 + V_-^2/2}{2U^2})|S4\rangle \pm \frac{V_+}{U}|0;\uparrow\downarrow,\uparrow\downarrow\rangle\Big) \end{aligned} \tag{C.8}$$

with $N_4^2 = 1 + \frac{(V_+^2+V_-^2/2)^2}{8V_+^2U^2} + \frac{(V_+^2+V_-^2/2)}{U^2}$.

Other states contributing to order V^2/U^2 are the triplet state

$$|T4\rangle \equiv \frac{1}{\sqrt{2}}\Big(|\uparrow;\uparrow\downarrow,\downarrow\rangle + |\downarrow;\uparrow\downarrow,\uparrow\rangle\Big) \tag{C.9}$$

and the $S_z = 2$ state

$$|\uparrow;\uparrow\downarrow,\uparrow\rangle \tag{C.10}$$

with energies $\epsilon_{T4} = U - 4\mu$.

Hole Excitations: $N = 2$, $S_z = 0$

The sector consisting of two particles has a structure analogous to the $N = 4$ subapace. The states $|0;\uparrow\downarrow,0\rangle$ and $|S2\rangle \equiv \frac{1}{\sqrt{2}}\Big(|\uparrow;\downarrow,0\rangle - |\downarrow;\uparrow,0\rangle\Big)$ are degenerate and have to be diagonalized exactly before admixing other states perturbatively, which leads to the states

$$|\mp 2\rangle^{(0)} = \frac{1}{\sqrt{2}}\Big(|0;\uparrow\downarrow,0\rangle \mp |S2\rangle\Big) \tag{C.11}$$

with energies $E^{(0)}_{\mp 2} = -2\mu \mp \sqrt{2}V_-$. These admix with the state

$$|E2\rangle^{(0)} = \frac{1}{N_{2E}}(V_-|\uparrow\downarrow;0,0\rangle + \frac{V_+}{\sqrt{2}}|S2ex\rangle) \tag{C.12}$$

where $N_{2E} = \sqrt{V_-^2 + V_+^2/2}$ and $|S2ex\rangle = \frac{1}{\sqrt{2}}\Big(|0;\uparrow,\downarrow\rangle - |0;\downarrow,\uparrow\rangle\Big)$, resulting in the Hamiltonian matrix

$$H_2 = \begin{pmatrix} -2\mu - \sqrt{2}V_- & 0 & -\sqrt{V_-^2 + V_+^2/2} \\ 0 & -2\mu + \sqrt{2}V_- & \sqrt{V_-^2 + V_+^2/2} \\ -\sqrt{V_-^2 + V_+^2/2} & \sqrt{V_-^2 + V_+^2/2} & U - 2\mu \end{pmatrix}. \tag{C.13}$$

By explicitly solving for the eigenvalues of H_2 and expanding to order V^3/U^2 we obtain the approximate eigenvalues

$$E_{\mp 2} = -2\mu \mp \sqrt{2}V_- - \frac{V_-^2 + V_+^2/2}{U}(1 - \frac{\sqrt{2}V_-}{U} + \frac{V_-^2 + V_+^2/2}{2\sqrt{2}V_-U}) \tag{C.14}$$

and eigenstates

$$\begin{aligned} |2\mp\rangle &= \frac{1}{N_2}\Big(\frac{1}{\sqrt{2}}(1 \mp \frac{V_-^2 + V_+^2/2}{2\sqrt{2}V_-U} + \frac{V_-^2 + V_+^2/2}{2U^2})|0;\uparrow\downarrow,0\rangle \pm \frac{V_+}{\sqrt{2}U}|S2ex\rangle \\ &\mp \frac{1}{\sqrt{2}}(1 \pm \frac{V_-^2 + V_+^2/2}{2\sqrt{2}V_-U} - \frac{V_-^2 + V_+^2/2}{2U^2})|S2\rangle \pm \frac{V_-}{U}|\uparrow\downarrow;0,0\rangle\Big) \end{aligned} \tag{C.15}$$

with $N_2^2 = 1 + \frac{(V_-^2+V_+^2/2)^2}{8V_-^2U^2} + \frac{(V_-^2+V_+^2/2)}{U^2}$.

Other states contributing to order V^2/U^2 are again the triplet state

$$|T2\rangle \equiv \frac{1}{\sqrt{2}}\Big(|\uparrow;\downarrow,0\rangle + |\downarrow;\uparrow,0\rangle\Big) \tag{C.16}$$

and the $S_z = -2$ state

$$|\downarrow;\downarrow,0\rangle \tag{C.17}$$

with energies $\epsilon_{T2} = -2\mu$.

Green Function

We can now determine the Green function, which is found to be

$$G(i\omega_n) = \frac{1}{4}\Bigg(\tag{C.18}$$
$$\frac{1-\frac{V_+^2+V_-^2/2}{\sqrt{2}V_+U}+\frac{\sqrt{2}V_+}{U}-\frac{V_-^2+V_+^2/2}{U^2}}{i\omega+\mu-U+\sqrt{2}V_+}+\frac{1+\frac{V_+^2+V_-^2/2}{\sqrt{2}V_+U}-\frac{\sqrt{2}V_+}{U}-\frac{V_-^2+V_+^2/2}{U^2}}{i\omega+\mu-U-\sqrt{2}V_+}+\frac{\frac{3V_+^2}{U^2}}{i\omega+\mu-U}$$
$$\frac{1-\frac{V_-^2+V_+^2/2}{\sqrt{2}V_-U}+\frac{\sqrt{2}V_-}{U}-\frac{V_+^2+V_-^2/2}{U^2}}{i\omega+\mu-\sqrt{2}V_-}+\frac{1+\frac{V_-^2+V_+^2/2}{\sqrt{2}V_-U}-\frac{\sqrt{2}V_-}{U}-\frac{V_+^2+V_-^2/2}{U^2}}{i\omega+\mu+\sqrt{2}V_-}+\frac{\frac{3V_-^2}{U^2}}{i\omega+\mu}\Bigg).$$

We see that upper and lower Hubbard bands are represented by three poles, respectively, which are located at energies $U-\mu\pm\sqrt{V_+}$ and $U-\mu$ for the upper band and at $-\mu\pm\sqrt{V_-}$ and $-\mu$ for the lower band. This is in good agreement with the numerical results even for larger cluster sizes.

In order to close the self-consistency, we have to collapse the respective three poles and determine the new $V_\pm$. Since $V_\pm << U$ the approximation involved is small. The new Green function is then given as

$$G(i\omega_n) = \frac{1}{2}\left(\frac{1-\frac{V_2^2-V_1^2}{U^2}}{i\omega+\mu}+\frac{1+\frac{V_2^2-V_1^2}{U^2}}{i\omega+\mu-U}\right). \tag{C.19}$$

The self-consistency condition now requires that $t^2G = \frac{V_+^2}{i\omega+\mu-U}+\frac{V_-^2}{i\omega+\mu}$. This can be fulfilled *only* for $V_+ = V_-$, which in turn implies that any transfer of weight is the result of the presence of states *at* the chemical potential in the metallic solution.

The insulatinng solution can be used to evaluate the coefficients entering the self-consistently projected low energy Hamiltonian. This is done in Appendix D.

Appendix D

The Self-Consistent Projective Technique: A $1+1$ Site Projected Toy Model

Qualitatively correct insights into the *critical behavior* of the Hubbard model at half filling can be obtained by considering the simplest case of the self-consistently projected effective problem (6.51), in which the low energy bath states are represented by a single site at the Fermi level, i.e. with $\epsilon = 0$. The high energy contributions in this case enter solely via the coefficients J_{pot} and J_{spin}.

The case in which the high energy contributions are treated to *lowest order*, i.e. consist of the high energy states $|0\rangle$ and $\uparrow\downarrow\rangle$ of the impurity only, can be treated easily to order V^4. [1]

The effective low energy Hamiltonian (6.51) derived in Chapter 6 in this case reduces to

$$\begin{aligned}
\mathcal{H}_{eff}^{toy} &= -2V^2 J_{spin}^{(1,toy)} \vec{S}\cdot\vec{s} - \frac{V^2}{2} J_{pot}^{(1,toy)} (n_\uparrow + n_\downarrow) \\
&- 4V^4 \left(\frac{1}{(U-\mu)^3} + \frac{1}{\mu^3} + \frac{1}{\mu^2(U-\mu)} + \frac{1}{\mu(U-\mu)^2} \right) \vec{S}\cdot\vec{s} \\
&+ \frac{V^4}{U-\mu} \left(\frac{1}{(U-\mu)^2} + \frac{1}{\mu^2} + \frac{1}{\mu(U-\mu)} \right) (n_\uparrow + n_\downarrow) \\
&- V^4 \left(\frac{1}{(U-\mu)^3} + \frac{1}{\mu^3} + \frac{2}{\mu^2(U-\mu)} + \frac{2}{\mu(U-\mu)^2} \right) n_{c\uparrow} n_{c\downarrow} \qquad \text{(D.1)}
\end{aligned}$$

[1] Note that the critical behavior obtained from this approach is determined by the same equation as the low frequency behavior of the toy $1+1$ site Anderson model. We will therefore simply show their equivalence and refer the reader to Appendix B for the consequences of the equation determining the critical behavior.

The projected operators (6.65) assume the form

$$\begin{aligned}
F_\uparrow &= -V\Big[(\frac{1}{\mu}-\frac{3V^2}{2\mu^3})|\uparrow\rangle\langle\uparrow|c_\uparrow \\
&- \Big(\frac{1}{U-\mu}-V^2(\frac{3}{(U-\mu)^3}+\frac{1}{2\mu^3}+\frac{5}{2\mu(U-\mu)^2}+\frac{3}{2\mu^2(U-\mu)})\Big)|\downarrow\rangle\langle\downarrow|c_\uparrow \\
&+ \Big(\frac{1}{U-\mu}+\frac{1}{\mu}-V^2(\frac{3}{(U-\mu)^3}+\frac{2}{\mu^3}+\frac{5}{2\mu(U-\mu)^2}+\frac{3}{2\mu^2(U-\mu)})\Big)|\downarrow\rangle\langle\uparrow|c_\downarrow \\
&- V^3\Big(\frac{1}{2(U-\mu)^3}+\frac{3}{2\mu^3}+\frac{3}{2\mu(U-\mu)^2}+\frac{5}{2\mu^2(U-\mu)})\Big)|\uparrow\rangle\langle\uparrow|n_{c\downarrow}c_\uparrow \\
&- V^3\Big(\frac{3}{2(U-\mu)^3}+\frac{1}{2\mu^3}+\frac{5}{2\mu(U-\mu)^2}+\frac{3}{2\mu^2(U-\mu)})\Big)|\downarrow\rangle\langle\downarrow|n_{c\downarrow}c_\uparrow \\
&- V^3\Big(\frac{-1}{(U-\mu)^3}+\frac{1}{\mu^3}+\frac{-1}{\mu(U-\mu)^2}+\frac{1}{\mu^2(U-\mu)})\Big)|\downarrow\rangle\langle\uparrow|n_{c\uparrow}c_\downarrow\Big]. \qquad \text{(D.2)}
\end{aligned}$$

The Hamiltonian can be diagonalized exactly and the low energy Green function is obtained as

$$\begin{aligned}
G_{low}(i\omega_n) &= \langle gs|F_\uparrow\frac{1}{i\omega-(H-E_0)}F_\uparrow^\dagger|gs\rangle+\langle gs|F_\uparrow^\dagger\frac{1}{i\omega+(H-E_0)}F_\uparrow|gs\rangle \\
&\approx \frac{V^2}{2i\omega_n}\Big[\frac{5}{(U-\mu)^2}+\frac{5}{\mu^2}+\frac{8}{\mu(U-\mu)} \qquad \text{(D.3)} \\
&\quad -V^2\Big(\frac{29}{(U-\mu)^4}+\frac{29}{\mu^4}+\frac{48}{\mu^3(U-\mu)}+\frac{48}{\mu(U-\mu)^3}+\frac{44}{\mu^2(U-\mu)^2}\Big)\Big].
\end{aligned}$$

We thus see immediately that by imposing self-consistency we recover the result obtained in (B.15).

A more accurate treatment can be achieved easily in the half-filled case, in which $J_{pot}=0$, such that the high energy contributions can be parametrized by $J_{spin}=2\langle\uparrow|f_\downarrow\frac{1}{H_{at}-E_{at}}f_\uparrow^\dagger|\downarrow\rangle$ only. This can be computed using the $2+1$ insulator solved in Appendix C and one obtains

$$J_{spin}^{(1,2+1)}=-2\frac{2D}{U}(1+\frac{6V_{high}^2}{U^2}). \qquad \text{(D.4)}$$

Since $\mu=U/2$ at half filling, and $J_{spin}=-2\frac{2D}{U}$ if the high energy states are treated to lowest order, we just have to make the replacement $\frac{2D}{U}\to\frac{2D}{U}(1+\frac{6V_{high}^2}{U^2})$ in the equations for Hamiltonian and operators.

The modified self consistency equation then reads

$$1=\frac{9}{4}(\frac{2D}{U})^2(1+\frac{6V_{high}^2}{U^2})^2(1-11V^2(\frac{2D}{U})^2(1+\frac{6V_{high}^2}{U^2})^2). \qquad \text{(D.5)}$$

At half filling the high energy spectral weight and thus V_{high} are given from the sumrule $D^2/4 = 2V_{high}^2 + V^2$, such that we finally obtain the low energy spectral weight as

$$w = 4V^2/D^2 = 0.52\frac{1}{D}(U_c - U) - 0.44\frac{1}{D^2}(U_c - U)^2 + o((U_c - U)^3). \tag{D.6}$$

The value of U_c is obtained as $U_c = 3.22$, which is too high compared to the correct value obtained numerically. This can be attributed to the fact that the low energy part of the $1+1$ toy model yields a spin-spin coupling of $\langle \vec{S} \cdot \vec{s} \rangle = -\frac{3}{4}$ which is considerably larger than the numerically obtained value at half-filling of -0.46.

By using $J_{pot}^{(1,2+1)}$ and $J_{spin}^{(1,2+1)}$ as obtained from the $2+1$ insulator we can also obtain an approximation to the critical μ_c. These coefficients are given as

$$\begin{aligned}
J_{pot}^{(1,2+1)} &= \frac{D}{U-\mu} + \frac{2DV^2}{(U-\mu)^3} - \frac{3DV^2}{2\mu U^2} \\
&- \frac{D}{2}\left(\frac{1 + \frac{V}{2\sqrt{2}U} - \frac{3DV^2}{2U^2}}{\mu - \sqrt{2}V + \frac{V^2}{2U^2}} + \frac{1 - \frac{V}{2\sqrt{2}U} - \frac{3V^2}{2U^2}}{\mu + \sqrt{2}V + \frac{V^2}{2U^2}} \right) \\
J_{spin}^{(1,2+1)} &= -\frac{D}{U-\mu} + \frac{DV^2}{2\mu U^2} + \frac{2DV^2}{U-\mu}\left(\frac{1}{U^2} - \frac{1}{(U-\mu)^2}\right) \\
&- \frac{D}{2}\left(\frac{1 + \frac{V}{2\sqrt{2}U} - \frac{3V^2}{2U^2}}{\mu - \sqrt{2}V + \frac{V^2}{2U^2}} + \frac{1 - \frac{V}{2\sqrt{2}U} - \frac{3V^2}{2U^2}}{\mu + \sqrt{2}V + \frac{V^2}{2U^2}} \right).
\end{aligned} \tag{D.7}$$

The critical μ_c can then be obtained using Eq. (7.40), i.e. the condition

$$1 = -\frac{1}{2}\left(J_{spin}^{(1)2}(\vec{S} \cdot \vec{s} - 3/8) - \frac{1}{8} J_{pot}^{(1)2} \right), \tag{D.8}$$

which together with Eq. (D.7) this leads to the asymptotic value of μ_c for $U \to \infty$, $\mu_c^\infty = 1.03$, i.e. the resonance is just outside the band. Again this is modified, if the correct spin-spin coupling is used.

Appendix E

From Continued Fraction to Partial Fraction – Determining the Poles and Weights of G

As shown in Chapter 2 the single particle Green function can be computed easily using a continued fraction representation, leading to particle and hole contributions of the form

$$\langle f_0^{p/h}|\frac{1}{\omega \mp (H-E_0)}|f_0^{p/h}\rangle = \cfrac{\langle f_0^{p/h}|f_0^{p/h}\rangle}{z - a_0^{p/h} \pm E_0 - \cfrac{b_1^{p/h2}}{z-a_1^{p/h}\pm E_0 - \cfrac{b_2^{p/h2}}{z-a_2^{p/h}\pm E_0 - \ldots}}}} \tag{E.1}$$

where p (h) denotes particle (hole) contributions. In order to obtain information about the position of the poles of the Green function, we would like write this in form of a spectral representation as

$$\langle f_0^{p/h}|\frac{1}{\omega \mp (H-E_0)}|f_0^{p/h}\rangle = \sum_n \frac{\langle f_0^{p/h}|n\rangle\langle n|f_0^{p/h}\rangle}{\omega \mp (E_n - E_0)}, \tag{E.2}$$

i.e. we would like to determine the E_n and the weights $\langle f_0^{p/h}|n\rangle\langle n|f_0^{p/h}\rangle$.

This goal can be achieved easily be noticing that the continued fraction representation of the Green function corresponds to a basis in which the Hamiltonian is *tridiagonal*, i.e. has the form

$$H_{TD} = \begin{pmatrix} a_0^{p/h} \mp E_0 & b_1^{p/h} & 0 & . & . & . & . & . \\ b_1^{p/h} & a_1^{p/h} \mp E_0 & b_2^{p/h} & 0 & . & . & . & . \\ 0 & b_2^{p/h} & a_2^{p/h} \mp E_0 & b_3^{p/h} & . & . & . & . \\ . & . & . & . & . & . & . & . \\ . & . & . & . & . & . & . & b_n^{p/h} \\ . & . & . & . & . & 0 & b_n^{p/h} & a_n^{p/h} \mp E_0 \end{pmatrix} \tag{E.3}$$

where the states $|f_n\rangle$ are arranged in the order $n = 0, ...n$ and where $\langle f_n|f_i\rangle = 0$ for $i < n$, i.e. the a given state is othogonal to all previous states.

We can now diagonalize the tridiagonal Hamiltonian, i.e. find a basis transformation

$$|\eta_\mu\rangle = \sum_j \alpha_{\mu j} |\tilde{f}_j\rangle \tag{E.4}$$

($|\tilde{f}_j\rangle = \frac{1}{\sqrt{\langle f_j|f_j\rangle}}|f_j\rangle$) such that the $|\eta_\mu\rangle$ are eigenstates of the Hamiltonian with corresponding eigenvalues E_μ. This enables us to obtain the Lehmann representation of G as

$$G^{p/h} = \sum_\mu \frac{\langle f_0^{p/h}|\eta_\mu\rangle\langle\eta_\mu|f_0^{p/h}\rangle}{i\omega \mp (E_\mu - E_0)} \tag{E.5}$$

using (E.4) and using the fact that $\langle f_n|f_i\rangle = 0$ for $i < n$ we thus obtain

$$G^{p/h} = \sum_\mu \frac{\alpha_{\mu 0}|\langle f_0^{p/h}|f_0^{p/h}\rangle|}{i\omega \mp (E_\mu - E_0)}. \tag{E.6}$$

We thus see that poles and weights are simply determined by diagonalizing the tridiagonal matrix, which is accomplished easily numerically, using i.e. the Numerical Recipes routine TQLI [68].

Appendix F

Stability of $d = \infty$ Solutions

In this appendix, we describe a method that can be used to examine the local stability of the $d = \infty$ self-consistency equations, Eqs. (9.2)-(9.5). The method is based on the observation that these equations can be derived using a variational approach, by extremizing a certain functional, in analogy with standard Landau-Ginsburg formulations of mean-field theory.

In the present case, this functional takes a form

$$F[\mathbf{G}_\sigma(i\omega_n)] = -\frac{1}{2}t^2\frac{1}{\beta}\sum_\sigma\sum_{\omega_n} tr[\mathbf{G}^2_\sigma(\omega_n)] + F_{imp}[\mathbf{G}_\sigma(i\omega_n)], \tag{F.1}$$

where $F_{imp}[\mathbf{G}_\sigma(i\omega_n)]$ is the free energy of the two-impurity model as defined by the action of Eqs. (9.4) and (9.5)

$$F_{imp}[\mathbf{G}_\sigma(i\omega_n)] = -\frac{1}{\beta}\ln\int Dc^*Dc e^{-S_{eff}[\mathbf{G}_\sigma(i\omega_n)]}. \tag{F.2}$$

Here, we consider Eqs. (9.4)-(9.5) as a *definition* of the effective action, so that $F[\mathbf{G}_\sigma(i\omega_n)]$ is a functional of a *arbitrary*, yet unspecified function $\mathbf{G}_\sigma(i\omega_n)$.

In analogy with conventional Landau-Ginsburg formulation, we think of $\mathbf{G}_\sigma(i\omega_n)$ as an order parameter (function), and the mean-field equations are then obtained by extremizing the above functional with respect to variations in the form of $\mathbf{G}_\sigma(i\omega_n)$. The extremum condition reads

$$\frac{\delta F[\mathbf{G}]}{\delta \mathbf{G}_\sigma(i\omega_n)} = 0, \tag{F.3}$$

giving

$$\mathbf{G}_\sigma(i\omega_n) = \mathbf{G}^{imp}_\sigma(i\omega_n). \tag{F.4}$$

Here, $\mathbf{G}^{imp}_\sigma(i\omega_n)$ is the local Green function of the impurity model corresponding to a *fixed* "bath" Green's function $\mathbf{G}_\sigma(i\omega_n)$

$$\mathbf{G}^{imp}_\sigma(i\omega_n) = \langle c^*_\sigma(i\omega_n)\ c_\sigma(i\omega_n)\rangle_{S_{eff}[G]}. \tag{F.5}$$

Note that $\mathbf{G}_\sigma^{imp}(i\omega_n)$ is also a *functional* of $\mathbf{G}_\sigma(i\omega_n)$.

Obviously, Eq. (F.5) is identical to Eq. (9.3), so that we recover the $d = \infty$ the self-consistency conditions Eq. (9.2)-(9.5).

Before going further, it is worthwhile to comment on the physical interpretation of the functional of Eqs. (F.1)-(F.2). Using the expressions for the free energy of $d = \infty$ models [53], it is not difficult to show that our functional reduces to the *free energy*, when evaluated for the value of $\mathbf{G}_\sigma(i\omega_n)$ corresponding to the solutions of the self-consistency conditions, Eqs. (9.2)-(9.5). We conclude that $F[\mathbf{G}]$ represents a *free energy functional*, in the usual Landau-Ginsburg sense.

When the self-consistency conditions are solved numerically, one typically makes an initial guess for $\mathbf{G}_\sigma(i\omega_n)$, defining the effective action of the impurity model using Eq. (9.5). The impurity model is then solved by any method available, and a *new* value of $\mathbf{G}_\sigma(i\omega_n)$ obtained from Eq. (9.3). In numerical analysis, this iterative procedure is known as the "substitution-iteration method", which is repeated until convergence is reached. In the following, we prove a general theorem that such an iterative procedure converges towards a local (nearest) *minimum* of the free energy functional. We note that the set of all possible functions $\mathbf{G}_\sigma(i\omega_n)$ form a vector space (more precisely an infinite dimensional Hilbert space), and for notational simplicity, denote these vectors by $\mathbf{x}$.

We define the *gradient* vector field $\mathbf{g}(\mathbf{x})$ as

$$\mathbf{g}(\mathbf{x}) = \partial_{\mathbf{x}} F[\mathbf{x}], \tag{F.6}$$

so that Eq. (F.3) can be written as

$$\mathbf{g}(\mathbf{x})|_{\mathbf{x}=\mathbf{x}_o} = 0. \tag{F.7}$$

Here, $\mathbf{x}_o$ corresponds to the solution of the self-consistency condition, i. e. a local stationary point of $F[\mathbf{x}]$. If we define further the quantity

$$\mathbf{f} = \mathbf{x} - \mathbf{g}(\mathbf{x}), \tag{F.8}$$

we find that at the stationary point

$$\mathbf{x}_o = \mathbf{f}(\mathbf{x}_o). \tag{F.9}$$

In this language, the "substitution-iteration' search for the solution can be written as

$$\mathbf{x}(n+1) = \mathbf{f}(\mathbf{x}(n)), \tag{F.10}$$

and the solution corresponds to

$$\mathbf{x}_o = \lim_{n\to\infty} \mathbf{x}(n). \tag{F.11}$$

Note that the *increment* of $\mathbf{x}(n)$ can be also written as

$$\Delta\mathbf{x}(n) = \mathbf{x}(n+1) - \mathbf{x}(n) \;=\; -\mathbf{g}(\mathbf{x}(n)). \tag{F.12}$$

As we can see, the iteration takes the vector $\mathbf{x}$ in the direction opposite to the gradient, i. e. "down the hill" , so that the iteration converges only in the vicinity of a *local minimum.*

On general grounds, we expect the physical solutions near first-order transitions to be *locally stable.* We can check this stability, by making a small modification in the initial conditions that produce the respective solutions. More precisely, we should first find the convergent metallic and insulating solutions $\mathbf{x}_o^M$ and $\mathbf{x}_o^I$. We can then examine the stability of, for example, the insulating solution by re-starting the iteration search from a new initial guess

$$\mathbf{x}^i(n=0) = (1-c)\mathbf{x}_o^I + c\mathbf{x}_o^M. \tag{F.13}$$

The solution is locally stable if for c sufficiently small the iteration procedure converges to $\mathbf{x} = \mathbf{x}_o^I$. We can similarly check the stability of the metallic solution by choosing $c \approx 1$.

In order to apply these ideas, we first test them in the well examined limit corresponding to $t_{ab} = 0$. We find that the metallic solution is stable throughout the coexistence region, but that the insulating solution becomes unstable as $T \to 0$. These findings are in complete agreement with the well established fact [69] that U_{c2} is a $T = 0$ critical point at which (upon reducing U) the insulating solution becomes unstable, and a new metallic solution emerges. We can apply these ideas for $t_{ab} \neq 0$, in which case *both* solutions are found to be locally stable, in agreement with a first-order scenario.

We conclude this discussion by an explicit construction of the "Landau-Ginsburg" functional, which represents a nice illustration of the above stability considerations. To do this, we note that in the case of the $d = \infty$ equations, the gradient vector takes the form

$$\mathbf{g} = \mathbf{G}^{imp}[\mathbf{G}] - \mathbf{G}, \tag{F.14}$$

which can be calculated by any method that solves the Anderson impurity model, e.g. the YY approach [58]. Once the gradient is available, it is possible to determine the evolution of $F[\mathbf{x}]$ along any particular direction in the $\mathbf{x}$ space. In particular, we expect the physical solutions to be local minima, separated by an unstable solution (local maximum or a saddle-point). It is thus useful to consider the direction (vector) connecting the two solutions, which can be parametrized as

$$\mathbf{x}(\ell) = (1 - \ell)\mathbf{x}_o^I + \ell \mathbf{x}_o^M. \tag{F.15}$$

The *increment* of $F[\mathbf{x}(\ell)]$ can be expressed as a line integral

$$\Delta F(\ell) = F[\mathbf{x}(\ell)] - F[\mathbf{x}_o^I] = \int_0^1 d\ell \cdot \mathbf{g}(\mathbf{x}(\ell)). \tag{F.16}$$

We can numerically compute this line integral by an appropriate discretization procedure, and typical results in the $t_{ab} = 0$ limit are plotted in Fig. (F.1). Here, we show $\Delta F(\ell)$ for $U = 2.5$ and for several different temperatures. As we can see, at $T \neq 0$ *both* the metallic and the insulating solution are locally stable, but the insulating one becomes unstable as $T \to 0$, in agreement with our stability considerations. We also note that as the temperature is increased, the free energy of the metallic solution ($\ell = 1$) increases, until the *spinodal* is reached, where the local minimum becomes an inflection point and becomes even locally unstable. Of course, this instability is *preempted* by a first order transition, which in this case happens at finite temperature, in agreement with findings of Refs. [12, 56].

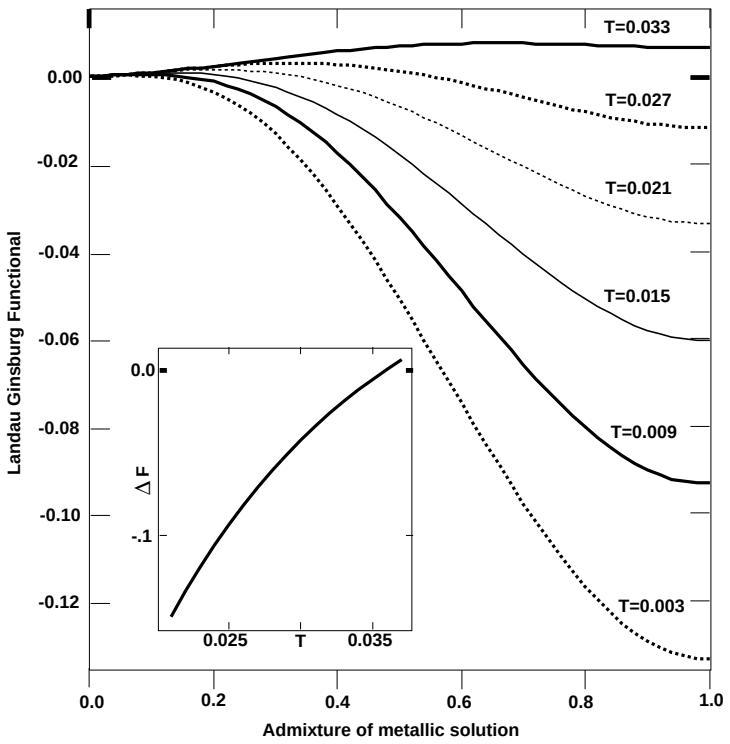

Figure F.1: Landau free energy for $t_{ab} = 0$, $U = 2.6$ and temperatures $T = 0.003 - 0.033$ in steps of $\Delta T = 0.006$. The inset shows the free energy difference between the two minima as a function of temperature.

References

[1] J. G. Bednorz and K. A. Müller. *Z. Phys. B*, 64:189, 1986.

[2] C. M. Varma, P. B. Littlewood, S. Schmitt-Rink, E. Abrahams and A. E. Ruckenstein. *Phys. Rev. Lett.*, 63:1996, 1989.

[3] A. M. Tsvelick, P. B. Wiegmann. *Adv. Phys*, 32:453, 1983; N. Andrei, F. Furuya, J. H. Loewenstein. *Rev. Mod. Phys.*, 55:331, 1983.

[4] A. C. Hewson. *The Kondo Problem to Heavy Fermions*. Cambridge University Press, Cambridge, 1993.

[5] D. Vollhardt. *Rev. Mod. Phys.*, 56:99, 1984.

[6] For a review of heavy fermion materials see, for example: N. Grewe, and F. Steglich, in *Handbook on Physics and Chemistry of Rare Earths*, edited by K. A. Gschneidner, Jr. and L. Eyring. Elsevier Science Publishers B. V., 1991.

[7] N. F. Mott. *Metal-Insulator Transitions*. Taylor and Francis, London, (1990).

[8] H. Romberg, M. Alexander, N. Nücker, P. Adelmann, and J. Fink. *Phys. Rev. B*, 42:8768, 1990.

[9] M. A. van Veenendaal, R. Schlatmann, and G. A. Sawatzky, W. A. Groen. *Phys. Rev. B*, 47:446, 1993.

[10] J. W. Allen et al. *Phys. Rev. Lett.*, 64:595, 1990; *Physica B.* 171:175, 1991.

[11] C.T. Chen et al. *Phys. Rev. Lett.*, 66:104, 1991.

[12] M. J. Rozenberg, G. Kotliar, and X. Y. Zhang. *Phys. Rev. B*, 49:10181, 1994.

[13] M. J. Rozenberg, G. Kotliar, and H. Kajueter. Rutgers University Preprint, 1994.

[14] P. W. Anderson. *Science*, 235:1196, 1987.

[15] C. M. Varma and T. Giamarchi. *Model for Copper-Oxide Metals and Superconductors*. Notes for the lectures presented at the Ecole de Physique Théorique des Houches at the session on "Strongly Interacting Fermions and High-T_c Superconductivity", August 1990.

[16] G. D. Mahan. *Many-Particle Physics*. Plenum Press, New York, 1990.

[17] E. H. Lieb and F. Y. Wu, *Phys. Rev. Lett.*, 20:1445, 1968.

[18] B. Sutherland. *An Introduction to the Bethe Ansatz* in *Exactly Solvable Problems in Condensed Matter and Relativistic Field Theory*, ed. S. Shastry, S. S. Jha, V. Singh, 1985.

[19] M. J. Rozenberg, X. Y. Zhang and G. Kotliar. *Phys. Rev. Lett.*, 69:1236, 1992.

[20] M. Jarrell. *Phys. Rev. Lett.*, 69:168, 1992.

[21] A. Georges and W. Krauth. *Phys. Rev. Lett.*, 69:1240, 1992.

[22] J. Hubbard. *Proc. Roy. Soc. A*, 276:238, 1963.

[23] J. Hubbard. *Proc. Roy. Soc. A*, 277:237, 1964.

[24] J. Hubbard. *Proc. Roy. Soc. A*, 281:401, 1964.

[25] M. C. Gutzwiller. *Phys. Rev.*, 137:A1726, 1965.

[26] W. F. Brinkman and T. M. Rice. *Phys. Rev. B*, 2:4302, 1970.

[27] H. Yokoyama and H. Shiba. *J. Phys. Soc. Jpn.*, 56:1490, 1987; ibid. 56:3570, 1987; ibid. 56:3582, 1987.

[28] F. Gebhard. *Phys. Rev. B*, 41:9452, 1990.

[29] P. Coleman. *Phys. Rev. B*, 29:3035, 1984.

[30] N. Read, D. N. Newns. *J. Phys. C*, 16:3273, 1983.

[31] G. Kotliar. *The Large-N Expansion in the Strong Correlation Problem.* Lectures delivered at the Les Houches summer school on strongly correlated Fermi systems, August 1991.

[32] G. Kotliar and A. E. Ruckenstein. *Phys. Rev. Lett.*, 57:1362, 1986.

[33] Th. Pruschke and N. Grewe. *Z. Phys. B*, 74:439, 1989.

[34] E. Dagotto. *Correlated Electrons in High Temperature Superconductors.* Submitted to Rev. Mod. Phys.

[35] Marcel Meinders. *Low-Energy Spectral Weights in Correlated Systems.* Ph. D. Thesis, University of Groningen, 1993.

[36] D. Vollhardt. *Correlated Electron Systems*, ed. V. Emery, World Scientific, Singapore, 1993.

[37] G. Kotliar. *The Mean-Field Theory of the Mott-Hubbard Transition*, Rutgers University Preprint.

[38] *Field Theories of Condensed Matter Systems.* Addison-Wesley, Menlo Park, 1991.

[39] *Electron Correlations in Molecules and Solids.* Springer Verlag, Berlin, 1991.

[40] M. Caffarel and W. Krauth. *Phys. Rev. Lett.* 72:1545, 1994.

[41] A. Georges and G. Kotliar. *Phys. Rev. B* 45:6479, 1992.

[42] K. G. Wilson. *Rev. Mod. Phys.*, 47:773, 1975.

[43] J. W. Negele, H. Orland. *Quantum Many-Particle Systems.* Addison-Wesley Publishing Company, 1988.

[44] W. Metzner and D. Vollhardt. *Phys. Rev. Lett.*, 62:324, 1989.

[45] G. Czycholl and Q. Qin. *Phys. Rev. Lett.*, 62:3244, 1992.

[46] E. Müller-Hartmann. *Z. Phys. B*, 74:507, 1989; *Z. Phys. B*, 76:211, 1989.

[47] H. Schweitzer and G. Czycholl. *Solid State Commun.*, 69:171, 1989.

[48] W. Metzner. *Z. Phys. B*, 77:253, 1989.

[49] W. Metzner and D. Vollhardt. *Phys. Rev. Lett.*, 59:121, 1987; *Phys. Rev. B*, 37:7382, 1988.

[50] U. Brandt and C. Mielsch. *Z. Phys. B*, 75:365, 1989, 79:295, 1990, 82:37, 1991.

[51] V. Dobrosavljević, G. Kotliar. *Acta Physica Polonica A*, 85:21, 1994; *Physical Review B*, 50:1430, 1994.

[52] G. Baym and L.P. Kadanoff. *Phys. Rev.* 124:287, 1961.

[53] A. Georges, G. Kotliar and Q. Si. *Int. J. Mod. Phys. B*, 6:705, 1992.

[54] A. Georges and G. Kotliar. Private communication.

[55] Q. Si, G. Kotliar, A. Georges. *Phys. Rev. B* 46:1261, 1992.

[56] A. Georges, W. Krauth. *Phys. Rev. B* 48:7167, 1993.

[57] X. Y. Zhang, M. J. Rozenberg and G. Kotliar. *Phys. Rev. Lett.*, 70:1666, 1993.

[58] K. Yoshida and K. Yamada. *Prog. Theor. Phys.*, N46:244, 1970.

[59] K. Yamada. *Prog. Theor. Phys.*, 53:970, 1975.

[60] K. Yoshida and K. Yamada. *Prog. Theor. Phys.*, 53:1286, 1975.

[61] A. Georges, G. Kotliar and W. Krauth. *Z. Phys. B* 92:313, 1993.

[62] J. Ferrer, A. Martin-Rodero, and F. Flores. *Phys. Rev. B*, 36:6149, 1987.

[63] Q. Si, M. J. Rozenberg, G. Kotliar and A. E. Ruckenstein. *Phys. Rev. Lett.*, 72:2761, 1994.

[64] H. Q. Lin and J. E. Gubernatis. *Computers in Physics*, 7:400, 1993.

[65] E. R. Davidson. *Computers in Physics*, 7:519, 1993.

[66] E. Gagliano, et al. *Phys. Rev. B*, 34:1677, 1986.

[67] E. R. Gagliano and C. A. Balseiro. *Phys. Rev. Lett.*, 59:2999, 1987.

[68] W. H. Press, S. A. Teukolsky, W. T. Vetterling, B. P. Flannery. *Numerical Recipes in Fortran*. Cambridge University Press, 2nd ed., 1992.

[69] M. J. Rozenberg, G. Moeller and G. Kotliar. *Modern Physics Letters B*, 8:535, 1994.

[70] L. M. Falicov and J. C. Kimball. *Phys. Rev. Lett.*, 22:997, 1969.

[71] A. E. Ruckenstein and C. M. Varma. *Proceedings of the Third International Conference on High T_c Superconductivity*. Kanazawa, Japan, 1991.

[72] F. Marsiglio, et al. *Phys. Rev. B*, 43:10882, 1991 and references therein.

[73] R. J. Elliot, J. A. Krumhansl, and P. L. Leath. *Rev. Mod. Phys.*, 46:465, 1974.

[74] A. Khurana. *Phys. Rev. Lett.*, 64:1990, 1990.

[75] J. R. Schrieffer. *Theory of Superconductivity*. Benjamin, Reading, Mass., 1964.

[76] M. Foëx. *C.R. Acad. Sci. Paris B*, 223:1126, 1946.

[77] N.F. Mott. *Proc. Roy. Soc. Sci. A*, 62:416, 1949.

[78] P. W. Anderson. *Phys. Rev.*, 115:2, 1959.

[79] P. W. Anderson. 50 Years of the Mott Phenomenon. Lecture series given at the Varenna summer school "Frontiers and Borderlines in Many Particle Physics", 1987.

[80] R. Haydock. *The Recursion Method and Its Applications*. Springer-Verlag, Berlin, Heidelberg, 1985.

[81] M. Lavagna. *Phys. Rev. B*, 41:142, 1990.

[82] M. Imada. Technical Report of ISSP, Ser.A No. 2641.

[83] N. Furukawa and M. Imada. *Physica B*, 186:931, 1993.

[84] H. Matsumoto, M. Sasaki and M. Tachiki. *Solid State Commun.*, 71:829, 1989.

[85] H. Eskes, M. Meinders, and G. A. Sawatzky. *Phys. Rev. Lett.*, 67:1035, 1991.

[86] M. Rozenberg. Private Communication.

[87] A. E. Ruckenstein and C. M. Varma. *Preprint*, 1992.

[88] G. Möller, A. E. Ruckenstein, and S. Schmitt-Rink. *Phys. Rev. B*, 46:7427, 1992.

[89] M. Meinders, H. Eskes, and G. A. Sawatzky. *Phys. Rev. B*, 48:3916, 1993.

[90] J. R. Schrieffer and P. A. Wolff. *Phys. Rev.* 149:491, 1966.

[91] I. Shavitt and L. T. Redmon. *J. Chem. Phys.*, 73:5711, 1980.

[92] N. F. Mott. *Phil. Mag.*, 6:287, 1961.

[93] G. Moeller, Q. Si, G. Kotliar, and M. J. Rozenberg, D. S. Fisher. Rutgers University Preprint, 1994.

[94] E. Dagotto and A. Moreo. *Phys. Rev. D*, 31:865, 1985.

[95] G. Kotliar. Private communication.

[96] H. Shiba. *Prog. Theor. Phys.*, 54:1153, 1975.

[97] Th. Pruschke, D. L. Cox, and M. Jarrell. *Phys. Rev. B*, 47:3553, 1993.

[98] A. Fujimori et al. *Phys. Rev. Lett.*, 69:1796, 1992.

[99] F. Lichtenberg et al. *Z. Phys. B*, 82:216, 1991.

[100] Y. Tokura et al. *Phys. Rev. Lett.* 70:2126, 1993.

[101] C. Castellani, G. Kotliar, R. Raimondi, M. Grilli, Z. Wang, and M. Rozenberg. *Phys. Rev. Lett.*, 68:2009, 1992.

[102] For a review see the articles by C. H. Pennington and C. P. Slichter, N. P. Ong, Y. Iye in *Physical Properties of High Temperature Superconductors*. edited by D. M. Ginsberg. World Scientific, Singapore, 1990.

[103] M. Jarrell, Th. Pruschke. *Z.Phys. B*, 90:187, 1993.

[104] M. Jarrell, Th. Pruschke. *Phys. Rev. B*, 49:1458, 1994.

[105] E. Müller-Hartmann. *Z. Phys. B*, 57:281, 1984.

[106] V. Dobrosavljević and G. Kotliar. *Phys. Rev. Lett.*, 71:3218, 1993.

[107] P. Coleman and J. Gan. *Physica B* , 1991. J. Gan and P. Coleman. *Phys. Rev. Lett.* 68:3476, 1992.

[108] For a recent review of doped semiconductors, see M. A. Paalanen, R. N. Bhatt. *Physica B*,169:231, 1991.

[109] R. N. Bhatt, D. S. Fisher. *Phys. Rev. Lett.*, 68:3072, 1992.

[110] V. Dobrosavljević, T. R. Kirkpatrick, G. Kotliar. *Phys. Rev. Lett.*, 69:1113, 1992.

[111] M. A. Paalanen, J. E. Graebner, R. N. Bhatt, S. Sachdev. *Phys. Rev. Lett.*, 61:597, 1988.

[112] R. N. Bhatt, P. A. Lee. *Phys. Rev. Lett.*, 48:344, 1982; D. S. Fisher. *Phys. Rev. Lett.*, 69:534, 1992.

[113] R. M. Fye, J. E. Hirsch, D. J. Scalapino. *Phys. Rev. B*, 35:4901, 1987.

[114] V. Zlatić and B. Horvatić. *Phys. Rev. B*, 28:6904, 1983.

[115] B. A. Jones, C. M. Varma, and J. W. Willkins. *Phys. Rev. Lett.*, 61:125, 1988; A. J. Millis, B. G. Kotliar, B. A. Jones, in *Field Theories in Condensed matter Physics: A Workshop*, ed. by Z. Tesanovic. Addison Wesley, New York, 1990.

[116] J. W. Rasul and P. Schlottmann. *Phys. Rev. Lett.*, 62:1701, 1989; P. Schlottmann and J. W. Rasul. *Physica B*, 163:544, 1990; S. Barle and A. E. Ruckenstein (unpublished).

[117] M. Grilli, G. Kotliar. *Phys. Rev. Lett.*, 64:1170, 1990; C. Castellani, M. Grilli, G. Kotliar. *Phys. Rev. B*, 43:8000, 1991.

[118] Q. Si and G. Kotliar. *Phys. Rev. Lett.*, 70:3143, 1993.

[119] Q. Si and G. Kotliar, *Phys. Rev. B*, 48:13881, 1993.

[120] H. Kajueter. Private communication.

Vita

Goetz Moeller

1984 Graduated from Goethe Oberschule, Berlin, Germany.

1985-88 Attended the Universität Hamburg, Hamburg, Germany. Majored in Physics, Minored in Philosophy.

1987 Vordiplom in Physics, Universität Hamburg.

1988-89 Graduate work at the University of Alabama, Tuscaloosa, Alabama. Fulbright Scholar.

1988-89 Teaching Assistant, Department of Physics, University of Alabama.

1989 M.Sc. in Physics, University of Alabama.

1988-94 Graduate work in Physics, Rutgers, The State University of New Jersey, New Brunswick, New Jersey.

1989-92 Teaching Assistant, Department of Physics, Rutgers, The State University of New Jersey, New Brunswick, New Jersey.

1992-94 Graduate Assistant, Department of Physics, Rutgers, The State University of New Jersey, New Brunswick, New Jersey.

1992 Götz Möller and A. E. Ruckenstein, S. Schmitt-Rink, Transfer of spectral weight in an exactly solvable model of strongly correlated electrons in infinite dimensions. ı(Phys. Rev. B), 46:7427-7432.

1994 M. J. Rozenberg, G. Moeller, and G. Kotliar, The metal-insulator transition in the Hubbard model at zero temperature II. ı(Modern Physics Letters B), 8:535-543.

1994 G. Moeller, Q. Si, G. Kotliar, M.J. Rozenberg, D. Fisher, Critical behavior near the Mott transition in the Hubbard model. ı(Rutgers preprint)

1994 G. Moeller, V. Dobrosavljević, and A. E. Ruckenstein, The two-impurity Kondo lattice. ı(Rutgers preprint)

1994 Ph.D. in Physics.